

Advances in Civil Engineering

# Advances in Planning, Design, Construction, and Management of Road Infrastructure

Lead Guest Editor: Markus Oeser

Guest Editors: Anupam Kumar, Pengfei Liu, Kun An, and Guoyang Lu





---

**Advances in Planning, Design, Construction,  
and Management of Road Infrastructure**



Advances in Civil Engineering

---

**Advances in Planning, Design,  
Construction, and Management of Road  
Infrastructure**

Lead Guest Editor: Markus Oeser

Guest Editors: Anupam Kumar, Pengfei Liu, Kun  
An, and Guoyang Lu



Copyright © 2022 Hindawi Limited. All rights reserved.

This is a special issue published in "Advances in Civil Engineering." All articles are open access articles distributed under the Creative Commons Attribution License, which permits unrestricted use, distribution, and reproduction in any medium, provided the original work is properly cited.








# Chief Editor

Cumaraswamy Vipulanandan, USA













## Associate Editors

Chiara Bedon , Italy  
Constantin Chalioris , Greece  
Ghassan Chehab , Lebanon  
Ottavia Corbi, Italy  
Mohamed ElGawady , USA  
Husnain Haider , Saudi Arabia  
Jian Ji , China  
Jiang Jin , China  
Shazim A. Memon , Kazakhstan  
Hossein Moayedi , Vietnam  
Sanjay Nimbalkar, Australia  
Giuseppe Oliveto , Italy  
Alessandro Palmeri , United Kingdom  
Arnaud Perrot , France  
Hugo Rodrigues , Portugal  
Victor Yepes , Spain  
Xianbo Zhao , Australia

## Academic Editors

José A.F.O. Correia, Portugal  
Glenda Abate, Italy  
Khalid Abdel-Rahman , Germany  
Ali Mardani Aghabaglou, Turkey  
José Aguiar , Portugal  
Afaq Ahmad , Pakistan  
Muhammad Riaz Ahmad , Hong Kong  
Hashim M.N. Al-Madani , Bahrain  
Luigi Aldieri , Italy  
Angelo Aloisio , Italy  
Maria Cruz Alonso, Spain  
Filipe Amarante dos Santos , Portugal  
Serji N. Amirkhania, USA  
Eleftherios K. Anastasiou , Greece  
Panagiotis Ch. Anastasopoulos , USA  
Mohamed Moafak Arbili , Iraq  
Farhad Aslani , Australia  
Siva Avudaiappan , Chile  
Ozgur BASKAN , Turkey  
Adewumi Babafemi, Nigeria  
Morteza Bagherpour, Turkey  
Qingsheng Bai , Germany  
Nicola Baldo , Italy  
Daniele Baraldi , Italy

Eva Barreira , Portugal  
Emilio Bastidas-Arteaga , France  
Rita Bento, Portugal  
Rafael Bergillos , Spain  
Han-bing Bian , China  
Xia Bian , China  
Huseyin Bilgin , Albania  
Giovanni Biondi , Italy  
Hugo C. Biscaia , Portugal  
Rahul Biswas , India  
Edén Bojórquez , Mexico  
Giosuè Boscato , Italy  
Melina Bosco , Italy  
Jorge Branco , Portugal  
Bruno Briseghella , China  
Brian M. Broderick, Ireland  
Emanuele Brunesi , Italy  
Quoc-Bao Bui , Vietnam  
Tan-Trung Bui , France  
Nicola Buratti, Italy  
Gaochuang Cai, France  
Gladis Camarini , Brazil  
Alberto Campisano , Italy  
Qi Cao, China  
Qixin Cao, China  
Iacopo Carnacina , Italy  
Alessio Cascardi, Italy  
Paolo Castaldo , Italy  
Nicola Cavalagli , Italy  
Liborio Cavaleri , Italy  
Anush Chandrappa , United Kingdom  
Wen-Shao Chang , United Kingdom  
Muhammad Tariq Amin Chaudhary, Kuwait  
Po-Han Chen , Taiwan  
Qian Chen , China  
Wei Tong Chen , Taiwan  
Qixiu Cheng, Hong Kong  
Zhanbo Cheng, United Kingdom  
Nicholas Chileshe, Australia  
Prinya Chindaprasirt , Thailand  
Corrado Chisari , United Kingdom  
Se Jin Choi , Republic of Korea  
Heap-Yih Chong , Australia  
S.H. Chu , USA  
Ting-Xiang Chu , China

Zhaofei Chu , China  
Wonseok Chung , Republic of Korea  
Donato Ciampa , Italy  
Gian Paolo Cimellaro, Italy  
Francesco Colangelo, Italy  
Romulus Costache , Romania  
Liviu-Adrian Cotfas , Romania  
Antonio Maria D'Altri, Italy  
Bruno Dal Lago , Italy  
Amos Darko , Hong Kong  
Arka Jyoti Das , India  
Dario De Domenico , Italy  
Gianmarco De Felice , Italy  
Stefano De Miranda , Italy  
Maria T. De Risi , Italy  
Tayfun Dede, Turkey  
Sadik O. Degertekin , Turkey  
Camelia Delcea , Romania  
Cristoforo Demartino, China  
Giuseppe Di Filippo , Italy  
Luigi Di Sarno, Italy  
Fabio Di Trapani , Italy  
Aboelkasim Diab , Egypt  
Thi My Dung Do, Vietnam  
Giulio Dondi , Italy  
Jiangfeng Dong , China  
Chao Dou , China  
Mario D'Aniello , Italy  
Jingtao Du , China  
Ahmed Elghazouli, United Kingdom  
Francesco Fabbrocino , Italy  
Flora Faleschini , Italy  
Dingqiang Fan, Hong Kong  
Xueping Fan, China  
Qian Fang , China  
Salar Farahmand-Tabar , Iran  
Ilenia Farina, Italy  
Roberto Fedele, Italy  
Guang-Liang Feng , China  
Luigi Fenu , Italy  
Tiago Ferreira , Portugal  
Marco Filippo Ferrotto, Italy  
Antonio Formisano , Italy  
Guoyang Fu, Australia  
Stefano Galassi , Italy


Junfeng Gao , China  
Meng Gao , China  
Giovanni Garcea , Italy  
Enrique García-Macías, Spain  
Emilio García-Taengua , United Kingdom  
DongDong Ge , USA  
Khaled Ghaedi, Malaysia  
Khaled Ghaedi , Malaysia  
Gian Felice Giaccu, Italy  
Agathoklis Giaralis , United Kingdom  
Ravindran Gobinath, India  
Rodrigo Gonçalves, Portugal  
Peilin Gong , China  
Belén González-Fonteboa , Spain  
Salvatore Grasso , Italy  
Fan Gu, USA  
Erhan Güneyisi , Turkey  
Esra Mete Güneyisi, Turkey  
Pingye Guo , China  
Ankit Gupta , India  
Federico Gusella , Italy  
Kemal Hacıfendioglu, Turkey  
Jianyong Han , China  
Song Han , China  
Asad Hanif , Macau  
Hadi Hasanzadehshooiili , Canada  
Mostafa Fahmi Hassanein, Egypt  
Amir Ahmad Hedayat , Iran  
Khandaker Hossain , Canada  
Zahid Hossain , USA  
Chao Hou, China  
Biao Hu, China  
Jiang Hu , China  
Xiaodong Hu, China  
Lei Huang , China  
Cun Hui , China  
Bon-Gang Hwang, Singapore  
Jijo James , India  
Abbas Fadhil Jasim , Iraq  
Ahad Javanmardi , China  
Krishnan Prabhakan Jaya, India  
Dong-Sheng Jeng , Australia  
Han-Yong Jeon, Republic of Korea  
Pengjiao Jia, China  
Shaohua Jiang , China



MOUSTAFA KASSEM , Malaysia  
Mosbeh Kaloop , Egypt  
Shankar Karuppanan , Ethiopia  
John Kechagias , Greece  
Mohammad Khajehzadeh , Iran  
Afzal Husain Khan , Saudi Arabia  
Mehran Khan , Hong Kong  
Manoj Khandelwal, Australia  
Jin Kook Kim , Republic of Korea  
Woosuk Kim , Republic of Korea  
Vaclav Koci , Czech Republic  
Loke Kok Foong, Vietnam  
Hailing Kong , China  
Leonidas Alexandros Kouris , Greece  
Kyriakos Kourousis , Ireland  
Moacir Kripka , Brazil  
Anupam Kumar, The Netherlands  
Emma La Malfa Ribolla, Czech Republic  
Ali Lakirouhani , Iran  
Angus C. C. Lam, China  
Thanh Quang Khai Lam , Vietnam  
Luciano Lamberti, Italy  
Andreas Lampropoulos , United Kingdom  
Raffaele Landolfo, Italy  
Massimo Latour , Italy  
Bang Yeon Lee , Republic of Korea  
Eul-Bum Lee , Republic of Korea  
Zhen Lei , Canada  
Leonardo Leonetti , Italy  
Chun-Qing Li , Australia  
Dongsheng Li , China  
Gen Li, China  
Jiale Li , China  
Minghui Li, China  
Qingchao Li , China  
Shuang Yang Li , China  
Sunwei Li , Hong Kong  
Yajun Li , China  
Shun Liang , China  
Francesco Liguori , Italy  
Jae-Han Lim , Republic of Korea  
Jia-Rui Lin , China  
Kun Lin , China  
Shibin Lin, China

Tzu-Kang Lin , Taiwan  
Yu-Cheng Lin , Taiwan  
Hexu Liu, USA  
Jian Lin Liu , China  
Xiaoli Liu , China  
Xuemei Liu , Australia  
Zaobao Liu , China  
Zhuang-Zhuang Liu, China  
Diego Lopez-Garcia , Chile  
Cristiano Loss , Canada  
Lyan-Ywan Lu , Taiwan  
Jin Luo , USA  
Yanbin Luo , China  
Jianjun Ma , China  
Junwei Ma , China  
Tian-Shou Ma, China  
Zhongguo John Ma , USA  
Maria Macchiaroli, Italy  
Domenico Magisano, Italy  
Reza Mahinroosta, Australia  
Yann Malecot , France  
Prabhat Kumar Mandal , India  
John Mander, USA  
Iman Mansouri, Iran  
André Dias Martins, Portugal  
Domagoj Matesan , Croatia  
Jose Matos, Portugal  
Vasant Matsagar , India  
Claudio Mazzotti , Italy  
Ahmed Mebarki , France  
Gang Mei , China  
Kasim Mermerdas, Turkey  
Giovanni Minafò , Italy  
Masoomah Mirrashid , Iran  
Abbas Mohajerani , Australia  
Fadzli Mohamed Nazri , Malaysia  
Fabrizio Mollaioli , Italy  
Rosario Montuori , Italy  
H. Naderpour , Iran  
Hassan Nasir , Pakistan  
Hossein Nassiraei , Iran  
Satheeskumar Navaratnam , Australia  
Ignacio J. Navarro , Spain  
Ashish Kumar Nayak , India  
Behzad Nematollahi , Australia

Chayut Ngamkhanong , Thailand  
Trung Ngo, Australia  
Tengfei Nian, China  
Mehdi Nikoo , Canada  
Youjun Ning , China  
Olugbenga Timo Oladinrin , United Kingdom  
Oladimeji Benedict Olalusi, South Africa  
Timothy O. Olawumi , Hong Kong  
Alejandro Orfila , Spain  
Maurizio Orlando , Italy  
Siti Aminah Osman, Malaysia  
Walid Oueslati , Tunisia  
SUVASH PAUL , Bangladesh  
John-Paris Pantouvakis , Greece  
Fabrizio Paolacci , Italy  
Giuseppina Pappalardo , Italy  
Fulvio Parisi , Italy  
Dimitrios G. Pavlou , Norway  
Daniele Pellegrini , Italy  
Gatheeshgar Perampalam , United Kingdom  
Daniele Perrone , Italy  
Giuseppe Piccardo , Italy  
Vagelis Plevris , Qatar  
Andrea Pranno , Italy  
Adolfo Preciado , Mexico  
Chongchong Qi , China  
Yu Qian, USA  
Ying Qin , China  
Giuseppe Quaranta , Italy  
Krishanu ROY , New Zealand  
Vlastimir Radonjanin, Serbia  
Carlo Rainieri , Italy  
Rahul V. Ralegaonkar, India  
Raizal Saifulnaz Muhammad Rashid, Malaysia  
Alessandro Rasulo , Italy  
Chonghong Ren , China  
Qing-Xin Ren, China  
Dimitris Rizos , USA  
Geoffrey W. Rodgers , New Zealand  
Pier Paolo Rossi, Italy  
Nicola Ruggieri , Italy  
JUNLONG SHANG, Singapore

Nikhil Saboo, India  
Anna Saetta, Italy  
Juan Sagaseta , United Kingdom  
Timo Saksala, Finland  
Mostafa Salari, Canada  
Ginevra Salerno , Italy  
Evangelos J. Sapountzakis , Greece  
Vassilis Sarhosis , United Kingdom  
Navaratnarajah Sathiparan , Sri Lanka  
Fabrizio Scozzese , Italy  
Halil Sezen , USA  
Payam Shafigh , Malaysia  
M. Shahria Alam, Canada  
Yi Shan, China  
Hussein Sharaf, Iraq  
Mostafa Sharifzadeh, Australia  
Sanjay Kumar Shukla, Australia  
Amir Si Larbi , France  
Okan Sirin , Qatar  
Piotr Smarzewski , Poland  
Francesca Sollecito , Italy  
Rui Song , China  
Tian-Yi Song, Australia  
Flavio Stochino , Italy  
Mayank Sukhija , USA  
Piti Sukontasukkul , Thailand  
Jianping Sun, Singapore  
Xiao Sun , China  
T. Tafsirojjan , Australia  
Fujiao Tang , China  
Patrick W.C. Tang , Australia  
Zhi Cheng Tang , China  
Weerachart Tangchirapat , Thailand  
Xiabin Tao, China  
Piergiorgio Tataranni , Italy  
Elisabete Teixeira , Portugal  
Jorge Iván Tobón , Colombia  
Jing-Zhong Tong, China  
Francesco Trentadue , Italy  
Antonello Troncone, Italy  
Majbah Uddin , USA  
Tariq Umar , United Kingdom  
Muahmmad Usman, United Kingdom  
Muhammad Usman , Pakistan  
Mucteba Uysal , Turkey







Ilaria Venanzi , Italy  
Castorina S. Vieira , Portugal  
Valeria Vignali , Italy  
Claudia Vitone , Italy  
Liwei WEN , China  
Chunfeng Wan , China  
Hua-Ping Wan, China  
Roman Wan-Wendner , Austria  
Chaohui Wang , China  
Hao Wang , USA  
Shiming Wang , China  
Wayne Yu Wang , United Kingdom  
Wen-Da Wang, China  
Xing Wang , China  
Xiuling Wang , China  
Zhenjun Wang , China  
Xin-Jiang Wei , China  
Tao Wen , China  
Weiping Wen , China  
Lei Weng , China  
Chao Wu , United Kingdom  
Jiangyu Wu, China  
Wangjie Wu , China  
Wenbing Wu , China  
Zhixing Xiao, China  
Gang Xu, China  
Jian Xu , China  
Panpan , China  
Rongchao Xu , China  
HE YONGLIANG, China  
Michael Yam, Hong Kong  
Hailu Yang , China  
Xu-Xu Yang , China  
Hui Yao , China  
Xinyu Ye , China  
Zhoujing Ye, China  
Gürol Yildirim , Turkey  
Dawei Yin , China  
Doo-Yeol Yoo , Republic of Korea  
Zhanping You , USA  
Afshar A. Yousefi , Iran  
Xinbao Yu , USA  
Dongdong Yuan , China  
Geun Y. Yun , Republic of Korea




Hyun-Do Yun , Republic of Korea  
Cemal YİĞİT , Turkey  
Paolo Zampieri, Italy  
Giulio Zani , Italy  
Mariano Angelo Zanini , Italy  
Zhixiong Zeng , Hong Kong  
Mustafa Zeybek, Turkey  
Henglong Zhang , China  
Jiupeng Zhang, China  
Tingting Zhang , China  
Zengping Zhang, China  
Zetian Zhang , China  
Zhigang Zhang , China  
Zhipeng Zhao , Japan  
Jun Zhao , China  
Annan Zhou , Australia  
Jia-wen Zhou , China  
Hai-Tao Zhu , China  
Peng Zhu , China  
QuanJie Zhu , China  
Wenjun Zhu , China  
Marco Zucca, Italy  
Haoran Zuo, Australia  
Junqing Zuo , China  
Robert Černý , Czech Republic  
Süleyman İpek , Turkey

# Contents

## **Estimation of Hydraulic Properties in Permeable Pavement Subjected to Clogging Simulation**

Guoyang Lu , Zijian He , Pengfei Liu , Zhihao He, Gaoyang Li, Hao Jiang, and Markus Oeser   
Research Article (13 pages), Article ID 5091895, Volume 2022 (2022)

## **Utilization of Waste Glass Powder and Glass Composite Fillers in Asphalt Pavements**

Jayvant Choudhary , Brind Kumar , and Ankit Gupta   
Research Article (17 pages), Article ID 3235223, Volume 2021 (2021)

## **Organosilane and Lignosulfonate Stabilization of Roads Unbound: Performance during a Two-Year Time Span**

Diego Maria Barbieri , Baowen Lou , Hao Chen , Benan Shu , Fusong Wang , and Inge Hoff   
Research Article (13 pages), Article ID 9367501, Volume 2021 (2021)

## **The Effects of Geocell Height and Lime Stabilization on Unpaved Road Settlements at Different Water Contents**

Erhan Burak Pancar  and Aytuğ Kumandaş   
Research Article (8 pages), Article ID 9190792, Volume 2021 (2021)



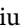
## **Maximum Likelihood Estimation of Parameters for Advanced Continuously Reinforced Concrete Pavement (CRCP) Punchout Calibration Model**

Liangliang Chen , Feng Zhang , and Changjun Zhou   
Research Article (8 pages), Article ID 7709027, Volume 2021 (2021)



## **The Impact of LED Colour Rendering on Reaction Time of Human Eyes in Tunnel Interior Zone**

Li-Li Dong , Qi Lou , Peng Liu , and Wen-Hai Xu   
Research Article (19 pages), Article ID 6987673, Volume 2021 (2021)

## **Optimization Model of Network-Level Pavement Maintenance Decision considering User Travel Time and Vehicle Fuel Consumption Costs**

Leilei Chen , Zepeng Fan , Pengfei Liu , and Zhendong Qian  
Research Article (9 pages), Article ID 4699838, Volume 2021 (2021)





## **Mixing Ratios and Cementing Mechanism of Similar Silty Mudstone Materials for Model Tests**

Hong-Yuan Fu, Shuang-Xing Qi , Zhen-Ning Shi , and Ling Zeng   
Research Article (19 pages), Article ID 2426130, Volume 2021 (2021)



## **Prediction-Based Maintenance of Existing Bridges Using Neural Network and Sensitivity Analysis**

Pengyong Miao   
Research Article (17 pages), Article ID 4598337, Volume 2021 (2021)

## **The Undrained Characteristics of Tengger Desert Sand from True Triaxial Testing**

Xuefeng Li , Weinan Lu , Zhigang Ma , and Ni Tuo   
Research Article (10 pages), Article ID 6320397, Volume 2021 (2021)

**Mechanical and Mesoscale Analyses of Cement Stabilized Macadam Prepared by Vibratory and Nonvibratory Mixing Techniques**

Jijing Wang  and Zhihua Tan 

Research Article (13 pages), Article ID 6663233, Volume 2021 (2021)

## Research Article

# Estimation of Hydraulic Properties in Permeable Pavement Subjected to Clogging Simulation

Guoyang Lu <sup>1</sup>, Zijian He <sup>1</sup>, Pengfei Liu <sup>2</sup>, Zhihao He,<sup>2</sup> Gaoyang Li,<sup>1</sup> Hao Jiang,<sup>3</sup> and Markus Oeser <sup>2</sup>

<sup>1</sup>Department of Civil and Environmental Engineering, The Hong Kong Polytechnic University, Hong Kong, China

<sup>2</sup>Institute of Highway Engineering, RWTH Aachen University, Aachen 52074, Germany

<sup>3</sup>Chinese National Engineering Research Centre for Steel Construction (Hong Kong Branch), Z106, Z Block, Phase 8, The Hong Kong Polytechnic University, Hong Kong, China

Correspondence should be addressed to Pengfei Liu; [liu@isac.rwth-aachen.de](mailto:liu@isac.rwth-aachen.de)

Received 29 July 2021; Revised 13 December 2021; Accepted 8 January 2022; Published 21 January 2022

Academic Editor: Ankit Gupta

Copyright © 2022 Guoyang Lu et al. This is an open access article distributed under the Creative Commons Attribution License, which permits unrestricted use, distribution, and reproduction in any medium, provided the original work is properly cited.

Permeable pavements are often affected by pore clogging, which leads to their functional failure and reduced service life. However, the clogging mechanism and its impact on the permeability and complex pore microstructures in pervious pavement remain unclear. The aim of current study is to quantify the clogging behavior in pervious pavement materials and carry out investigations on the development of pore characteristics and permeability. Novel polyurethane-bound pervious mixture (PUPM) was adopted for comparative study in present research with conventional Porous Asphalt (PA). The Aachen Polishing Machine (APM) was selected to perfectly serve as a simulator for clogging process of pavement in the actual service condition. The permeability and pore microstructure of the pervious pavement material were then characterized by using the self-developed permeameter and X-ray Computed Tomography (CT) scanning, respectively. The development of pore characteristics in terms of clogging was experimentally illustrated. Based on the pore characteristics, the flow behavior of PUPM subjected to different clogging periods was predicted based on the developed non-Darcy flow model. The developed experiments and analysis can further strengthen the understanding of the clogging mechanism within the porous pavement material. The results can also serve for the optimization of the pervious pavement design in the engineering application.

## 1. Introduction

Permeable pavement is a type of pavement that allows rainwater and runoff to directly infiltrate into the pavement, rather than accumulating on the pavement surface. During the infiltration process, permeable pavement can also filter pollutants and particle matters from the water. So, the groundwater volume is not only replenished but the water quality can be also improved [1–3].

Permeable pavement systems exhibit water treatment potential and can retain up to 90% of particulate matter (PM) and total suspended solids (TSS), 65% of total phosphorus (TP), and 80% of total nitrogen (TN) [4, 5]. However, on the other hand, these particles that are present in the surface runoff can remain in the pores during the

infiltration process. This buildup causes clogging in the pores, thereby gradually but significantly changing the hydraulic properties of the permeable pavement, which in turn will affect the mechanical performance of pavement [6–9]. Based on the previous research, clogging can be mainly due to two types of siltation processes: (a) long-term clogging process by urban runoff with fine particles and (b) short-term clogging by a sudden slump or landslide [10]. As the long-term service performance is greatly hindered by these clogging characteristics, studies have been conducted by applying fine particles accumulating in the void spaces of porous pavements based on different watering methods [11]. Clogging is found to be highly correlated with the particle size and volume, the flow rate, and pore characteristics of the pavement [12].

Previous research has been primarily focused on the observation of field measurement and macroscopic laboratory experiments. The microscopic characterization of the clogging such as the development of pore characteristics, particle distribution, and kinematics are still not clarified. A systematic understanding of the development of hydraulic and clogging mechanisms within the permeable pavement should be further established. Additionally, because most of the existing clogging experiments are based on modified permeameter by only changing the flow conditions, none of them can effectively simulate the clogging by considering the tires-road interaction.

In the present study, the objective is to quantify the clogging behavior in the permeable pavement materials (PPM) and the investigations on the development of pore characteristics and permeability taking into consideration the clogging effect. Thus, a more comprehensive understanding of the hydraulic properties of the PPM can be achieved. With the help of the derived non-Darcy flow equations in the previous study [13], the hydraulic properties of PPM during the clogging periods can be estimated. This could be a guideline for the accurate evaluation of the hydraulic properties of the PPM for future studies and practical application.

## 2. Materials and Methods

**2.1. Materials.** The porous pavement can achieve a high permeability performance because of its void-rich structure. However, the combination of this open-graded aggregate distribution design and the low shear force resistance binder, such as bitumen, results in weaknesses in durability and adhesion failure in the porous pavement. For this reason, a polyurethane-bound pervious mixture (PUPM) was developed by using the polyurethane (PU) to replace bitumen as the binder. Numerous researches have verified that PUPM has the notable mechanical and functional performance to be realized [14–17]. Moreover, during construction, PU can be cured at room temperature. Hence, a significant environmental benefit can be also achieved when compared to the conventional heating construction method of asphalt [18].

**2.1.1. Mix Design.** To investigate the pore characteristics of the PUPM, three types of the PUPM with different porosities were produced in this study: PUPM 8-H, PUPM 8, and PUPM 8-L, which denote mixture with maximum aggregate size 8 mm and high, normal, and low porosity levels, respectively. Conventional PPM, Porous Asphalt, PA 8, was also selected as the reference material to evaluate the properties of PUPM in this study, which is one of standard permeable pavement materials (RSto12, Guidelines for the Standardisation of Pavement Structures of Traffic Areas, edition 2012). The grain size distribution of all four chosen samples which were used in this study is illustrated in Figure 1.

**2.1.2. Preparation of the PUPM Specimen.** Figure 2 shows the manufacturing process of PUPM. The two components of the polyurethane (polymerize polyol and isocyanate) were mixed firstly to activate polymerization reaction. Once the binder

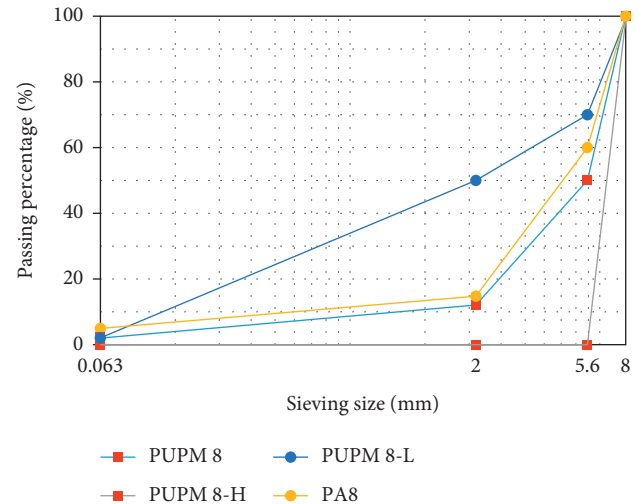


FIGURE 1: Grain size distribution of PUPM 8-H, PUPM 8, PUPM 8-L and PA 8.

was fully polymerized, they were mixed with aggregate. After all the aggregates can be observed evenly coated with polyurethane, the mixture was put into a mold with a length and width of 320 mm and 260 mm and a height of 40 mm for compaction. After a curing time of around 24 hours, 100 mm diameter cores were drilled. They were then weighted and used in the clogging simulation. The whole procedure of the specimen mixture was conducted at room temperature.

**2.2. Laboratory Tests.** To investigate the influence of the clogging behavior on the hydraulic properties of the specimens, several experimental procedures were designed. The first step was the simulation of clogging behavior in the specimens. The second step was to determine the clogging concentration of the influent and effluent. The third step was to evaluate the permeability of the specimens by conducting the permeability tests, and lastly, the pore characteristics of the specimens based on XCT were to be evaluated.

**2.2.1. Clogging Simulation.** To simulate the clogging in the laboratory, a simulation based on the Aachen Polishing Machine (APM) was carried out, as shown in Figure 3. By the aid of the APM, pavement samples can be exposed to a real tire loading (Type: Vanco 8, 165/75 R14 C 8PR 97/95RTL from Continental with shore hardness between 72 and 75 in level A). The main components of the APM are two independently working tires and a framework that can move forward and back. The sample is anchored to the track, and the wheels drive back and forward to simulate the condition on the pavement when a vehicle passes by. Since the pressure of the wheels in the APM system can be adjusted, the instrument can imitate all kinds of vehicle loads. For the clogging simulation in this study, sand, which has a grain size of up to 2 mm, was chosen as the clogging material. During the simulation, two different specimens were anchored to the track. Then, 40 grams of sand was sprinkled on the surface of the specimen. The vehicle tire in the APM then



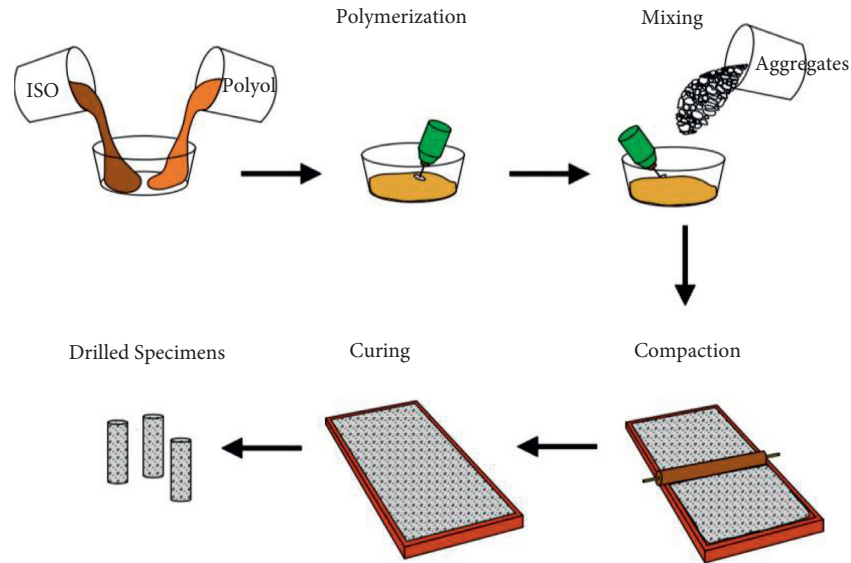


FIGURE 2: Manufacturing process of the PUPM specimens.

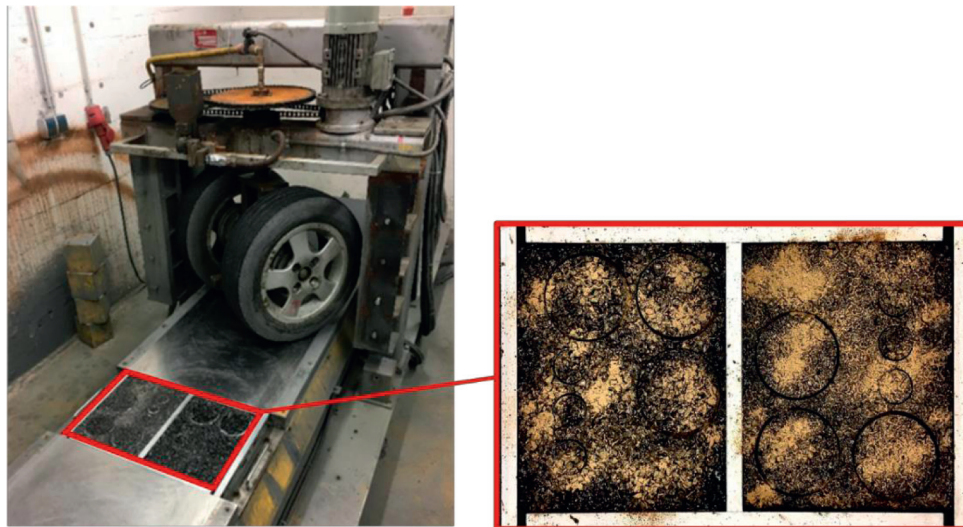


FIGURE 3: Clogging simulated by Aachen Polishing Machine (APM).

moved back and forth along the sample. The sled moved horizontally 9 times back and forth per minute, while the tires spun 41 rotations per minute. During the whole polishing process, water was sprinkled on the surface of the specimens. In this way, the sand would enter the void of the sample with the water and the pressure of the tire. All variants of the specimen (PUPM 8, PUPM 8-H, PUPM 8-L, and PA 8) were conducted with simulation. Each sample was processed for four different clogging periods: 20 minutes, 40 minutes, 60 minutes, and 80 minutes. These samples were then applied to the permeability tests. More information can be found in [19].

**2.2.2. Clogging Concentration at Influent and Effluent.** To investigate the clogging behaviors in the specimens, the clogging concentration at the influent and effluent from each

specimen was tested. This can be described by two parameters: the strained clogging amount mass in the specimens and the particle mass separation efficiency.

The clogging period was set at 5 minutes. After the test started, the effluent flow through the test specimens as well as the overflow was collected in a pot. Every 5 minutes a new pot was replaced. The strained clogging agents from the collected effluents and overflow were dried and measured. In this way, the strained clogging mass during the clogging periods can be calculated by the subtraction of the clogging mass (in the effluent and overflow) from the influent. It can be illustrated from the following equation:

$$m_s = m_i - m_o - m_e, \quad (1)$$

where  $m_i$ ,  $m_o$ , and  $m_e$  denote the dry clogging agents' mass in the influent, overflow, and effluent.

The particle mass separation efficiency  $\eta_m$  illustrates the percentage of the clogging amount throughout the specimen, and the equation is expressed as follows:

$$\eta_m(t) = \left( 1 - \frac{[m_e](t)}{[m_i](t)} \right) \times 100\%. \quad (2)$$

**2.2.3. Permeability Test.** Permeability describes the ability of a porous material to conduct water. The higher the permeability of a material, the faster the liquid can pass through. The permeability coefficient is a predictable indicator to represent the hydraulic characteristic of a material. In general, the permeability of the specimen can be described in horizontal and vertical directions. In this study, the vertical permeability of the specimens was investigated.

Based on the standard DIN EN 12697-19, a customized constant falling head permeameter, as in Figure 4 shown, is implemented for the test. More details can be referred to in the previous publication [19].

**2.2.4. XCT Scanning.** In order to quantify the pore characteristics of the specimens, a High-Resolution Computed Tomography and X-ray System (XCT) was used in this study. The X-ray system consists of a generator with 250-KV and a rotating scan table for the specimens. During the operation, the specimen was placed on the rotating scan table in the XCT system, then the X-ray generator of the XCT system shot a radiation beam to the specimen, and the reflected signal was received by the receptor and passed to the system for the analysis. In this study, all the scanning was accomplished by the XCT.

### 2.3. Models of Different Flow Behaviors

**2.3.1. Flow Behavior with Low Velocity.** The permeability of a porous media can be estimated not only by the experimental measurement but also by using empirical methods. Many researchers have attempted to estimate permeability with different models. One of the most recognized models was developed by Hazen; however, around one century later, Kozeny and Carman made a further step, which approached to delivering more accurate results [20].

The Kozeny–Carman model (KCM) is one of the well-known models that relates both permeability and porosity. It describes the relationship between the properties of the medium and the flow resistance in the pore channels. With the semiempirical-theoretical formula expressed in the following equation, the permeability of the porous media can be predicted [21].

$$K_{kcm} = \frac{\gamma_w}{\mu_w \cdot C_{k-c}} \cdot \frac{1}{S_{Ae}^2} \cdot \frac{n_{eff}^3}{(1 - n_{eff})^2}, \quad (3)$$

where  $K_{kcm}$  is the Kozeny–Carman model permeability,  $\gamma_w$  is the unit weight of water,  $\mu_w$  is the viscosity of water,  $C_{k-c}$  is

the empirical Kozeny–Carman coefficient,  $S_{Ae}$  is the effective specific surface area, and  $n_{eff}$  is the effective porosity.

$S_{Ae}$  can be obtained by the particle size distribution for the nonuniform spheres:

$$D_{eff} = \frac{100\%}{\sum(\phi_i/D_{li}^{0.5} \cdot D_{si}^{0.5})}, \quad (4)$$

where  $D_{eff}$  is the effective diameter,  $\phi_i$  is the percentage fraction of grain between the largest sieve size  $D_{li}$  and the smallest sieve size  $D_{si}$ .

Thus, the KCM model emphasizes grain size distribution (GSD) can be rewritten as follows:

$$K_{KCM}^{GSD} = \frac{\gamma_w}{\mu_w \cdot C_{k-c}} \cdot \left( \frac{100\%}{\sum(\phi_i/D_{li}^{0.5} \cdot D_{si}^{0.5})} \right)^2 \cdot \frac{1}{S_{Ae}^2} \cdot \frac{n_{eff}^3}{(1 - n_{eff})^2}. \quad (5)$$

Calculating with the conventional KCM can lead to a result with deviation because the equations parameters are dependent on uniform sphere particles and surrogate indices. Moreover, the aggregates of pavements are mostly irregular. Thus, a modified KCM is required for an appropriate prediction of permeable pavement. By considering the tortuosity  $\tau$ , equation (3) can be rewritten as follows:

$$K_{KCM}^m = \frac{\gamma_w}{\mu_w \cdot C_{k-c}} \cdot \frac{n_{eff}}{\tau^2 S_{Ae}^2}. \quad (6)$$

**2.3.2. Flow Behavior with High Velocity.** Many researchers have used different methods to approach the characteristics of flow with high velocity. They can be classified into two groups: theoretical and empirical models. So, the empirical models in this study applied are from the Ergun and Ward, and the theoretical models are based on the capillary models [13].

Based on the known information that the energy loss flow of the porous media is caused by the dissipation of viscous and kinematic energy, this energy loss is represented by a decrease in pressure. Ergun combined the theory of Reynolds and the method of Kozeny [21]. After numerous experiments, he corrected the parameters of the two relations which depend on the flow rates, namely, the linear relation with viscous energy loss and the term of  $(1 - n_{eff})^2/n_{eff}^3$ , and the nonlinear relation with kinetic energy loss and the term of  $1 - n_{eff}/n_{eff}^3$ . So, by considering the effects of the particle size and shape, as well as extending the models from Kozeny–Carman in the linear laminar regime and the Burke and Plummer in the turbulent regime, the equation which he has proposed can generally describe all types of flow in the porous media. So, the Forchheimer coefficient for high flow rates can be expressed by the following equation:

$$\beta_E = \frac{1.75}{g} \cdot \frac{1 - n_{eff}}{n_{eff}^3} \cdot \frac{1}{D_p}, \quad (7)$$

where  $D_p$  is the particle diameter.

By combining the effects from the granular material with permeability, another approach to the Forchheimer coefficient can be expressed with the following equation:

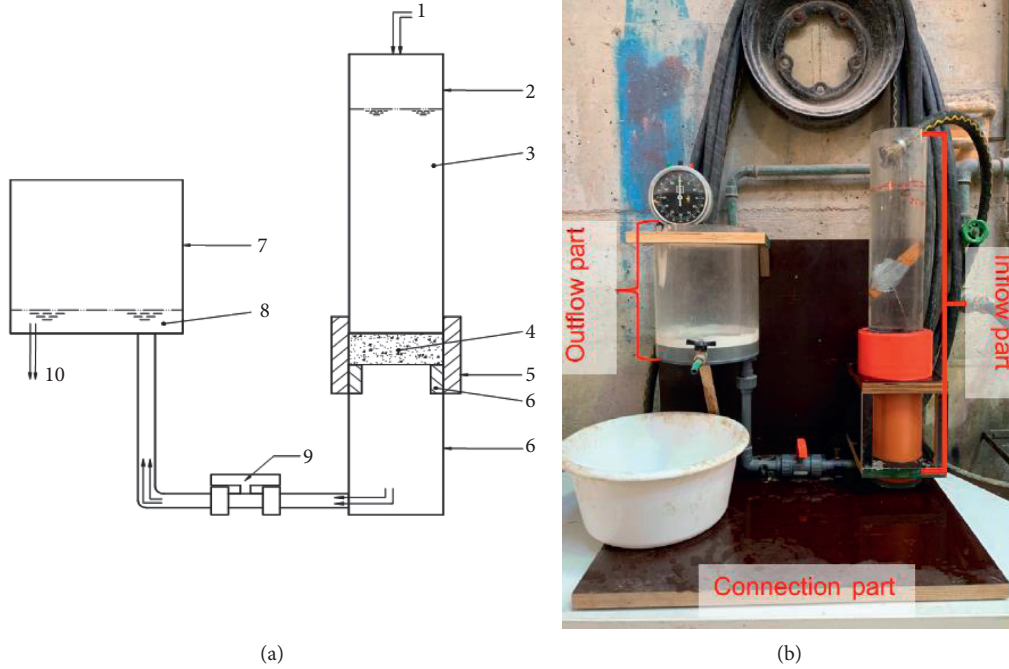


FIGURE 4: Apparatus for permeability test. (a) Schematic diagram of apparatus (1: water inlet; 2: graduated plastic cylinder; 3: influent water head; 4: specimen; 5: upper rubber sleeve; 6: lower rubber sleeve; 7: outflow tube; 8: effluent water head; 9: water shut-off valve; and 10: water outflow). (b) Physical map of apparatus.

$$\mathcal{B}_w = \frac{0.55}{k^{0.5}} \quad (8)$$

Based on the concept that considers the porous media as the capillary model, many researchers contributed in this direction to theoretically analyze the flow behavior. Through the arrangement of these capillary tubes, these models can be distinguished into series and parallel bounded [19].

The equation for the parallel-type model can be expressed as follows:

$$\mathcal{B}_t^n = \frac{c_0}{K^{0.5} \cdot n_{eff}^{1.5}} \quad (9)$$

And for the serial-type model,

$$\mathcal{B}_t^\tau = \frac{c_1 \cdot \tau}{K^{0.5} \cdot n_e} \quad (10)$$

where  $\mathcal{B}_t^n$  denotes the Forchheimer equation by applying the porosity, as well as  $\mathcal{B}_t^\tau$  by using tortuosity,  $c_0$  and  $c_1$  are the constants, which denote the inertia and pore size distribution. From the previous study [13], the constants have been proposed for both models, which can properly estimate the flow behaviors in the clean-bed PUPM. So, the equations for the PUPM mixtures can be rewritten as the following equations:

The parallel-type model:

$$\mathcal{B}_t^n = \frac{0.0487}{K^{0.5} \cdot n_{eff}^{1.5}} \quad (11)$$

The serial-type model:

$$\mathcal{B}_t^\tau = \frac{5.9435 \cdot 10^{-7} \cdot \tau}{k \cdot n_e} \quad (12)$$

### 3. Results and Discussion

**3.1. Clogging Concentration.** During the clogging simulation, the clogging concentration in the first 30 minutes was observed. The influent, overflow, and effluent flow through the specimens during the clogging simulation were collected, and the clogging agents in the liquid were dried and weighed. The obtained data were analyzed and plotted in Figure 5. The results illustrate the increasing trends of clogging concentrations in both specimens. During the first 5 minutes of the clogging period, more than half of the clogging agents stuck in the PA 8, while these in the PUPM 8 were only 42%. The clogging concentration in PA 8 continued to rise sharply; after 20 minutes, the rate of growth became stable. After the loading time exceeded 30 minutes, more than 90% of the clogging agents can be found in PA 8. This denotes that the most hydraulic flow channels in PA 8 were blocked. By contrast, the clogging concentration in PUPM 8 increased slowly throughout the whole period. During the clogging periods, only around 52% of the clogging mass of the influent was accumulated in PUPM 8.

In conclusion, both specimens can be affected by the clogging issue. But the clogging situation in PUPM 8 is more optimal than that in PA 8.



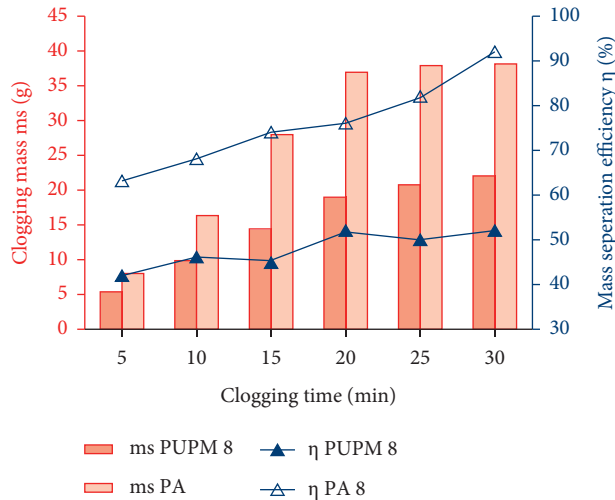


FIGURE 5: Plot of clogging concentrations in the PA 8 and PUPM 8 specimens during the clogging periods.

**3.2. Permeability of Specimens during the Clogging Development.** During the permeability test of the specimens, the data were collected in 5 hydraulic heads (from 100 to 300 mm with interval of 50 mm). In each level, four measurements for each specimen were recorded and then analyzed, respectively.

**3.2.1. Flow Characteristics in terms of a Constant Hydraulic Head.** As can be seen in Figure 6, the permeability coefficients at 300 mm hydraulic head of the specimens during the clogging periods were obtained. The specimens PUPM 8-H with the highest permeability can conduct  $1.72 \times 10^{-3}$  m/s of water. Followed by the PUPM 8 with the second highest permeability, and at the third position is the PA 8. In the figure, it can be recognized that the PUPM 8-L has the lowest permeability with  $4.55 \times 10^{-3}$  m/s.

For PA 8, the permeability of PA 8 decreased sharply once the clogging period started. In the first 20 minutes, the specimen's permeability sharply reduced from  $1.08 \times 10^{-3}$  m/s to  $2.9 \times 10^{-4}$  m/s, approximately 26% of its initial permeability. Conversely, during the same periods, the permeability of the PUPM 8 reduced slowly. Unlike the PA, the PU can perfectly cover the surface of the aggregates and provide a smooth surface for the aggregates. Therefore, the sediments can be easier caught in the PA specimen. The characteristic of the binder of the PA is, however, another influencing factor. Because of the high viscosity of the bitumen, the sediments tend to become attached to the bitumen. The flow behavior of the PA in the experiment is consistent with the previous study [13]. After 20 minutes of clogging simulation, the permeability of the PA 8 decreases continuously and steadily. 60 minutes later, the permeability of PA 8 reaches  $7.5 \times 10^{-5}$  m/s, which can be classified as permeable. However, the initial permeability was highly permeable. In comparison with the PUPM 8 and PUPM 8-H, the permeabilities of PA 8 are nineteen to thirteen times lower than that of PUPM 8 and PUPM 8-H.

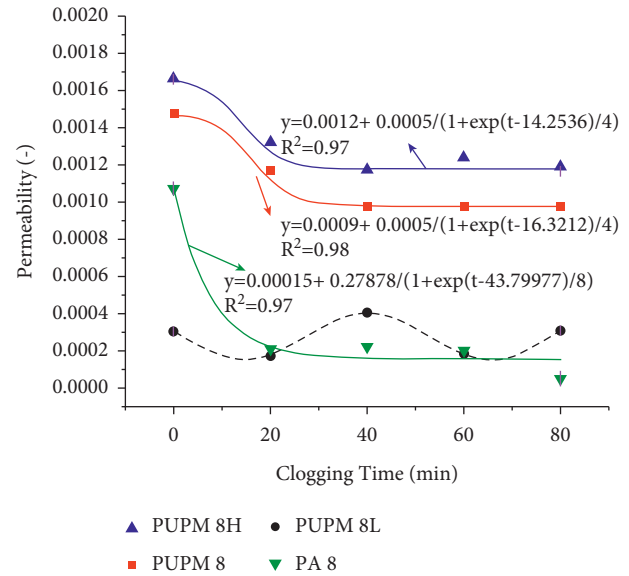


FIGURE 6: Plot of permeability coefficients for PUPM specimens and PA specimen at the hydraulic head of 300 mm during the clogging development [19].

With regard to PUPM 8, PUPM 8-H, and PUPM 8-L, according to Figure 6, two different decline trends of permeability coefficients can be observed. During the total clogging period, the permeability coefficients of the PUPM 8 and PUPM 8-H present similar downward trends. The permeability of the PUPM 8 reduced sharply, while this of the PUPM 8-H reduced much more steadily. After 80 minutes, the permeability of PUPM 8 reached  $1.04 \times 10^{-3}$  m/s, which is slightly lower than that of PUPM 8-H. By contrast, during the same clogging period, the permeability of PUPM 8-L shows a wave trend. A reason for this fluctuated trend could be that in the PUPM 8-L the continuous grading of aggregates was used, resulting in a high-density specimen with much lower porosity. In conjunction with that, the pressure from the tire of the clogging simulation and the impact of the flow causes two different effects. First, these forces push a little number of clogging agents into the specimen, while most of them stay on the surface of the specimen. Secondly, as the clogging loading time develops, some of these clogging agents would be then washed out by these forces. This consists of the shown permeability development of the PUPM 8-L. Nevertheless, after the whole clogging simulation, three kinds of PUPM can be classified as highly permeable.

In conclusion, all the four specimens have high initial permeability and can be affected by the clogging. However, the PA 8 is more influenced by the clogging than PUPM variants. After 80 minutes of clogging simulation, the permeability of all PUPM variants can still be recognized as highly permeable, but the PA 8 can be only classified as permeable.

**3.2.2. Flow Characteristics in terms of Changing Hydraulic Gradients.** This study is aimed to analyze the hydraulic properties of PUPM 8-H; the PUPM 8-L and PUPM 8 are no longer taken into consideration. By changing the hydraulic

head, the permeability coefficients of the specimens at the hydraulic gradient from 2.5 to 7.5 were evaluated and plotted in Figure 7. As can be seen from this figure, the rate of the permeability reduction slows down, as the clogging time and the hydraulic gradients increase. The study also found that the change of hydraulic gradient has a greater impact on the permeability coefficient without polishing, and this impact also decreases with the increase of polishing time.

As far as the flow behavior of the specimens, when the specimens were not subjected to the clogging, a non-Darcy flow behavior of all four specimens can be noticed. However, as the clogging time develops, the characteristic of linear flow become more obvious. It denotes that the viscous force is dominating the kinematic force, as the clogging development in the specimen. Nevertheless, as can be seen that at the clogging periods of 40 minutes, the permeabilities of the PUPM 8-H are the lowest during the whole clogging developments, which is not reasonable. Hence, an analysis for this can be conducted by combining with the pore characteristics of the specimens during the clogging development.

**3.3. Pore Characteristics during the Clogging.** With the help of the XCT methods, the aid of MATLAB and Avizo software, the aggregate, polyurethane binder, and clogging mixture was successfully separated based on the OTSU method [13, 19]. The 3D visualization of PUPM 8-H is shown in Figure 8. The data of pore characteristics of the specimens during the clogging were thus obtained and analyzed.

The effective void content distribution, the specific surface area, and the tortuosity of the PUPM 8-H during the clogging periods are listed in Table 1. No obvious variant trends of PUPM 8-H during the whole clogging periods can be observed. However, combining the results of XCT analysis and the variation of the permeability by changing the applied hydraulic gradients, it can be noticed that with the increase of the value of tortuosity, the effective porosity of the specimens reduces faster. Additionally, the variation of its permeability during the clogging development follows the same trend. This denotes the fact that the tortuosity of the porous material affects its ability of resistance to the clogging particles. This could be the reason that the permeabilities at the clogging periods of 40 minutes are lower than those of other clogging periods, and the permeabilities at clogging periods of 80 minutes are similar with those at 60 minutes as well. To investigate the correlation of the pore characteristics that influence on the its permeability, it is assumed that a different tortuosity can be formed at a different clogging period; this would also cause a different clogging resistance, resulting in a different effective porosity; thus, a different permeability dissipation can be observed. To transfer this assumption into the mathematic equations, the initial porosity is multiplied by a clogging resistance term to obtain the effective porosity after a certain clogging period. This relationship can be expressed by the following equation:

$$n_{eff} = n_i \cdot c_R, \quad (13)$$

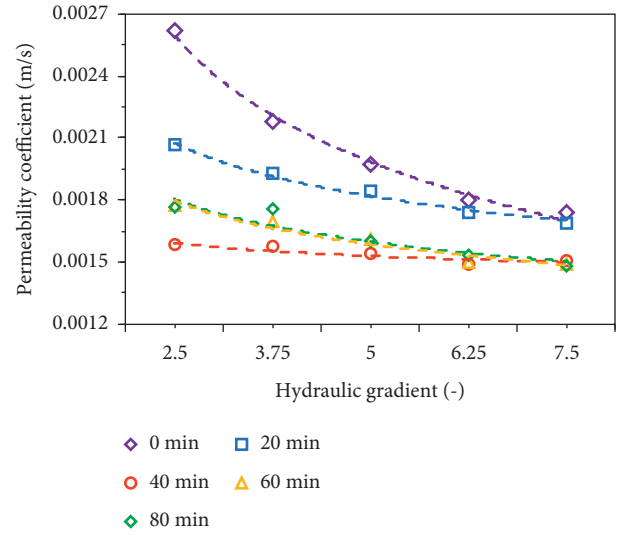


FIGURE 7: Plot of the variation of the permeability coefficients of PUPM 8-H at different hydraulic gradients during the clogging periods of 20, 40, 60, and 80 minutes.

where  $n_{eff}$  is the effective porosity,  $n_i$  is the initial porosity of the PUPM 8-H, and  $c_R$  is the term of the clogging resistance. As assumed that the tortuosity is a function of the clogging resistance term, the relationship between the clogging resistance and tortuosity was derived by fitting data, and it can be described by following equation:

$$c_R = 1.1958 \cdot e^{-0.469 \cdot \tau}, \quad (14)$$

where  $\tau$  is tortuosity. By adopting equation (14) into (13), equation (13) can be rewritten as

$$n_{eff} = n_i \cdot 1.1958 \cdot e^{-0.469 \cdot \tau} (R^2 = 1). \quad (15)$$

Because the initial state of the specimen was not considered during the XCT scan analysis, the data of its pore characteristics are unknown. However,  $n_i$  of the PUPM 8-H can be approximated by fitting data and it has the value of 43.62.

**3.4. Prediction of the Hydraulic Properties of PUPM during the Clogging Development.** To estimate the hydraulic properties of the PUPM 8-H under the clogging effects, several models were carried out. From the flow velocity perspective, these properties were observed in two aspects.

**3.4.1. Estimation of the Permeability of PUPM during the Clogging Development.** As in the literature review mentioned, based on the pore characteristic parameters such as effective porosity, tortuosity, and specific surface area, the permeability of a porous material can be predicted with the KCM models. In this study, the results from XCT were modeled with three KCM models: the original KCM, the KCM GSD, and the modified KCM. The obtained permeability from these three models will be compared and discussed.



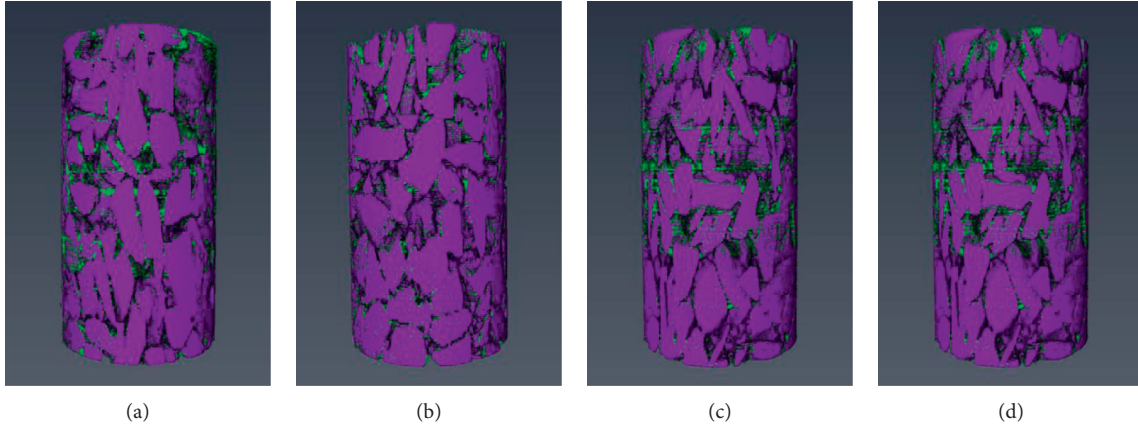


FIGURE 8: 3D visualization of PUPM 8-H at the clogging period of (a) 20, (b) 40, (c) 60, and (d) 80 minutes [19].

TABLE 1: Void content distribution measurements for PUPM specimens at 20, 40, 60, and 80 min clogging simulation.

Specimens	Clogging time (min)	Effective void content (%)	Specific surface area (1/m <sup>-1</sup> )	Tortuosity (-)
PUPM 8H	20	40.71	361.27	2.228
PUPM 8H	40	39.02	678.49	2.875
PUPM 8H	60	40.84	453.41	2.168
PUPM 8H	80	39.19	500.78	1.553

The permeability coefficients of PUPM 8-H, derived from three KCM models, were compared with the results of the measurement. The comparison is illustrated in Figure 9.

As expected, the original model has the highest dispersion from the measured permeability. As mentioned in the previous section, the focus of the original model was only on the porosity and the specific surface area of the materials, and all the aggregates are uniformly sharp. Thus, it delivers the most inaccurate results. The GSD model also delivered results with great deviations. In this model, the grain size distribution is taken into consideration. However, this parameter is highly dependent on uniform spheres and surrogate indices. The modified KCM has the best prediction for the permeability coefficients. In the modified KCM model, the tortuosity was taken into consideration because the aggregates of the material are irregular; through this, the pore structure in the porous material can be better described. This proves that the flow behavior can be modeled accurately only when the structure of the porous media is accurately described.

Compared with GSD and the original models, the modified model can predict the flow behavior in PUPM 8-H better, but it is not perfect. The modified KCM still cannot perfectly predict the flow behavior in the PUPM 8-H. The figure above shows that the values derived from this model are smaller than those measured in the permeability test. From the theoretical aspect, the modified KCM was used for the clean-bed specimens. Therefore, to predict the flow behavior of the porous media under the clogging periods accurately, the modified KCM model needs to be justified.

Based on the observation of the XCT results, the variation of the pore characteristics is very complicated. Regardless, a trend of the permeability coefficient of PUPM 8-H, which is similar to the exponential function, can be identified. The modified KCM model is incapable of

estimating the permeability of the specimen perfectly. The deviation of the ascertained experimental data and the estimated permeability is caused by the clogging effect in the PUPM 8-H. To further improve the prediction on the permeability of the PUPM 8-H, the clogging issue is considered in a specific term, named the curve fitting function, and added to the modified KCM model in MATLAB. This curve fitting function was approximated to fit experimental data. Thus, the modified KCM in terms of the time-related clogging effects for the PUPM 8-H was derived. It is expressed as follows:

$$K_{KCM}^c = \frac{\gamma_\omega}{\mu_\omega \cdot C_{k-c}} \cdot \frac{n_e}{\tau^2 S_{Ae}^2} \cdot \left( A_1 + A_2 * e^{(-A_3 * t)} \right), \quad (16)$$

where  $K_{KCM}^c$  is defined as the KCM permeability during the clogging periods.  $A_1$ ,  $A_2$ , and  $A_3$  are the coefficients. The values of these coefficients for equation (16) are listed in Table 2.

To test whether the modified KCM model for clogging can predict the permeability of the PUPM 8-H during the clogging periods properly, equation (16) was implemented for the calculation of the permeability of the PUPM 8-H. The results of both models were then compared with the measured permeability. These results are illustrated in Table 3.

As can be seen from the above table, the modified KCM model for clogging exhibits favorable results, as expected. In comparison with the modified KCM model and the modified KCM model for clogging, the relative error to the measured permeability coefficient is significantly lower for PUPM 8-H by applying the modified KCM model for clogging. Thus, in this case, it can be concluded, from comparing the maximum of the relative errors, that the estimated permeability can be more accurately calculated to be closer to the actual permeability in PUPM 8-H specimens during the clogging periods.

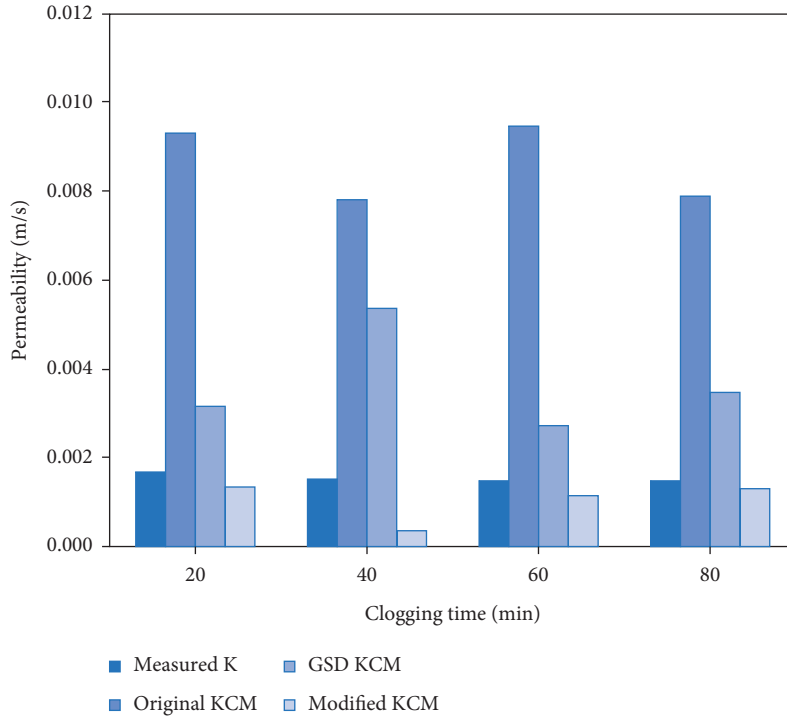


FIGURE 9: Comparison of measured permeability and estimated permeability with KCM models for PUPM 8-H during the clogging periods of 20, 40, 60, and 80 minutes.

TABLE 2: Constant parameters of the modified KCM models in terms of the clogging for PUPM 8-H.

Specimens	Constant parameters			$R^2$
	$A_1$	$A_2$	$A_3$	
PUPM 8-H	0.156	0.3	0.13	0.99

TABLE 3: Comparison results of permeability for PUPM 8-H.

Clogging time (min)	Measured K (m/s)	Modified KCM (m/s)	Relative error (%)	Modified KCM, clogging (m/s)	Relative error (%)
20	$1.69E-03$	$1.32E-03$	-21.86	$1.69E-03$	0.00
40	$1.50E-03$	$3.40E-04$	-77.31	$1.50E-03$	0.00
60	$1.48E-03$	$1.12E-03$	-24.02	$1.48E-03$	0.00
80	$1.48E-03$	$1.29E-03$	-12.90	$1.48E-03$	0.00

3.4.2. Estimation of the Non-Darcy Flow in the PUPM during Clogging Development. As stated in the previous section, the kinematic force in the porous material becomes significant, as the flow velocity increases. After a certain point, Darcy’s law is no longer suitable to be applied to describe the flow behavior. To investigate the nonlinear flow behavior in the PUPM 8-H, the Reynolds number (Re) number and pressure drop were carried out.

Figure 10 shows the variation of values of the Re for the flows in the PUPM 8-H at the hydraulic gradients from 2.5 to 7.5 during the clogging development. According to Figure 10, growing trends of Re with the increase of the hydraulic gradients in the PUPM 8-H can be observed.

Many researchers suggest different values of the Re number to limit the upper threshold of Darcy’s law; these values mostly range from 1 to 10. As can be seen from Figure 10, almost half of values of the Re for PUPM 8-H are found in the range of 1–10, which is a common

phenomenon at a low hydraulic gradient. Therefore, the flow in PUPM 8-H is experiencing a critical region, where a transition period from the non-Darcy to the Darcy regime takes place.

In conclusion, within the applied hydraulic gradients, the values of Re for PUPM 8-H approach the Darcy regime area gradually with the increase of the clogging time. This is consistent with the conclusion from the permeability test in the previous section that the viscosity force in the specimens becomes notable with the increase of clogging development. Thus, Forchheimer’s law is applicable for analyzing the behavior of non-Darcy flow in the PUPM 8-H.

Based on the existing study [13], the conventional Forchheimer models are needed to fit the prediction of the pressure drops in the PUPM 8-H to the actual measurements during the applied clogging periods. The nonlinear flow behavior in the PUPM 8-H can be predicted by fitting the capillary models to the experimental data. To estimate this

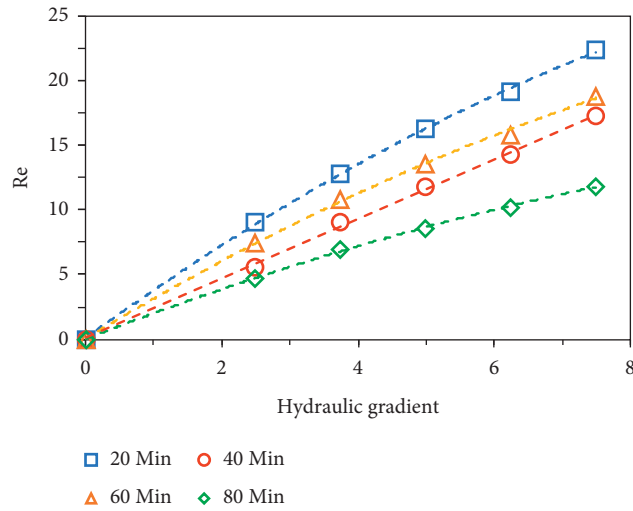


FIGURE 10: Plot of Re and hydraulic gradient for PUPM 8-H during the 20-, 40-, 60-, and 80-minute clogging periods.

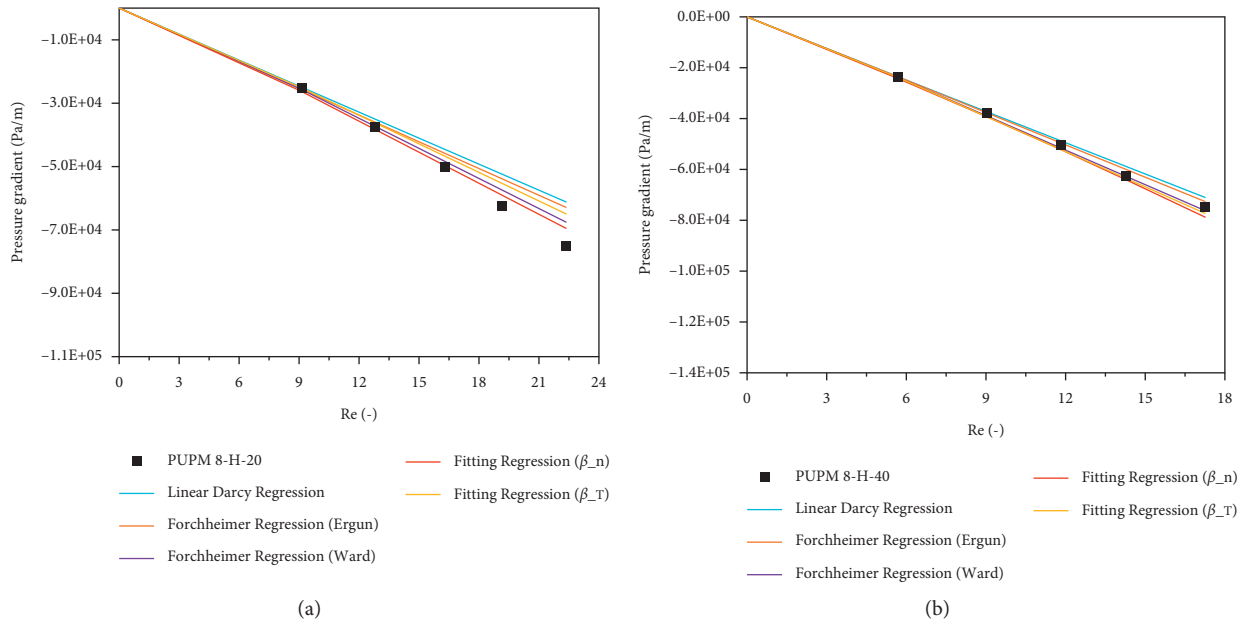


FIGURE 11: Continued.

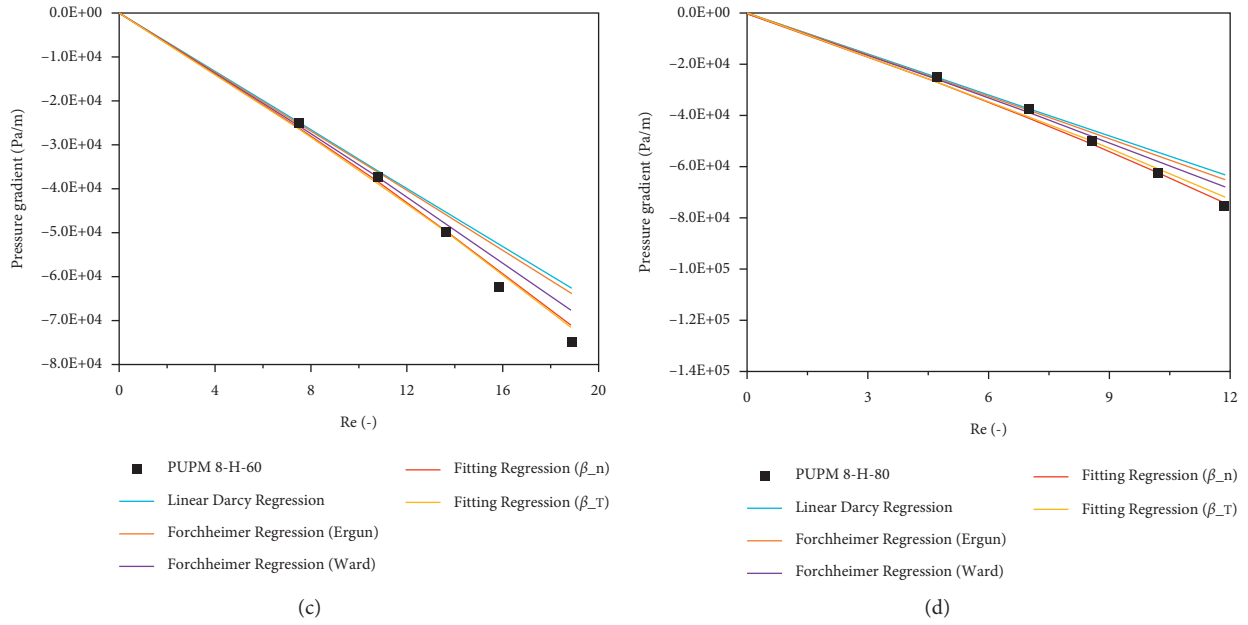


FIGURE 11: Modified Forchheimer's regressions and previous regressions for PUPM 8-H at different clogging periods (minutes): (a) 20; (b) 40; (c) 60; and (d) 80.

nonlinear flow behavior under the consideration of clogging, the curve fitting function in MATLAB was carried out.

For PUPM 8-H, the Forchheimer coefficient with the parallel type of the capillary model can be remodeled as follows:

$$\mathcal{B}_c^n = \frac{0.0487 \cdot a_n \cdot e^{b_n t}}{k^{0.5} \cdot n_e^{1.5}} \quad (17)$$

And with the serial type of the capillary model,

$$\mathcal{B}_c^\tau = \frac{5.9435 \cdot 10^{-7} \cdot (a_\tau \cdot e^{b_\tau t} + c_\tau \cdot t) \cdot \tau}{k \cdot n_e} \quad (18)$$

By adopting equations (17) and (18) into Forchheimer's law, the flow property of PUPM 8-H can be predicted as follows:

$$\nabla P_n^c = -\frac{\mu}{k_{KCM}^m} v_D - \frac{0.0487 \cdot a_n \cdot e^{b_n t}}{k^{0.5} \cdot n_e^{1.5}} \rho v_D^2 (R^2 = 0.97) \quad (19)$$

$$\nabla P_n^c = -\frac{\mu}{k_{KCM}^m} v_D - \frac{5.9435 \cdot 10^{-7} \cdot (a_\tau \cdot e^{b_\tau t} + c_\tau \cdot t)}{k \cdot n_e} \tau \rho v_D^2 (R^2 = 0.94) \quad (20)$$

where  $a_n = 2.6345$ ;  $b_n = 0.01035$ ;  $a_\tau = 0.2019$ ;  $b_\tau = 0.012$ ; and  $c_\tau = 0.0623$ .

The predicted non-Darcy flow model can be seen in Figure 11.

As shown in Figure 11, during the whole clogging period, both remodeled Forchheimer's equations gave closer results to the experimental measurements than those of Ergun and Ward's model. It can be concluded that the remodeled equations have a more accurate prediction for the nonlinear flow in the PUPM 8-H.

## 4. Conclusions

Based on the clogging simulation and permeability test, the clogging mechanism and development of hydraulic properties within the PPM were analyzed in depth. Detailed findings were listed in the following points:

- (1) The initial permeability of the PUPM is higher than that of PA 8. During the clogging simulation with the Aachen Polishing Machine (APM), the permeability of PUPM decreases gradually, while in the PA 8, it

drops sharply in the first 20 minutes. After 80 minutes of the clogging simulation, the PUPM maintains a high permeability, while the PA 8 loses 74% of the initial permeability. It indicates that the PUPM can withstand the impact of the clogging agents with a size of up to 2 mm better than PA mixtures. Therefore, it can be concluded that the PUPM not only can provide a longer service lifespan but also has a significantly better water drainage performance than the PA mixtures.

- (2) Based on the results from XCT, the pore characteristics such as the pore size, the porosity, the tortuosity, and specific surface area of the PUPM 8-H specimens were evaluated. Most values of all these characteristics during the clogging developments have no obvious trend. A relationship between the effective porosity and the tortuosity of the PUPM 8-H was found; it provides a clarification for the fluctuated trends of the pore characteristics.
- (3) The equations related to the hydraulic properties of the PUPM 8-H in the clogging development were derived. They are based on the results from previous research and the clogging related term which was obtained from fitting the data of the permeability and pore characteristics of the PUPM 8-H. With the modeled equations, the loading time-dependent hydraulic conductivity and the pressure drops of the PUPM 8-H can be estimated [22].

### Data Availability

The testing result data used to support the findings of this study are available from the corresponding author upon request.

### Conflicts of Interest

The authors declare that they have no conflicts of interest regarding the publication of this paper.

### Authors' Contributions

The authors confirm contribution to the paper as follows. Study conception and design: Pengfei Liu and Markus Oeser. Data collection: Guoyang Lu and Zhihao He. Analysis and interpretation of results: Guoyang Lu, Zijian He, Zhihao He, and Hao Jiang. Draft manuscript preparation: Guoyang Lu, Zijian He, Zhihao He, Pengfei Liu, and Gaoyang Li. All authors reviewed the results and approved the final version of the manuscript.

### Acknowledgments

The work described in this paper was supported by a grant from the Germany/Hong Kong Joint Research Scheme sponsored by the Research Grants Council of Hong Kong (Ref. no. G-PolyU505/21) and the German Academic Exchange Service of Germany (Grant no. 57601840). The German Research Foundation (Grant no. OE 514/15-1, 459436571) is gratefully acknowledged as well.

### References

- [1] B. Huang, H. Wu, X. Shu, and E. G. Burdette, "Laboratory evaluation of permeability and strength of polymer-modified pervious concrete," *Construction and Building Materials*, vol. 24, no. 5, pp. 818–823, 2010.
- [2] W. Sun, G. Lu, C. Ye et al., "The state of the art: application of green technology in sustainable pavement," *Advances in Materials Science and Engineering*, vol. 2018, 2018.
- [3] N. Xie, M. Akin, and X. Shi, "Permeable concrete pavements: a review of environmental benefits and durability," *Journal of Cleaner Production*, vol. 210, pp. 1605–1621, 2019.
- [4] Z. Teng and J. Sansalone, "In situ partial exfiltration of rainfall runoff. II: particle separation," *Journal of Environmental Engineering*, vol. 130, no. 9, pp. 1008–1020, 2004.
- [5] S.-S. Pathapati and J. J. Sansalone, "Modeling particulate matter resuspension and washout from urban drainage hydrodynamic separators," *Journal of Environmental Engineering*, vol. 138, no. 1, pp. 90–100, 2012.
- [6] W. D. Carrier, "Goodbye, hazen; hello, kozeny-carman," *Journal of Geotechnical and Geoenvironmental Engineering*, vol. 129, no. 11, pp. 1054–1056, 2003.
- [7] S. Ergun, "Fluid flow through packed columns," *Chemical Engineering Progress*, vol. 48, pp. 89–94, 1952.
- [8] D. Li and T. W. Engler, "Literature review on correlations of the non-Darcy coefficient," in *Proceedings of the SPE Permian Basin Oil and Gas Recovery Conference*, OnePetro, Midland, Tex, USA, May 2001.
- [9] J. Zhang, F. Li, L. Zeng, J. Peng, and J. Li, "Numerical simulation of the moisture migration of unsaturated clay embankments in southern China considering stress state," *Bulletin of Engineering Geology and the Environment*, vol. 80, no. 1, pp. 11–24, 2021.
- [10] J. Zhang, R. She, Z. Dai et al., "Experimental simulation study on pore clogging mechanism of porous pavement," *Construction and Building Materials*, vol. 187, pp. 803–818, 2018.
- [11] H. Zhou, H. Li, A. Abdelhady, X. Liang, H. Wang, and B. Yang, "Experimental investigation on the effect of pore characteristics on clogging risk of pervious concrete based on CT scanning," *Construction and Building Materials*, vol. 212, pp. 130–139, 2019.
- [12] J. Zhang, X. Cui, L. Li, and D. Huang, "Sediment transport and pore clogging of a porous pavement under surface runoff," *Road Materials and Pavement Design*, vol. 18, no. sup3, pp. 240–248, 2017.
- [13] J. Jiang, Z. Zhang, Q. Dong, and F. Ni, "Characterization and identification of asphalt mixtures based on convolutional neural network methods using X-ray scanning images," *Construction and Building Materials*, vol. 174, pp. 72–80, 2018.
- [14] G. Lu, Z. Wang, P. Liu, D. Wang, and M. Oeser, "Investigation of the hydraulic properties of pervious pavement mixtures: characterization of Darcy and non-Darcy flow based on pore microstructures," *Journal of Transportation Engineering, Part B: Pavements*, vol. 146, no. 2, Article ID 04020012, 2020.
- [15] G. Lu, P. Liu, T. Törzs, D. Wang, M. Oeser, and J. Grabe, "Numerical analysis for the influence of saturation on the base course of permeable pavement with a novel polyurethane binder," *Construction and Building Materials*, vol. 240, Article ID 117930, 2020.
- [16] G. Lu, L. Renken, T. Li, D. Wang, H. Li, and M. Oeser, "Experimental study on the polyurethane-bound pervious mixtures in the application of permeable pavements," *Construction and Building Materials*, vol. 202, pp. 838–850, 2019.

- [17] G. Lu, T. Törzs, P. Liu et al., “Dynamic response of fully permeable pavements: development of pore pressures under different modes of loading,” *Journal of Materials in Civil Engineering*, vol. 32, no. 7, Article ID 04020160, 2020.
- [18] G. Lu, H. Wang, T. Törzs et al., “In-situ and numerical investigation on the dynamic response of unbounded granular material in permeable pavement,” *Transportation Geotechnics*, vol. 25, Article ID 100396, 2020.
- [19] S. Xu, G. Lu, B. Hong et al., “Experimental investigation on the development of pore clogging in novel porous pavement based on polyurethane,” *Construction and Building Materials*, vol. 258, Article ID 120378, 2020.
- [20] G. Lu, P. Liu, Y. Wang, S. Faßbender, D. Wang, and M. Oeser, “Development of a sustainable pervious pavement material using recycled ceramic aggregate and bio-based polyurethane binder,” *Journal of Cleaner Production*, vol. 220, pp. 1052–1060, 2019.
- [21] X. Kuang, J. Sansalone, G. Ying, and V. Ranieri, “Pore-structure models of hydraulic conductivity for permeable pavement,” *Journal of Hydrology*, vol. 399, no. 3-4, pp. 148–157, 2011.
- [22] J. Zhang, J. Peng, L. Zeng, J. Li, and F. Li, “Rapid estimation of resilient modulus of subgrade soils using performance-related soil properties,” *International Journal of Pavement Engineering*, vol. 22, no. 6, pp. 732–739, 2021.



## Research Article

# Utilization of Waste Glass Powder and Glass Composite Fillers in Asphalt Pavements

Jayvant Choudhary <sup>1</sup>, Brind Kumar <sup>2</sup>, and Ankit Gupta <sup>2</sup>

<sup>1</sup>Department of Civil Engineering, Madhav Institute of Technology and Science, Gwalior, India

<sup>2</sup>Department of Civil Engineering, Indian Institute of Technology (Banaras Hindu University), Varanasi, India

Correspondence should be addressed to Ankit Gupta; [ankit.civ@iitbhu.ac.in](mailto:ankit.civ@iitbhu.ac.in)

Received 22 April 2021; Revised 31 August 2021; Accepted 21 September 2021; Published 13 October 2021

Academic Editor: Guoyang Lu

Copyright © 2021 Jayvant Choudhary et al. This is an open access article distributed under the Creative Commons Attribution License, which permits unrestricted use, distribution, and reproduction in any medium, provided the original work is properly cited.

Today, researchers around the globe are looking for suitable alternatives of conventional fillers which can form flexible pavements with satisfactory engineering performance in an environmental friendly and cost-effective manner. This study investigated the engineering, economical, and environmental viability of recycling waste glass powder (GP) and glass-hydrated lime (GL) composite as alternative fillers, in place of stone dust (SD). All fillers were characterized, and asphalt concrete mixes incorporating them at different proportions (4–8.5%) were designed using the Marshall mix design method. The engineering performance of asphalt mixes was analyzed using the static creep analysis, indirect tensile fatigue test, Cantabro test, modified Lottman test, resilient modulus test, mixing time analysis, and boiling water test. Additionally, the design of single km of two-lane flexible pavements utilizing aforesaid mixes was done as per the mechanistically empirical method suggested in IRC 37 guideline. Finally, the economic and environmental analysis was done by comparing their material cost and global warming potential (GWP). GL and GP mixes exhibited better resistance against rutting, fatigue, and low temperature cracking at lower optimum asphalt content than SD mixes. However, GP mixes also displayed poor moisture resistance and adhesion due to the high amount of silica in GP. GL mixes had satisfactory moisture resistance up to 7% filler content due to the fine nature and anti-stripping properties of hydrated lime. The pavement containing GL and GP fillers also reduced material cost and GWP up to 35% while consuming up to 74 tons of GP.

## 1. Introduction

In recent years, reclaim, reuse, and recycling of wastes in place of virgin materials have become a recurring theme of growing importance. Transportation infrastructures play a key role in this context, as any new construction or rehabilitation consumes a huge amount of natural materials [1]. Utilization of wastes as alternative to virgin materials solves two important issues: the issues regarding the eco-friendly disposal of wastes as well as fulfilling the need to find suitable alternative to conventional/virgin materials. Global pavement network majorly consists of flexible pavements which use asphalt concrete mixes as their surface and base courses. Asphalt mix is a heterogeneous multiphase material which primarily comprises aggregates

of various shapes and sizes, asphalt binder, and filler. Asphalt mixes are extensively adopted in flexible pavements around the world as surface and binder courses which are with the combination of aggregates and asphalt binder. Various sizes of mineral aggregates in the asphalt mixes make up a rigid skeleton while the asphalt binder behaves as an adhesive. The aggregate portion which passes through the No. 200 sieve ( $75\ \mu\text{m}$ ) is termed as filler, which influences the mechanical behavior and durability of the asphalt mix [2–4]. The filler present in the asphalt mix combines with asphalt binder to form asphalt mastic. The filler activity in the mastic is due to the physical hardening and chemical interaction [5]. Based on this activity, the fillers can be generally classified into two categories known as active fillers and passive (inert) fillers. The fillers which

exhibit chemical activity in the mastic due to their alkaline nature and acidic nature of binder are termed as active fillers [5–7]. This chemical reaction is reported to improve the anti-aging potential, adhesion, and high temperature resistance in asphalt mastic and mixes [7, 8]. It is majorly dependent on the compositional and elemental characteristics of filler and binder. The fillers such as hydrated lime, cement, steel slag, and so on fall under the category of active fillers. On the other hand, the inert or passive fillers exhibit little to no chemical activity in asphalt mastic. However, they are usually responsible for causing stiffness or physical hardening in the asphalt mastic owing to their physical characteristics. The fillers such as stone dust, limestone, and granite fall in the category of passive fillers [9]. Overall, the performance of asphalt mixes against distresses like permanent deformation, load and non-load dependent cracking, aging, and moisture sensitivity is largely dependent on the physical and chemical characteristics of fillers [3, 10–12]. Hence, it can be said that nature and quantity of fillers are essential to ensure the cost effectiveness and long-lasting performance of flexible pavements. The cement, stone dust, and lime are primarily used as conventional fillers. However, various agencies are promoting the utilization of waste and secondary by-products in place of conventional materials not only to reduce landfill waste and to save the cost of conventional materials but also to ensure sustainable pavement construction by limiting the amount of greenhouse gas emission. It is essential that the asphalt mixes made with alternative materials should exhibit satisfactory engineering performance in a cost-effective and environmental friendly manner. The enhanced performance of asphalt mixes containing alternative solid waste fillers such as bauxite residue [13]; biomass ashes [14]; brick dust [15]; coal fly ash [16, 17]; and lime kiln dust [18] as fillers has inspired researchers to investigate the viability of other wastes to form technically, economically, and environmentally feasible flexible pavements. However, majority of the available studies are concerned with the examining the engineering performance of asphalt mix and very limited attention has been given in analyzing the material cost and environmental suitability of asphalt pavements made with these mixes.

Glass is one of the primarily used commodities which have numerous applications such as utensils, lighting, window shelves, flooring, appliances, solar panel, and fibre optic cables. The disposal of waste glass has become a primary environmental concern due to growing demand for landfill spaces and increasing emphasis on carbon footprint reduction of construction industries. Glass is a non-biodegradable material due to its inert nature. Non-recyclable waste glass takes around 1 million years to decompose and occupies precious landfill spaces. The waste glass disposal has emerged as a primary environmental concern due to the growing demand for landfill spaces and increasing emphasis on carbon footprint reduction of construction industries. Glass is one of the widely used materials whose annual global production is estimated to exceed 130 million tons [19]. Waste glass is usually referred to as a by-product of

crushed bottles, window panes, and other glass items obtained from streams of industrial and municipal wastes. However, a significant quantity of waste is also obtained as waste slurry which is produced during cutting and polishing operations of glass slabs in glass industries [20]. Recently, waste glass has been successfully utilized in manufacturing products like cementitious binding material [21], acid resistant concrete [22], pavement base course [23], geopolymers [24], and ceramics [25]. However, there are only a few studies which have attempted to recycle the crushed glass and glass powder as aggregates (fine and coarse) and filler in asphalt mixes, respectively. Earlier studies [26, 27] have observed that the incorporation of glass powder in different quantities as filler led to the formation of asphalt mixes with higher Marshall stability in comparison to the asphalt mixes containing conventional fillers like cement and limestone dust. Arabani et al. [15] observed that the asphalt mixes containing glass powder as filler exhibited superior Marshall stability and rutting and fatigue resistance than conventional asphalt mixes. They concluded that the physical and chemical characteristics of glass powder filler are responsible for its better physicochemical interaction with asphalt binder that ultimately improved the performance of their asphalt mixes.

Simone et al. [28] also observed that incorporation of glass powder as filler increased the stiffness of asphalt mastics which may result in formation of asphalt mixes having better bearing capacity and rutting resistance. However, despite the superior performance of asphalt mixes against rutting and cracking, a few recent studies [29–31] have reported the poor behavior of asphalt mixes containing glass powder against stripping and ravelling. This was attributed to low asphalt absorption by the glass and high silica content in its composition [29, 31, 32]. In order to establish glass as alternative filler, it is vital that the asphalt mixes made with it exhibit satisfactory moisture resistance. Hence, attempts are needed to be made to introduce glass powder along with an anti-stripping agent in the form of a composite filler to ensure satisfactory performance of the asphalt mixes against moisture resistance. However, the primary challenge in this approach is to identify the appropriate anti-stripping agent along with its optimum proportion in the composite filler.

Hydrated lime is a well-known anti-stripping agent used in reducing moisture damage (stripping). Hydrated lime not only strengthens the asphalt-aggregate bond but also reacts with the highly polar molecules in asphalt to form strong chemical bonds to reduce stripping. The addition of hydrated lime also stiffens the mix and reduces the stripping by increasing the mechanical strength of the asphalt-aggregate bond. Hence, the addition of a small amount of hydrated lime with glass powder can reduce the possibility of stripping and can increase the allowable percentage of glass in the mix. The hydrated lime addition improved mechanical properties of asphalt mix and its aging resistance [33]. Hence, hydrated lime could be admixed in an optimum amount to the glass powder to form a glass-hydrated lime composite filler which could form asphalt mixes with superior rutting and cracking resistance without compromising its moisture sensitivity.

There are very limited studies which have utilized glass as a construction material along with hydrated lime. Lachance-Tremblay et al. [34] examined the effect of glass aggregate and hydrated lime content on linear viscoelastic (LVE) properties of asphalt mixes, and asphalt mixes containing glass aggregates were found to have lower stiffness values than conventional asphalt mixes (i.e., no glass aggregates). Raschia et al. [35] investigated the performance of glass filler alone and in combination with hydrated lime as composite filler in cold emulsion asphalt mixes. Results indicated that after the curing period of three days, mixes stabilized with glass powder were unable to reach satisfactory resilient modulus and mechanical performance due to the poor reactivity of the silica with the asphalt binder/water. On the other hand, the composite filler formed with glass and hydrated lime delivered better performances due to the reaction between silica and calcium hydroxide. In this study, the authors have performed the investigation herein described to fill the huge research gap by developing a glass-hydrated lime composite filler and analyzing the engineering suitability of asphalt mixes containing glass powder and glass-hydrated lime composite (newly developed) fillers against conventional asphalt mixes containing stone dust filler. Additionally, this is the first study which has investigated the economical and environmental suitability of asphalt mixes containing glass powder and glass-hydrated lime composite mixes.

## 2. Objectives and the Brief Outline of the Study

The overall objective of this study is to maximize the utilization of waste glass powder (GP) in asphalt concrete mixes as filler without compromising with the engineering, economical, and environmental suitability of asphalt mixes. Previous literatures observed that the GP is notorious in causing stripping in asphalt mixes, and hence the GP is incorporated not only as filler but also in the form of glass-hydrated lime composite (GL) filler. GL as filler was prepared with an intention of avoiding the possibility of formation of the moisture-sensitive mix due to high silica content in glass by adding a nominal amount of HL as an anti-stripping agent.

To achieve this objective, the study is divided into four parts: (1) prequalification assessment of glass powder (GP), hydrated lime (HL), and stone dust (SD) fillers; (2) design of asphalt mixtures containing GP, GL, and SD fillers at different quantities (4, 5.5, 7, and 8.5% by weight of asphalt mix); (3) evaluation of mechanical and durability performance of designed mixes with relevant static and dynamic tests; and (4) design and cost analysis of flexible pavements using MEPDG-based IITPAVE software utilizing designed mixes in the surface course. Waste glass powder was collected from dumping ground of glass factory, where it was generated as dried slurry. The GL filler was prepared by fixing the proportion of hydrated lime at 2% in the respective filler proportion of the mix (4–8.5%) and assigning the balance part to GP. The maximum permissible limit of HL used in the asphalt mix is specified as 2% by Indian pavement design guidelines [4]. Hence, the proportion of

hydrated lime is fixed at 2% in GL to envisage the maximum utilization of GP (as per the objective) without compromising the asphalt mix's moisture resistance. The asphalt mix design was done as per MS-2 specification [36]. The asphalt mixes were compared in aspects such as strength, volumetric properties, rutting, fatigue and low temperature cracking resistance, moisture sensitivity, ravelling resistance, resilient modulus, and active and passive adhesion as per relevant testing specifications. The design and cost analysis of flexible pavements utilizing the aforesaid mixes in their surface course was done with IITPAVE software according to Indian pavement design guideline IRC 37: 2018 [37]. The research methodology of the study is displayed in the form of flow chart as shown in Figure 1.

## 3. Materials and Experimental Investigation

**3.1. Materials.** Dolomite aggregates were utilized, and their characteristics are mentioned in Table 1. The design gradation for the preparation of the asphalt concrete is stated in Table 2.

VG 30 asphalt binder (synonymous to PG 76-XX binder), whose properties are mentioned in Table 1, was used in the study. SD and HL were collected locally from Varanasi city, while GP was procured from the glass factory's dump yard situated in Bhopal city, India.

**3.2. Tests on Filler.** Various characterization properties of fillers were obtained as per relevant specifications. Specific gravity was assessed according to ASTM D854-14 [38]. Particle size distribution curves of fillers was drawn with Malvern mastersizer, and fineness modulus (FM) and mean particle size ( $D_{50}$ ) were assessed. Scanning electron microscopy (SEM) analysis was performed to analyze the shape and texture of fillers. The German filler test was done to determine the porosity of fillers [39]. X-ray diffraction (XRD) analysis was done with a Rigaku benchtop XRD device to obtain the minerals in fillers. The harmful clay content was assessed as per EN 933-9 [40]. Finally, the relative affinity of fillers towards binder and water was compared by determining their hydrophilic coefficients as per JTG E42 [41] specification.

### 3.3. Testing of Asphalt Concrete

**3.3.1. Marshall and Volumetric Properties.** Asphalt mixes were designed as per Marshall mix design procedure, in which binder content corresponding to 4% air voids is considered as OAC [4, 42]. The binder content was varied in the range of 4.5–6.5%, and three specimens were prepared at each binder level, and a total of 240 specimens (5 binder contents  $\times$  4 types of fillers  $\times$  4 filler contents  $\times$  3 replicates) were prepared for the determination of OAC. The gradation for the mix is chosen as per MoRTH specification as shown in Table 2, and filler content was varied between 4, 5.5, 7, and 8.5% by the weight of the aggregates. The filler proportion was increased by reducing the fine aggregate proportions which help to maintain the chosen gradation. As stated in

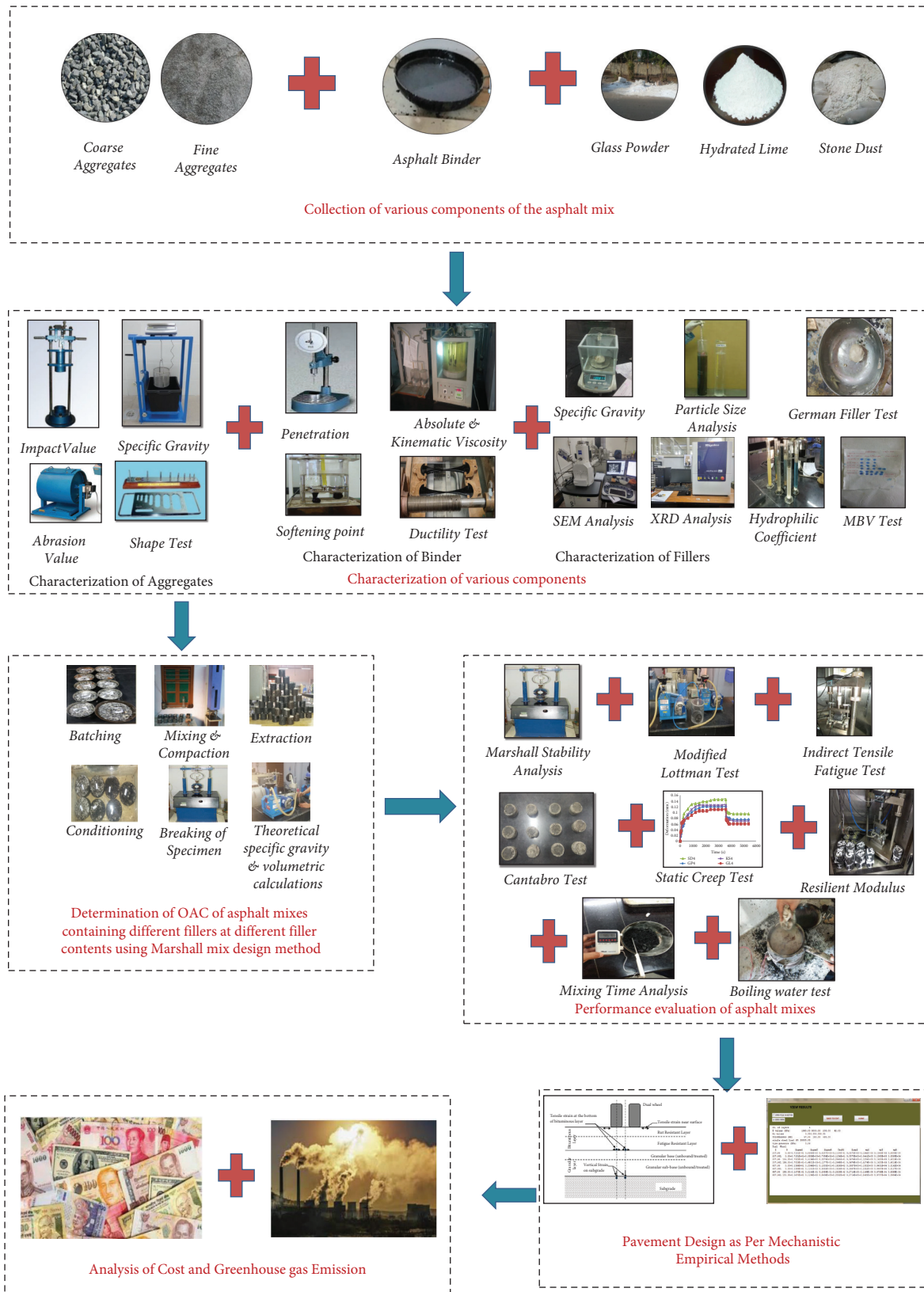


FIGURE 1: Flowchart showing entire research methodology of the study.

TABLE 1: Properties of aggregate and asphalt.

Material	Property	Specification	Results	Requirements
Aggregates	Bulk specific gravity of coarse aggregate	ASTM C127	2.795	-
	Bulk specific gravity of fine aggregate	ASTM C128	2.720	-
	Water absorption of coarse aggregate (%)	ASTM C127	0.374	2% (max)
	Aggregate impact value (%)	IS:2386 (Part IV)	11.1%	24% (max)
	Los Angeles abrasion value (%)	IS:2386(Part IV)	13.4%	30% (max)
	Combined flakiness and elongation index	IS: 2386(Part I)	21.3%	35% (max)
Asphalt	Absolute viscosity at 60°C (poise)		2692	2400–3600
	Penetration at 25°C (0.1 mm)		62	50–70
	Softening point (°C)	IS 73: 2013	51.5	47 (min)
	Ductility at 27°C (cm)		>100	75 (min)
	Specific gravity		0.999	0.98–1.04

TABLE 2: Adopted gradation of asphalt concrete mix.

Sieve sizes (mm)	19	13.2	9.5	4.75	2.36	1.18	0.6	0.3	0.15	0.075
Allowable limits (%)	100	90–100	70–88	53–71	42–58	34–48	26–38	19–28	12–20	4–10
Adopted gradation (%)	100	91	74	62	50	43	35	25	14	4, 5.5, 7, and 8

the previous section, asphalt concrete mixes incorporating GL filler were designed by replacing 2% GP at each filler dosage level with HL. The average Marshall (stability and flow) and volumetric properties (voids in mineral aggregates (VMA) and voids filled with binder (VFB)) of mixes were also determined at OAC. The three specimens were prepared at each OAC, and a total of 48 specimens (4 types of fillers  $\times$  4 filler contents  $\times$  1 OAC  $\times$  3 replicates) were prepared for the calculation of Marshall and volumetric properties, and average values are reported. The apparent film thickness (AFT) of mixes was estimated as per the following equation:

$$\text{AFT} = \frac{1000VBE}{S_s P_s G_{mb}}, \quad (1)$$

where  $S_s$  = specific surface of aggregates ( $\text{m}^2/\text{kg}$ );  $P_s$  = percentage of aggregates (%);  $G_{mb}$  = bulk specific gravity; and  $VBE$  = effective asphalt content (%)

**3.3.2. Rutting Resistance.** The rutting resistance was determined using a uniaxial static creep test. The testing was done as per BS 598-111 by imposing a static compressive load to specimen and determining its axial deformation with time [43]. The evaluation of the reversible part of deformation is determined by removing load and measuring the deformation recovered. The constant load was applied to the specimen to generate 100 kPa axial stress during the loading period of 60 minutes, while the unloading period of the test is taken as 30 minutes. The three specimens were prepared at each OAC, and a total of 48 specimens (4 types of fillers  $\times$  4 filler contents  $\times$  1 OAC  $\times$  3 replicates) were prepared for the calculation of rutting resistance, and average values are reported.

**3.3.3. Cracking Resistance.** There are two primary types of cracking in asphalt mixes, namely, thermal cracking at low temperature and fatigue cracking. Cracking at low

temperature is generated due to excessive tensile stresses generated in the mixes due to low temperature and embrittlement [44]. The low temperature cracking was determined at 0°C by calculating the indirect tensile strength (ITS) per ASTM D 6931-12 [45] specification. Higher ITS value corresponds to higher resistance to low temperature cracking and vice versa [44, 46].

Fatigue cracking is initiated at bottom of layer of asphalt mixes by the generation of tensile stresses due to repeated traffic loading at intermediate temperature [47]. The fatigue life of asphalt mixes was calculated as per EN 12697-24 guideline. The test was done at 25°C under controlled stress condition, and the testing stress is taken as 40% of the ITS. The haversine loading is applied through the haversine load pulse with loading period of 0.1 s and rest period of 0.4 s. The three specimens were prepared at each OAC, and a total of 48 specimens (4 types of fillers  $\times$  4 filler contents  $\times$  1 OAC  $\times$  3 replicates) were prepared for the calculation of low temperature cracking and fatigue resistance, and average values are reported.

**3.3.4. Asphalt Aggregate Adhesion and Moisture Susceptibility.** An asphalt mix must have good adhesion between asphalt binder and aggregates in both dry and wet conditions. The adhesion loss in the aggregate-binder interface is one of the primarily responsible mechanisms for high moisture susceptibility in the mixes. It could be divided into two components, namely, active adhesion and passive adhesion. Active adhesion is the ability of binder to completely coat aggregates in mixing operation of asphalt mixes [48, 49]. Active adhesion can also be represented by the term mixability. On the other hand, passive adhesion is the ability of the asphalt binder to remain coated on the surface of aggregate while being subjected to the external moisture and traffic (also represented as moisture susceptibility) [48, 49].

The effect of various fillers on the active adhesion was analyzed by measuring the time required by the aggregates in

the mix to get uniformly coated with the binder. The total time elapsed between the moment of the addition of binder to the moment of all aggregates in the mix getting 100% coated is measured. In this study, the analysis of passive adhesion/moisture susceptibility of loose mixes and the compacted specimen was conducted using two empirical tests as per ASTM D 3625-12 [50] and AASHTO T283 guidelines, respectively. The loose asphalt mixes were submerged in the boiling water for 10 minutes (maintained at a temperature between 85 and 100°C), and the retained asphalt binder coating on aggregates was calculated by visual observation. The three specimens were prepared at each OAC, and sets of 48 specimens (4 types of fillers  $\times$  4 filler contents  $\times$  1 OAC  $\times$  3 replicates) were prepared for the calculation of active adhesion and passive adhesion of loose mixes, while the moisture resistance of compacted mixes was estimated by comparing their tensile strength ratio (TSR) [51]. In this analysis, two sets of Marshall specimens (conditioned and unconditioned) were prepared at 7% air voids for each mix. The six specimens were prepared at each OAC, and a set of 96 specimens (4 types of fillers  $\times$  4 filler contents  $\times$  1 OAC  $\times$  2 conditions of specimens  $\times$  3 replicates) were prepared for the calculation of TSR. The conditioned specimens were then subjected to a cycle of freeze-thaw conditioning. The TSR of the mixes was then determined as the ratio of mean ITS of conditioned specimens to the mean ITS of unconditioned specimens. The mix having higher TSR value exhibited lower moisture susceptibility.

**3.3.5. Ravelling Resistance.** The ravelling resistance of asphalt mixes was estimated with the Cantabro loss test as per Spanish norm NLT-352/86 [52]. In this test, Marshall specimens were placed in the Los Angeles abrasion (without steel charges) and were subjected to 300 rotations at the rate of 33 rpm. Three specimens were prepared for each type of mix, and a total of 48 specimens (4 types of fillers  $\times$  4 filler contents  $\times$  1 OAC  $\times$  3 replicates) were prepared for the calculation of ravelling resistance, and average values are reported. The percentage loss of weight suffered by the specimens was measured and termed as Cantabro loss. The mix which suffered lesser Cantabro loss exhibited better resistance against ravelling and vice versa.

**3.3.6. Resilient Modulus.** Resilient modulus ( $M_r$ ) is an integral parameter used in pavement design using mechanistic-empirical pavement design guidelines which analyze the ability of pavement layer to disperse load.  $M_r$  of Marshall specimens was determined according to ASTM D4123-82 [53] at 35°C using a universal testing machine. The stress level used in testing should lie between 10 and 50% of the ITS, and hence the load corresponding to 10% of ITS was used for testing [53]. The haversine load pulse was used in analysis at 1 Hz frequency (0.1 s load and 0.9 s rest period), while Poisson's ratio of each mix was taken as 0.35 [15, 54]. Three specimens were prepared for each type of mix, and a total of 48 specimens (4 types of fillers  $\times$  4 filler contents  $\times$  1

OAC  $\times$  3 replicates) were prepared for the calculation of resilient modulus, and average values are reported. The resilient modulus was determined using the following equation:

$$M_r = \frac{P(\nu + 0.27)}{t\Delta\delta}, \quad (2)$$

where  $M_r$  = resilient modulus (MPa),  $P$  = repeated load (N),  $\nu$  = Poisson ratio,  $t$  = specimen thickness (mm), and  $\delta$  = recoverable horizontal deformation (mm).

### 3.4. Design and Analysis of Flexible Pavements

**3.4.1. Design of Flexible Pavements.** This objective of this section is to design most economical flexible pavement section utilizing various asphalt concrete mixes as surface course to support similar design traffic. The analysis was done according to IRC 37: 2018 specification which considers pavement as a multilayer system and uses "linear elastic layered theory" for its analysis [37]. In all sections, the pavement system was assumed to have asphalt surfacing, asphalt binder course, granulous base, and subbase course and subgrade. The primary material properties (stiffness moduli and Poisson's ratio) and layer thickness for each course are shown in Figure 2. Resilient modulus values of mixes determined in the previous section were adopted as elastic modulus values for the surface course. The design traffic volume is selected as the total traffic volume which pavement encounters during its service life. In this study, the design traffic volume is assumed to be 200 million standard axles (msa), which corresponds to a standard busy highway section having a very heavy traffic volume.

As per IRC 37: 2018, the layer thickness of the surface course should be selected in such a manner that the stress and strain obtained at the critical locations should not exceed the allowable strains. The allowable stress or strain is termed as the maximum stress or strain occurring at critical locations of the pavement system which leads to its failure. In this particular case, the tensile strain at the bottom fibre of the bottommost asphalt layer (binder course) and compressive strain at the top of the subgrade are considered as critical locations.

The allowable strains at these locations can be determined using subgrade rutting and asphalt fatigue equations (3) and (4) at a 90% reliability factor with respective air void volume and bitumen volume in the mixtures [37].

Allowable vertical compressive strain at the top of the subgrade was calculated from the following equation:

$$N_r = 1.41 \times 10^{-8} \left[ \frac{1}{\varepsilon_v} \right]^{4.5337}, \quad (3)$$

where  $N_r$  is design traffic volume and  $\varepsilon_v$  is the vertical compressive strain at the top of the subgrade.

Allowable tensile strain at the bottom fibre of the binder course was calculated from the following equation:



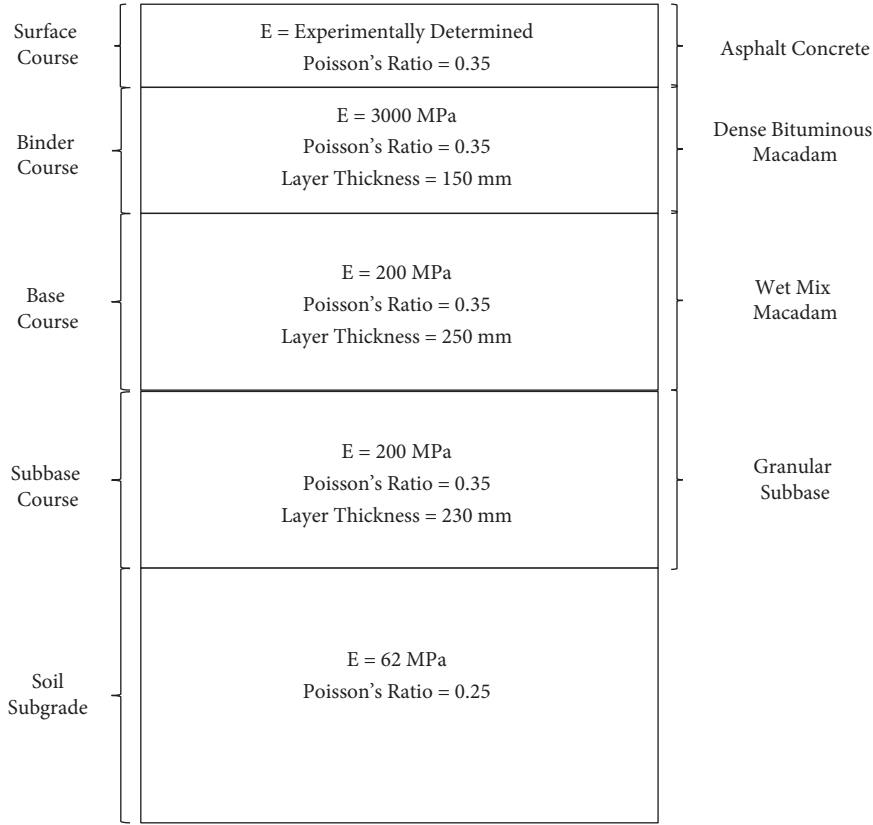


FIGURE 2: Pavement structure designed in this study.

$$N_f = 0.5161 \times C \times 10^{-4} \times \left[ \frac{1}{\varepsilon_t} \right]^{3.89} \times \left[ \frac{1}{M_R} \right]^{0.854}, \quad (4)$$

where  $N_f$  is design traffic volume,  $\varepsilon_t$  is the horizontal tensile strain at the bottom fibre of the binder course, and  $M_R$  is the resilient modulus (MPa) of the binder layer.

The factor "C" is termed as the adjustment factor which is used to take account for the effect of variation in the volumetric parameters (air voids and effective binder volume) on the fatigue life of the bottommost asphalt course.

$$C = 10^M, \quad (5)$$

$$M = 4.84 \left( \frac{V_{be}}{V_{be} + V_a} - 0.69 \right), \quad (6)$$

where  $V_{be}$  and  $V_a$  represent effective binder volume and volume of air voids in the binder course of the pavement. In this study, binder course is assumed to have  $V_{be}$  and  $V_a$  equal to 3% and 11.5%, respectively. These are commonly preferred at the pavement site to ensure satisfactory pavement performance [37]. Hence, the value of  $C$  corresponding to these volumetric properties was calculated and taken as 3.155.

For each pavement system, the thickness of the surface course was assumed by trial and error (keeping other layer thicknesses constant) to ensure that the strains that occurred at critical locations should not exceed the allowable strains. The strains at different locations of the pavement system

were determined using IITPAVE software which is prescribed by IRC: 37 guideline. The design thickness for the surface course was finalized as the minimum layer thickness (most economical) at which strains at critical locations should not exceed the allowable strains.

#### 3.4.2. Cost Analysis of Designed Pavement Surface Course.

The cost of materials needed to construct a single km of two-lane (7.00 m) pavement surface course for design traffic volume is calculated in this section. The expenditures related to workmanship and machinery are not taken in the analysis, but only the material costs are taken into consideration. The surface layer thickness was determined in previous section, and the quantity of ingredients was calculated accordingly. The detailed steps involved in the assessment of the material quantity and their cost can be referred from the recently published study of the authors [30]. The price of pavement materials was taken according to the specification of Central Public Works Department, India [55]. GP was obtained directly from its dumping grounds, and hence its cost is taken as zero. The cost required in transferring SD from the stone crusher to pavement location was assumed to be same of that of transporting GP from its dumping ground to pavement site. The GP needed minimal processing since it was found to be already fine in their natural state. The GP processing (labour) cost was implied as 0.5% of the total material cost [30]. The cost incurred in transporting waste materials was assumed to be the same as that incurred in

transferring conventional SD from its quarries to the pavement site.

**3.4.3. Analysis of Global Warming Potential (GWP) of Designed Surface Courses.** According to Intergovernmental Panel on Climate Change (IPCC), the GWP comprised of all substances which contribute to the climate change [56]. To analyze the GWP, the lifetime of a substance and its efficiency to act as a GHG are estimated. The life cycle of any pavement comprised of four different phases: material production, construction, use, and maintenance [57]. In this study, the GWP for various asphalt mixes was determined by comparing the GHG emission happened during the material production that is required to manufacture 1 km of flexible pavement section utilizing all twelve types of asphalt mixes as surface course.

The GWP for various asphalt mixes was assessed by comparing the green house gas (GHG) emission occurred in manufacturing 1 km of flexible pavement section utilizing all twelve types of asphalt mixes as a surface course. After the calculation of optimum design thickness for the surface courses for each type of mixes, the amount of material needed to construct 1 km of two-lane (7 m) surface course was calculated. The standard amount of emission (in terms of kg of CO<sub>2</sub> equivalent) by different materials (coarse and fine aggregates, stone dust (SD), hydrated lime (HL), and asphalt binder) was taken from the several previously published peer reviewed studies [58–61]. European Union's Waste Framework Directive (2008/98/EC) defines "waste" as any substance or object which the holder discards or intends or is required to discard [62]. Since GP is discarded by its agency, it can be considered as waste. It was also stated beforehand that these materials were incorporated in the asphalt mixes directly without any physical or chemical modification. Hence, considering all these factors, the GWP of GP was assumed as zero. For the sake of simplification, construction, use, and maintenance phases were not taken into analysis. This is justified by the assumption that different production setups for every construction material do not influence the use and maintenance of the pavement.

## 4. Discussion of Results

**4.1. Filler Characterization.** The characteristics of fillers are stated in Table 3 and Figures 3(a) and 3(b). SD has the highest specific gravity while HL and GP had almost similar specific gravities. Thus, SD occupies lower volume in asphalt mix per unit weight. Particle size distribution curves are shown in Figure 3(a). HL was the finest filler while SD and GP were the coarsest fillers and have higher FM and D<sub>50</sub> values. SEM images of fillers are shown in Figure 3(b). GP and SD have relatively large, angular particles with smooth texture, while HL had smaller particles with rough texture. GP and HL fillers displayed relatively higher porosity as compared to SD as seen from their lower German filler values. The high porosity of filler may increase the OAC and rutting resistance of asphalt mixes [16]. Active clay in fillers

can swell in presence of water and lower the adhesion between filler and asphalt, which weakens the asphalt mix. However, all fillers had low active clay content as indicated by their lower methylene blue value. HL and SD were found to have a predominance of Portlandite and dolomite in their composition. Both of them comprised of calcium-based minerals which reduce moisture sensitivity of asphalt mixes. GP consists of a high amount of silica as quartz which is usually linked with greater moisture sensitivity of asphalt mix [63]. However, all fillers displayed hydrophobic nature and exhibited superior affinity towards asphalt binder. Based on detailed preliminary characterization, all materials fulfilled the requirements of fillers in asphalt mixes.

## 4.2. Performance of Asphalt Concrete Mixes

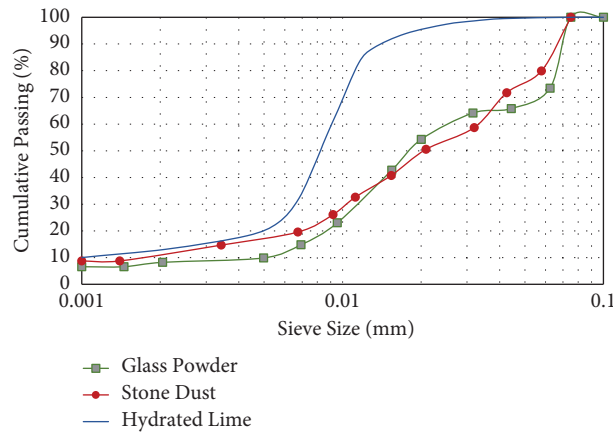
**4.2.1. Marshall Properties.** The Marshall and volumetric properties of most of the mixes fulfilled the requirements specified in Indian specification (Table 4) [4]. However, mixes prepared with 8.5% of GL had marginally lower (13.9%) VMA value than required.

Up to 7% filler content, Marshall stability (MS) of mixes tends to improve with filler content because of toughening of asphalt mastic because of simultaneous growth in quantity of filler as well as lowering in OAC. However, there is a marginal drop in MS in GP and GL mixes containing 8.5% filler which might be attributed to the adhesion loss in mastic due to lower OAC and higher silica content of fillers. In general, it is observed that GL mixes had higher MS followed by SD and GP mixes due to the strengthening of asphalt mastic due to the greater fineness of HL. However, at 8.5% filler, mixes with SD had the highest stabilities followed by GL and GP mixes that may be because of the reduction in adhesion in GP and GL mixes caused by high silica content in the glass [64]. OAC reduced with the increase in filler amount due to asphalt "extender" behavior of fillers, which enable them to form same amount of mastic with higher filler content and lower binder content. Hence, mixes prepared with higher filler contents require lower binder content to the specified air voids [11, 16, 64]. Asphalt mixes containing GP exhibited lowest OAC followed by GP and SD mixes. HL is the finest filler followed by GP and SD. Hence, GL showed better asphalt extender effect than other fillers. Additionally, HL and GP have lower specific gravities, and hence they occupy larger volume when incorporated in same weight proportion. It consequently leaves a lower volume for binder accumulation, thus resulting in lowering of OAC in their mixes [18, 65].

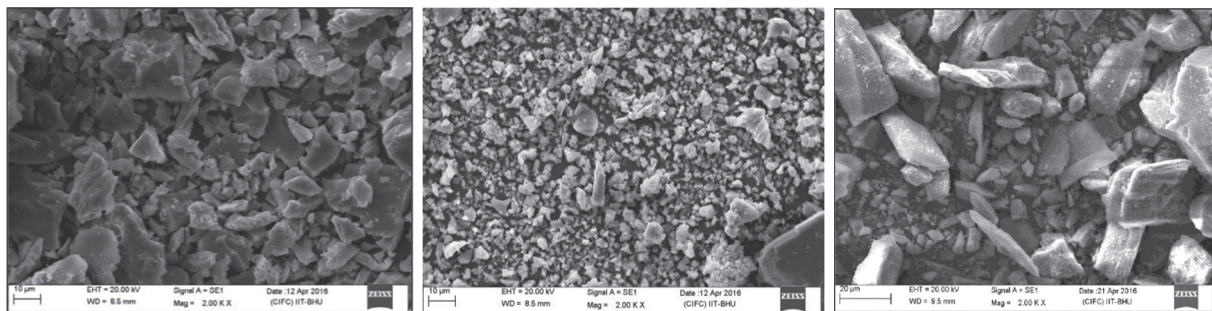
**4.2.2. Rutting Resistance.** The permanent deformation (creep) of asphalt mixes decreased with the increase in filler content (Table 5). The trend is consistent for all filler contents and agrees with results obtained in previous studies [16, 17, 64]. For all mixes, both VMA and AFT decreased with increase in filler content. Previous studies have suggested that the mixes having lower VMA and apparent film thickness (AFT) tend to display better rutting resistance [44, 66]. In general, GL mixes displayed the maximum

TABLE 3: Details of characterization properties of fillers.

Filler property	Glass powder (GP)	Hydrated lime (HL)	Stone dust (SD)	Inferences
Specific gravity	2.370	2.363	2.698	GP and HL have lower specific gravity than SD, and thus they occupy larger volume in asphalt mix in comparison to SD. Hence mixes containing GP and HL has lower OAC than conventional asphalt mixes containing SD.
Methylene blue value (g/kg)	1.25	0.25	3.25	All fillers have low MBV (less than 10) which indicated the presence of lower harmful clay content per unit weight of material.
German filler value (g)	75	35	85	HL and SD were found to have lowest and highest porosity/fractional voids per unit weight, respectively.
Fineness modulus $D_{50}$ ( $\mu\text{m}$ )	4.66 19	2.93 9	5.38 21	SD and HL were found to be coarsest and finest fillers, respectively.
Particle shape and texture (SEM)	Angular particles with smooth texture	Subangular and granulous particles with a rough texture	Angular particles with smooth to rough texture	Particles with rough texture may negatively affect workability and can also cause higher asphalt absorption.
Primary mineralogical composition (XRD)	Quartz ( $\text{SiO}_2$ )	Portlandite ( $\text{Ca}(\text{OH})_2$ ), calcite ( $\text{CaCO}_3$ )	Dolomite ( $\text{CaMg}(\text{CO}_3)_2$ ), quartz ( $\text{SiO}_2$ ), ertixite ( $\text{Na}_2\text{Si}_4\text{O}_9$ )	Absence of any harmful expansive clay minerals. SD and HL consist of dolomite and Portlandite, respectively, which is a calcium-based water-insoluble mineral having good asphalt adhesion. Quartz is associated with poor moisture sensitivity.
Hydrophilic coefficient	0.81	0.75	0.77	All materials displayed a higher affinity towards asphalt in comparison to water.



(a)



(b)

FIGURE 3: (a) Particle size distribution curves of various fillers. (b) SEM images of various fillers.

TABLE 4: Marshall and volumetric properties of various mixes (standard deviations are mentioned in the parenthesis).

Type of filler	Filler content (% of the weight of aggregates)	OAC (% of the total weight of mix)	Bulk specific gravity	VMA (%)	VFA(%)	Marshall stability (kN)	Flow (mm)	AFT ( $\mu\text{m}$ )
Stone dust	4.0	6.20	2.430 (0.005)	17.02 (0.18)	74.22 (0.94)	12.22 (0.30)	3.43 (0.18)	7.85
	5.5	5.95	2.444 (0.006)	16.21 (0.18)	74.43 (1.01)	13.99 (0.47)	3.62 (0.18)	7.34
	7.0	5.38	2.453 (0.010)	15.31 (0.31)	74.79 (1.95)	15.96 (0.29)	3.50 (0.31)	6.47
	8.5	5.34	2.466 (0.005)	14.70 (0.19)	72.01 (1.06)	16.58 (0.33)	3.22 (0.19)	5.77
Glass powder	4.0	6.03	2.427 (0.005)	16.51 (0.17)	74.85 (0.93)	12.98 (0.46)	3.38 (0.17)	7.38
	5.5	5.81	2.431 (0.009)	15.96 (0.29)	73.92 (1.64)	13.46 (0.52)	3.18 (0.29)	6.83
	7.0	5.48	2.441 (0.011)	14.85 (0.38)	72.97 (2.06)	14.93 (0.88)	3.37 (0.38)	6.17
	8.5	5.26	2.448 (0.008)	14.23 (0.28)	72.27 (1.67)	14.52 (0.62)	2.95 (0.28)	5.62
Glass-hydrated lime	4.0	5.65	2.448 (0.006)	15.43 (0.19)	74.18 (1.11)	14.32 (0.27)	3.21 (0.19)	6.99
	5.5	5.38	2.457 (0.010)	14.62 (0.36)	70.79 (2.05)	15.04 (0.30)	3.06 (0.36)	6.07
	7.0	5.12	2.455 (0.006)	14.22 (0.21)	69.15 (1.17)	16.78 (0.75)	3.30 (0.21)	5.50
	8.5	5.05	2.452 (0.010)	13.92 (0.37)	69.33 (2.15)	16.10 (0.40)	2.88 (0.37)	5.25
Requirements [4] (min)	4–10	-	-	14.00 (min)	65–75	9.00	2–4	

TABLE 5: Various properties of asphalt mixes at different filler contents (standard deviations are mentioned in the parenthesis).

Type of filler	Filler content (%)	Properties of asphalt mix							
		Permanent deformation (mm)	Indirect tensile strength (kPa)	Fatigue life (cycles)	Mixing time (s)	Retained asphalt coverage (%)	Tensile strength ratio (%)	Cantabro loss (%)	Resilient modulus (MPa)
Stone dust	4.0	0.095 (0.01)	2614 (132)	2491 (164)	84 (2.65)	100 (0.00)	94.23 (1.23)	4.74 (0.84)	1360 (117)
	5.5	0.085 (0.01)	2774 (184)	4201 (221)	89 (4.04)	100 (0.00)	93.28 (1.02)	3.86 (0.65)	1991 (97)
	7.0	0.072 (0.02)	3124 (226)	6036 (272)	93 (4.14)	97 (2.89)	89.26 (1.96)	3.42 (0.23)	2630 (101)
	8.5	0.06 (0.01)	3312 (118)	6964 (187)	108 (6.11)	93 (2.89)	85.59 (3.01)	5.32 (0.77)	2930 (88)
Glass powder	4.0	0.075 (0.01)	2964 (148)	4324 (267)	107 (5.57)	75 (5.00)	54.05 (4.85)	3.94 (0.61)	1610 (136)
	5.5	0.067 (0.01)	3108 (166)	5932 (174)	133 (9.17)	68 (2.89)	39.47 (5.59)	3.56 (0.47)	2134 (157)
	7.0	0.045 (0.01)	3452 (202)	6432 (265)	153 (3.46)	55 (5.00)	17.65 (6.38)	5.16 (0.88)	2834 (103)
	8.5	0.032 (0.01)	3654 (154)	5321 (301)	192 (3.51)	42 (2.89)	9.18 (2.46)	5.84 (0.28)	3072 (102)
Glass-hydrated lime	4.0	0.06 (0.02)	3024 (157)	4971 (144)	90 (2.00)	95 (0.00)	88.58 (1.21)	4.22 (1.01)	2042 (106)
	5.5	0.04 (0.01)	3392 (209)	6326 (212)	120 (4.51)	85 (0.00)	85.34 (1.32)	4.00 (0.52)	2542 (96)
	7.0	0.025 (0.00)	3712 (119)	7422 (314)	142 (6.51)	82 (2.89)	81.12 (2.54)	5.75 (0.84)	3111 (131)
	8.5	0.015 (0.00)	3796 (102)	6886 (137)	183 (4.73)	68 (2.89)	71.27 (3.99)	5.95 (0.36)	3512 (114)

rutting resistance followed by GP and SD mixes. GL mixes displayed the lowest permanent deformation trailed by mixes containing GP and SD because of their lowest VMA and AFT. Both waste and composite filler mixes displayed lower permanent deformation and higher rutting resistance than conventional SD mixes. High resistance of GL mixes against permanent deformation may also be due to finest particle size of HL, which tends to uniformly distribute in the mix and increase their stiffness.

**4.2.3. Cracking Resistance.** The ITS values of the mixes at 0°C were increased with filler content irrespective of the filler type (Table 5). The increase in ITS with filler content is due to increase in mastic strength due to the growth in filler proportion and decline in binder proportion. An increase in filler content in mixes also increased the density of mixes, which might also be a possible reason for the increase in ITS values [67]. The mixes having waste fillers showed superior ITS than SD mixes. GL mixes showed the highest ITS

followed by GP and SD mixes. The increase in the volume fraction of filler tends to increase the stiffness of the mastic and mixes, thus improving the ITS. Since GL and GP occupied the highest volume due to their low specific gravity, they exhibited higher ITS values. High ITS values of GL and GP mixes might be attributed to their fineness due to which they distribute uniformly and form an integrated structure which resulted in superior ITS [54, 68].

Fatigue lives of GL and GP mixes improved with filler quantity up to 7%. However, in case of SD mixes, fatigue life increased up to 8.5% filler content (Table 5). The primary reason for this phenomenon is the tendency of filler to display “crack pinning” behavior in the filler binder mastic which slows down the growth of microcracks by acting as barriers and deflects the crack propagation [69–71]. Another reason for the improvement in fatigue life with filler content may be due to the mode of testing. It was observed that fatigue life of mixes improved with growth in stiffness, when controlled stress mode of testing is adopted [72, 73]. In general, GL mixes displayed highest fatigue lives followed by

GP and SD mixes. HL and GP have lower specific gravity than SD, while their mixes have lower OAC than SD mixes. Hence, fillers in higher volume behave as barrier in relatively less quantity of binder, which deflected more number of cracks and improved the fatigue lives of their mixes. The asphalt mix's fatigue life is also dependent on the filler bitumen bonding. In the case of mixes having 8.5% filler, the SD filler maintained its bonding with bitumen (due to dolomite in composition), while the bond GP and GL fillers got weakened (high silica concentration) which led to a decrease in the fatigue life of their mixes.

**4.2.4. Asphalt Aggregate Adhesion and Moisture Susceptibility.** SD mixes displayed superior active and passive adhesion followed by GL and GP mixes, respectively (Table 5). They had the least mixing time and highest bitumen coverage than GL and GP mix, respectively (Table 5). The dolomite in SD and higher OAC of their mixes may be responsible factors for their better adhesion. GP mix showed adhesions due to presence of high amount of silica [29, 31]. Fillers containing high amount of silica form weak mechanical (van der Waals force) bond with asphalt binder which resulted in poor adhesion [74, 75]. GL mixes have displayed almost similar performance as SD mixes at 4% content, which may be due to the adhesion promoter behavior of HL. However, this influence seemed to diminish at higher filler contents (7% and 8.5%) and GL mixes delivered performance almost similar to GP mixes.

The passive adhesion in the compacted specimen is shown in Table 5. TSR values of mixes reduced with the higher filler quantity which was caused due to lowering in OAC and AFT of mixes. All asphalt mixes should have at least 80% TSR as per Indian specifications [4]. GP mixes displayed poor performance against moisture, and none of the GP modified mixes satisfied the given criteria (Table 5). However, it was found that replacement of 2% glass powder with hydrated lime (HL) had dramatically improved the values of TSR. The improvement in performance is due to anti-stripping nature of HL which contains Portlandite ( $\text{Ca}(\text{OH})_2$ ) in it [12, 33]. The hydrated lime was found to improve the moisture resistance of asphalt mixes by interacting with carboxylic acid in binder and forming water-insoluble calcium salts [76]. The improvement in moisture resistance in GL mixes might also be due to the formation of cementitious compounds because of the reaction of pozzolanic compound  $\text{SiO}_2$  and lime in the presence of water [77]. GL mixes displayed significantly high TSR values than GP mixes and have shown satisfactory TSR up to 7% of filler content in the mix. Hence, it can be said that up to 5% of GP along with 2% of HL can be satisfactorily utilized as a filler.

**4.2.5. Ravelling Resistance.** Ravelling resistance of all mixes was assessed by comparing their Cantabro loss (Table 5). It seemed that Cantabro losses reduced with filler content up to a limit followed by a marginal decline. The reduction in Cantabro loss might be attributed to mastic hardening with

the increase in filler proportion, which improved the impact resistance of the mixes [78]. However, excessive stiffening and lowering of OAC at higher filler contents reduced the adhesion which consequently increased the losses. GP and GL mixes showed lower Cantabro losses (at 4 and 5.5%) than SD mixes, while SD mixes displayed better performance at higher filler contents (7 and 8.5%).

**4.2.6. Resilient Modulus.** The resilient modulus ( $M_r$ ) of mixes is stated in Table 5 and was found to increase with the filler content. It is due to the lower OBC of waste filler modified mixes and due to fineness of filler particles [54, 75]. In general, GL mixes showed highest  $M_r$  values followed by GP and SD mixes. Hence, flexible pavements with GP and GL mixes may support same volume of traffic with relatively lower layer thickness than SD mix.

### 4.3. Analysis of Flexible Pavements

**4.3.1. Structural Design of Flexible Pavements.** The allowable vertical compressive and horizontal tensile strains at critical locations were found to be  $0.273 \times 10^{-4}$  and  $0.134 \times 10^{-3}$ , respectively, as per equations (4) and (5). The minimum surface layer thickness which ensures that the strain in critical location remains lower than allowable strains was determined using IITPAVE software [37]. The thicknesses corresponding to each mix are stated in Table 6. It is seen that the growth in filler content significantly improved the stiffness of mixes, which ultimately resulted in a considerable reduction in required surface layer thickness. The comparison of layer thickness of various mixes with SD mix containing 4% filler (SD 4) is also reported in Table 6. GL mixes displayed the lowest layer thickness followed by GP and SD mixes. The use of waste fillers seemed to significantly reduce the required thickness which resulted in a momentous saving in material and workmanship.

**4.3.2. Cost Analysis of Flexible Pavements.** The amount of ingredients consumed to construct 1 km of 2-lane surface course is stated in Table 7 along with their respective cost. The cost comparison of various surface courses with SD mix containing 4% filler (SD 4) mix is made in Table 8. It can be clearly seen that cost of surface courses significantly declined with increase in filler content. Since binder has the highest cost, the reduction in cost of different mixes was attributed to the its relative savings. Asphalt mixes containing GL mixes were found to be most economical followed by GP and SD mixes. The use of GL and GP resulted in momentous savings of 33 and 35%, respectively. In the case of SD mixes, the growth in filler content from 4 to 8.5% has resulted in a cost reduction of up to 30%.

**4.3.3. Analysis of GWP of Flexible Pavements.** The GWP of various surface courses was analyzed by comparing their GHG, which is shown in Tables 9 and 10. Similar to the cost analysis, the growth in filler content tends to significantly reduce the GWP of surface courses. The GP mixes can be

TABLE 6: The adopted thickness and computed strains (using IITPAVE).

Type of filler	Percentage of filler in the mix (%)	Resilient modulus at 35°C (MPa)	The adopted thickness of surface course (mm)	Computed vertical compressive strain at top of the subgrade	Computed horizontal tensile strain at the bottom of the bottommost bituminous layer	Comparison of the surface layer thickness of different mixes with respect to SD 4 mix (%)
Stone dust	4	1360	70	$0.2374 \times 10^{-3}$	$0.1335 \times 10^{-3}$	100
	5.5	1991	62	$0.2330 \times 10^{-3}$	$0.1339 \times 10^{-3}$	88.57
	7	2630	57	$0.2294 \times 10^{-3}$	$0.1339 \times 10^{-3}$	81.43
	8.5	2930	56	$0.2271 \times 10^{-3}$	$0.1334 \times 10^{-3}$	80.00
Glass powder	4	1610	66	$0.2358 \times 10^{-3}$	$0.1339 \times 10^{-3}$	94.29
	5.5	2134	61	$0.2319 \times 10^{-3}$	$0.1337 \times 10^{-3}$	87.14
	7	2834	56	$0.2281 \times 10^{-3}$	$0.1338 \times 10^{-3}$	80.00
	8.5	3072	54	$0.2267 \times 10^{-3}$	$0.1336 \times 10^{-3}$	77.14
Glass-hydrated lime	4	2042	62	$0.2323 \times 10^{-3}$	$0.1335 \times 10^{-3}$	88.57
	5.5	2542	58	$0.2294 \times 10^{-3}$	$0.1336 \times 10^{-3}$	82.86
	7	3111	55	$0.2263 \times 10^{-3}$	$0.1334 \times 10^{-3}$	78.57
	8.5	3512	53	$0.2247 \times 10^{-3}$	$0.1331 \times 10^{-3}$	75.71

TABLE 7: Cost analysis of various mixes.

Type of filler	Filler content (%)	Quantity of bitumen (ton/km)	Quantity of coarse aggregate (m <sup>3</sup> /km)	Quantity of fine aggregate (m <sup>3</sup> /km)	Quantity of SD (m <sup>3</sup> /km)	Quantity of GP (m <sup>3</sup> /km)	Quantity of hydrated lime (ton/km)	Total material cost (INR/km)	Processing cost (0.5% of material cost) (INR/km)	Final cost (INR/km)
CPWD rates		INR 39570/ton	INR 1350/m <sup>3</sup>	INR 1350/m <sup>3</sup>	INR 1400/m <sup>3</sup>	0	INR 2900/ton			
Stone dust	4.0	78.70	151.18	236.68	16.49	0	0	36,60,976	0	36,60,976
	5.5	67.10	135.09	206.01	20.25	0	0	31,44,147	0	31,44,147
	7.0	55.65	125.50	186.31	23.95	0	0	26,56,573	0	26,56,573
	8.5	54.53	124.01	179.08	28.74	0	0	26,07,250	0	26,07,250
Glass powder	4.0	71.95	142.66	223.34	0	17.71	0	33,41,227	16,706	33,57,933
	5.5	64.03	132.42	201.95	0	22.60	0	29,85,075	14,925	30,00,000
	7.0	55.48	122.55	181.93	0	26.62	0	26,06,267	13,031	26,19,298
	8.5	51.38	118.82	171.59	0	31.34	0	24,24,978	12,125	24,37,103
Glass-hydrated lime composite	4.0	63.62	135.80	212.59	0	8.43	19.98	30,45,777	15,229	30,61,006
	5.5	56.72	127.91	195.07	0	13.89	18.82	27,34,973	13,675	27,48,648
	7.0	51.00	121.57	180.47	0	18.86	17.88	24,77,864	12,389	24,90,254
	8.5	48.38	117.10	169.10	0	23.62	17.23	23,50,835	11,754	23,62,589

Note. 1 \$=74.82 INR (on 13/08/2020).

considered as most environmentally friendly, and use of GP at higher quantities (8.5%) is expected to reduce the GHG emission by 35%. This might be due to lower consumption of bitumen by these mixes. Interestingly, it can be observed that GL mixes displayed higher GHG emission amongst all mixes, despite having lower OAC and surface layer thickness. The higher GWP of these mixes might be attributed to the hydrated lime which generates good amount of CO<sub>2</sub> during its production. It must also be noted that surface course containing GL filler at 7 and 8.5% exhibited almost similar GHG as SD 4 mixes. Hence, utilization of GL at higher filler contents could not only be environmentally friendly but also be significantly cheaper than conventional SD 4 mixes. The use of GP and GL as fillers also conserves momentous amount of non-removable resources (aggregates, stone dust, and asphalt binder) in each km of surface

layer construction (Table 9). The single km of two-lane surface course made with GL and GP fillers is expected to conserve up to 324 and 312 tons of aggregates and stone dust in comparison to SD 4 mixes. The use of GL and GL surface course also saves up to 27 and 30 tons of asphalt binder in each km of road construction. It will also be helpful in reducing the cost of transportation, workmanship, and the time of road construction. Up to 74 tons of waste GP can be consumed in the construction of a single km of such pavement, while up to 56 tons of waste GP can be consumed in the form of GL composite. This will significantly resolve the issue regarding the safe disposal of GP. GL 7 mix can be considered as the most superior amongst all mixes. Not only this mix showed satisfactory resistance against moisture and superior stiffness and cracking resistance than SD 4 mix but also surface courses made with it were found to be 21% more



TABLE 8: Comparison of the final cost of different mixes.

Filler type	The total cost of mixes with respect to SD mix containing 4% filler (SD 4)			
	Filler content			
	4%	5.5%	7%	8.5%
Stone dust	100	85.88	72.56	71.22
Glass powder	91.27	81.95	71.55	66.57
Glass lime	86.31	75.08	68.02	64.53

TABLE 9: Global warming potential of various mixes.

Type of filler	Quantity of bitumen (ton/km)	Quantity of coarse aggregate (ton/km)	Quantity of fine aggregate (ton/km)	Quantity of SD (ton/km)	Quantity of GP (ton/km)	Quantity of hydrated lime (ton/km)	Total emission (kgCO <sub>2</sub> equivalent)	Savings in conventional aggregates with respect to SD 4 mix (ton)	Savings in bitumen with respect to SD 4 mix (ton)
GHG emission (kgCO <sub>2</sub> equivalent/kg)	0.426	0.0026	0.0026	0.0026	0	0.785			
Stone dust	4.0	78.70	422.56	644.96	44.48	0	36419	0	0
	5.5	67.10	377.56	561.38	54.65	0	31170	138.75	11.70
	7.0	55.65	350.78	507.70	64.62	0	26107	229.18	23.05
	8.5	54.53	346.61	487.99	77.53	0	25602	265.97	24.17
Glass powder	4.0	71.95	398.74	608.61	0	41.97	33270	104.65	6.75
	5.5	64.03	370.12	550.31	0	53.57	29670	191.57	14.67
	7.0	55.48	342.53	495.77	0	63.10	25813	273.71	23.22
	8.5	51.38	332.11	467.57	0	74.29	23695	312.32	27.32
Glass lime composite	4.0	63.62	379.55	579.31	0	19.98	45277	153.14	15.08
	5.5	56.72	357.51	531.56	0	32.93	41245	222.93	21.98
	7.0	51.00	339.78	491.79	0	44.71	37928	280.43	27.70
	8.5	48.38	327.30	460.80	0	55.99	36183	323.90	30.32

TABLE 10: Comparison of GWP of different mixes.

Filler type	GWP of mixes with respect to SD mix containing 4% filler (SD 4)			
	Filler content			
	4%	5.5%	7%	8.5%
Stone dust	100	85.59	71.69	70.30
Glass powder	91.35	81.47	70.88	65.06
Glass lime	124.32	113.25	104.14	99.35

economical. The construction of single km of GL 7 surface course can also conserve up to 280 and 28 tons of aggregates and asphalt binder, respectively, as well as utilize 45 tons of GP.

The comparison of obtained results is also made with the previous major literatures as stated in Table 11. It can be clearly observed that in comparison to the previous literatures, current study explored the performance of asphalt mixes containing variable amounts of GP and GL fillers in more multifaceted manner. Unlike previous studies, it addressed a critical issue

concerning the moisture sensitivity of asphalt mixes containing GP in significant detail. Additionally, it also explored the vital aspects concerning the cost and environmental sustainability of GP incorporation, which has not been done before. This study not only conclusively proved that the incorporation of GP alone as filler can increase moisture sensitivity of asphalt mix but also suggested a manner to maximize the utilization of GP in the form of GL composite filler, while maintaining the engineering, economical, and environmental viability of prepared asphalt mixes.

TABLE 11: Comparison of results of this study with the previous studies.

Comparison of performance of GP incorporated asphalt mixes with the conventional asphalt mixes having same filler content						
Property of mix	Previous literatures				Current study	
	Saltan et al. [27] Stone dust	Arabani et al. [15] Stone dust	Simone et al. [28] Stone dust	Choudhary et al. [30] Stone dust	GP Stone dust	GL Stone dust
OAC	10% (↑)	6% (↓)	0%	2% (↑)	1–3% (↓)	5–9% (↓)
Marshall stability	24% (↓)	21% (↑)	—	6% (↓)	12% (↓) - 6% (↑)	3% (↓) - 17% (↑)
Rutting resistance	—	51% (↑)	—	—	0–100% (↓)	0–100% (↓)
Cracking resistance	—	124% (↑)	12% (↓) - 15% (↑)	5% (↑)	24% (↓) - 73% (↑)	1% (↓) - 100% (↑)
Moisture resistance	—	—	—	80% (↓)	42–89% (↓)	6–16% (↓)
Ravelling resistance	—	—	—	—	17% (↑) - 10% (↓)	11% (↑) - 21% (↓)
Resilient modulus	—	118% (↑)	0–15% (↑)	8% (↑)	5–18% (↑)	20–50% (↑)
Cost	—	—	—	2% (↑)	9% (↓) - 2% (↑)	6–9% (↓)
GHG emission	—	—	—	2% (↓)	7–10% (↓)	24–40% (↑)

Note. (↑): increase in comparison to conventional mix; (↓): decrease in comparison to conventional mix.

## 5. Conclusions

The conclusions obtained are as follows:

- (i) GP, SD, and HL displayed traits of good fillers because of their fineness, low clay content, and hydrophobic nature. All asphalt concrete mixes prepared with GP and GL fillers (except GL mixes prepared at 8.5% filler content) showed superior Marshall and volumetric properties than conventional SD mixes.
- (ii) OAC of all mixes decreased with growth in filler content due to filler's asphalt binder extender action. GL filler modified mixes displayed the lowest OAC in all cases and have the highest Marshall stabilities in most of the cases.
- (iii) The resistance against cracking and rutting increased with the filler content. GL mixes exhibited better resistance due to the fine nature of GL and low VMA of the prepared mixes. GL and GP mixes also displayed satisfactory resistance against ravelling at lower filler contents.
- (iv) GP displayed poor performance against moisture and in terms of adhesion. GP mixes failed to fulfill the minimum requirement of TSR at any filler content. GL mixes displayed satisfactory TSR values up to 7% filler content (5% GP+ 2% lime). Hence, GP can be utilized up to 5% along with 2% HL to form mixes with satisfactory moisture resistance.
- (v) GL and GP mixes had higher resilient modulus and displayed better load distribution behavior than SD mixes. The pavement structure containing these mixes supported similar design traffic at a much lower thickness of pavements.
- (vi) The pavement consisting of GL and GP mixes resulted in reduction of cost of the pavements up to 35 and 33% in comparison to conventional SD 4 mix. The construction of each km of surface course with these mixes can also conserve 324

and 312 tons of natural aggregates, respectively. GP mixes were found to be most environmentally friendly since they displayed 35% lower GWP than SD 4 mixes

- (vii) GL 7 mix was found to be the most superior amongst all mixes. It exhibited better laboratory performance, and the asphalt pavements made with it was also found to be 21% more economical. Use of this mix can also conserve 280 tons and 28 tons of conventional aggregates and binder, respectively.

In conclusion, it could be said that the utilization of GP in the form of waste and composite filler could be an efficient solution for the ecofriendly disposal of glass waste. The utilization of GP and GL fillers was proven to form asphalt mixes exhibiting superior engineering performance in a more economical and environmentally friendly manner.

## Data Availability

All data and models generated or used during the study are included within the article.

## Conflicts of Interest

The authors declare that there are no conflicts of interest.

## References

- [1] A. Gupta, P. Kumar, and R. Rastogi, "Mechanistic-empirical approach for design of low volume pavements," *International Journal of Pavement Engineering*, vol. 16, no. 9, pp. 797–808, 2015.
- [2] J. Choudhary, B. Kumar, and A. Gupta, "Performance evaluation of bauxite residue modified asphalt concrete mixes," *European Journal of Environmental and Civil Engineering*, vol. 48, pp. 1–17, 2019.
- [3] A. Kuity, S. Jayaprakasan, and A. Das, "Laboratory investigation on volume proportioning scheme of mineral fillers in

- asphalt mixture,” *Construction and Building Materials*, vol. 68, pp. 637–643, 2014.
- [4] MoRTH (Ministry of Road Transport and Highways), *Specifications for Road and Bridge Works (Fifth Revision)*, Indian Road Congress, New Delhi, India, 2013.
- [5] B. Barra, L. Momm, Y. Guerrero, and L. Bernucci, “Characterization of granite and limestone powders for use as fillers in bituminous mastics dosage,” *Anais da Academia Brasileira de Ciências*, vol. 86, no. 2, pp. 995–1002, 2014.
- [6] D. Lesueur, A. Teixeira, M. M. Lázaro, D. Andaluz, and A. Ruiz, “A simple test method in order to assess the effect of mineral fillers on bitumen ageing,” *Construction and Building Materials*, vol. 117, pp. 182–189, 2016.
- [7] C. Li, Z. Chen, S. Wu, B. Li, J. Xie, and Y. Xiao, “Effects of steel slag fillers on the rheological properties of asphalt mastic,” *Construction and Building Materials*, vol. 145, pp. 383–391, 2017.
- [8] A. K. Das and D. Singh, “Investigation of rutting, fracture and thermal cracking behavior of asphalt mastic containing basalt and hydrated lime fillers,” *Construction and Building Materials*, vol. 141, pp. 442–452, 2017.
- [9] Y. Chen, S. Xu, G. Tebaldi, and E. Romeo, “Role of mineral filler in asphalt mixture,” *Road Materials and Pavement Design*, pp. 1–40, 2020.
- [10] J. Choudhary, B. Kumar, and A. Gupta, “Application of waste materials as fillers in bituminous mixes,” *Waste Management*, vol. 78, no. 8, pp. 417–425, 2018.
- [11] B. Huang, X. Shu, and X. Chen, “Effects of mineral fillers on hot-mix asphalt laboratory-measured properties,” *International Journal of Pavement Engineering*, vol. 8, no. 1, pp. 1–9, 2007.
- [12] A. R. Pasandín, I. Pérez, A. Ramírez, and M. M. Cano, “Moisture damage resistance of hot-mix asphalt made with paper industry wastes as filler,” *Journal of Cleaner Production*, vol. 112, pp. 853–862, 2016.
- [13] H. Zhang, H. Li, Y. Zhang, D. Wang, J. Harvey, and H. Wang, “Performance enhancement of porous asphalt pavement using red mud as alternative filler,” *Construction and Building Materials*, vol. 160, pp. 707–713, 2018.
- [14] A. Ameli, R. Babagoli, F. Jalali, and M. Khabooshani, “Investigating the influence of replacing two biomass ashes with conventional filler on high and intermediate temperature performance of mastic and mixture,” *Advances in Civil Engineering Materials*, vol. 9, no. 1, pp. 169–194, 2020.
- [15] M. Arabani, S. A. Tahami, and M. Taghipoor, “Laboratory investigation of hot mix asphalt containing waste materials,” *Road Materials and Pavement Design*, vol. 18, no. 3, pp. 713–729, 2017.
- [16] S. Chandra and R. Choudhary, “Performance characteristics of bituminous concrete with industrial wastes as filler,” *Journal of Materials in Civil Engineering*, vol. 10, 2013.
- [17] V. Sharma, S. Chandra, and R. Choudhary, “Characterization of fly ash bituminous concrete mixes,” *Journal of Materials in Civil Engineering*, vol. 22, no. 12, pp. 1209–1216, 2010.
- [18] R. C. West and R. S. James, “Evaluation of a lime kiln dust as a mineral filler for stone matrix asphalt,” *Transportation Research Board*, vol. 750, pp. 1–18, 2006.
- [19] Iea, “International energy agency tracking industrial energy efficiency and CO<sub>2</sub> emissions,” 2007, [http://www.iea.org/publications/freepublications/publication/tracking\\_emissions.pdf](http://www.iea.org/publications/freepublications/publication/tracking_emissions.pdf).
- [20] J. Choudhary, B. Kumar, and A. Gupta, “Laboratory evaluation on recycling waste industrial glass powder as mineral filler in hot mix asphalt,” in *Proceedings of the Civil Engineering Conference-Innovation for Sustainability*, pp. 352–359, Hamirpur, India, July 2016.
- [21] X. Gao, Q. Yu, X. S. Li, and Y. Yuan, “Assessing the modification efficiency of waste glass powder in hydraulic construction materials,” *Construction and Building Materials*, vol. 263, Article ID 120111, 2020.
- [22] K. Bisht, K. I. S. A. Kabeer, and P. V. Ramana, “Gainful utilization of waste glass for production of sulphuric acid resistance concrete,” *Construction and Building Materials*, vol. 235, Article ID 117486, 2020.
- [23] R. Xiao, P. Polaczyk, M. Zhang et al., “Evaluation of glass powder-based geopolymer stabilized road bases containing recycled waste glass aggregate,” *Transportation Research Record: Journal of the Transportation Research Board*, vol. 2674, no. 1, pp. 22–32, 2020.
- [24] Y. Zhang, R. Xiao, X. Jiang, W. Li, X. Zhu, and B. Huang, “Effect of particle size and curing temperature on mechanical and microstructural properties of waste glass-slag-based and waste glass-fly ash-based geopolymers,” *Journal of Cleaner Production*, vol. 273, Article ID 122970, 2020.
- [25] S. Zhao, B. Liu, Y. Ding et al., “Study on glass-ceramics made from MSWI fly ash, pickling sludge and waste glass by one-step process,” *Journal of Cleaner Production*, vol. 271, Article ID 122674, 2020.
- [26] H. H. Jony, I. Y. Jahad, and M. F. Al-Rubaie, “The effect of using glass powder filler on hot asphalt concrete mixtures properties,” *Engineering and Technology Journal*, vol. 29, no. 1, pp. 44–57, 2011.
- [27] M. Saltan, B. Öksüz, and V. E. Uz, “Use of glass waste as mineral filler in hot mix asphalt,” *Science and Engineering of Composite Materials*, vol. 22, no. 3, pp. 271–277, 2015.
- [28] A. Simone, F. Mazzotta, S. Eskandarsefat et al., “Experimental application of waste glass powder filler in recycled dense-graded asphalt mixtures,” *Road Materials and Pavement Design*, vol. 20, pp. 1–16, 2017.
- [29] J. Choudhary, B. Kumar, and A. Gupta, “Effect of filler on the bitumen-aggregate adhesion in asphalt mix,” *International Journal of Pavement Engineering*, vol. 21, no. 12, pp. 1482–1490, 2020.
- [30] J. Choudhary, B. Kumar, and A. Gupta, “Evaluation of engineering, economic and environmental suitability of waste filler incorporated asphalt mixes and pavements,” *Road Materials and Pavement Design*, vol. 22, pp. 1–17, 2021.
- [31] H. Khani Sanij, P. Afkhamy Meybodi, M. Amiri Hormozaky, S. H. Hosseini, and M. Olazar, “Evaluation of performance and moisture sensitivity of glass-containing warm mix asphalt modified with zycotherm™ as an anti-stripping additive,” *Construction and Building Materials*, vol. 197, pp. 185–194, 2019.
- [32] J. Choudhary, B. Kumar, and A. Gupta, “Potential utilization of construction wastes in asphalt pavements as fillers using ranking framework,” *Construction and Building Materials*, vol. 277, Article ID 122262, 2021.
- [33] D. Lesueur, J. Petit, and H.-J. Ritter, “The mechanisms of hydrated lime modification of asphalt mixtures: a state-of-the-art review,” *Road Materials and Pavement Design*, vol. 14, no. 1, pp. 1–16, 2013.
- [34] É. Lachance-Tremblay, M. Vaillancourt, D. Perraton, and H. Di Benedetto, “Linear viscoelastic (LVE) properties of asphalt mixtures with different glass aggregates and hydrated lime content,” *International Journal of Pavement Engineering*, vol. 21, no. 10, pp. 1170–1179, 2020.
- [35] S. Raschia, S. Badeli, A. Carter, A. Graziani, and D. Perraton, “recycled glass filler in cold recycled materials treated with

- bituminous emulsion,” in *Proceedings of the 97th Annual Conference Of Transportation Research Board*, Washington, DC, USA, January 2018.
- [36] Asphalt Institute, *Mix Design Methods for Asphalt Concrete and Other Hot-Mix Types: Manual Series No. 2 (MS-2)*, Asphalt Institute, Lexington, MV, USA, 6th edition, 1997.
- [37] IRC 37, *Guidelines for the Design of Flexible Pavements, 4th Revision*, Indian Roads Congress, New Delhi, India, 2018.
- [38] ASTM D854-14, *Standard Test Methods for Specific Gravity of Soil Solids by Water Pycnometer*, ASTM, West Conshohocken, PA, USA, 2014.
- [39] Napa (National Asphalt Pavement Association), *Evaluation of Baghouse Fines For Hot Mix Asphalt. Information Series*, Napa (National Asphalt Pavement Association), Lanham, MD, USA, 1999.
- [40] EN 933-9, *Tests for Geometrical Properties Of Aggregates-Part 9-Assessment Of Fines Methylene Blue Test*, EN 933-9, Brussels, Belgium, 1999.
- [41] J. T. G. E42, *Test Methods of Aggregate for Highway Engineering Research*, Institute of Highway Ministry of Transport, Beijing, China, 2005, (in Chinese).
- [42] Asphalt Institute, *Mix Design Methods for Asphalt Concrete and Other Hot-Mix Types: Manual Series No. 2 (MS-2)*, Asphalt Institute, Lexington, KY, USA, 7th edition, 2014.
- [43] BS 598-111, *Sampling and Examination of Bituminous Mixtures for Roads and Other Paved Areas Part 111: Method for Determination of Resistance to Permanent Deformation of Bituminous Mixtures Subject to Unconfined Uniaxial Loading*, BSI Group, London, UK, 1995.
- [44] D. W. Christensen and R. F. Bonaquist, *Evaluation of Indirect Tensile Test (IDT) Procedures For Low-temperature Performance Of Hot Mix Asphalt*, vol. 530, Transportation Research Board, Washington, DC, USA, 2004.
- [45] ASTM D6931-12, *Indirect Tensile (IDT) Strength For Bituminous Mixtures*, ASTM, West Conshohocken, PA, USA, 2012.
- [46] W. Si, N. Li, B. Ma, Y.-x. Tian, and X.-y. Zhou, “Temperature response to tensile characteristics of the hot asphalt mixtures,” *KSCE Journal of Civil Engineering*, vol. 20, no. 4, pp. 1336–1346, 2016.
- [47] M. T. Nguyen, H. J. Lee, and J. Baek, “Fatigue analysis of asphalt concrete under indirect tensile mode of loading using crack images,” *Journal of Testing and Evaluation*, vol. 41, no. 1, pp. 148–158, 2013.
- [48] P. Cui, S. Wu, Y. Xiao, F. Wang, and F. Wang, “Quantitative evaluation of active based adhesion in Aggregate-Asphalt by digital image analysis,” *Journal of Adhesion Science and Technology*, vol. 33, pp. 1–14, 2019.
- [49] A. R. Pasandín and I. Pérez, “The influence of the mineral filler on the adhesion between aggregates and bitumen,” *International Journal of Adhesion and Adhesives*, vol. 58, pp. 53–58, 2015.
- [50] ASTM D3625-12, *Standard Practice For Effect Of Water On Bituminous Coated Aggregate Using Boiling Water*, ASTM, West Conshohocken, PA, USA, 2005.
- [51] AASHTO, *Resistance of Compacted Bituminous Mixture to Moisture-Induced Damage*, AASHTO, Washington, DC, USA, 1989.
- [52] NIT-352/86, *Caracterización De Las Mezclas Bituminosas Abiertas Por Medio Del ensayo Cantabro De Pérdida Por Desgaste*, NIT-352/86, Madrid, Spain, 1986.
- [53] ASTM D4123-82, *Standard Test Method for Indirect Tension Test for Resilient Modulus of Bituminous Mixtures*, ASTM, West Conshohocken, PA, USA, 1995.
- [54] A. Modarres and P. Alinia Bengar, “Investigating the indirect tensile stiffness, toughness and fatigue life of hot mix asphalt containing copper slag powder,” *International Journal of Pavement Engineering*, vol. 20, no. 8, pp. 977–985, 2019.
- [55] CPWD (Central Public Works Department), *Delhi Schedule of Rates-Vol. 1*, CPWD, New Delhi, India, 2018.
- [56] P. Forster, V. Ramaswamy, P. Artaxo et al., “Changes in atmospheric constituents and in radiative forcing.” Chapter 2,” in *Climate Change 2007. The Physical Science Basis*, IAEA, Vienna, Austria, 2007.
- [57] F. Gschösser, H. Wallbaum, and M. E. Boesch, “Life-cycle assessment of the production of swiss road materials,” *Journal of Materials in Civil Engineering*, vol. 24, no. 2, pp. 168–176, 2012.
- [58] J. Choudhary, B. Kumar, and A. Gupta, “Feasible utilization of waste limestone sludge as filler in bituminous concrete,” *Construction and Building Materials*, vol. 239, Article ID 117781, 2020.
- [59] S. R. M. Fernandes, H. M. R. D. Silva, and J. R. M. Oliveira, “Carbon dioxide emissions and heavy metal contamination analysis of stone mastic asphalt mixtures produced with high rates of different waste materials,” *Journal of Cleaner Production*, vol. 226, pp. 463–470, 2019.
- [60] S. Sreedhar, P. Jichkar, and K. P. Biligiri, “Investigation of carbon footprints of highway construction materials in India,” *Transportation Research Procedia*, vol. 17, pp. 291–300, 2016.
- [61] P. White, J. S. Golden, K. P. Biligiri, and K. Kaloush, “Modeling climate change impacts of pavement production and construction,” *Resources, Conservation and Recycling*, vol. 54, no. 11, pp. 776–782, 2010.
- [62] D. Hall, *Waste Management in Europe: Framework, Trends and Issues*, European Federation of Public Service Unions, London, UK, 2010.
- [63] U. Bagampadde, U. Isacson, and B. M. Kiggundu, “Classical and contemporary aspects of stripping in bituminous mixes,” *Road Materials and Pavement Design*, vol. 5, no. 1, pp. 7–43, 2004.
- [64] H. Akbulut, C. Güreş, S. Çetin, and A. Elmacı, “Investigation of using granite sludge as filler in bituminous hot mixtures,” *Construction and Building Materials*, vol. 36, pp. 430–436, 2012.
- [65] A. Habibnejad Korayem, H. Ziari, M. Hajiloo, and A. Moniri, “Rutting and fatigue performance of asphalt mixtures containing amorphous carbon as filler and binder modifier,” *Construction and Building Materials*, vol. 188, pp. 905–914, 2018.
- [66] C. W. Jenks, C. F. Jencks, E. T. Harrigan, M. Adcock, E. P. Delaney, and H. Freer, *NCHRP Report 673: A Manual for Design of Hot Mix Asphalt with Commentary*, Transportation Research Board, Washington, DC, USA, 2011.
- [67] A. Diab and M. Eneib, “Investigating influence of mineral filler at asphalt mixture and mastic scales,” *International Journal of Pavement Research and Technology*, vol. 11, no. 3, pp. 213–224, 2018.
- [68] A. Modarres, M. Rahmanzadeh, and P. Ayar, “Effect of coal waste powder in hot mix asphalt compared to conventional fillers: mix mechanical properties and environmental impacts,” *Journal of Cleaner Production*, vol. 91, pp. 262–268, 2015.
- [69] A. G. Evans, “The strength of brittle materials containing second phase dispersions,” *Philosophical Magazine*, vol. 26, no. 6, pp. 1327–1344, 1972.
- [70] B. J. Smith and S. A. M. Hesp, “Crack pinning in asphalt mastic and concrete: regular fatigue studies,” *Transportation*

- Research Record: Journal of the Transportation Research Board*, vol. 1728, no. 1, pp. 75–81, 2000.
- [71] K. Sobolev, I. Flores Vivian, R. Saha, N. M. Wasiuddin, and N. E. Saltibus, “The effect of fly ash on the rheological properties of bituminous materials,” *Fuel*, vol. 116, pp. 471–477, 2014.
- [72] C. L. Monismith, S. C. S. Tangella, J. Craus, and J. A. Deacon, “Summary report on fatigue response of asphalt mixtures,” Report TM-UCB-A-003A-89-3, University of California Berkley, Berkeley, CA, USA, 1990.
- [73] B. J. Smith, “Low-temperature and dynamic fatigue toughening mechanisms in asphalt mastics and mixtures,” Post-graduate Dissertation, Queen’s University, Kingston, Canada, 2001.
- [74] J. Choudhary, B. Kumar, and A. Gupta, “Analysis and comparison of asphalt mixes containing waste fillers using a novel ranking methodology,” *Journal of Materials in Civil Engineering*, vol. 32, no. 5, Article ID 04020064, 2020c.
- [75] V. Antunes, A. C. Freire, L. Quaresma, and R. Micaelo, “Influence of the geometrical and physical properties of filler in the filler-bitumen interaction,” *Construction and Building Materials*, vol. 76, pp. 322–329, 2015.
- [76] D. N. Little and D. R. Jones, “Chemical and mechanical mechanisms of moisture damage in hot mix asphalt pavements,” in *Proceedings of the National Seminar in Moisture Sensitivity*, San Diego, CA, USA, February 2003.
- [77] A. Modarres and M. Rahmanzadeh, “Application of coal waste powder as filler in hot mix asphalt,” *Construction and Building Materials*, vol. 66, pp. 476–483, 2014.
- [78] M. Kumari, G. D. R. N. Ransinchung, and S. Singh, “A laboratory investigation on dense bituminous macadam containing different fractions of coarse and fine RAP.” *Construction and Building Materials*, vol. 191, pp. 655–666, 2018.

## Research Article

# Organosilane and Lignosulfonate Stabilization of Roads Unbound: Performance during a Two-Year Time Span

Diego Maria Barbieri <sup>1</sup>, Baowen Lou <sup>1,2</sup>, Hao Chen <sup>1</sup>, Benan Shu <sup>3</sup>, Fusong Wang <sup>4</sup>, and Inge Hoff <sup>1</sup>

<sup>1</sup>Norwegian University of Science and Technology, Department of Civil and Environmental Engineering, Høgskoleringen 7A, Trondheim, 7491, Trøndelag, Norway

<sup>2</sup>Chang'an University, School of Materials and Science Engineering, Nan Er Huan Road (Mid-Section), Xi'an 710064, Shaanxi, China

<sup>3</sup>Foshan Transportation Science and Technology Co. Ltd, Kuiqi Second Road 18, Foshan 528000, Guangdong, China

<sup>4</sup>State Key Laboratory of Silicate Materials for Architectures, Wuhan University of Technology, Luoshi Road 122, Wuhan 430070, Hubei, China

Correspondence should be addressed to Diego Maria Barbieri; [diego.barbieri@ntnu.no](mailto:diego.barbieri@ntnu.no)

Received 13 July 2021; Revised 8 August 2021; Accepted 7 September 2021; Published 30 September 2021

Academic Editor: Pengfei Liu

Copyright © 2021 Diego Maria Barbieri et al. This is an open access article distributed under the Creative Commons Attribution License, which permits unrestricted use, distribution, and reproduction in any medium, provided the original work is properly cited.

The construction of the new Norwegian E39 highway comprises the excavation of extended tunnelling systems, which lead to a tremendous amount of blasted rocks. Among others, a sustainable cost-benefit application of these resources is represented by their local use as construction material in the unbound layers of the roads. Two types of nontraditional additives are investigated to improve the mechanical properties of aggregates; this is particularly useful for those rocks that do not fulfil the design requirements in their natural status. This work focuses on the field application of two innovative stabilizing technologies based on organosilane and lignosulfonate. The performance of these additive agents is characterized by considering three typical road base layer sections built on purpose according to real practice and added with water (no treatment), organosilane, and lignosulfonate. The test sections are subjected to climatic actions only as neither traffic nor surface courses are applied. With the investigation covering two years, the layers' stiffness, deformation, and resistance to penetration are evaluated by employing a light-weight deflectometer and dynamic cone penetrometer. Both organosilane and lignosulfonate significantly enhance the mechanical properties of the treated base layers.

## 1. Introduction

By fulfilling the “ferry-free coastal highway route E39” project, the Norwegian Public Roads Administration (NPRA) aims at improving the viability along the south-western Norwegian coast from Trondheim to Kristiansand coast for an overall length of about 1100 km [1, 2]. The project comprises the creation of extended tunnelling systems, thus leading to the generation of a tremendous amount of blasted rocks. Among others, a sustainable way to employ these natural resources as construction materials is represented by their use in the unbound layers of the roads built in the proximity of the tunnel infrastructures. This solution

would engender remarkable advantages from several points of view and curtail the consumption of natural resources and related pollutant emissions [3–7]. In addition, the importance of sustainable and environmentally friendly solutions is becoming more and more significant in the world as well as in Norway as the country pursues climate neutrality [8].

To avoid encountering premature damage [9], the Norwegian pavement design manual specifies some requirements for unbound granular materials (UGMs) to be used in the road unbound layers [10, 11]; among others, the Los Angeles (LA) value [12] and microdeval (MDE) value [13] are usually the most stringent criteria to be fulfilled [14]. The geology spread along the highway alignment is largely



various and comprises both rocks that meet the design requirements (“strong” aggregates, generally igneous rocks), while other rocks (“weak” aggregates, generally sedimentary and metamorphic rocks) do not [15].

Several traditional stabilization technologies have been thoroughly characterized to improve the mechanical properties of unbound layers, for example, cement, bitumen, fly ash, lime, and gypsum [16–21]. Recently, two nontraditional stabilizing agents have shown promising results to improve the mechanical response of crushed rock aggregates [22–24]. The two additives are based on organosilane and lignosulfonate, here also referred to as polymer-based (P) agent and lignin-based (L) agent, respectively.

Considering that the previous investigations dealing with the stabilization potentials of the P-based and L-based products were largely based on laboratory tests performed on clayey and silty materials [25–32], this study expands the previous findings by encompassing a field test on crushed rock aggregates covering the time span of two years. Three typical base road sections were built according to the actual Norwegian construction practice and added with water (no treatment), organosilane and lignosulfonate, respectively. The test sections were only subjected to climatic actions as neither traffic nor surface courses were applied. Across a time span of two years, the stiffness and the deformation properties have been assessed using a light-weight deflectionometer (LWD) [33] and dynamic cone penetrometer (DCP) [34]. Aggregates that fulfil standard code requirements were used in this study as performing the field test with enough quantities of “weak” aggregates was not feasible.

## 2. Materials and Methods

**2.1. Crushed Rock Aggregates.** The field test was performed in the Vassfjellet locality close to Trondheim (Trøndelag, Norway). The rocks available in this place, mainly characterized by metamorphic reactions, are particularly rich in gabbro/metagabbro and greenschist [35]; moreover, they are commonly employed for road construction in the central part of Norway [36]. X-ray diffractometry (XRD) and X-ray fluorescence (XRF) analyses were preliminarily performed to thoroughly characterize the aggregates. A Bruker D8 Advance instrument displaying a cobalt tube with wavelength of 1.79 Å was used to perform XRD analysis and examine the composition based on the Rietveld approach, and the proportions of the most abundant minerals are reported in Figure 1. Hornblende (amphibole), chlorite, albite (feldspar), and clinozoisite (epidote) were the predominant minerals. The XRF analysis was attained employing a PANalytical Zetium 4 kW X-ray spectrometer. The major elements as well as the Loss On Ignition (LOI) are reported in Table 1, and silicon was the major component.

According to the requirements specified by the Norwegian pavement design manual N200 [10, 11], crushed rocks can be used as construction material in the base and in the subbase of a road considering the results of the Los Angeles standard test (LA value) and the microdeval standard test (MDE value). As the threshold values for base layers are set to 30 and 15, the crushed rocks deriving from

Vassfjellet fulfil the code requirements (LA = 18.2 and MDE = 14.2). Anyway, this did not obstruct the general goal of the study, namely, to evaluate whether organosilane and lignosulfonate can enhance the mechanical properties of crushed rocks; consequently, the achieved improvements may even be greater for poorer rock aggregates. Figure 2(a) displays the grain curve used in the field investigation as well as the gradation range [37]; the maximum aggregate size was 32 mm. The optimum moisture content (OMC) was also evaluated [38] and found equal to 5% for bulk density approximately equal to 2.5 t/m<sup>3</sup> as depicted in Figure 2(b).

**2.2. Stabilization Technologies.** The existing nontraditional technologies effective for stabilization of coarse-graded roads unbound can be categorized as [39]: synthetic polymer, organic nonpetroleum, organic petroleum, clay, and brine salt. Organosilane is a synthetic polymer, whereas lignosulfonate is an organic nonpetroleum product. The safety data sheets of both the additives do not report any environmental hazards, and the degradation is environmentally acceptable [40, 41]. Currently, the largest amount of research focuses on polymeric and plant-based technologies as they are the newest stabilization solutions [42].

Polymeric stabilizers were first introduced during the 60s as synthetic monomers with dimension ranging from 0.05 μm to 5 μm in diameter [43, 44]. Their stabilizing process is based on the coalescence, which indicates the creation of a film forming physical bonds after the emulsion evaporation [45]. Polymeric products can be classified as acrylate, polyurethane, styrene butadiene, or acetate [46]. The organosilane is a nanoscale non-leachable and UV- and heat-stable acrylate based on two components, namely an emulsion based on acetic acid and methanol (component C1) and a fine dispersion based on propylene glycol and alkoxy-alkyl silyl (component C2). After combination with the silicates naturally present on the aggregate surface forming siloxane linkages (=Si-O-Si=), the additive promotes the formation of a 4–6-nm layer of hydrophobic alkyl siloxane as depicted in Figure 3 [30, 47–49]. The main physical properties of the organosilane used in this study are reported in Table 2. The chemical bindings are damaged if exposed to base substances [50] or temperature above 200°C [51].

Lignosulfonate is an organic polymer that consists of both hydrophilic and hydrophobic groups; it is a renewable substance deriving from lignin extracted by paper and pulp industries. The product is water soluble and not toxic [25, 28, 52]. Thanks to its cementitious properties, lignosulfonate binds the aggregate particles together as depicted in Figure 4 [31]. When applied as a stabilizer for roads unbound, the potential leaching under wet conditions can be partially hindered by providing a proper surface drainage or surface treatment. The main physical properties of the lignosulfonate used in this study are reported in Table 3. Considering the engendered physical cementation action (minor or no chemical effects), it has been indicated that the stabilization process may augment with the decreased surface area,

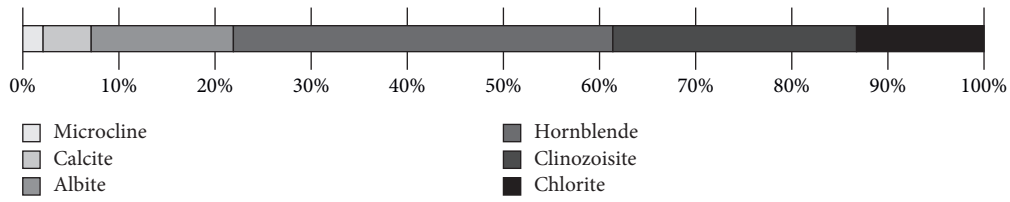


FIGURE 1: Bulk mineralogy of crushed rock aggregates.

TABLE 1: Chemical composition of crushed rock aggregates (weight percent of major oxides).

SiO <sub>2</sub>	Al <sub>2</sub> O <sub>3</sub>	Fe <sub>2</sub> O <sub>3</sub>	CaO	MgO	Na <sub>2</sub> O	TiO <sub>2</sub>	SO <sub>3</sub>	K <sub>2</sub> O	LOI
44.1	13.0	12.8	11.5	10.2	1.91	0.91	0.20	0.10	5.01

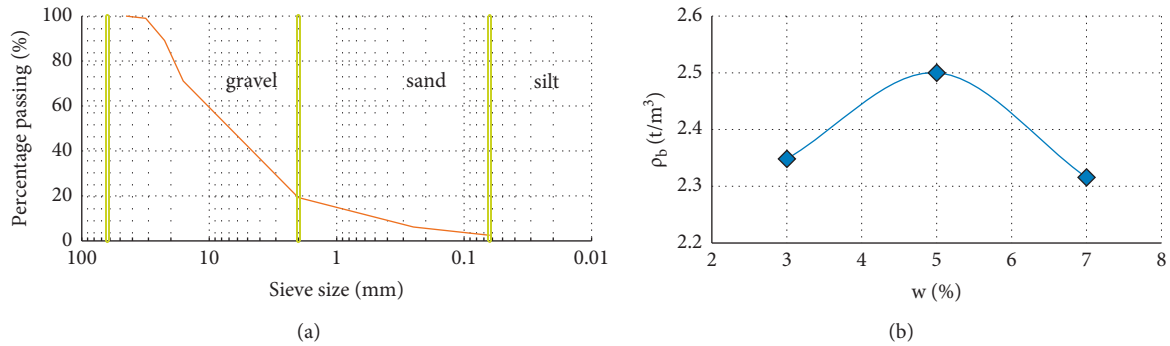


FIGURE 2: Grain size distribution curve (a) and assessment of OMC (b).

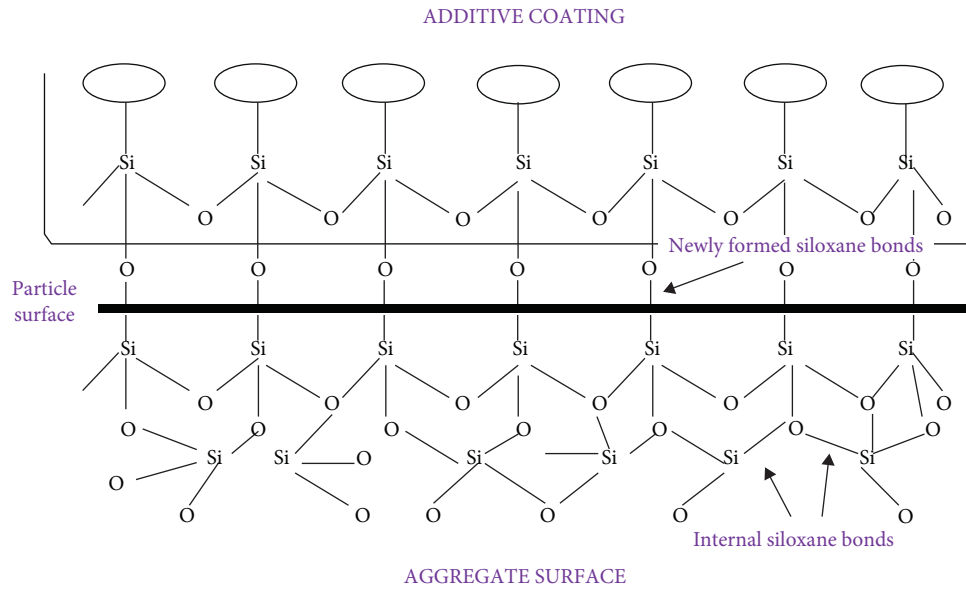


FIGURE 3: Stabilization mechanism for silicate-containing aggregates with organosilane [30].

TABLE 2: Main physical properties and water contained in organosilane (from technical representatives).

Component	Freezing point (°C)	Boiling point (°C)	Viscosity (cP @ 30°C)	Density (kg/m <sup>3</sup> )
P-BASED	C1	0	20–200	1010
	C2	<–5	188	200–600

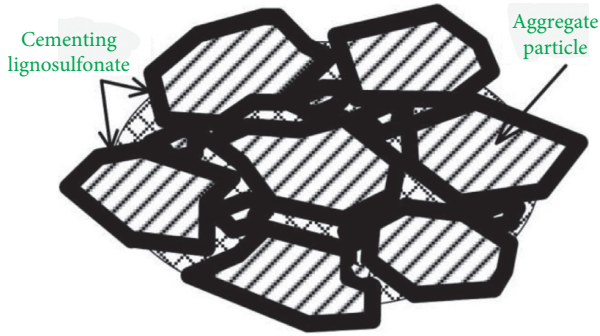


FIGURE 4: Stabilization mechanism for aggregates with lignosulfonate [31].

TABLE 3: Main physical properties and water contained in lignosulfonate (from technical representatives).

	Freezing point	Boiling point	Viscosity	Density
L-BASED	(°C)	(°C)	(cP @ 30°C)	(kg/m <sup>3</sup> )
	-5-0	100	550	1250

namely, improving when moving from applications for fine-graded soils to coarse-graded aggregates [39].

**2.3. Test Sections and Test Procedures.** The field test was performed in an open space located in a quarry in Vassfjellet (Trøndelag, Norway). Considering the grain size distribution curve reported in Figure 2(a), three base layer sections were built and were treated according to three different procedures: water only/untreated (section L0), polymer-based additive (location L1), and lignin-based additive (location L2). Width, length, and approximate thickness of each section were 3.5 m × 10 m × 17 cm thick, respectively. The main operational stages to build the road test locations illustrated in Figure 5 were accomplished in May 2018; further information regarding the construction procedure can be found in [24]. Table 4 reports on the amount of the admixtures employed.

The light weight deflectometer (LWD) is a single-person-use portable instrument employed for the determination of the mechanical properties of the test sections and to characterize their spatial distribution [33, 53, 54]. The device used in this investigation is manufactured by the HMP company [55]. The test consists in subjecting the road base layer to a pulse load applied via a steel plate; a geophone records the speed of the plate movement. The LWD is made of the following parts as illustrated in Figure 6: loading mechanism handle (1), release mechanism (2), bubble level (3), guide rod allowing the falling weight to drop from a distance of 72 cm (4), 10-kg drop-weight (5), transportation lock pin (6), and elastic element with prestressed disc springs (7). The load plate is 30 cm in diameter and comprises a cap with a sensor (8), a sensor socket to connect the measuring cable (9), and a load plate carrying handles (10). The sensor which serves to measure the settlement is positioned under the cap (8) of the load plate [56]. The loading mechanism generates a defined impulsive load, and the total settlement

of the layer under the load plate is measured; the maximum impact force is 7.07 kN, the duration of the impact is  $17.0 \pm 1.5$  ms, and the deflection range measured is  $0.1$  to  $2.0$  mm  $\pm 0.02$  mm. After the completion of three measurements, the deflection transducer (geophone) evaluates the average settlement  $S_m$  and the resilient modulus  $E_{LWD}$  according to the circular plate half-space theory assuming homogeneous, isotropic, linear elastic material behavior [58,59]. Different from a falling weight deflectometer (FWD) device, the LWD employs a shorter load pulse and a smaller force action [60,61].

The dynamic cone penetrometer (DCP) device was also employed to appraise the stabilizing potentials of P-based and L-based technologies in addition to the LWD in terms of their resistance to penetration. This test was accomplished by driving a metal cone into the base layer by releasing an 8-kg weight from a distance of 575 mm as illustrated in Figure 6 [34, 57]. The DCP was adopted here as a further practical approach to better evaluate the admixtures' performances in addition to the LWD as the DCP results may be correlated to other properties, for example, resilient modulus and bearing capacity [62–64].

LWD measurements were performed daily during the first 50 days starting after construction completion (May and June 2018). Moreover, LWD tests were also carried out from day 110 to day 115 (September 2018), from day 365 to day 370 (May 2019), and from day 730 to day 735 (May 2020) after construction completion. DCP tests were performed during day 115, day 370, and day 735. The field investigation thus covered an overall time span of two years. The LWD and DCP measurements in each location were performed for 15 spots, and average values are presented here.

The measuring operations were accomplished after it had stopped raining in case of precipitation. Skjetlein and Saupstad weather stations daily recorded the precipitation amount and the average, minimum, and maximum temperature [65]; average values are reported in this study according to the distance weighting method [66]. The two chosen weather stations are the closest ones to the test site, being approximately located 5 km away from the quarry.

### 3. Results and Discussion

**3.1. Aggregate Coating and Field Conditions.** The surfaces of untreated and treated crushed rocks were probed in the laboratory by two means as depicted in Figure 7. A microscope operating at 40x magnification enabled the reconnaissance of the main minerals, namely amphibole, feldspar, and epidote as reported in Section 2.1. Both the P-based and L-based additive completely covered the aggregates surface. The organosilane was characterized by spherical structures (gas bubbles) created in conjunction with the foaming process, whereas the polygonal structures related to lignosulfonate formed an irregular mesh-shaped coating. Scanning electron microscopy (SEM) analysis was also performed to investigate the microstructure and morphology using an emission current of  $10 \mu\text{A}$  and an acceleration voltage of 10 kV. Both organosilane and lignosulfonate utterly covered the aggregate matrix surface as the smaller fragmented particles were no longer visible.



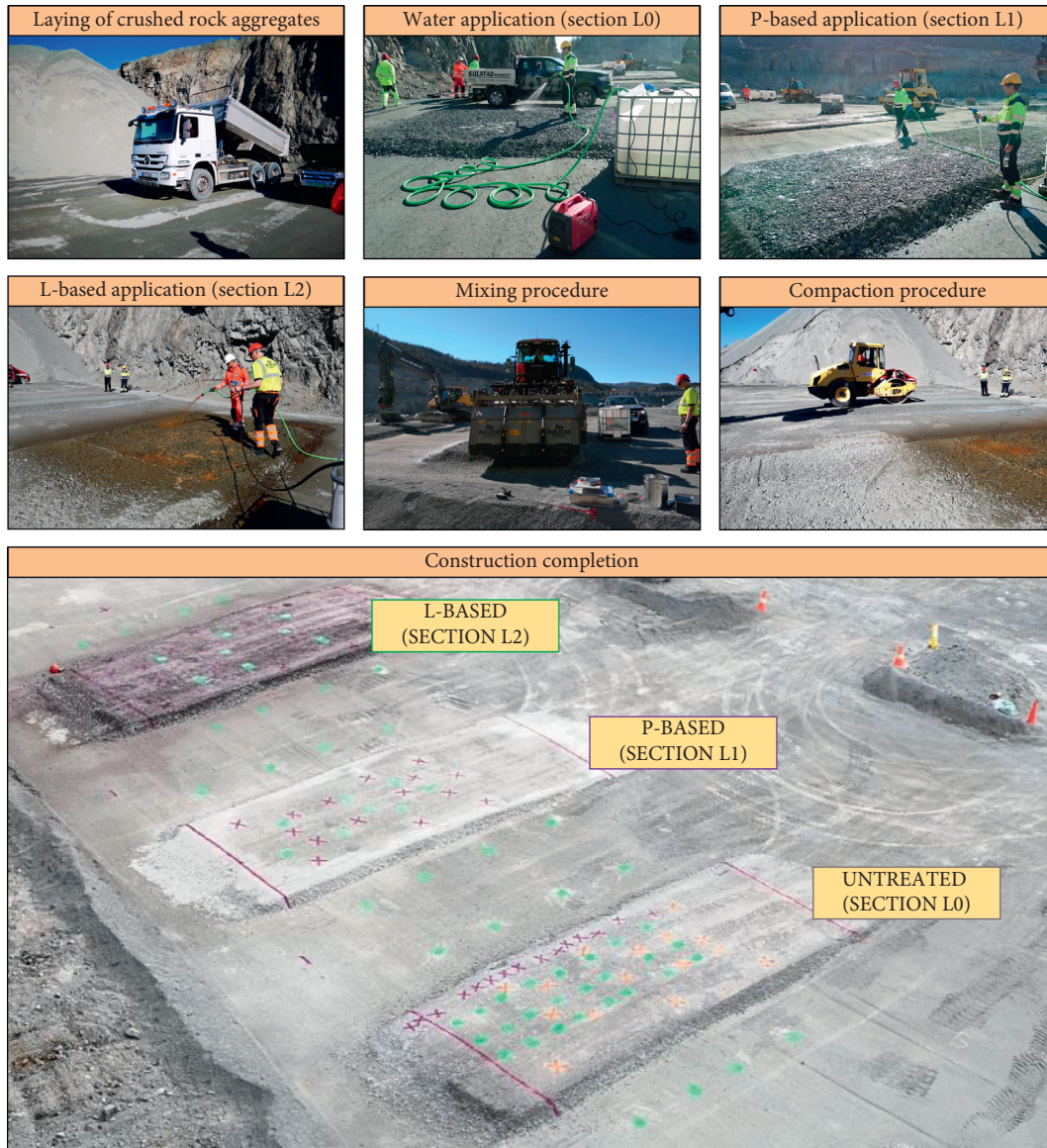


FIGURE 5: Main stages of the construction operations to build the road rest sections.

TABLE 4: Quantity of admixtures used in each location.

Location	Water (kg)	P-based additive (kg)	L-based additive (kg)
L0	500	0	0
L1	500	26 (C1) + 26 (C1)	0
L2	500	0	150

The density of the test sections was evaluated, thanks to the excavation method [67], and the calculated bulk density  $\rho_b$ , dry density  $\rho_d$  and water content  $w$  are displayed in Figure 8. The amount of lignosulfonate used in location L2 was remarkably higher than the admixtures employed in the other two locations; consequently, location L2 was oversaturated, and the measurements here were performed after 5 days.

During the two-year time span, the test sections were exposed to the temperature variations depicted in Figure 9. In this regard, Figure 10 reports more details regarding the

time when the LWD and DCP measurements were performed. From day 1 to day 50 (May and June 2018), the average temperature was comprised between 5°C and 20°C with small precipitations (Figure 10(a)); this situation was exceptionally dry and warm for the Norwegian context [68]. Considering the three temporal frames day 110–day 115 (September 2018), day 365–day 370 (May 2019), and day 730–day 735 (May 2020), the average temperatures were 12.5°C, 5.4°C and 10.0°C and the cumulated amounts of precipitation were 13.4 mm, 21.1 mm, and 6.7 mm, respectively (Figures 10(b)–10(d)).

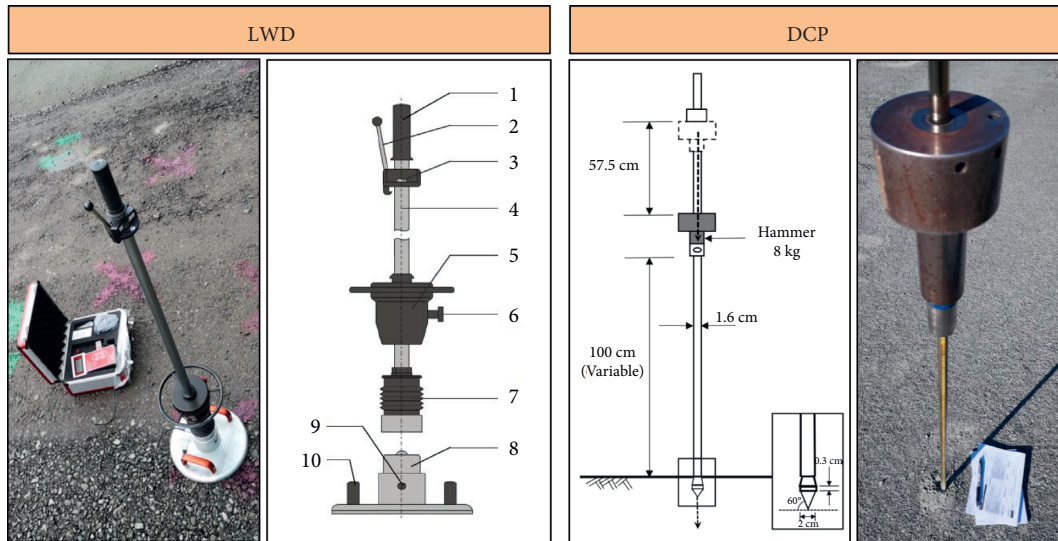


FIGURE 6: Components of the LWD and DCP used in the field test [56, 57].

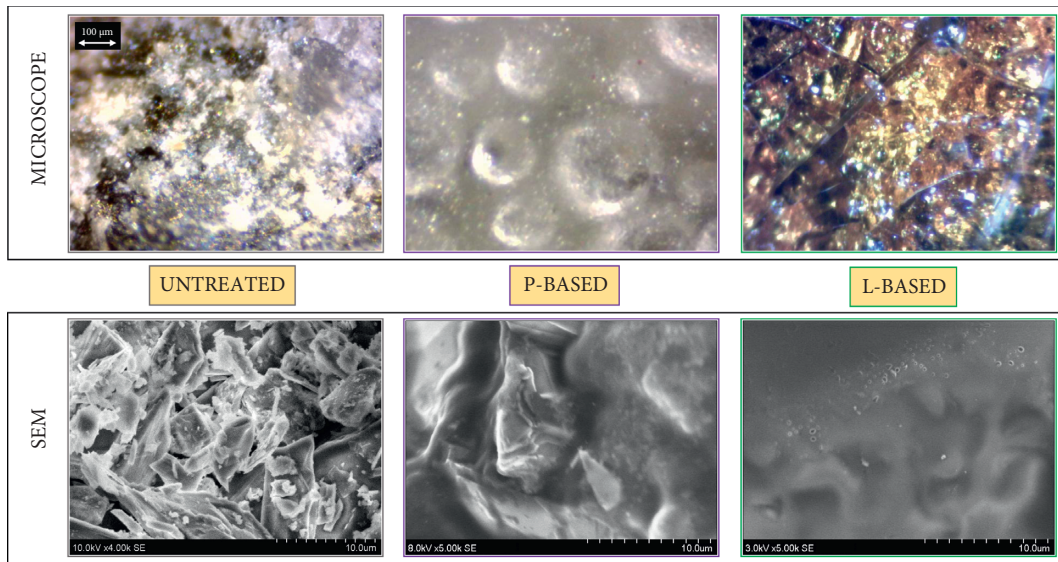


FIGURE 7: Appearance of the surface of crushed rock aggregates probed with the microscope (scale bar 100  $\mu\text{m}$ ) and SEM (scale bar 10  $\mu\text{m}$ ).

The surface appearance of the three road sections during the two-year time span is depicted in Figure 11. In this regard, the clearest differences regarding the aggregate surfaces could be observed after construction completion when the untreated unbound matrix only contained water and the materials treated with organosilane and lignosulfonate displayed a less rough surface with colors fading to grey and brown, respectively. Afterwards, owing to the complete exposure of the test sections to natural actions, the appearance of the stabilized surfaces became slightly different. Even if after two years, the additives did not completely coat the surface of the crushed rocks, and the presence of a bound matrix could still be clearly observed among the aggregates when inspecting the surface carefully.

**3.2. Light Weight Deflectometer Measurements.** The first sequence of LWD measurements was performed during the first 50 days after construction completion of the road sections. Figures 12(a) and 12(b) report the resilient modulus  $E_{LWD}$  and the settlement  $S_{LWD}$ , respectively. During this period, the location L1 treated with organosilane registered the highest  $E_{LWD}$  value (163.5 MPa) and the lowest  $S_{LWD}$  value (0.14 mm). Meanwhile, the effect of the lignosulfonate became evident at a slower pace (most likely due to the initial oversaturation of location L2) and the highest values of  $E_{LWD}$  and  $S_{LWD}$  for the lignosulfonate-based treated materials were equal to 133.4 MPa and 0.18 mm, respectively. Moreover, despite the fact that the surfaces of all the test sections were not graded according to a cross profile to promote water discharge, it is worth noting that precipitations exerted a



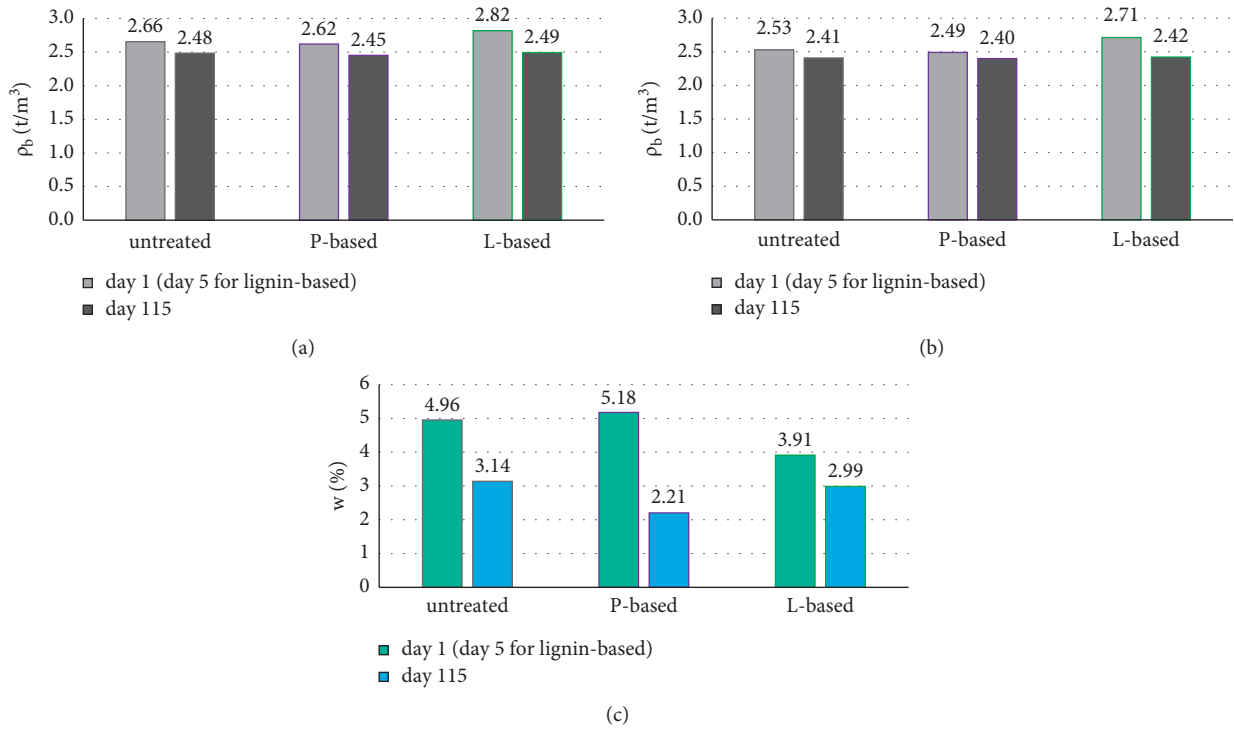


FIGURE 8: Bulk density (a), dry density (b), and water content (c). of the three test locations after construction and after 115 days [24].

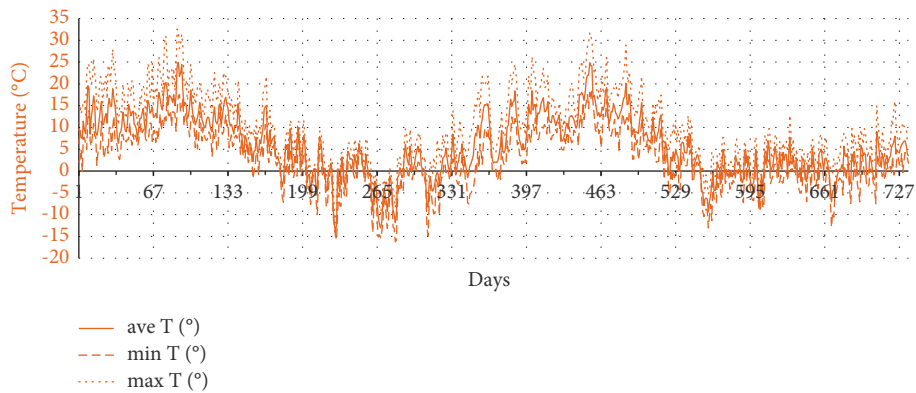


FIGURE 9: Climatic conditions for the two-year time span: average, minimum, and maximum temperature.

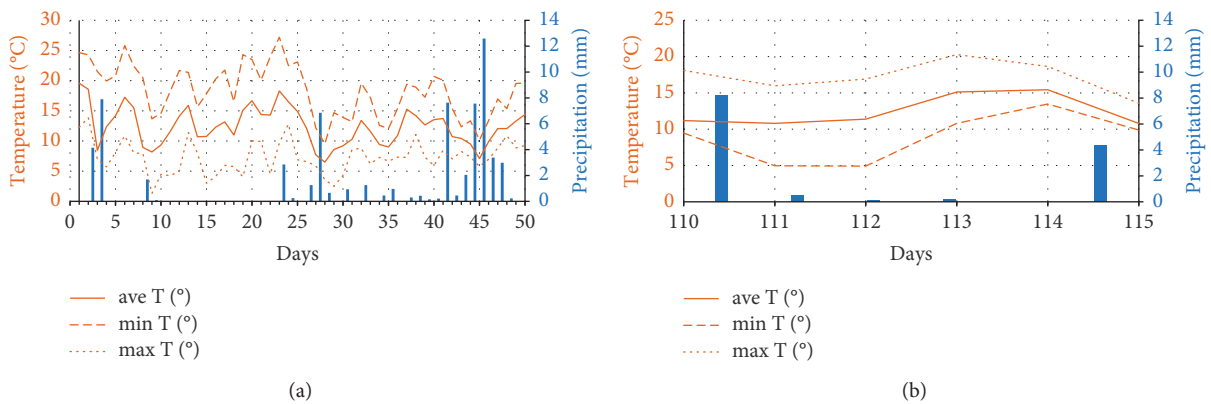


FIGURE 10: Continued.



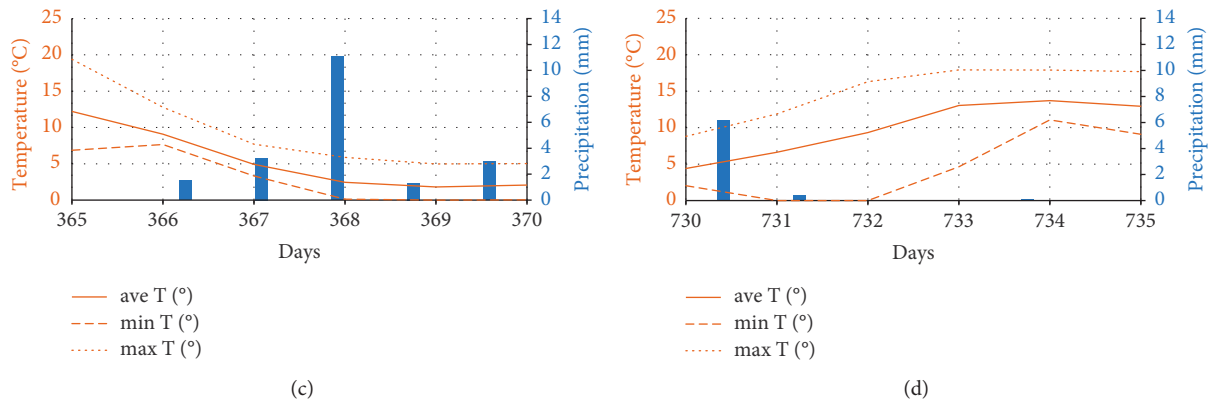


FIGURE 10: Weather conditions in the field. Day 1–day 50 (a), day 110–day 115 (b), day 365–day 370 (c) [24], and day 730–day 735 (d): average, minimum, and maximum temperature and precipitation.



FIGURE 11: Surface appearance of the tested road sections during a two-year time span (the maximum size of the rock aggregates is 32 mm).

major effect only for the untreated location L0, while small daily variations were observed for locations L1 and L2. Figures 12(c)–12(d) report  $E_{LWD}$  and  $S_{LWD}$ , respectively, during day 110–day 115. These measurements prove that the treated areas had mechanical performances that were significantly higher than location L0. The average values of

$E_{LWD}$  were 42.2 MPa, 102.5 MPa, and 103.9 MPa, and the average values of  $S_{LWD}$  were 0.46 mm, 0.22 mm, and 0.23 mm for L0, L1, and L2, respectively. Compared to the measurements related to day 1–day 50, the significant amount of precipitation that took place between day 50 and day 110 could account for the smaller values measured

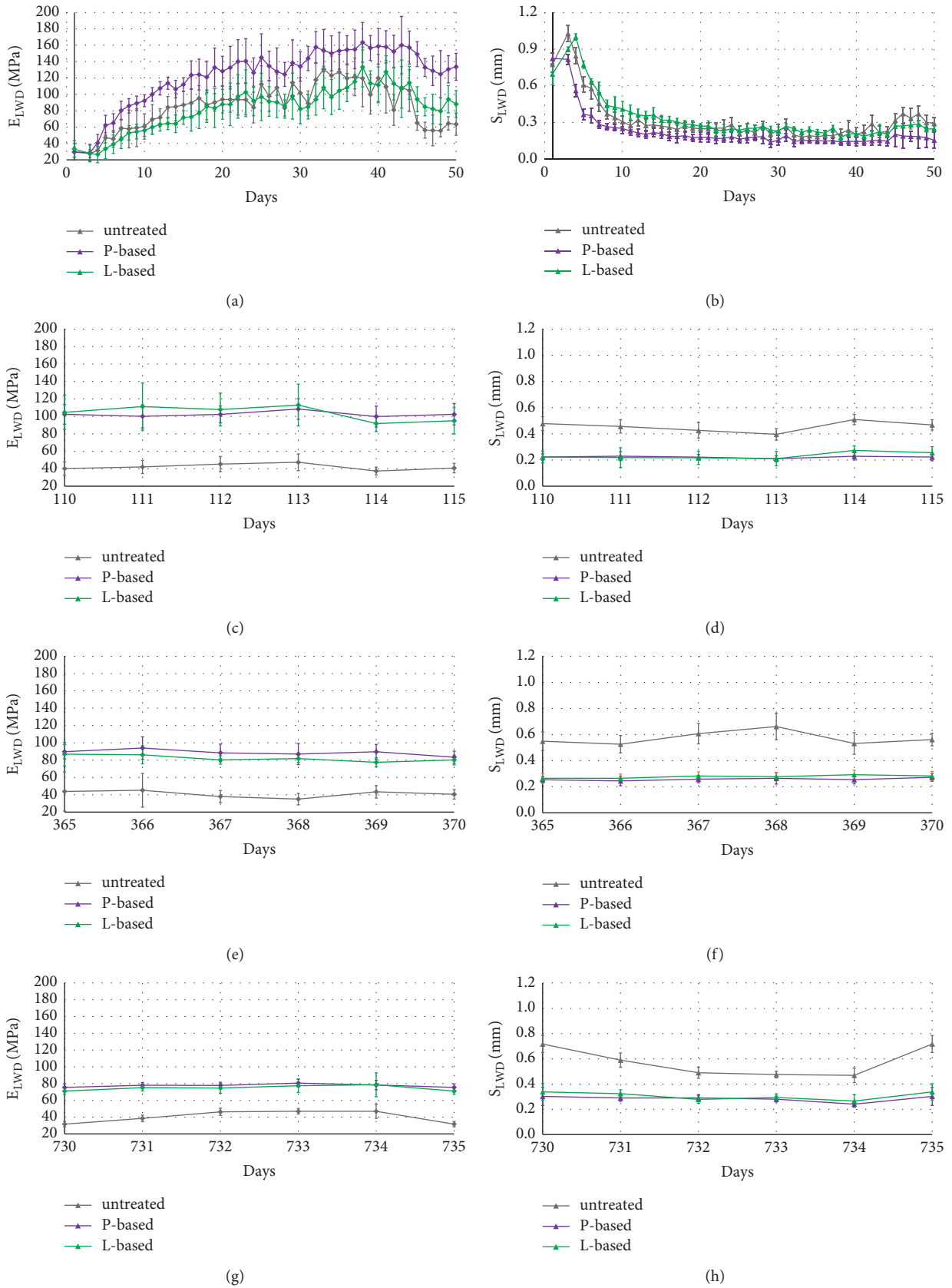


FIGURE 12: Resilient modulus  $E_{LWD}$  (a, c, e, g) and settlement  $S_{LWD}$  (b, d, f, h) for day 1–day 50, day 110–day 115, day 365–day 370 [24] and day 730–day 735.

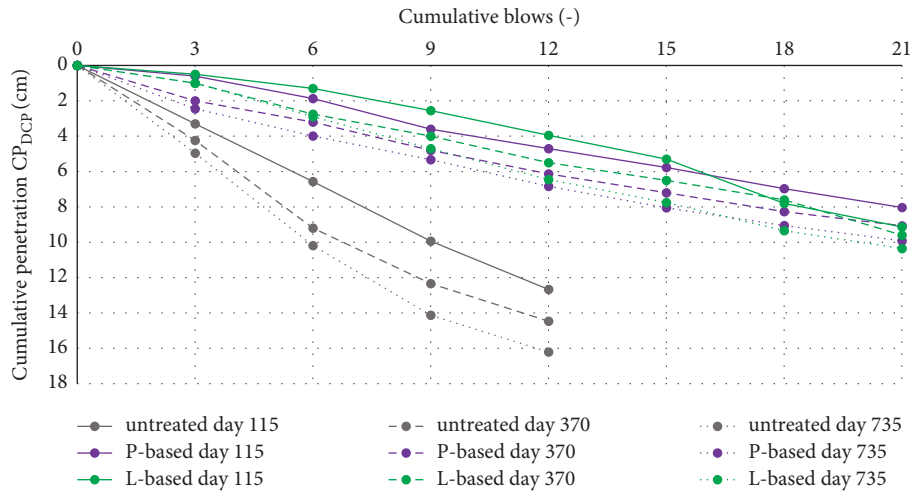


FIGURE 13: Cumulative penetration  $CP_{DCP}$  measured on day 115, day 370 [24], and day 735.

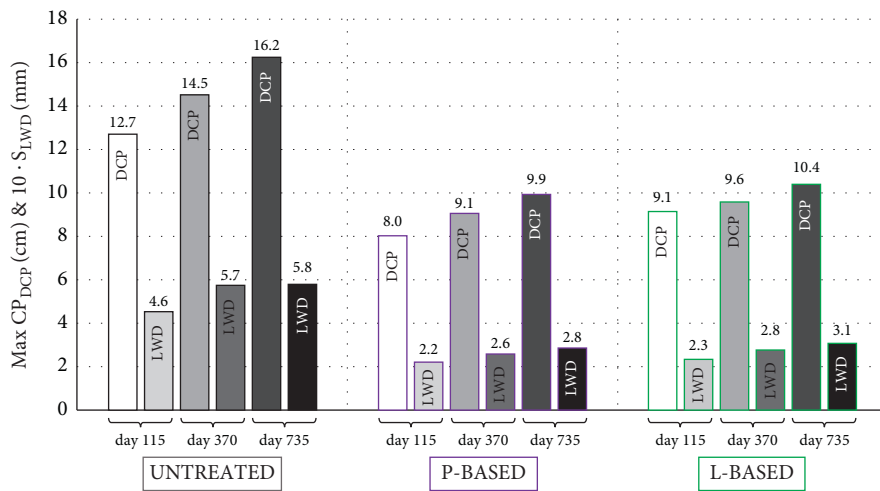


FIGURE 14: Values of maximum cumulative penetration  $CP_{DCP}$  and settlement  $S_{LWD}$ .

during day 110–day 115. Figures 12(e)–12(f) display the mechanical performance after one year of construction, namely during day 365–day 370, despite the general decrease in the values of  $E_{LWD}$  and  $S_{LWD}$ , the treated locations continued to perform much better than the untreated locations. The average values of  $E_{LWD}$  were 41.0 MPa, 88.7 MPa, and 82.2 MPa, and the average values of  $S_{LWD}$  were 0.57 mm, 0.26 mm, and 0.28 mm for L0, L1, and L2, respectively. Considering the measurements achieved after two years, namely during day 730–day 735, it is evident that both organosilane and lignosulfonate continued to entail positive effects. The average values of  $E_{LWD}$  were 40.4 MPa, 77.6 MPa, and 74.7 MPa, and the average values of  $S_{LWD}$  were 0.58 mm, 0.28 mm, and 0.31 mm for L0, L1, and L2, respectively.

Considering the whole general trend of the mechanical properties measured during the two-year life span, both organosilane and lignosulfonate performed satisfactorily, attaining better results compared to the untreated material. Referring for example to the resilient modulus, the average values after 115 days, 1 year, and 2 years were 42.2 MPa,

41.0 MPa, and 40.4 MPa for untreated aggregates, 102.5 MPa, 88.7 MPa, and 77.6 MPa for P-based treated materials, and 103.9 MPa, 82.2 MPa, and 74.7 MPa for L-based treated materials, respectively. Even if the stabilized aggregates always performed better than the untreated material, a slowly decreasing mechanical response of the former ones was registered and this phenomenon can be attributed to their complete exposure to atmospheric actions such as rain and snow. For instance, feasible solutions to prevent or reduce this effect would be represented by covering the treated course with an overlying (i.e., bituminous) course or ensuring the presence of a proper water drainage system (e.g., transversal profile and ditches).

**3.3. Dynamic Cone Penetrometer Measurements.** A DCP test comprised 7 measurement sequences with 3 blows each. Figure 13 displays the depth of cumulative penetration  $CP_{DCP}$  measured from the layer surface at the end of each sequence. The results referring to location L0 only comprised 4 sequences, namely 12 blows, as a higher number of blows was enough to penetrate the entire layers' thickness (17 cm). Overall, the



treated locations L1 and L2 were always stiffer than the untreated location L0. Considering the trends across the two-year time span, the location L0 underwent the largest variations; on the other hand, the application of organosilane and lignosulfonate proved to be an effective way to stabilize both locations L1 and L2. Despite the reduction in the mechanical response over time most likely due to the total exposure to climatic actions, the stabilized materials always performed better than the untreated aggregates. As mentioned in Section 3.2, the detrimental effects on the additive effectiveness supported by natural precipitations could be reduced or hindered by implementing some good construction practices.

The results of DCP cumulative penetration and the findings obtained from LWD equipment were in good agreement as both the tests indicated that (i) the stabilized road sections performed better than the untreated area and that (ii) the mechanical response related to organosilane and lignosulfonate gradually reduced over time.

To further characterize the results deriving from the two-testing device, Figure 14 compares the values of maximum cumulative penetration  $CP_{DCP}$  and settlement  $S_{LWD}$  obtained from DCP and LWD, respectively. Overall, the trends are in good agreement as all the values assessed for each test section tend to increase over time. A relationship between the two quantities can be defined as

$$S_{LWD} (mm) = a \cdot CP_{DCP} (mm). \quad (1)$$

Considering the experimental values reported in Figure 14, the calculation employing a least-square method indicates that  $a$  value is 0.0032 in this investigation.

#### 4. Conclusions

The study characterized the use of two nontraditional stabilizing agents based on organosilane and lignosulfonate to enhance the mechanical properties of crushed rock aggregates to be employed as construction materials in the unbound layers of road pavements. Organosilane reacted with the silicates naturally present on the aggregate surface forming chemical covalent polar bonds, whereas lignosulfonate physically cemented the aggregate particles together. The surfaces of the treated materials were initially completely covered by the additives as probed with the microscope and SEM. The effectiveness of the stabilizing technologies was evaluated in a field test displaying three base road sections, each of which was added with only water (untreated), organosilane, and lignosulfonate. The test had a temporal duration covering two years, and neither traffic nor surface courses were applied; the layers were only subjected to natural climatic actions. The mechanical properties in terms of stiffness, deformation, and resistance to penetration were characterized by the LWD and DCP. The following conclusions can be drawn:

- (1) Both organosilane and lignosulfonate were effective technologies to enhance the mechanical performance of crushed rocks to be used as aggregates in

the road base layers. The LWD and DCP measurements performed within the two-year time frame highlighted the persistent effectiveness of the stabilizing agents.

- (2) Based on the data collected during the first 50 days, the organosilane had a more rapid stabilizing effect compared to the lignosulfonate; nevertheless, similar performance was observed during the other periods when measurements were undertaken.
- (3) The results deriving from LWD and DCP were in good agreement as both the test equipment indicated that the stabilized aggregates performed better than the untreated ones and that the mechanical response related to the investigated additive technologies gradually reduced over time.
- (4) The test sections were built comprising aggregates that fulfilled the standard code requirements. Therefore, using the investigated nontraditional stabilizing agents can lead to even greater benefits for those “weak” aggregates that do not meet the requirements specified by the design manual.

As an input for future research efforts, some considerations can be made to indicate the directions to expand the investigation. Even if the test results of this study were positive, the outcomes could be generalized even more by employing other rock types. Moreover, mixing proportions containing different additive percentages as well as the exposure to different climates and temperatures could be investigated. Finally, compound modification of the polymer-based and lignin-based stabilizing agents could also be explored.

#### Data Availability

The data are available by contacting the corresponding author at [diego.barbieri@ntnu.no](mailto:diego.barbieri@ntnu.no).

#### Disclosure

The main results of this work were presented at “World Transport Convention 2021” (15–19 June 2021, Xi’an, China) with the title “Performance of road base layers stabilized with organosilane and lignosulfonate during a two-year time span.”

#### Conflicts of Interest

The authors declare that there are no conflicts of interest regarding the publication of this paper.

#### Acknowledgments

The support kindly provided by the laboratory assistants Jan Erik Molde, Bent Lervik, Lisbeth Johansen, Torill Sørlokk, and Laurentius Tjihuis is greatly acknowledged. Organosilane additive was supplied by Sparks AS, Asker, Norway and Zydex Industries, Vadodara, India. Lignosulfonate additive was supplied by Borregaard AS, Sarpsborg, Norway.

Materials and field test area was provided by Franzefoss Pukkverk avd. Vassfjell, Heimdal, Norway. The research was supported by Norwegian Public Roads Administration (grant no. 25134404).

## References

- [1] K. K. Dunham, "Coastal highway route E39 - extreme crossings," *Transportation Research Procedia*, vol. 14, pp. 494–498, 2016.
- [2] NPRA, "The E39 coastal highway route," 2017, <https://www.vegvesen.no/en/roads/Roads+and+bridges/Road+projects/e39coastalhighwayroute;jsessionid=99D143CB28F87A072777C744BBCA31E8?lang=nn>.
- [3] A. Gomes Correia, M. G. Winter, and A. J. Puppala, "A review of sustainable approaches in transport infrastructure geotechnics," *Transportation Geotechnics*, vol. 7, pp. 21–28, 2016.
- [4] G. Petkovic, "Recycling in Norwegian conditions," in *Proceedings of the 5th International Conference Bear. Capacit. Roads Airfields, Tapir, Trondheim*, R. S. Nordal and G. Refsdal, Eds., , 2005.
- [5] P. P. Riviera, R. Bellopede, P. Marini, and M. Bassani, "Performance-based re-use of tunnel muck as granular material for subgrade and sub-base formation in road construction," *Tunnelling and Underground Space Technology*, vol. 40, pp. 160–173, 2014.
- [6] E. Hoxha, H. R. Vignisdottir, D. M. Barbieri et al., "Life cycle assessment of roads: exploring research trends and harmonization challenges," *The Science of the Total Environment*, vol. 759, p. 143506, 2021.
- [7] D. M. Barbieri, B. Lou, F. Wang et al., "Assessment of carbon dioxide emissions during production, construction and use stages of asphalt pavements," *Transp. Res. Interdiscip. Perspect.* vol. 11, 2021.
- [8] Teknologirådet, "Teknologirådet | norge 2030 arkiver," 2012, <https://teknologiradet.no/category/norge-2030/>.
- [9] D. M. Barbieri, I. Hoff, and H. Mork, "Laboratory investigation on unbound materials used in a highway with premature damage," in *Proceedings of the 10th International Conference Bear. Capacit. Roads, Railw. Airfields*, Athens, Greece, June 2017.
- [10] Npra, *Handbook N200 Vegbygging*, Vegdirektoratet, Oslo, Norway, 2018.
- [11] Npra, *Handbook N200 Vegbygging*, Vegdirektoratet, Oslo, Norway, 2014.
- [12] Cen, I. S. O. *1097-2 Tests for Mechanical and Physical Properties of Aggregates. Part 2: Methods for the Determination of Resistance to Fragmentation*, Standard, Delhi, India, 2010.
- [13] Cen, I. S. O. *1097-1 Tests for Mechanical and Physical Properties of Aggregates. Part 1: Determination of the Resistance to Wear (Micro-deval)*, Standard, Delhi, India, 2011.
- [14] S. Adomako, C. J. Engelsens, R. T. Thorstensen, and D. M. Barbieri, "Review of the relationship between aggregates geology and Los Angeles and micro-Deval tests," *Bulletin of Engineering Geology and the Environment*, 2021.
- [15] D. M. Barbieri, I. Hoff, and M. B. E. Mørk, "Mechanical assessment of crushed rocks derived from tunnelling operations," in *Proceedings of the 5th GeoChina International Conference 2018*, W.-C. Cheng, J. Yang, and J. Wang, Eds., pp. 225–241, Springer, HangZhou, China, July 2019.
- [16] A. Behnood, "Soil and clay stabilization with calcium- and non-calcium-based additives: a state-of-the-art review of challenges, approaches and techniques," *Transportation Geotechnics*, vol. 17, pp. 14–32, 2018.
- [17] Y. J. Jiang and L. F. Fan, "An investigation of mechanical behavior of cement-stabilized crushed rock material using different compaction methods," *Construction and Building Materials*, vol. 48, pp. 508–515, 2013.
- [18] J. Myre, *The Use of Cold Bitumen Stabilized Base Course Mixes in Norway*, pp. 1–14, Vegdirektoratet, Oslo, Norway, 2014.
- [19] NPRA, *Kalde Bitumen- Stabiliserte Bærelag*, Vegdirektoratet, Oslo, Norway, 2014.
- [20] K. Siripun, P. Jitsangiam, and H. Nikraz, "Characterization analysis and design of hydrated cement treated crushed rock base as a road base material in Western Australia," *International Journal Pavement Reserach Technol.* vol. 10, pp. 39–47, 2010.
- [21] Z. Liu, B. Lou, D. M. Barbieri, A. Sha, T. Ye, and Y. Li, "Effects of pre-curing treatment and chemical accelerators on Portland cement mortars at low temperature (5°C)," *Construction and Building Materials*, vol. 240, 2020.
- [22] D. M. Barbieri, I. Hoff, and C.-H. Ho, "Crushed rocks stabilized with organosilane and lignosulfonate in pavement unbound layers: repeated load triaxial tests," *Frontiers of Structural and Civil Engineering*, 2021.
- [23] D. M. Barbieri, I. Hoff, and M. B. E. Mørk, "Innovative stabilization techniques for weak crushed rocks used in road unbound layers: a laboratory investigation," *Transportation Geotechnics*, vol. 18, pp. 132–141, 2019.
- [24] D. M. Barbieri, I. Hoff, and M. B. E. Mørk, "Organosilane and lignosulfonate as innovative stabilization techniques for crushed rocks used in road unbound layers," *Transp. Geotech.* vol. 22, 2020.
- [25] D. P. Alazigha, B. Indraratna, J. S. Vinod, and A. Heitor, "Mechanisms of stabilization of expansive soil with lignosulfonate admixture," *Transportation Geotechnics*, vol. 14, pp. 81–92, 2018.
- [26] Q. Chen, B. Indraratna, J. Carter, and C. Rujikiatkamjorn, "A theoretical and experimental study on the behaviour of lignosulfonate-treated sandy silt," *Computers and Geotechnics*, vol. 61, pp. 316–327, 2014.
- [27] J. Daniels and M. S. Hourani, "Soil improvement with organosilane," *U.S.-China Work Government Improvement Technol.*, 2009.
- [28] R. L. Santoni, J. S. Tingle, and S. L. Webster, "Stabilization of silty sand with nontraditional additives," *Transportation Research Record: Journal of the Transportation Research Board*, vol. 1787, no. 1, pp. 61–70, 2002.
- [29] B. Ta'negonbadi and R. Noorzad, "Physical and geotechnical long-term properties of lignosulfonate-stabilized clay: an experimental investigation," *Transp. Geotech.* vol. 17, pp. 41–50, 2018.
- [30] O. O. Ugwu, J. B. Arop, C. U. Nwoji, and N. N. Osadebe, "Nanotechnology as a preventive engineering solution to highway infrastructure failures," *Journal of Construction Engineering and Management*, vol. 139, no. 8, pp. 987–993, 2013.
- [31] T. Zhang, G. Cai, and S. Liu, "Application of lignin-stabilized silty soil in highway subgrade: a macroscale laboratory study," *Journal of Materials in Civil Engineering*, vol. 30, 2018.
- [32] D. M. Barbieri, M. Tangerås, E. Kassa, I. Hoff, Z. Liu, and F. Wang, "Railway ballast stabilising agents: comparison of mechanical properties," *Construction and Building Materials*, vol. 252, 2020.

- [33] ASTM International, *Standard Test Method for Measuring Deflections Using a Portable Impulse Plate Load Test Device*, ASTM International, West Conshohocken, PA, USA, 2015.
- [34] ASTM International, *Standard Test Method for Use of the Dynamic Cone Penetrometer in Shallow Pavement Applications*, ASTM International, West Conshohocken, PA, USA, 2018.
- [35] T. Grenne, G. Grammeltvedt, and F. M. Vokes, "Ophiolites type sulphide deposits in the western Trondheim district, central Norwegian caledonides," in *Proceedings of the International Ophiolite Symposium*, pp. 727–743, Geological Survey Department, Nicosia, Cyprus, 1980.
- [36] G. Petkovic, C. J. Engelsens, A.-O. Håøya, and G. Breedveld, "Environmental impact from the use of recycled materials in road construction: method for decision-making in Norway," *Resources, Conservation and Recycling*, vol. 42, no. 3, pp. 249–264, 2004.
- [37] CEN, *ISO 14688-1 Geotechnical Investigation and Testing. Identification and Classification of Soil*, International Organization for Standardization (ISO), Geneva, Switzerland, 2018.
- [38] CEN, *ISO 13286-4 Test Methods for Laboratory Reference Density and Water Content - Vibrating Hammer*, International Organization for Standardization (ISO), Geneva, Switzerland, 2003.
- [39] J. S. Tingle, J. K. Newman, S. L. Larson, C. A. Weiss, and J. F. Rushing, "Stabilization mechanisms of nontraditional additives," *Transportation Research Record: Journal of the Transportation Research Board*, vol. 1989-2, no. 1, pp. 59–67, 2007.
- [40] B. K. Kunz, E. E. Little, and V. L. Barandino, "Aquatic toxicity of chemical road dust suppressants to freshwater organisms," *Archives of Environmental Contamination and Toxicology*, vol. 2, 2021.
- [41] DD CEN/TS, *Characterization of Waste. Leaching Behaviour Tests. Up-Flow Percolation Test*, under specified conditions, 2006.
- [42] D. Jones, "Guidelines for the selection, specification, and application of chemical dust control and stabilization treatments on unpaved roads," 2017, <https://escholarship.org/uc/item/0347c9zj>.
- [43] A. A. Fungaroli and S. R. Prager, "Evaluation of some acrylic polymers as soil stabilizers," *Product R&D*, vol. 8, no. 4, pp. 450–453, 1969.
- [44] Y. Ohama, "Polymer-based admixtures," *Cement and Concrete Composites*, vol. 20, no. 2-3, pp. 189–212, 1998.
- [45] E. H. Tan, E. M. M. Zahran, and S. J. Tan, "A review of chemical stabilisation in road construction," *IOP Conference Series: Materials Science and Engineering*, vol. 943, 2020.
- [46] D. Jones and R. Surdahl, "New procedure for selecting chemical treatments for unpaved roads," *Transportation Research Record: Journal of the Transportation Research Board*, vol. 2433, no. 1, pp. 87–99, 2014.
- [47] M. C. Roco, "Broader societal issues of nanotechnology," *Journal of Nanoparticle Research*, vol. 5, no. 3/4, pp. 181–189, 2003.
- [48] K. Sobolev, "Modern developments related to nanotechnology and nanoengineering of concrete," *Frontiers of Structural and Civil Engineering*, vol. 10, no. 2, pp. 131–141, 2016.
- [49] K. Sobolev and S. P. Shah, *Nanotechnology in Construction Proc. NICOM5*, K. Sobolev and S. P. Shah, Eds., p. 509, Springer, NEW YORK, NY, USA, 2015.
- [50] S. R. Wasserman, Y. T. Tao, and G. M. Whitesides, "Structure and reactivity of alkylsiloxane monolayers formed by reaction of alkyltrichlorosilanes on silicon substrates," *Langmuir*, vol. 5, no. 4, pp. 1074–1087, 1989.
- [51] H. K. Kim, J. P. Lee, C. R. Park, H. T. Kwak, and M. M. Sung, "Thermal decomposition of alkylsiloxane self-assembled monolayers in air," *The Journal of Physical Chemistry B*, vol. 107, no. 18, pp. 4348–4351, 2003.
- [52] T. Zhang, Y. L. Yang, and S. Y. Liu, "Application of biomass by-product lignin stabilized soils as sustainable geomaterials: a review," *The Science of the Total Environment*, vol. 728, Article ID 138830, 2020.
- [53] G. Dondi, C. Sangiorgi, and C. Lantieri, "Applying geostatistics to continuous compaction control of construction and demolition materials for road embankments," *Journal of Geotechnical and Geoenvironmental Engineering*, vol. 140, no. 3, Article ID 06013005, 2014.
- [54] C. Sangiorgi, C. Lantieri, and G. Dondi, "Construction and demolition waste recycling: an application for road construction," *International Journal of Pavement Engineering*, vol. 16, no. 6, pp. 530–537, 2015.
- [55] HMP-LFG, *The Light Drop Weight Tester*, Magdeburg prüfgeratebau GmbH, Magdeburg, Germany, 2018, <https://www.hmp-online.com/en/>.
- [56] HMP-LFG, *HMP-LFG4 Instruction Manual*, Magdeburg prüfgeratebau GmbH, Magdeburg, Germany, 2017.
- [57] H. Chennarapu, T. K. Garala, R. Chennareddy, U. Balunaini, and G. Venkata Narasimha Reddy, "Compaction quality control of earth fills using dynamic cone penetrometer," *Journal of Construction Engineering and Management*, vol. 144, no. 9, Article ID 04018086, 2018.
- [58] J. Boussinesq, *Application des potentiels à l'étude de l'équilibre et du mouvement des Solids Elastiques*, Gauthier-Villars, Paris, France, 1885.
- [59] P. Vennapusa and D. White, "Comparison of light weight deflectometer measurements for pavement foundation materials," *Geotechnical Testing Journal*, vol. 32, 2009.
- [60] P. Fleming, M. Frost, and J. Lambert, "Review of lightweight deflectometer for routine in situ assessment of pavement material stiffness," *Transport Research Record Journal Transportation Research Board*, pp. 80–87, 2004.
- [61] M. A. Mooney and P. K. Miller, "Analysis of lightweight deflectometer test based on in situ stress and strain response," *Journal of Geotechnical and Geoenvironmental Engineering*, vol. 135, no. 2, pp. 199–208, 2009.
- [62] D. H. Chen, D. Lin, P. Liao, and J. Bilyeu, "A correlation between dynamic cone penetrometer values and pavement layer moduli," *Geotechnical Testing Journal*, vol. 28, 2005.
- [63] J. Chen, M. Hossain, and T. M. Latorella, "Use of falling weight deflectometer and dynamic cone penetrometer in pavement evaluation," *Transportation Research Record: Journal of the Transportation Research Board*, vol. 1655, no. 1, pp. 145–151, 1999.
- [64] J. Siekmeier, D. Young, and D. Beberg, "Comparison of the dynamic cone penetrometer with other tests during subgrade and granular base characterization in Minnesota," in *Non-destruct. Test. Pavements Backcalc. Modul. 3rd Vol*, S. D. Tayabji and E. O. Lukanen, Eds., American Society for Testing Materials, West Conshohocken, PA, USA, 2000.
- [65] Norwegian Meteorological Institute, "eKlima," 2020, [http://sharki.oslo.dnmi.no/portal/page?\\_pageid73,=39035,73\\_39049&\\_dad=portal&\\_schema=PORTAL](http://sharki.oslo.dnmi.no/portal/page?_pageid73,=39035,73_39049&_dad=portal&_schema=PORTAL).
- [66] US National Weather Service, "Precipitation measurements," 2020, <https://www.weather.gov/abr/cmap>.
- [67] CEN, "ISO 11272 Soil quality - determination of dry bulk density," 2017, <https://www.iso.org/standard/68255.html>.
- [68] A. S. Norsk rikskringkasting, "Varmerekord i Sør-Norge i mai," 2018, <https://www.nrk.no/hordaland/varmerekord-i-sor-norge-i-mai-1.14054641>.



## Research Article

# The Effects of Geocell Height and Lime Stabilization on Unpaved Road Settlements at Different Water Contents

Erhan Burak Pancar  and Aytuğ Kumandaş 

Department of Civil Engineering, Ondokuz Mayıs University, Samsun, Turkey

Correspondence should be addressed to Erhan Burak Pancar; [erhanpancar@hotmail.com](mailto:erhanpancar@hotmail.com)

Received 12 April 2021; Revised 17 June 2021; Accepted 24 August 2021; Published 6 September 2021

Academic Editor: Kumar Anupam

Copyright © 2021 Erhan Burak Pancar and Aytuğ Kumandaş. This is an open access article distributed under the Creative Commons Attribution License, which permits unrestricted use, distribution, and reproduction in any medium, provided the original work is properly cited.

In this study, lime stabilization and geocell reinforcement methods were investigated for a clayey subgrade of unpaved road at different water contents. This study is especially important in terms of determining the soil improvement method for road construction on wet lands. The effects of the geocell height (50, 100, 150, and 200 mm) and lime content (3, 6, and 12%) on the settlement of the subgrade soil at different water contents (25, 28, 30, 32, and 35%) were analyzed. Accordingly, a large scale plate loading test was designed, and it is utilized to achieve loading-settlement curves. The bearing capacity and modulus of subgrade ( $k$ ) of soil were determined. It was detected that the geocell height and lime content have different effects at different water contents, and the modulus of subgrade reaction became stable beyond a constant height of the geocell. It was understood that none of these two improvements did not meet the Highways Technical Specifications. It is detected that at least these two improvement techniques are needed to be applied together to meet the specifications for the soil examined in this study.

## 1. Introduction

Performance and bearing capacity of the road surfacing significantly depend on the specifications of the ground that it subsides. Therefore, foundation floors must safely withstand the stresses caused by traffic loads. Therefore, base soils need to safely withstand the stresses that traffic loads constitute. Generally, soil type, water content, and degree of compaction affect the bearing capacity of the foundation soil. Swelling or blistering of the base soil depends on its moisture content. No superstructure constructed on this type of base soils can withstand against cracking and settlements. Base soils must be able to withstand high level loads without excessive settlements. Base soils that are not suitable for the road superstructure should be improved and stabilized adequately. With the improvement of the base soil, the bearing capacity and surfacing performance increase, while settlements and, thus, the surfacing thickness decrease [1].

With the addition of lime to the soil, the strength and modulus of elasticity of the soil increases. Thus, an increase in the strength of the soil occurs [2]. In general, lime leads to

a decrease in the dry volume weight of the soil, a change in the plastic features, and an improvement in the bearing capacity of the soil. Thanks to the lime stabilization, the difference between the liquid limit and the plastic limit is reduced. This means that the plasticity index decreases [1]. Lime stabilization is commonly used in the fillings done from clayey soils and especially road constructions. Dasha and Hussain [3] determined the optimum lime content as 5% for residual soil-rich samples and 9% for expanding soils. Excessive lime treatments increase the swell potential of soils and decrease the soil strength. Dasha and Hussain [3] stated that this content is 9% for coarse-grained soils and 5% for fine-grained soils. Pancar and Akpınar [1] demonstrated that the settlement of the unpaved road subgrade with 12% lime content was less than the subgrade with 6% lime content, and the settlement of subgrade with 6% lime content was also less than the subgrade with 3% lime content at a high water content by 10% increasing the optimum water content. In their studies, Sivapullaiah et al. [4] investigated the behavior of Terra rossa soil with the addition of 1% lime, 1% cement, and 20% bentonite.

They concluded that the strength of Terra rossa soil increased rapidly within 7 days with the addition of the cement-bentonite mixture; on the other hand, the increase occurred after 7 days with the addition of the bentonite-lime mixture [4].

In their study, Keskin and Kavak [5] reviewed the effects of improvement of a road base clayey soil by lime stabilization. The soil water content was 35%, and this ratio was 12% more than the optimum water content. It was concluded that the CBR values increased up to 8 times in 28 days.

Madhavi Latha and Somwanshi [6] showed that the most advantageous form of the soil reinforcement technique is different forms of geosynthetic reinforcement (i.e., randomly distributed mesh elements, planar layers, and geocell) of the geocell. Tafreshi and Dawson [7] stated that more than 200% increase in the bearing capacity and up to 75% reduction in settlements can be achieved with geocell reinforcement. In addition, it has been determined that geocell reinforcement is more preferred than planar reinforcement [7, 8].

Dash et al. [8] stated that the overall frictional resistance on the geocell walls increases with the increase in the geocell mattress height, and the increase in the geocell height reduces the beneficial effect of the geocell. It has been observed that the overall performance improvement is significant, up to a geocell height of 2.1 times the diameter of the footing. However, only marginal improvement was observed beyond this geocell height. In addition, it was concluded that a seven-fold increase in the bearing capacity of the circular footing is possible by using geocell and geogrid reinforcements together.

Zhou and Wen [9] stated that the settlement can be reduced by 44% by geocell reinforcement. Dash et al. [10] stated that when a planar geogrid is added to the base of the geocell, an increase of 30% more than the increase in the bearing capacity of the foundation obtained using the geocell alone can be achieved.

Zhang et al. [11] determined that the two effects are very important for the increase in the bearing capacity of the foundation soil and stated that these effects are the “vertical stress distribution effect” and the “membrane effect.”

In their study, Dash et al. [10] stated that the bearing strength used in geocell production is not a critical parameter when evaluating geocell performance. Sofiev and Pancar [12] investigated the effect of heterogeneity on parametric instability of axially excited orthotropic conical shells, similar to the vertical stress distribution effect of the geocell, and stated that the area of the main instability regions decreases with increasing  $L/R_1$  (slant length/small mean radii) ratio.

It was indicated that the geocell shape of 1:1.2 (width: height), which was filled with sand, and the geocell shape of 1:0.8, which was filled with sedimentary clay gave the largest ultimate bearing capacity [13]. Engineering properties of the modified soil and ground improving materials and techniques are still being observed [14–20].

Kong et al. [14] modified the soil to produce a restoration material for silty earthen sites. They used lime and starch

ether both separately and together to modify the soil. They found that the shear strength and the compressive ability of the soil have been improved for both single-mixed modification and multiple-mixed modification. They stated that the optimum lime and starch ether contents for single-mixed soil were 9% and 5%, respectively, while these values were 6% and 5%, respectively, for multiple-mixed soil.

Yünkül et al. [16] investigated the uplift behavior of the horizontal square anchor in cohesionless soil reinforced with or without geocell using PLAXIS 3D finite element software and determined the optimum design parameters, including geocell properties, according to the dimensionless breakout factor ( $F_q$ ). As a result of their study, they found that the optimum values for the geocell width ratio ( $B_g/B$ ), geocell height ratio ( $h/B$ ), geocell distance ratio ( $U/B$ ), and geocell stiffness are 2.5, 0.75, 0, 1000 kN/m, respectively. In addition to these values, they indicated that the geocell pocket size ratio ( $a/B$ ) significantly affects the uplift capacity of the plate anchor. When  $a/B$  is decreased, the uplift capacity of the plate anchor increases.

Tiwari and Satyam [18] investigated the behavior of lime and silica fume treated coir geotextile reinforced expansive soil subgrade. They found that the upward swelling pressure decreased 52.19% in single-layer and 81.89% in double-layer with the lime treated coir geotextile. Jahandari et al. [19] treated clayey soil with lime and geogrid and investigated the mechanical properties of treated soil within 365 days curing period. As a result of their experimental study, they found that geogrids and lime improve the geotechnical properties of clayey soils.

In this study, the effect of lime and geocell reinforcement has been studied under varying moisture contents. The overall goal of this study was to analyze the effects of the geocell height (50, 100, 150, and 200 mm) and lime content (3, 6, and 12%) on the settlement of the clayey pavement subgrade at different water contents (25, 28, 30, 32, 35%). This comparison has not been made before in other studies.

## 2. Materials and Method

In this article, clayey soils with different water contents (25, 28, 30, 32, and 35%) have been subjected to a number of experiments. The soil is classified according to the AASHTO and the unified soil classification system. Accordingly, sieve analysis, consistency limit, and hydrometer analyzes were performed on the soil, respectively. Proctor tests were carried out on the samples in order to determine the optimum water content and dry unit weight of the clay material. In this study, model plate loading experiments were conducted on the mixtures that were prepared from optimum water content (25%) and high water contents (28, 30, 32, and 35%). In these experiments, soil was reinforced at different heights (50, 100, 150, and 200 mm) of the geocell, and lime was mixed to soil at the rates of 3, 6, and 12%. These treatments were made solely and together at different water contents (25, 28, 30, 32, and 35%). The sieve analysis of the soil used as a subgrade is given in Table 1.

In accordance with ASTM D2487 [21], the soil to be used as the subgrade is specified as Class CH. Clays in the CH

TABLE 1: Sieve analysis.

Sieve no	Sieve diameter (mm)	Sieve analysis		
		Residue of sieving (gr)	Sieved (gr)	Sieved percent (%)
3/8"	9, 53	0	420	100
4	4, 76	42, 7	377, 3	90
10	2	30, 1	347, 2	83
40	0, 42	18, 73	328, 47	78
100		15, 4	313, 07	75
200	0, 074	11, 5	301, 57	72
Pan		301, 57		

class have high plasticity. Its liquid limit and plastic limit are found to be 57% and 26%, respectively.

Dry sand was preferred as the infilling material for the geocell (Figure 1). It was used as a base layer for the unreinforced test section. The effective particle size ( $D_{10}$ ) was 1.2 mm, specific gravity was 2.64, coefficient of uniformity (Cu) was 2.25, and coefficient of curvature (Cc) was 1.05. It is classified as poorly graded sand (SP) according to the unified soil classification system [21]. The void ratio of the sand was 0.42, and the internal friction angle was  $37^\circ$ .

The technical properties of the geocell specified by the manufacturer are given in Table 2. In addition to the features in the table, there are drainage holes with a diameter of 10 mm in the geocell cell walls.

Laboratory scale loading tests were used to investigate the influence of lime stabilization (3 different lime contents were used) and geocell (4 different geocell heights were used) reinforcement on increasing the bearing capacity of clayey soil with 3 different water contents in a steel box.

The inner dimensions of the box are given in Figure 2. As can be seen from this figure, the box is 1.2 m long, 1.2 m wide, and 1.2 m high. Unpaved road test sections were made inside the box.

Dash et al. [8] indicated that, when the pocket diameter/footing width is around 0.8, it gives maximum performance. The pocket diameter was 25 cm, and the diameter of circular footing was 30 cm to get maximum performance in this study. The footing was loaded with a hydraulic actuator.

The acceptable range of settlements was not considered in some studies [8, 10, 22], and bearing capacity was estimated to be unreal. The value of footing settlement equals 12% of footing width (s/B) and is considered an absolute upper limit [7].

In this study, the peak load was selected to simulate a single wheel load of 40 kN (equivalent to an axle load of 80 kN and a tire contact pressure of 550 kPa).

The test box was filled with clayey soil with optimum water content (25%) and high water contents (28, 30, 32, and 35%). The soil was used as a subgrade and placed in 3 layers with 25 cm thickness for each layer. The placed layers were compacted in lifts inside a box using a vibratory plate compactor. After preparing the subgrade, three strain gages were installed on the top of the subgrade. 5 pressure cells were installed on the surface of the subgrade at the center, 15 cm, and 30 cm away from the center of the loading plate, respectively. A linear variable differential transducer (LVDT) was also placed on the footing model to provide the value of footing settlement during the loading (Figure 1).



FIGURE 1: Filling the geocell with sand.

TABLE 2: Technical properties of the geocell.

Properties	Values
Density (gr/cm <sup>3</sup> )	0.94
Welding size (cm)	40
Cell length (mm)	300
Cell width (mm)	250
Thickness (mm)	2
Cell height (cm)	5-10-15-20

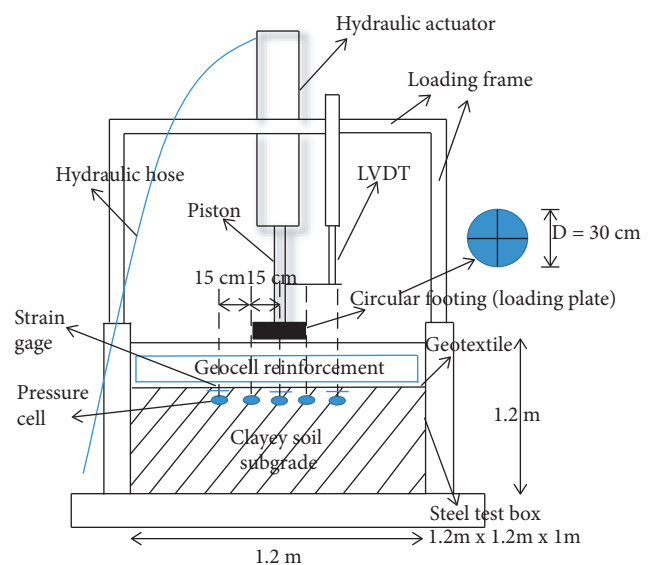


FIGURE 2: Schematic diagram for the set-up of the plate loading test.

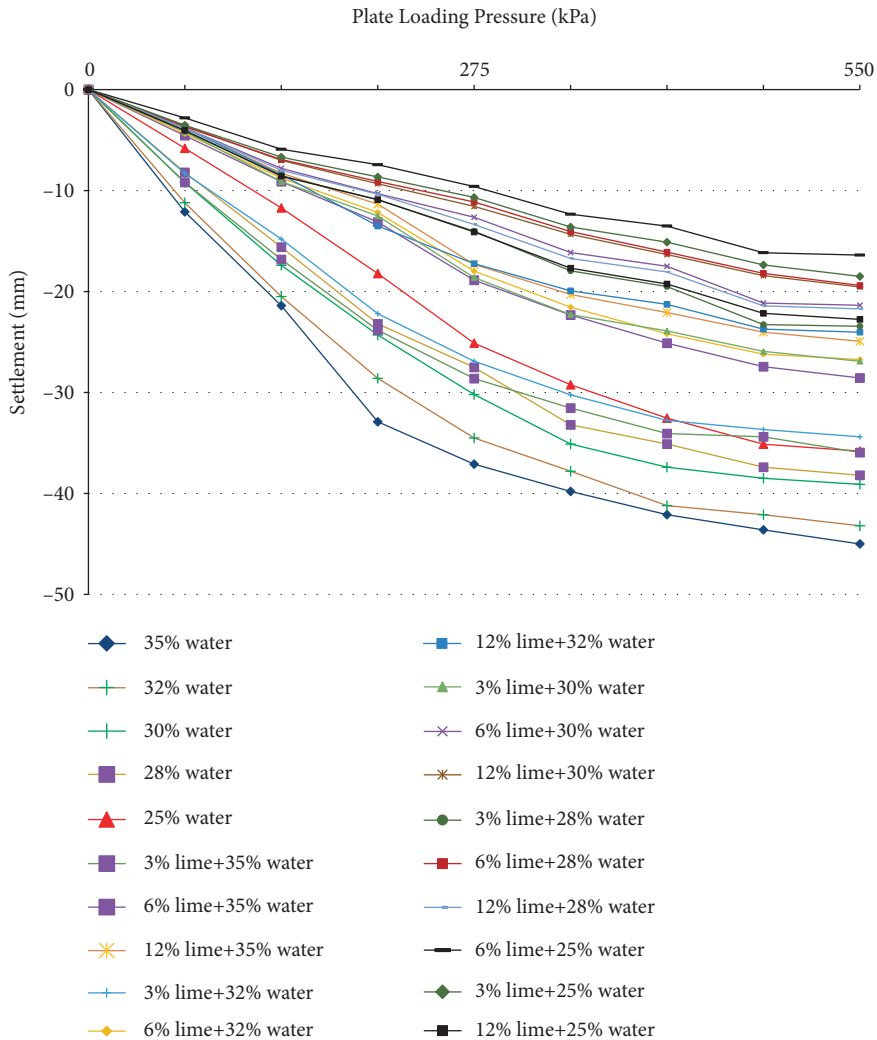


FIGURE 3: Loading-settlement curve for lime stabilizations at different water contents.

After the installation of pressure cells and strain gages, a geocell was placed on top of the subgrade. The top of the geocell mattress was at a depth of 3 cm from the bottom of the footing to get optimum test results as Tafreshi and Dawson [7] indicated in their study.

32 unpaved road test sections were prepared in the test box. Settlements of lime stabilized and geocell (with different heights) reinforced soils with different water contents were examined.

### 3. Results and Discussion

Comparison between the improvement of the clayey unpaved road subgrade with geocell and lime stabilizations at different water contents was made in the laboratory. The height of the geocell used in this study was 50, 100, 150, and 250 mm. The lime content was 3, 6, and 12%. The water content was 25 (optimum), 28, 30, 32, and 35%.

Effects of lime stabilization at a rate of 3, 6, and 12% at 25, 28, 30, 32, and 35% water contents are shown in Figure 3.

The settlement in soil with 25, 28, 30, and 32% water contents was 0.80, 0.85, 0.87, and 0.96 times the settlement in soil with 35% water content under 550 kPa, respectively.

Lime stabilization at a rate of 12, 12, 12, 6, and 6% was most effective at 35, 32, 30, 28, and 25% water contents, respectively. The settlement in soil with 35% water content was 1.8, 1.6, and 1.3 times the settlement of 12, 6, and 3% lime-stabilized soil at the same water content under 550 kPa, respectively. The settlement in soil with 32% water content was 1.8, 1.6, and 1.3 times the settlement of 12, 6, and 3% lime-stabilized soil at the same water content under 550 kPa, respectively. The settlement in soil with 30% water content was 2, 1.8, and 1.4 times the settlement of 12, 6, and 3% lime-stabilized soil at the same water content under 550 kPa, respectively. The settlement in soil with 28% water content was 1.8, 2, and 1.6 times the settlement of 12, 6, and 3% lime-stabilized soil at the same water content under 550 kPa, respectively. The settlement in soil with 25% water content was 1.6, 2.2, and 2 times the settlement of 12, 6, and 3% lime-stabilized soil at the same water content under 550 kPa, respectively. Adequate quantities of lime must be added into

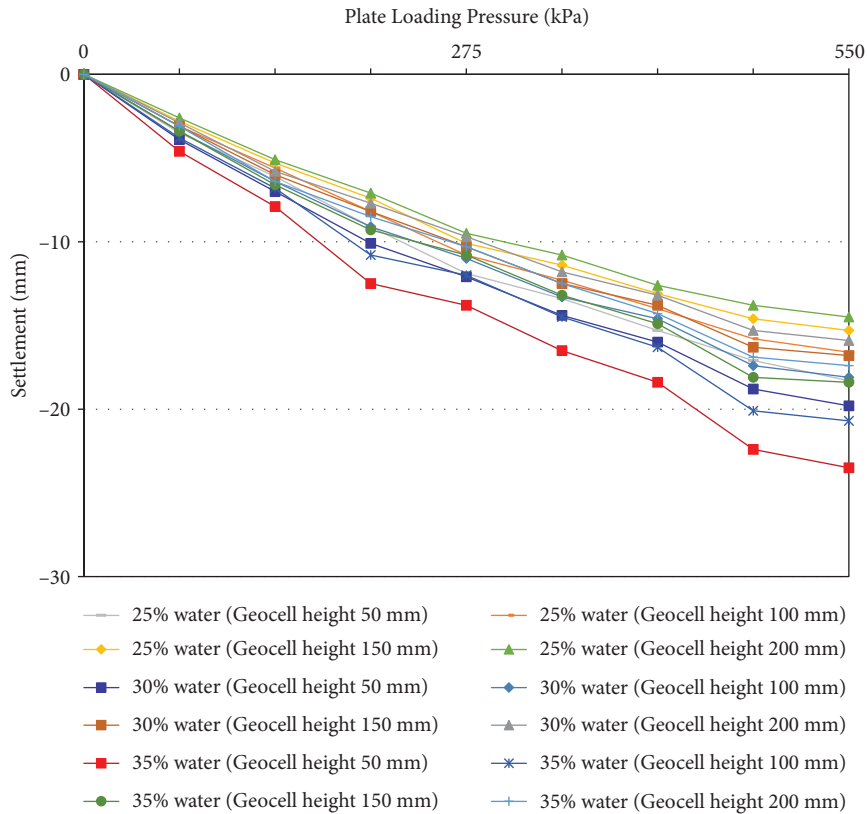


FIGURE 4: Loading-settlement curve for geocell reinforced soil at different water contents.

the soil to get minimum settlements under loading. Although better results were obtained by using 12% lime content for soils at 30, 32, and 35% water contents, it was seen that the lime content must be decreased to 6% for soils with 28 and 25 (optimum)% water contents. Dash and Hussain [3] explained the effect of lime on the liquid and plastic limit of the soil in their study, and they determined that the optimum lime content giving maximum strength was 3% for residual soil. When the lime is added into soil, lime is hydrated. The water content of the soil is important for hydration. Hydrated lime reacts with clay particles. This reaction produces additional drying because it reduces the soil's moisture holding capacity. Determining different optimum lime contents for soils with different water contents in this study is due to these reasons.

Soil settlements under pressure when the soil is reinforced by geocell with 4 different geocell heights at 3 different water contents are shown in Figure 4.

The ratio between the settlement of the soil at 35% water content under 550 kPa and geocell reinforced soil with 200 mm height at the same water content was 2.6. The ratio between the settlement of the soil at 30% water content under 550 kPa and geocell reinforced soil with 200 mm height at the same water content was 2.5. The ratio between the settlement of the soil at 25% water content under 550 kPa and geocell reinforced soil with 200 mm height at the same water content was 2.5.

When the height of the geocell was 50 mm at geocell-reinforced soil at 35% water content, the settlement was 1.1,

1.3, and 1.4 times the settlement when the height of the geocell was 100, 150, and 200 mm under 550 kPa, respectively. When the height of the geocell was 50 mm at geocell-reinforced soil at 30% water content, the settlement was 1.1, 1.2, and 1.3 times the settlement when the height of the geocell was 100, 150, and 200 mm under 550 kPa, respectively. When the height of the geocell was 50 mm at geocell-reinforced soil at 25% water content, the settlement was 1.1, 1.2, and 1.3 times the settlement when the height of the geocell was 100, 150, and 200 mm under 550 kPa, respectively.

The effect of the height of the geocell on settlement of soil was different for soils at different water contents. Soil settlement differences between different heights of geocell at 25, 30, and 35% water contents are shown in Figure 5. In these Figures, cell 200, cell 150, cell 100, and cell 50 means that the geocell height is 200 mm, 150 mm, 100 mm, and 50 mm, respectively.

The modulus of subgrade reaction values ( $k$ ) for lime-stabilized soil at different water contents was calculated with the help of Figure 3 by determining the inclinations of the loading-settlement curves. " $k$ " values were also calculated for soil reinforced by geocell with different heights at different water contents with the help of Figure 4. These values are listed in Table 3. As it is seen from Table 3, the " $k$ " value (three biggest value) was 27.500, 25.000, and 24.750  $\text{kN/m}^3$  for soil stabilized with 6% lime at 25% water content, 3% lime at 25% water content, and 6% lime at 28% water content, respectively. According to Highways Technical Specifications in Turkey, this value is to be no less than 55.000  $\text{kN/m}^3$  and none of them met this requirement.

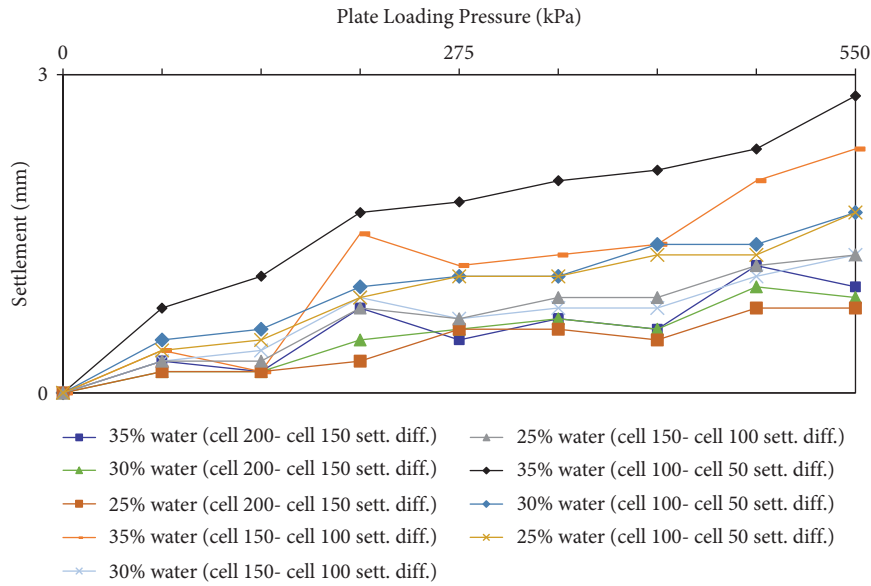


FIGURE 5: Settlement differences between different heights of the geocell at different water contents.

TABLE 3: Modulus of subgrade reactions (k) for lime-stabilized soils and geocell reinforcements.

States	Modulus of subgrade reaction (k) (kN/m <sup>3</sup> )
35% water content	6.550
32% water content	6.880
30% water content	8.100
28% water content	9.050
25% water content	11.460
3% lime at 35% water	8.490
12% lime at 35% water	15.100
3% lime at 32% water	9.170
6% lime at 32% water	14.470
12% lime at 32% water	14.600
3% lime at 30% water	14.030
6% lime at 30% water	15.800
12% lime at 30% water	24.700
3% lime at 28% water	14.750
6% lime at 28% water	24.750
12% lime at 28% water	15.350
3% lime at 25% water	25.000
6% lime at 25% water	27.500
12% lime at 25% water	15.280
Geocell height 200 mm at 35% water content	27.500
Geocell height 150 mm at 35% water content	26.190
Geocell height 100 mm at 35% water content	22.900
Geocell height 50 mm at 35% water content	18.300
Geocell height 200 mm at 30% water content	28.950
Geocell height 150 mm at 30% water content	27.230
Geocell height 100 mm at 30% water content	25.000
Geocell height 50 mm at 30% water content	18.350
Geocell height 200 mm at 25% water content	29.570
Geocell height 150 mm at 25% water content	28.650
Geocell height 100 mm at 25% water content	26.250
Geocell height 50 mm at 25% water content	18.950

Lime stabilization increased the “k” value 2.1, 1.9, 2, 1.8, and 1.4 times the value in soil at 35, 32, 30, 28, and 25% water contents, respectively. As it is seen, these increments decrease while water content decrease. The best lime

content to get the highest “k” value was 6% for soils at 25 and 28% water contents. 12% lime content was the best alternative to get the highest “k” value for soil at 30, 32, and 35% contents.



TABLE 4: Bearing capacities of lime-stabilized soils and geocell reinforcements.

States	Bearing capacity (kN/m <sup>2</sup> )
35% water content	28
32% water content	31
30% water content	38
28% water content	43
25% water content	60
3% lime at 35% water	38
12% lime at 35% water	86
3% lime at 32% water	44
6% lime at 32% water	74
12% lime at 32% water	75
3% lime at 30% water	74
6% lime at 30% water	95
12% lime at 30% water	110
3% lime at 28% water	86
6% lime at 28% water	115
12% lime at 28% water	95
3% lime at 25% water	127
6% lime at 25% water	142
12% lime at 25% water	86
Geocell height 200 mm at 35% water content	138
Geocell height 150 mm at 35% water content	121
Geocell height 100 mm at 35% water content	93
Geocell height 50 mm at 35% water content	86
Geocell height 200 mm at 30% water content	140
Geocell height 150 mm at 30% water content	135
Geocell height 100 mm at 30% water content	120
Geocell height 50 mm at 30% water content	103
Geocell height 200 mm at 25% water content	148
Geocell height 150 mm at 25% water content	138
Geocell height 100 mm at 25% water content	120
Geocell height 50 mm at 25% water content	112

It was determined that the modulus of the subgrade reaction increases when the height of the geocell increased. It was also observed that the modulus of the subgrade reaction increase stopped at 200 mm geocell height at 25, 30, and 35% water contents.

Half of the stress corresponding to 10 mm settlement at the load-deformation curve obtained from the plate loading experiment gives the bearing capacity of the base soil. By starting from this information, half of the stresses corresponding to 10 mm at load-deformation curves were calculated, and bearing capacity values were determined. The bearing capacity values for lime-stabilized soils are given in Table 4.

As it is seen from Table 4, the bearing capacity (three biggest value) was 142, 127, and 115 kN/m<sup>2</sup> for soil stabilized with 6% lime at 25% water content, 3% lime at 25% water content, and 6% lime at 28% water content, respectively. The bearing capacity was increased maximum 3.1, 2.4, 2.9, 2.7 and 2.4 times by lime treatment at 35, 32, 30, 28, and 25% water contents, respectively. The bearing capacity values for reinforced soils by geocell with different heights at different water contents are also given in Table 4.

When the height of the geocell was 200 mm, the highest bearing capacities were obtained as it was expected. The

effect of height of the geocell on the bearing capacity of soil decreases at all water contents in this study.

The bearing capacity was increased 5, 3.7, and 2.5 times by geocell reinforcement of soil at 35, 30, and 25% water contents, respectively. The bearing capacity ratio between the geocell reinforcement and lime stabilization (maximum bearing capacity by using geocell/maximum bearing capacity by lime stabilization) was 1.60, 1.27, and 1.04 at 35, 30, and 25% water contents, respectively. It was determined that, when the water content decreases, lime stabilization can be used instead of geocell reinforcement.

#### 4. Conclusion

Lime stabilization and geocell reinforcement can be used to improve soil. In this study, lime stabilization and geocell reinforcements were made at different water contents for clayey subgrade of the unpaved road. Different lime contents and geocell heights were investigated for this purpose. Model plate loading experiments were done in the laboratory. Thirty-two different unpaved road test sections were examined. The peak load was selected to simulate a single wheel load of 40 kN (equivalent to an axle load of 80 kN and a tire contact pressure of 550 kPa). The effects of lime content and geocell height were investigated on the bearing capacity and the modulus of subgrade reaction of soil at different water contents. It was examined whether those improvements met the requirement of Highways Technical Specifications or not. These comparisons have not been made before in the literature for thirty-one different states examined in this study.

From the data presented in this study, the following conclusions can be drawn:

- (1) The settlement in lime-stabilized soil was at most between 1.8 and 2.2 times the settlement in unstabilized soil.
- (2) The settlement in geocell reinforced soil was at most between 2.5 and 2.6 times the settlement in unreinforced soil.
- (3) The effect of the height of the geocell on the settlement of soil under pressure decreases when the water content of the soil decreases.
- (4) It was observed that, when the height of the geocell increased, the modulus of the subgrade reaction also increased and became stable beyond 200 mm geocell height at 25, 30, and 35% water contents.
- (5) The bearing capacity was increased maximum 5 times by geocell reinforcement.

It is recommended that at least lime stabilization and geocell reinforcement need to be applied together to meet the Highways Technical Specifications for wetlands.

#### Data Availability

The data used to support the findings of this study are available from the corresponding author upon request.

## Conflicts of Interest

The authors declare that they have no competing interests.

## References

- [1] E. B. Pancar and M. V. Akpınar, "Comparison of effects of using geosynthetics and lime stabilization to increase bearing capacity of unpaved road subgrade," *Advances in Materials Science and Engineering*, vol. 2016, Article ID 7129356, 8 pages, 2016.
- [2] G. P. Broderick and D. E. Daniel, "Stabilizing compacted clay against chemical attack," *Journal of Geotechnical Engineering*, vol. 116, no. 10, pp. 1549–1567, 1990.
- [3] S. K. Dash and M. Hussain, "Lime stabilization of soils: reappraisal," *Journal of Materials in Civil Engineering*, vol. 24, no. 6, pp. 707–714, 2012.
- [4] P. V. Sivapullaiah, H. L. Kantha, and K. M. Kiran, "Geotechnical properties of stabilised indian red earth," *Geotechnical & Geological Engineering*, vol. 21, no. 4, pp. 399–413, 2003.
- [5] E. Keskin and A. Kavak, "Yüksek su muhtevasında killi bir zeminin kireç stabilizasyonu ile iyileştirilmesi ve yol kesitine etkileri, XI. Kil Sempozyumu," Ege Üniversitesi, İzmir, 2003.
- [6] G. Madhavi Latha and A. Somwanshi, "Effect of reinforcement form on the bearing capacity of square footings on sand," *Geotextiles and Geomembranes*, vol. 27, no. 6, pp. 409–422, 2009.
- [7] S. N. M. Tafreshi and A. R. Dawson, "Comparison of bearing capacity of a strip footing on sand with geocell and with planar forms of geotextile reinforcement," *Geotextiles and Geomembranes*, vol. 28, no. 1, pp. 72–84, 2010.
- [8] S. Dash, S. Sireesh, and T. G. Sitharam, "Model studies on circular footing supported on geocell reinforced sand underlain by soft clay," *Geotextiles and Geomembranes*, vol. 21, no. 4, pp. 197–219, 2003.
- [9] H. Zhou and X. Wen, "Model studies on geogrid- or geocell-reinforced sand cushion on soft soil," *Geotextiles and Geomembranes*, vol. 26, no. 3, pp. 231–238, 2008.
- [10] S. Dash, N. R. Krishnaswamy, and K. Rajagopal, "Bearing capacity of strip footings supported on geocell-reinforced sand," *Geotextiles and Geomembranes*, vol. 19, no. 4, pp. 235–256, 2001.
- [11] L. Zhang, M. Zhao, C. Shi, and H. Zhao, "Bearing capacity of geocell reinforcement in embankment engineering," *Geotextiles and Geomembranes*, vol. 28, no. 5, pp. 475–482, 2010.
- [12] A. H. Sofiyev and E. B. Pancar, "The effect of heterogeneity on the parametric instability of axially excited orthotropic conical shells," *Thin-Walled Structures*, vol. 115, no. 2017, pp. 240–246, 2017.
- [13] E. C. Shin, H. H. Kang, J. K. Kang, and H. S. Shin, "Effect of geocell shape and filling material characteristics on bearing capacity geocell reinforced soils," *Japanese Geotechnical Society Special Publication*, vol. 2, no. 66, pp. 2244–2247, 2016.
- [14] D. Kong, J. Chen, R. Wan, and H. Liu, "Study on restoration materials for historical silty earthen sites based on lime and starch ether," *Advances in Materials Science and Engineering*, vol. 2020, Article ID 2850780, 16 pages, 2020.
- [15] Z. Zuo, G. Yang, H. Wang, and Z. Wang, "Experimental investigations on pullout behavior of HDPE geogrid under static and dynamic loading," *Advances in Materials Science and Engineering*, vol. 2020, Article ID 5408064, 13 pages, 2020.
- [16] K. Yüncül, Ö. F. Usluoğulları, and A. Gürbüz, "Numerical analysis of geocell reinforced square shallow horizontal plate anchor," *Geotechnical & Geological Engineering*, vol. 39, no. 4, pp. 3081–3099, 2021.
- [17] V. S. Jayawardane, V. Anggraini, A. T. Li-Shen, S. C. Paul, and S. Nimbalkar, "Strength enhancement of geotextile-reinforced fly-ash-based geopolymer stabilized residual soil," *International Journal of Geosynthetics and Ground Engineering*, vol. 6, no. 4, p. 50, 2020.
- [18] N. Tiwari and N. Satyam, "An experimental study on the behavior of lime and silica fume treated coir geotextile reinforced expansive soil subgrade," *Engineering Science and Technology, an International Journal*, vol. 23, no. 5, pp. 1214–1222, 2020.
- [19] S. Jahandari, S. F. Mojtahedi, F. Zivari et al., "The impact of long-term curing period on the mechanical features of lime-geogrid treated soils," *Geomechanics and Geoengineering*, vol. 2020, Article ID 1739753, 2020.
- [20] B. Hu, X. Li, and L. Zheng, "Influences of urban viaduct pier caps on uneven settlement of roadbed," *Advances in Civil Engineering*, vol. 2019, Article ID 4151278, 20 pages, 2019.
- [21] Astm, *Standard Practice for Classification of Soils for Engineering Purposes (Unified Soil Classification System)*, Vol. D2487, ASTM International, West Conshohocken, PA, 2006.
- [22] S. Sireesh, T. G. Sitharam, and S. K. Dash, "Bearing capacity of circular footing on geocell-sand mattress overlying clay bed with void," *Geotextiles and Geomembranes*, vol. 27, no. 2, pp. 89–98, 2009.

## Research Article

# Maximum Likelihood Estimation of Parameters for Advanced Continuously Reinforced Concrete Pavement (CRCP) Punchout Calibration Model

Liangliang Chen <sup>1</sup>, Feng Zhang <sup>2</sup>, and Changjun Zhou <sup>3</sup>

<sup>1</sup>National Engineering Laboratory for Surface Transportation Weather Impacts Prevention, Broadvision Engineering Consultants, No. 9, Shijiaxiang Tuodong Road, Kunming 650041, China

<sup>2</sup>School of Transportation Science and Engineering, Harbin Institute of Technology, No. 73, Huanghe Road, Harbin 150090, China

<sup>3</sup>School of Transportation and Logistics, Dalian University of Technology, 2 Linggong Street, Dalian 116023, China

Correspondence should be addressed to Liangliang Chen; [dongtianai@163.com](mailto:dongtianai@163.com) and Changjun Zhou; [zhouchangjun@dlut.edu.cn](mailto:zhouchangjun@dlut.edu.cn)

Received 18 June 2021; Accepted 24 August 2021; Published 3 September 2021

Academic Editor: Hugo Rodrigues

Copyright © 2021 Liangliang Chen et al. This is an open access article distributed under the Creative Commons Attribution License, which permits unrestricted use, distribution, and reproduction in any medium, provided the original work is properly cited.

Pavement performance prediction is the essential part of the pavement design, which is very important for highway agencies for the purpose of budget allocating. This study introduces a model of local calibration for punchout, which is the major structural distress of continuously reinforced concrete pavement (CRCP). It is assumed that the number of equivalent single axle loads' (ESALs) leads to punchout follows a Weibull distribution. The parameters of Weibull distribution were estimated by maximum likelihood estimation (MLE). Additionally, an approach of estimating the initial value of the parameters was also presented before applying the Newton method for solving the likelihood equations. The regression result was found to fit the performance-monitoring data from LTPP very well. The proposed calibration model is capable of describing the punchout and can be employed to predict the failure rate and reliability of CRCP in the pavement design and the arrangement of rehabilitation activities.

## 1. Introduction

Predicting the pavement performance under various combinations of traffic levels, environmental conditions, pavement structures, and materials are a key component for highway agency to make a proper budget decision of the maintenance and rehabilitation activities [1]. Undoubtedly, the accuracy of the distress prediction depends on the calibration and validation of the mechanistic-empirical (ME) design models with independent datasets. Pavement engineers can definitely gain confidence in the design procedure when the ME models were calibrated by establishing an acceptable correlation between predicted and measured distresses in field. Local calibration is a systematic and mathematical process to minimize the difference between observed and predicted results by modifying, for

instance, empirical calibration parameters that eventually would be found to be a function of the key factors as a means to improve the accuracy of the prediction models [2]. No mechanistic pavement design models can be applied in practice for pavement performance prediction without calibration due to the great variety of environmental conditions, pavement structures, materials, and traffic loads. In order to improve the accuracy, reliability, and robustness of the performance prediction model, field investigation data from LTPP was utilized in the calibration process [3]. LTPP database is worthy of the name of the largest pavement performance database, test sections from LTPP were used extensively in the calibration process, which can provide pavement engineers with historically recorded climate information, monitoring of distress and response, materials testing, maintenance, and especially pavement performance

monitoring data. LTPP data were employed to conduct local and national calibration of the pavement performance by many researchers on both in-service flexible and rigid pavements [4–7], as well as survival analysis for preventive maintenance [8, 9].

However, as mentioned by Prozzi and Madanat [10], the pavement distress is an event of high variety, and it was more reasonable to describe the failure of pavement by a function of probability density rather than by a fixed-point estimation. It is worth noting that the distress investigation was not conducted continuously in LTPP data; moreover, the development of distresses is inconsistent [7]. The recording of punchouts as well as other types of distress is not simultaneous with the occurrence of pavement failure. Instead, only the number of punchouts formulated during the interval is available in the LTPP database. Pavement performance investigation is usually conducted at irregular intervals, ranging from 1–6 years. Therefore, the assumption that all the punchouts occur at the end of each interval will unavoidably underestimate the probability of the occurrence of punchouts.

The number of ESALs leading to punchout for a CRCP panel was assumed to follow Weibull distribution and the maximum likelihood estimation (MLE) of the parameters was introduced to estimate the parameters, due to insufficient data, to build the calibration model. The likelihood equations were solved by the Newton method, and least square regression was proposed to estimate the initial values. As a consequence, investigation data of field performance from LTPP GPS-5 (for CRCP) were extracted in Section 3 to illustrate the reliability and validity of the calibration procedure developed in this study.

## 2. Calibration Model

**2.1. Weibull Distribution.** Weibull distribution is the most popular and is widely used in the analysis of lifetime data and reliability since it was first introduced by Weibull in 1950s [11]. It has been proven to be very effective in modelling and analyzing lifetime data in medical, biological, and engineering sciences [12]. For instance, Weibull accelerated the failure time model and was successfully applied in prediction of pavement fatigue [13].

It is postulated that the fatigue process of pavement follows a Weibull distribution. The probability density of a two-parameter Weibull distribution is

$$f(x; \lambda, \beta) = \lambda\beta(\lambda x)^{\beta-1}e^{-(\lambda x)^\beta}, \quad x \geq 0. \quad (1)$$

The fatigue life pavement structures is defined as  $T$  and the duration function  $F(t)$  indicates the probability that the pavements will be distressed, cracked, or punchout for CRCP until time  $t$ , say  $P(T \leq t)$ ; thus,

$$F(t) = P(T \leq t) = 1 - e^{-(\lambda t)^\beta}, \quad t > 0. \quad (2)$$

The survival function of Weibull distribution, which is the probability that the pavement cannot be distressed at least up to time  $t$ , can be expressed as follows:

$$\begin{aligned} S(t) &= P(T \geq t) \\ &= 1 - F(t) = e^{-(\lambda t)^\beta}, \quad t > 0. \end{aligned} \quad (3)$$

The hazard rate function is corresponding to the probability that failures occur at the short interval  $[t, t + \Delta t)$ , as  $\Delta t$  approaches zero. The hazard rate function for a Weibull distribution is

$$\begin{aligned} h(t) &= \lim_{\Delta t \rightarrow 0} \frac{\Pr(t \leq T < t + \Delta t | T \geq t)}{\Delta t} \\ &= \frac{f(t)}{S(t)} \\ &= \lambda\beta(\lambda t)^{\beta-1}. \end{aligned} \quad (4)$$

Weibull distribution has a great variety of the shapes and is capable of describing the decreasing or increasing hazard rate of sample failure [14]. The hazard rate can be varied with the shape parameter  $\beta$ . A value of  $\beta > 1$  indicates that the failure rate will increase with time and will decrease if  $\beta < 1$ .

Weibull distribution is believed to be more advantageous to describe the formulation of pavement distress than exponential distribution because the pavement materials' mechanical properties such as elastic modulus and modulus of rupture are all in a decreasing state with the increasing life of pavement and will increase the probability of concrete failure for CRCP. Therefore, the failure rate could not be a constant value ( $\beta = 1$ ).

Portland cement concrete (PCC) slabs may fail in terms of transverse cracking, longitudinal cracking, faulting, spalling, etc. This research is focused on punchout, the major structural distress of CRCP. It was pointed out by Zollinger and Barenberg [15] that the nature of punchout distress is fatigue related. The performance of CRCP is mainly affected by not only concrete materials but also the base layer [16], noted that poor support conditions coupled with short transverse cracking intervals usually lead to punchout distress. The current ME pavement design guide provides an empirical calibration model as follows [17]:

$$PO = \frac{a}{1 + b \cdot FD^c}, \quad (5)$$

where PO denotes the total predicted number of punchouts per mile, FD is accumulated fatigue damage (due to slab bending in the transverse direction), and  $a$ ,  $b$ , and  $c$  are calibration constants for the locally or nationally calibrated model.

As suggested by Jung and Zollinger [18], the fatigue-based damage FD can be determined by

$$FD = \frac{N_e}{N_f}, \quad (6)$$

where  $N_e$  is the number of equivalent single axle loads (ESALs) and  $N_f$  is allowable equivalent traffic loads to failure.

Therefore, the survival function for CRCP can be expressed as a function of  $N_e$  rather than survival time.  $N_e$  is

assumed to follow the Weibull distribution, and the probability density function is

$$f(N_e; \lambda, \beta) = \lambda \beta (\lambda N_e)^{\beta-1} e^{-(\lambda N_e)^\beta}, \quad N_e \geq 0. \quad (7)$$

Since the monitoring of distress is not consecutive, only the number  $n_j$  occurred during each interval of  $N_e$  [ $N_{j-1}, N_j$ ], and the total number of the intervals is  $k+1$ , and  $j = 1, 2, \dots, k$ ,  $0 = N_0 < N_1 < \dots < N_k < N_{k+1} = \infty$ .

The probability of punchout that occurred in the interval [ $N_{j-1}, N_j$ ] can be expressed by

$$p_j(N_e) = P(X \in [N_{j-1}, N_j]) \\ = e^{-(\lambda N_{j-1})^\beta} - e^{-(\lambda N_j)^\beta}. \quad (8)$$

The total number of punchouts is observed in the most recent investigation is  $n_p$ , and then, the number of panel  $n_l$  which denotes the number of concrete panels that was lost to the observation in the site was

$$n_l = n_t - n_p, \quad (9)$$

where  $n_t$  is the total number of panels in the life test for a LTPP test section.

The survival function of the Weibull distribution:

$$S(N_e) = 1 - F(N_e) = e^{-(\lambda N_e)^\beta}. \quad (10)$$

2.2. *Maximum Likelihood Estimation of Parameters.* Maximum likelihood estimation is widely used to estimate parameters of Weibull distribution [19], and the likelihood function is

$$L = \left( \prod_{j=1}^k p_j^{n_j} \right) \cdot S^{n_l}(N_e > N_k), \quad (11)$$

$$\log L = \sum_{j=1}^k n_j \ln \left( e^{-(\lambda N_{j-1})^\beta} - e^{-(\lambda N_j)^\beta} \right) - n_l (\lambda N_k)^\beta. \quad (12)$$

We differentiate equation (12) with respect to the two unknown parameters and equal the resulting equation to zero as follows:

$$\frac{\partial L}{\partial \lambda} = \sum_{j=1}^k n_j \frac{\beta \lambda^{\beta-1} \left[ T_j^\beta e^{-(\lambda N_j)^\beta} - T_{j-1}^\beta e^{-(\lambda N_{j-1})^\beta} \right]}{e^{-(\lambda N_{j-1})^\beta} - e^{-(\lambda N_j)^\beta}} - n_l \beta N_k \cdot (\lambda N_k)^{\beta-1} \\ = 0, \quad (13)$$

$$\frac{\partial L}{\partial \beta} = \sum_{j=1}^k n_j \frac{(\lambda N_j)^\beta \log(\lambda N_j) e^{-(\lambda N_j)^\beta} - (\lambda N_{j-1})^\beta \log(\lambda N_{j-1}) e^{-(\lambda N_{j-1})^\beta}}{e^{-(\lambda N_{j-1})^\beta} - e^{-(\lambda N_j)^\beta}} \\ - n_l \ln(\beta N_k) \cdot (\lambda N_k)^\beta \\ = 0. \quad (14)$$

Equations (13) and (14) can be solved using the Newton method, which can solve the nonlinear system equations by the iteration method [20].

For the given equations,

$$F(x) = 0, \\ F(x) = (f_1, f_2, \dots, f_n)^T. \quad (15)$$

Truncating the Taylor expansion of  $f_i$  at  $x_0$  after the linear terms gives

$$f_i(x^0) + \sum_{j=1}^n \frac{\partial f_i}{\partial x_j}(x^0) \cdot (x_j - x_j^0). \quad (16)$$

The Newton method for the solution of a system of equations is

$$x^{i+1} = x^i - J_i^{-1} F(x_i), \quad (17)$$

where  $J_i$  is the Jacobi matrix of  $f$  at  $x^i$ , as shown in the following expression:

$$J_i = F'(x^i) \\ = \begin{bmatrix} \frac{\partial f_1}{\partial x_1^i} & \frac{\partial f_1}{\partial x_2^i} & \dots & \frac{\partial f_1}{\partial x_n^i} \\ \frac{\partial f_2}{\partial x_1^i} & \frac{\partial f_2}{\partial x_2^i} & \dots & \frac{\partial f_2}{\partial x_n^i} \\ \vdots & \vdots & \vdots & \vdots \\ \frac{\partial f_n}{\partial x_1^i} & \frac{\partial f_n}{\partial x_2^i} & \dots & \frac{\partial f_n}{\partial x_n^i} \end{bmatrix}. \quad (18)$$

**2.3. Estimation of Initial Values.** To ensure the convergence of the iterative methods and make it converge fast, an initial value must be estimated before the application of the Newton method.

Similar to Qian and Correa [21], assuming that the subjects that lost to the follow-up process (just as panels with punchout occurs) live up to at least halfway of the period. It was assumed that all the punchout occurred at the mid for each interval, say  $N'_j$ :

$$\begin{aligned} S(N'_j) &= e^{-(\lambda N'_j)^\beta}, \\ N'_j &= \frac{(N_{j-1} + N_j)}{2}. \end{aligned} \quad (19)$$

Taking natural logarithm of equation (19), we obtain

$$\left. \begin{aligned} \ln S(N'_j) &= -(\lambda N'_j)^\beta \\ \ln[-\ln S(N'_j)] &= \beta \ln \lambda + \beta \ln N'_j \end{aligned} \right\} \quad (20)$$

Make  $y = \ln[-\ln S(N'_j)]$  and  $x = \ln N'_j$ ; then, equation (20) can be linearized as follows into the  $y = mx + b$  format. Least square regression was employed to estimate the intercept  $b$  and the slope  $m$ , and we get an estimation of the initial values  $\beta_0$  and  $\lambda_0$ :

$$\begin{aligned} \beta_0 &= m, \\ \lambda_0 &= \exp\left(\frac{b}{m}\right). \end{aligned} \quad (21)$$

**2.4. Determination of ESALs.** The life of a CRCP panel is quantified as the total number of 80 kN ESALs in the design lane that leads to the formulation of punchout. The distressed-based equivalent single axle load ( $N_e$ ) can be obtained by the methodology proposed by Chen and Zollinger [22].

### 3. Validation with LTPP Data

**3.1. Summary Information of GPS-5 Test Sections.** There are 85 test sections in the General Pavement Studies GPS-5 for

CRCP performance research, located in 29 states across United States of America. The collection of LTPP data has been under way since 1989 [23]. Two test sections were selected to illustrate the effectiveness of the approach introduced, as shown in Table 1. One section is from South Carolina and the other from Texas.

The number of ESALs of the two sites was determined according to the procedure proposed by Chen et al. [22] and the information in detail is shown in Table 2. Notably, continuously investigations were carried out for both the sections since 1990s to 2000s, and the number of punchouts was increasing in an almost consecutive manner during the period. Unfortunately, investigation data, since the latest investigation, which were not updated, are found and are listed in Table 2.

**3.2. Number of Panels in Each Section.** About 90% of punchouts were observed on PCC panels between a pair of transverse cracks with crack spacing between 0.3 and 0.9 m [24]; in addition, punchout was defined as the area enclosed by two closely spaced (usually <0.9 m) transverse cracks, a short longitudinal crack, and the edge of the pavement or a longitudinal joint. And, "Y" cracks that exhibit spalling, breakup, or faulting are also included [25]. Furthermore, an advanced model of punchout prediction was proposed by Jung and Zollinger [18], and the number of punchout can be determined by equation (22):

$$N_{PO} = NC_{cs < 0.9m} \times P_e \times P_{fc}, \quad (22)$$

where  $N_{PO}$  is the number of punchout,  $NC_{cs < 0.9m}$  is the number of cracks with crack spacing less than 0.9 m,  $P_e$  is probability of erosion, and  $P_{fc}$  is probability of fatigue cracking.

Consequently, the number of PCC panels between two transverse cracks spaced less than 0.9 m was taken as the total number of samples that placed in the life test, and the distribution of the transverse crack spacing was found to be possibly following the Weibull distribution. Therefore, the probability of the transverse crack spacing between LU and LL can be determined by the following expression [24]:

$$\text{Prob}(L_U \geq L \geq L_L) = 100 \left\{ \exp\left[-\left(\frac{L_L - L_{\min}}{\alpha}\right)^\gamma\right] - \exp\left[-\left(\frac{L_U - L_{\min}}{\alpha}\right)^\gamma\right] \right\}. \quad (23)$$

And, the probability of crack spacing less than 0.9 m can be determined by

$$\text{Prob}(L_U \geq L) = 100 \left\{ 1 - \exp\left[-\left(\frac{L_U - L_{\min}}{\alpha}\right)^\gamma\right] \right\}. \quad (24)$$

where  $\text{Prob}(L_U \geq L \geq L_L)$  is probability of crack spacing between  $L_U$  and  $L_L$  (%),  $L_U$  is the upper limit of the cracking interval (m),  $L_L$  is the lower limit of the cracking interval

(m), and  $L_{\min}$  is minimum length of crack spacing (m); this value is set to be 0.2 m according to field investigation of transverse cracking pattern.

Here,  $\alpha$  and  $\gamma$  are the scale and shape parameters of the crack spacing distribution, respectively. And, the parameters presented by Selezneva et al. [24] were employed in this paper to determine the number of CRCP panels with the crack spacing less than 0.9 m (Table 3).



TABLE 1: Summary information on LTPP data.

State	SHRP_ID	Date open to traffic	Annual daily truck traffic at beginning year	Mean crack spacing (m)	Steel content (%)	PCC thickness (mm)	Base type
South Carolina	45_5035	10/1/1975	257	0.75	0.63	203	Cement-treated subgrade soil
Texas	48_5323	9/1/1980	768	0.71	0.61	229	HMA and lime-treated soil

TABLE 2: Pavement performance monitoring in LTPP.

State and ID	Investigation date	Number of punchouts	ESALs
45_5035	3/17/1992	21	8.42 E+06
	6/8/1993	28	9.00 E+06
	6/25/1997	30	1.05 E+07
	2/10/1999	39	1.16 E+07
	2/27/2002	58	1.35 E+07
	2/4/2003	75	1.40 E+07
48_5323	6/11/1991	17	5.44 E+06
	5/19/1993	22	6.44 E+06
	8/10/1995	23	7.44 E+06
	5/14/1997	39	8.44 E+06
	6/16/1999	71	9.45 E+06
	6/25/2002	55	1.10 E+07

TABLE 3: number of panels with the length less than 0.9 m

Section no.	Count	$\alpha$	$\gamma$	$N(L_{0.9} \geq L)$
45_5035	199	25.887	1.165	143
48_5323	210	22.860	1.812	176

TABLE 4: Estimation of the shape and scale parameters.

Section no.	Initial value		Solutions		Number of iterations
	$\lambda_0$	$\beta_0$	$\lambda$	$\beta$	
45_5035	0.0434	1.3067	0.0560	1.3193	3
48_5323	0.0326	1.0956	0.0690	1.1868	4

## 4. Result and Discussion

A numerical program in accordance with the methodology in section 2 was written to estimate the values of  $\lambda$  and  $\beta$ . It can be seen from Table 4 that the Newton iteration converged to the root of equations very quickly, and the number of iterations is only 3 to 4.

**4.1. The Estimation of the Threshold Value of  $N_e$  for Punchout Occurrence.** The threshold value of  $N_e$  is the equivalent traffic loads under which the probability of the occurrence of punchout is zero; then, the function can be expressed as follows:

$$\begin{aligned} F(N_e) &= 0, & N_e \leq N_{e0}, \\ F(N_e) &= 1 - e^{-[\lambda(N_e - N_{e0})]^\beta}, & N_e > N_{e0}. \end{aligned} \quad (25)$$

With the values of  $\lambda$   $\beta$  in Table 4, it is advantageous to estimate the value of  $N_{e0}$  by the iteration method to find the minimum standard deviation of the predicted number of punchout. The standard deviation of the predicted results under a series of  $N_{e0}'$  can be determined by equations (26) and (27):

$$\sigma = \sqrt{\sum_{i=1}^N \frac{(\text{POU}_{oi} - \text{POU}_{pi})^2}{N}}, \quad (26)$$

$$\text{POU}_{pi} = N C_{cs < 0.9m} \times \left(1 - e^{-[\lambda(N_e - N_{e0}')^\beta]}\right). \quad (27)$$

where  $\sigma$  is standard deviation,  $N$  is the number of pavement performance investigation,  $\text{POU}_{oi}$  is the number of punchouts recorded at the investigation  $i$ ,  $\text{POU}_{pi}$  is the predicted number of punchouts for investigation  $i$ , and  $N_{e0}'$  is the assigned value of  $N_{e0}$  in the iteration.

The value of  $N_{e0}$  should be in the range of  $[0, N_{e1})$ , where  $N_{e1}$  is the equivalent traffic loads when the 1<sup>st</sup> investigation with punchouts is conducted. Substitute a series of  $N_{e0}'$  into (28) to calculate  $\sigma$  for each ease of  $N_{e0}'$ , as shown in Figures 1 and 2.

**4.2. Hazard Function.** The shape parameters  $\beta$  of both the test sections are greater than 1, which indicates that the hazard rate of occurrence of punchout will increase with the accumulation of ESALs (Figures 3 and 4). In practice, the probability of fatigue cracking as well as that of base erosion with the time elapsing is increasing. The potential of punchout occurrence will increase as a result of the deterioration of the pavement structure. Theoretically, the estimation of the characteristic assuming Weibull distribution agrees well with the engineering practice. The punchout of CRCP is expressed as the product of probability of base erosion and the probability of fatigue cracking, as shown in equation (22). Interestingly, the base types of Section 45-5035 and Section 48-5323 are cement-treated base (CTB) and hot mix asphalt (HMA), respectively. Comparing

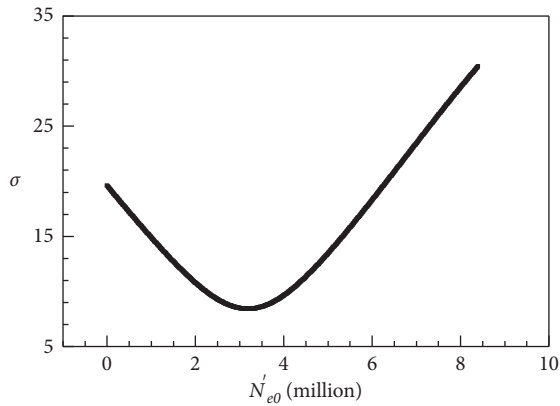


FIGURE 1: Determination of  $N_{e0}$  for 45\_5035.

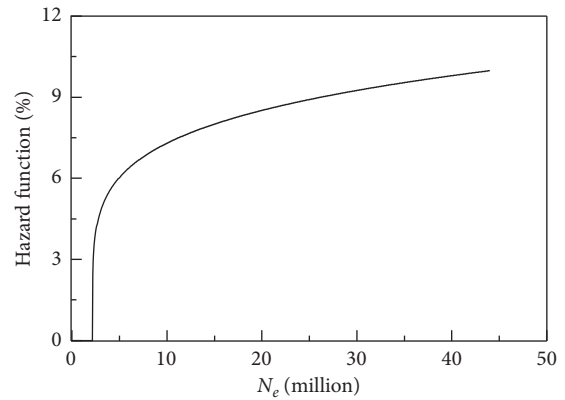


FIGURE 4: Hazard function for site 48\_5323.

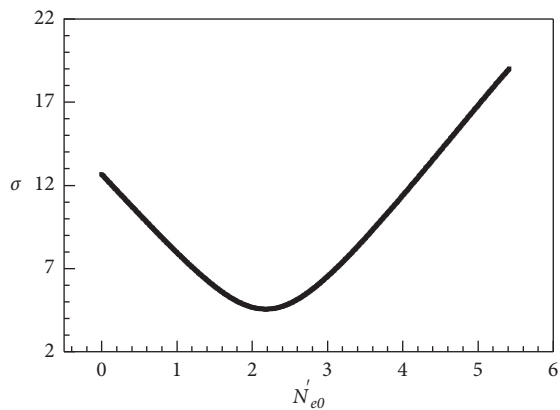


FIGURE 2: Determination of  $N_{e0}$  for 48\_5323.

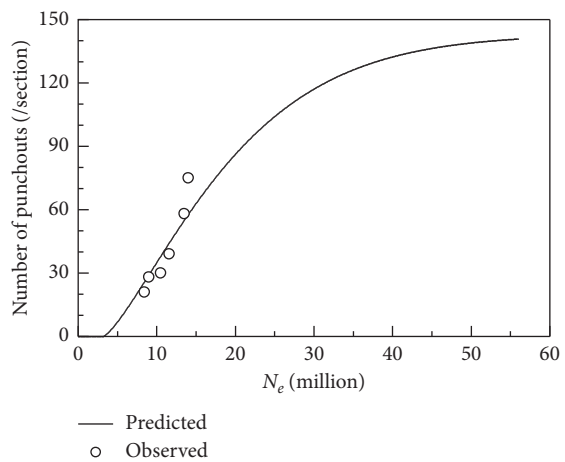


FIGURE 5: Prediction with Weibull fitting for site 45\_5035.

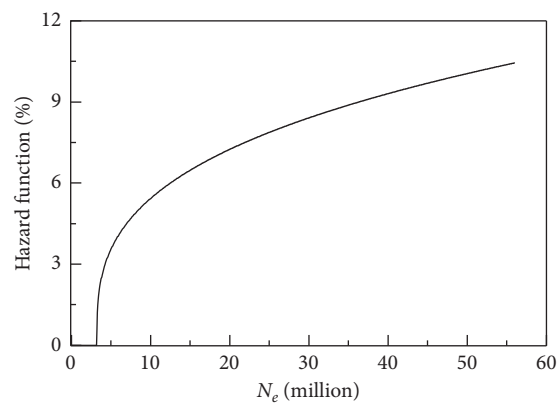


FIGURE 3: Hazard function for site 45\_5035.

Figures 3 and 4, it obviously shows that the hazard rate of CRCP with CTB base increases much more rapidly than that supported by asphalt treated base (ATB) when  $N_e$  is less than 10 million. Thus, from the hazard rate prediction, the type of base has presumably decisive influence on the formulation of punchout. Actually, ATB exhibits much better resistance of erosion than CTB [26, 27].

**4.3. Distribution Function.** The most concerned application of the pavement performance is the perdition of the level of distress, for instance, number of punchouts for CRCP. The prediction result will help the highway agencies in the decision-making processes related to the maintenance and rehabilitation. In Texas, USA, four levels of treatment are required: (1) preventive maintenance, (2) light rehabilitation, (3) medium rehabilitation, and (4) heavy rehabilitation or reconstruction [28]. The highway agencies may set a limit of number of punchout per unit length, for instance, 10 punchouts/km, at which a preventive pavement maintenance needs to be performed.

As the scale and shape parameters have been determined, it is possible to predict the number of punchouts at a specific traffic level  $N_j$ :

$$N_{PO} = N_{C_{cs < 0.9m}} \cdot \left[ 1 - \exp\left(-(\lambda \cdot N_j)^\beta\right) \right], \quad (28)$$

where  $N_{PO}$  is the number of punchout at a specific traffic level  $N_j$ ;

As it is shown in Figures 5 and 6, the predicted number of punchouts matches very well with the values from field investigations, and the proposed approach provides a reliable pavement performance-forecasting model.

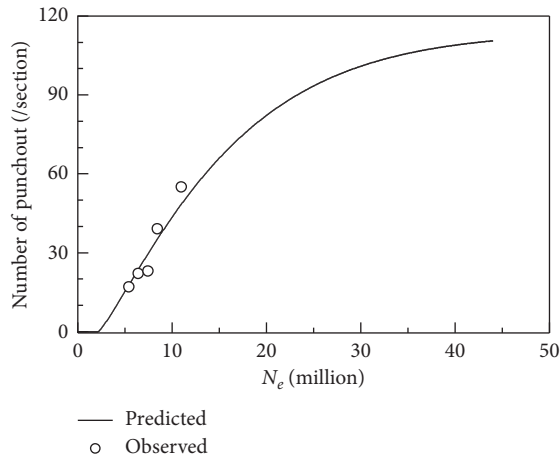


FIGURE 6: Prediction with Weibull fitting for site 48\_5323.

**4.4. Discussion.** The number and accuracy of the LTPP observation datasets play a key role on the reliability and validity of pavements' survival analysis. Unfortunately, the punchouts of CRCP has not been continuously monitored since latest investigation in 2000s for the two sections. Extensive research need to be conducted when some new datasets can be obtained.

## 5. Conclusions

In this study, an advanced calibration model for punchout distress in CRCP was proposed. Considering that LTPP database only records the number of punchouts occurred in each interval, which was recognized as grouped data, the number of ESALs was assumed to follow Weibull distribution. The maximum likelihood estimation was proposed to determine the parameters in Weibull distribution. The proposed calibration model was validated with the data from two test sections in LTPP database. The following conclusions can be drawn:

- (i) The number of ESALs that leads to punchout distress is found to follow the Weibull distribution
- (ii) The maximum likelihood estimation is effective in determining the parameters of the Weibull distribution
- (iii) The proposed calibration model is capable of describing the punchout and can be employed to predict the failure rate and reliability of CRCP in the pavement design and arrangement of rehabilitation activities

## Data Availability

Some or all data, models, or code generated or used during the study are available from the corresponding author by reasonable request.

## Conflicts of Interest

The authors declare that they have no conflicts of interest.

## Acknowledgments

The authors appreciate the generous help and constructive ideas from Dr. Dan G. Zollinger in Texas A&M University. This research was funded by Science and Technology Innovation Program of the Department of Transportation, Yunnan Province, (Grant no. [2020]15-1), Yunnan Fundamental Research Projects (Grant no. 2019FD004), and Applied Basic Research Foundation of Yunnan Province (Grant no. 2016FB099)

## References

- [1] J. A. Prozzi and S. M. Madanat, "Using duration models to analyze experimental pavement failure data," *Transportation Research Record: Journal of the Transportation Research Board*, vol. 1699, no. 1, pp. 87-94, 2000.
- [2] H. L. V. Quintus, M. I. Darter, and J. Mallela, *Local Calibration Guide for the Recommended Guide for Mechanistic-Empirical Design of New and Rehabilitated Pavement Structures*, Applied Research Associates, Inc.: Roud Rock, Texas, USA, 2003.
- [3] C. Rao, O. Selezneva, M. I. Darter, L. T. Glover, and L. Khazanovich, "Calibration of mechanistic-empirical performance model for continuously reinforced concrete pavement punch-outs," *Transportation Research Record: Journal of the Transportation Research Board*, vol. 1896, no. 1, pp. 15-22, 2004.
- [4] Y. J. Jiang and M. I. Darter, "Factors affecting rigid pavement performance: evaluation of the LTPP SPS-2 experiment," in *Proceedings of Geotechnical Engineering for Transportation Projects*, pp. 1050-1057, CA, USA, July 2004.
- [5] J. J. Hajek and T. J. Kazmierowski, "Use of long-term pavement performance data for calibration of pavement design models," *Transportation Research Record: Journal of the Transportation Research Board*, vol. 1778, no. 1, pp. 149-155, 2001.
- [6] A. Banerjee, J. P. M. Aguiar, and J. A. Prozzi, "Calibration of mechanistic-empirical pavement design guide permanent deformation models," *Transportation Research Record: Journal of the Transportation Research Board*, vol. 2094, no. 1, pp. 12-20, 2009.
- [7] Y. Wang, K. C. Mahboub, and D. E. Hancher, "Survival analysis of fatigue cracking for flexible pavements based on long-term pavement performance data," *Journal of Transportation Engineering*, vol. 131, no. 8, pp. 608-616, 2005.
- [8] Q. Dong and B. Huang, "Failure probability of resurfaced preventive maintenance treatments," *Transportation Research Record: Journal of the Transportation Research Board*, vol. 2481, no. 1, pp. 65-74, 2015.
- [9] Q. Dong, B. Huang, and S. Richards, "Evaluation of influence factors on crack initiation of LTPP resurfaced-asphalt pavements using parametric survival analysis," *Journal of Performance of Constructed Facilities*, vol. 28, no. 2, pp. 412-421, 2014.
- [10] J. A. Prozzi and S. M. Madanat, "Using duration models to analyze experimental pavement failure data," *Transportation Research Record: Journal of the Transportation Research Board*, vol. 1699, no. 1, pp. 87-94, 2000.
- [11] W. Weibull and S. Sweden, "A statistical distribution function of wide applicability," *Journal of Applied Mechanics*, vol. 18, no. 3, pp. 293-297, 1951.

- [12] J. F. Lawless, *Statistical Models and Methods for Lifetime Data*, John Wiley & Sons, Inc, NJ, USA, 1982.
- [13] B.-W. Tsai, J. T. Harvey, and C. L. Monismith, "Application of Weibull theory in prediction of asphalt concrete fatigue performance," *Transportation Research Record: Journal of the Transportation Research Board*, vol. 1832, no. 1, pp. 121–130, 2003.
- [14] S. J. Almalki and S. Nadarajah, "Modifications of the Weibull distribution: a review," *Reliability Engineering & System Safety*, vol. 124, pp. 32–55, 2014.
- [15] D. G. Zollinger and E. J. Barenberg, *Continuously Reinforced Pavements: Punchouts And Other Distresses And Implications For Design*; FHWA/IL/UI 227, University of Illinois, Urbana, IL, 1990.
- [16] X. Shi, A. Mukhopadhyay, and D. Zollinger, "Long-term performance evaluation of concrete pavements containing recycled concrete aggregate in Oklahoma," *Transportation Research Record: Journal of the Transportation Research Board*, vol. 2673, no. 5, pp. 429–442, 2019.
- [17] I. Ara, *ERES Consultants Division. Guide For Mechanistic-Empirical Design Of New and Rehabilitated Pavement Structures*, Washington D.C., USA, 2004.
- [18] Y. S. Jung, D. G. Zollinger, and B. M. Ehsanul, "Improved mechanistic-empirical continuously reinforced concrete pavement design approach with modified punchout model," *Transportation Research Record: Journal of the Transportation Research Board*, vol. 2305, no. 1, pp. 32–42, 2012.
- [19] N. Balakrishnan and M. Kateri, "On the maximum likelihood estimation of parameters of Weibull distribution based on complete and censored data," *Statistics and Probability Letters*, vol. 78, no. 17, pp. 2971–2975, 2008.
- [20] W. Gautschi, *Numerical Analysis*, Springer, New York, NY, USA, 2nd edition, 2012.
- [21] L. Qian and J. Correa, "Estimation of Weibull parameters for grouped data with competing risks," *Journal of Statistical Computation and Simulation*, vol. 73, no. 4, pp. 261–275, 2003.
- [22] L. Chen, D. G. Zollinger, and B. Tian, "Approach to local calibration of an advanced model for punchout distress using LTPP data," *Journal of Transportation Engineering*, vol. 141, no. 8, Article ID 04015014, 2015.
- [23] S. D. Tayabji, O. Selezneva, and Y. J. Jiang, *Preliminary Evaluation Of LTPP Continuously Reinforced Concrete (CRC) Pavement Test Section*; FHWA-RD-99-086, pp. 1–3, ERES Consultants, Inc., Columbia, Maryland, 1999.
- [24] O. Selezneva, M. Darter, D. Zollinger, and S. Shoukry, "Characterization of transverse cracking spatial variability: use of long-term pavement performance data for continuously reinforced concrete pavement design," *Transportation Research Record: Journal of the Transportation Research Board*, vol. 1849, no. 1, pp. 147–155, 2003.
- [25] J. S. Miller and W. Y. Bellinger, *Distress Identification Manual For the Long-Term Pavement Performance Program*; FHWA-RD-03-031; Office of Infrastructure Research and Development, pp. 77–79, Federal Highway Administration, McLean, VA, USA, June 2003.
- [26] Y. Jung, *Advancement of Erosion Testing, Modeling, and Design of Concrete Pavement Subbase Layers*, Texas A&M University, College Station, Texas, United States, 2010.
- [27] Y. S. Jung, D. G. Zollinger, and A. J. Wimsatt, "Test method and model development of subbase erosion for concrete pavement design," *Transportation Research Record: Journal of the Transportation Research Board*, vol. 2154, no. 1, pp. 22–31, 2010.
- [28] A. M. Ioannides and P. K. Tallapragada, "An overview and A case study of pavement performance prediction," *International Journal of Pavement Engineering*, vol. 14, no. 7, pp. 629–644, 2013.

## Research Article

# The Impact of LED Colour Rendering on Reaction Time of Human Eyes in Tunnel Interior Zone

Li-Li Dong , Qi Lou , Peng Liu , and Wen-Hai Xu 

*School of Information Science and Technology, Dalian Maritime University, Dalian 116026, China*

Correspondence should be addressed to Li-Li Dong; [donglili@dlmu.edu.cn](mailto:donglili@dlmu.edu.cn)

Received 7 May 2021; Accepted 14 August 2021; Published 28 August 2021

Academic Editor: Kun An

Copyright © 2021 Li-Li Dong et al. This is an open access article distributed under the Creative Commons Attribution License, which permits unrestricted use, distribution, and reproduction in any medium, provided the original work is properly cited.

The long reaction time of human eyes will increase the probability of traffic accidents in tunnels which can be reduced by improving lighting conditions. In recent years, light-emitting diodes (LEDs) have replaced the traditional lighting source in a tunnel. Colour rendering index 2012 (CRI2012, a colour rendering evaluation index) is the most suitable evaluation method for colour rendering of LEDs. In order to study the impact of colour rendering of LEDs on the reaction time of human eyes, a driving simulation environment was designed. First, three CCTs (correlated colour temperatures), four CRI2012s, and eight colours of targets were assessed using mesopic photometry model MES-2. The calculation results indicated that the contrast of targets had a positive correlation with CRI2012 and had a negative correlation with CCT. Then, reaction time experiment was conducted in simulated tunnel environments. There are 30 observers who participated. The results show that the LEDs with higher CRI2012 and lower CCT in tunnel is conducive to reducing the reaction time of human eyes. High CRI2012 enables drivers to accurately and quickly identify colours. This paper provides a reference for the design of light source parameters, roads, walls, and warning signs in the tunnel.

## 1. Introduction

The chance of traffic accidents at the tunnel interior zone is less than open roads [1]; because of the special structure of the tunnel, the accidents will be more serious than the open road such as large number of casualties and property losses [2, 3]. So, it is significant to analyse the causes of accidents, improve the traffic conditions, and reduce the probability of accidents in the tunnel interior zone.

Traffic accidents in the tunnel interior zone include rear-end collision and collision wall [1]. The main reason for traffic accidents in the tunnel is that the driver has a longer reaction time to the vehicle or wall [4]. Reaction time is the time required from seeing the target unclearly to clearly [2]. The possibility of traffic accidents in the tunnel is positively correlated with the reaction time [5]; the longer reaction time will lead to further braking distance, so it is more likely to cause traffic accidents [6–8]. If the reaction time can be shortened, the safety of driving in a tunnel can be improved. Reaction time is mainly affected by tunnel lighting environment [2]. For a long time, CCT and colour rendering of

lighting sources at tunnels are fixed by the limitation of lighting lamps. So, the setting of tunnel lighting is only based on the luminance in China [9, 10].

Recently, the LEDs are replacing the traditional light source in the tunnel [11–14] because characteristics of high luminous efficiency and long life of LEDs [15, 16]. Consider the influence of the colour rendering and CCT of the LEDs on driving in the tunnel because the colour rendering and the CCT of the LED are not fixed.

Compared with colour rendering, CCT on tunnel driving safety-related research is relatively comprehensive [17–20]. In 2007 [21], Yamamoto et al. conducted experiments in a tunnel using high-frequency fluorescent lamps and low-pressure sodium lamps. The experimental results show that the use of light source of high colour rendering can more accurately show the colour of the equipment and the car ahead in the tunnel. In 2016 [22], Deng et al. used two light sources with different colour rendering properties to observe small targets in tunnels. They found that the better the colour rendering of tunnel light sources is, the stronger the driver's recognition ability of obstacles is, which is more conducive



to driving safety and lighting energy saving. In 2017 [23], Zhang et al. used 15 lighting combinations with a different luminance and CCT in the tunnel. Experiments show that the appropriate combination of CCT and colour rendering of LED can improve the lighting efficiency of the light source in the tunnel and show better visual performance.

Although there are few studies on the application of colour rendering in tunnel lighting, more in indoor scenarios [24–28], the LEDs with high colour rendering are positive for indoor lighting. However, the results of these studies are basically based on the subjective feelings of the observer, and the impact of CCT on vision is not considered. Most of the experimental objectives are set to single colour; in real tunnels, the colour of targets cannot be single. The luminance in the tunnel is in mesopic vision luminance. In this luminance range, the human eye can perceive the colour of the object [29].

According to the aforementioned studies, the colour rendering has a significant impact on human eyes, but few studies have linked colour rendering to tunnel traffic safety. Therefore, this paper studies the impact of LED colour rendering on the safety of the tunnel interior zone and mainly the impact of different colour rendering of LEDs on reaction time of human eyes, considering the impact of different colours of target and CCTs on the reaction time. The research results will provide some suggestions for the formulation of tunnel lighting rules.

## 2. The Evaluation Method for Colour Rendering of LED

Colour rendering is generally expressed by CRI in the range of 0–100, and the CRI of sunlight is 100 [30]. CRI has some problems in evaluating LEDs. So, two new evaluation methods appear, Colour Quality Scale (CQS) and CRI2012 (based on CRI) [31, 32]. Therefore, in order to study the impact of LED colour rendering on reaction time of human eyes, firstly, a most suitable evaluation index to evaluate the colour rendering of the LED needs to be selected.

In 2005, Yoshi and Wendy, scholars of the National Institute of Standards and Technology (NIST), presented a new objective evaluation method CQS. CQS uses the CAT02 chromatic adaptation formula to improve the accuracy of the chromatic adaptation formula and replaces the mean value with the root mean square error to improve the statistical rationality. Comparing with CRI, CQS is more exact in evaluating the colour rendering of LEDs. However, Nicola Pousset et al. [33] validated the colour preference degree of the CQS and found that the true colour quality of the LEDs differed greatly from the CQS value. CQS could not accurately represent the colour quality of the light source.

Based on the previous problems in colour rendering evaluation, CIE established TCI-90 technical committee, which proposed CRI2012. The improvement of the CRI2012 evaluation system includes use of CAM02-UCS colour space and CAT02 chromatic adaptation formula, use of new 17 colour samples H17 with uniform spectral distribution, which can help to correctly evaluate the colour rendering of spectral discontinuous light sources, and use of new calculation formulas to enhance the influence of extreme values

of special colour rendering index on general colour rendering index. These improvements make CRI2012's evaluation of the colour rendering of LEDs more consistent with the results of visual experiments.

Therefore, CRI2012 will be more suitable for the evaluation of colour rendering of LED. Therefore, in this paper, CRI2012 is selected as the evaluation index of colour rendering.

## 3. Impact of CRI2012 on Contrast of the Target

Driving safety is closely related to reaction time of human eyes. The reaction time is directly affected by the contrast of the target. The higher the contrast, the shorter the reaction time [34–36]. In order to study the influence of CRI2012 on driving safety in the tunnel, it is necessary to study the effect of CRI2012 on the contrast of targets. In order to study the impact of CRI2012 on the contrast of targets, it is necessary to give the contrast calculation formula:

$$C = \left| \frac{L_t - L_b}{L_b} \right|, \quad (1)$$

where  $C$  is the contrast,  $L_t$  is the luminance of the target, and  $L_b$  is the luminance of the background. Contrast is only affected by target luminance and background luminance. Contrast represents the difference between the target luminance and the background luminance. The larger the difference is, the higher the contrast is and the better to reduce the reaction time of human eyes.

According to the research, the luminance measured by the instrument is not consistent with the actual perception luminance by the human eyes (perception luminance for short) at the mesopic vision luminance [20, 37]. So, the perceived luminance under the mesopic vision luminance needs to be calculated. The calculation method of the perceptual luminance to the targets and background ( $L_t$  and  $L_b$ ) is shown in formulas (2) and (3):

$$L_t = \int k_m V_{\text{mes}}(\lambda) L_{\text{TSPD}}(\lambda) d\lambda, \quad (2)$$

$$L_b = \int k_m V_{\text{mes}}(\lambda) L_{\text{BSPD}}(\lambda) d\lambda, \quad (3)$$

where  $k_m$  refers to maximum spectral light performance corresponding to mesopic vision luminance,  $V_{\text{mes}}(\lambda)$  is the mesopic spectral luminous efficiency function, and  $L_{\text{TSPD}}(\lambda)$  and  $L_{\text{BSPD}}(\lambda)$  refer to the spectral power distribution (SPD) of the target and the background measured by the spectral radiance meter.

3.1.  $L_{\text{TSPD}}(\lambda)$  and  $L_{\text{BSPD}}(\lambda)$ .  $L_{\text{TSPD}}(\lambda)$  and  $L_{\text{BSPD}}(\lambda)$  refer to the SPDs of the target and the background measured by the spectral radiance meter. Before measuring  $L_{\text{TSPD}}(\lambda)$  and  $L_{\text{BSPD}}(\lambda)$ , we need to set up the LED used in the experiment. Four CRI2012s and three CCTs are selected in this experiment, four CRI2012s are 55, 65, 75, and 85 and three CCTs are 2800k, 4500k, and 6400k, and there are 12 lighting conditions. The SPDs of LEDs are shown in Figure 1. Table 1 shows the comparison of theoretical and practical

parameters of the LED. In order to not only meet the tunnel lighting rules but also make the experimental conclusion more universal, we set the ambient luminance of the experiment as 1 cd/m<sup>2</sup>.

The SPD of 9 colours under 12 lighting conditions was tested, as shown in Figure 2. The background colour is similar to asphalt. All the SPDs measured by spectrophotometer Konica-Minolta CS-2000 and cs-s10w are shown in Figure 3.

3.2.  $kV_{\text{mes}}(\lambda)$ .  $kV_{\text{mes}}(\lambda)$  refers to the mesopic spectral luminous efficiency function. The luminance of tunnel lighting is 1–10 cd/m<sup>2</sup>. And, the luminance environment is 1 cd/m<sup>2</sup> in this experiment. This luminance is at the mesopic vision luminance, and we choose the MES-2 [38–42] model to calculate  $V_{\text{mes}}(\lambda)$ . The calculation of  $V_{\text{mes}}(\lambda)$  formula is as follows; then,  $k_m$  can be calculated by 5. The whole  $k_m V_{\text{mes}}(\lambda)$  calculation process is shown in Figure 4:

$$L_p = \int 683V(\lambda)L_{\text{SPD}}(\lambda)d\lambda, \quad (4)$$

$$k_m = \frac{683\text{lm} \cdot \text{W}^{-1}}{V_{\text{mes}}(\lambda_0)}, \quad (5)$$

$$V_{\text{mes}}(\lambda) = 683 \frac{m_2 V(\lambda) + (1 - m_2) V'(\lambda)}{m_2 + (1 - m_2) V'(\lambda_0)} \quad (0 \leq m_2 \leq 1), \quad (6)$$

$$m_{2,n} = 0.3334 \log L_{\text{mes},n} + 0.767 \quad (0 \leq m_{2,n} \leq 1), \quad (7)$$

$$L_{\text{mes},n} = \frac{m_{2,n-1} + (1 - m_{2,n-1})(S/P)V'(\lambda_0)}{m_{2,n-1} + (1 - m_{2,n-1})V'(\lambda_0)} L_p, \quad (8)$$

$$\frac{S}{P} = \frac{1700 \int_{380}^{730} V'(\lambda)L_{\text{SPD}}(\lambda)d\lambda}{683 \int_{380}^{730} V(\lambda)L_{\text{SPD}}(\lambda)d\lambda}. \quad (9)$$

$V_{\text{mes}}(\lambda_0 = 555\text{nm})$  is the value of  $V_{\text{mes}}(\lambda)$  when  $\lambda = 555\text{nm}$ .  $L_p$  refers to the luminance of targets and background in the photopic vision, whose units of measurement is cd/m<sup>2</sup>.  $m_2$  refers to the luminance adaptation factor.  $V(\lambda)$  refers to the value of scotopic spectral sensitivity function. Figure 5 shows  $V(\lambda)$  and  $V'(\lambda)$ ,  $V'(\lambda)$  is the curve of scotopic, and  $V(\lambda)$  is the curve of photopic.  $V'(\lambda_0) = 683/1700$ .  $L_{\text{mes},n}$  refers to the mesopic luminance.  $L_{\text{SPD}}(\lambda)$  refers to  $L_{\text{TSPD}}(\lambda)$  and  $L_{\text{BSPD}}(\lambda)$ , respectively. The value of S/P refers to scotopic to photopic luminous flux ratios of targets.

3.3.  $C$ .  $C$  is calculated by (1). The calculation process of  $C$  is shown in Figure 6.  $C$  of different colours of targets is shown in Figure 7. We assume that the probability of each colour of targets appearing in the tunnel is the same. We assume that

the probability of each colour of targets appearing in the tunnel is the same. In order to discuss the relationship between CRI2012 and contrast, Figure 8 shows the average  $C$  of eight colours which are normalized.

As shown in Figure 7,  $C$  is affected by the CRI2012 and CCT. Under a certain CCT,  $C$  and CRI2012 show a positive correlation trend in most cases. Under a certain CRI2012,  $C$  and CCT show a negative correlation trend in most cases. When the colour is considered, except for black and blue, the law between the change of CRI2012 and CCT and the change of contrast is basically the same as the above law. Some colours at high CCT do not show law. This may involve in-depth optical problems. This paper mainly discusses driving safety in the tunnel, and the complex optical problems are not considered. However, the calculation results are not completely consistent with the actual condition, and it still needs experimental verification.

## 4. Experiment

In order to test the real impact of different CRI2012s on human vision, we designed an experiment to measure the reaction time of human eyes. Three CCTs (2800K, 4500K, 6400K), four CRI2012s (55, 65, 75, 85), and eight colours were selected. 30 observers participated in the experiment.

4.1. *Experimenter*. In this experiment, there were 30 observers, 19 males, and 11 females. They are all qualified to drive cars, and Shintaro Ishihara's colour vision is normal.

4.2. *Experimental Parameters*. Three CCTs (2800k, 4500k, and 6400k), four CRI2012 (55, 65, 75, and 85), and eight targets of different colours are selected in the experiment. LED cube is used as the light source. The SPD of LED cube and ambient luminance settings are the same as in Section 3.1.

Landolt chart is selected in the experiment as the observation target, also named "C" visual chart. Eight targets of different colours, which are the same as those in Section 3.1, are selected. As shown in Figure 8, the orientation of "C" is random to prevent the subjects from remembering the object orientation and affect the experimental results. The outer diameter of the target 'C' was 20 mm. Preliminary experiments prove that 20 mm is the most suitable.

4.3. *Experimental Device*. Figure 9 shows the schematic diagram of the experimental device. The experiment was carried out in a simulated tunnel. The simulated tunnel is the same proportion as the real tunnel. The material of the inner wall is the same as that of the real tunnel. The LED cube is 1m higher than the experimental platform, and the horizontal distance between the two LED cube is 0.5 m. The horizontal distance between the blackboard and observation window is 3m. As a simulated pavement surface, the experimental platform is painted with asphalt colour similar to the asphalt pavement, to restore the internal environment of the tunnel

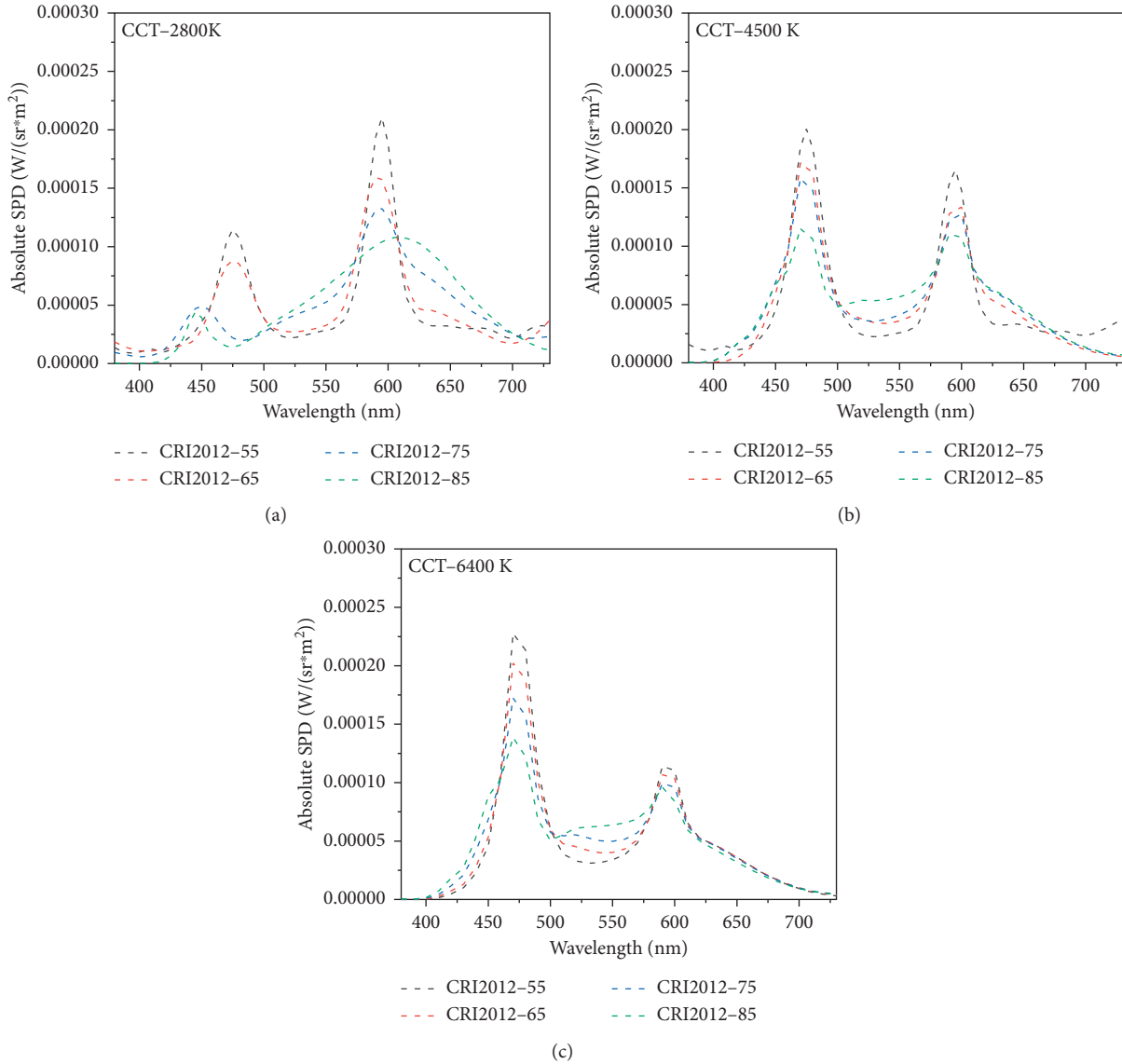


FIGURE 1: Relative SPDs of LEDs with different CRI2012s and CCTs, measured by Spectrometer I1-pro.

TABLE 1: Simulated real parameters of 12 lighting conditions in the tunnel.

Experiment parameter		Actual value	
CCT	CRI2012	CCT	CRI2012
2800K	55	2782	57
	65	2894	65
	75	2760	76
	85	2743	86
4500K	55	4485	55
	65	4653	66
	75	4518	75
	85	4536	85
6400K	55	6482	55
	65	6413	64
	75	6479	76
	85	6408	84

as much as possible. Figure 10 shows a panoramic view of the simulated tunnel.

**4.4. Procedure Specification.** Firstly, the observer held the timer and sat in front of the observation window. Before hearing the begin timing, the observer was asked not to look directly at the blackboard, but to saccade the pavement.

Secondly, the observers got orders began to search for the target on the blackboard and pressed the timer. When the observer finds the target and fully sees the direction of the "C," the timer is pressed again to stop timing, and the time obtained is the reaction time. And, the observers were asked to identify the colour of target in first experiment.

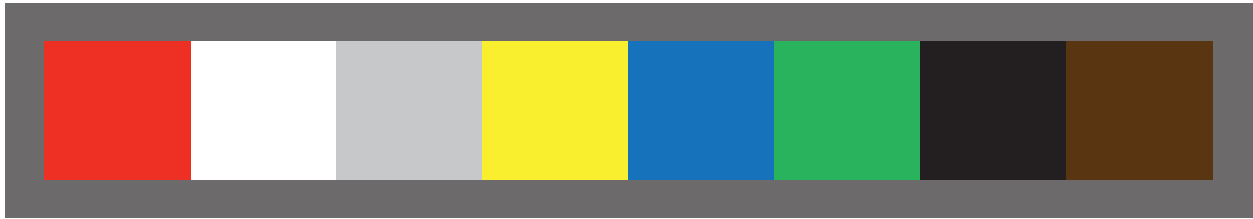
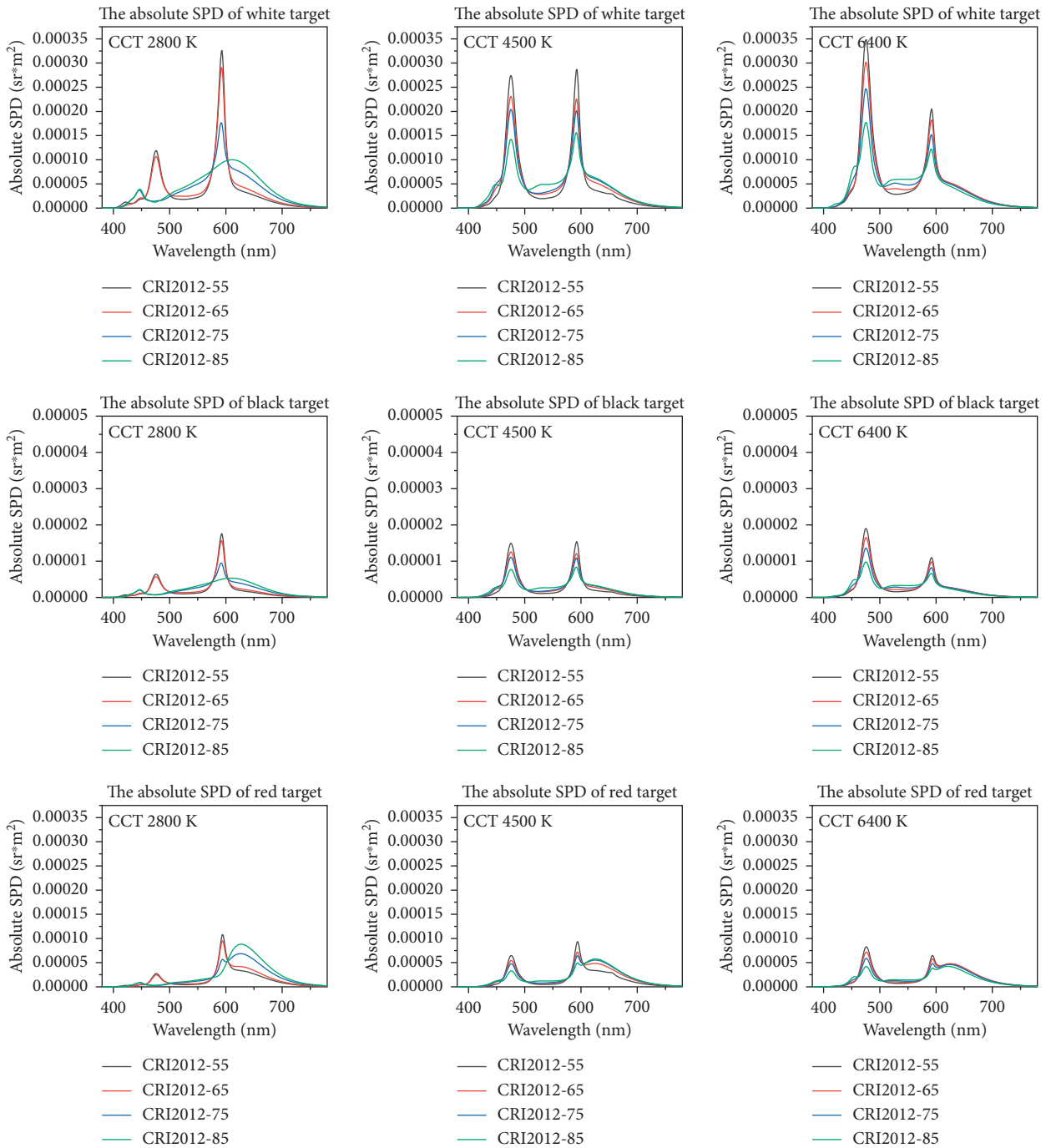
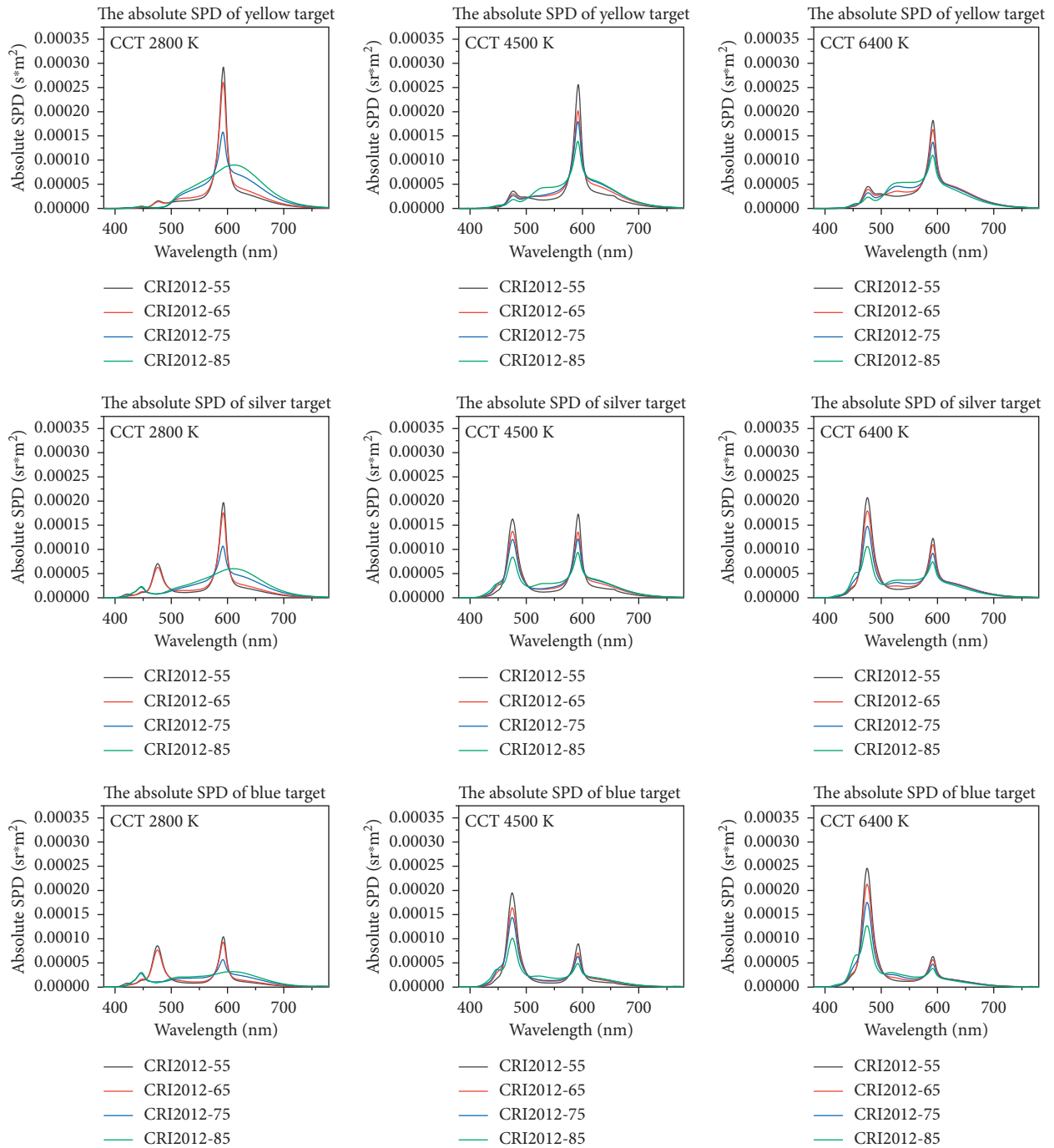


FIGURE 2: Eight colours.



(a)

FIGURE 3: Continued.



(b)

FIGURE 3: Continued.



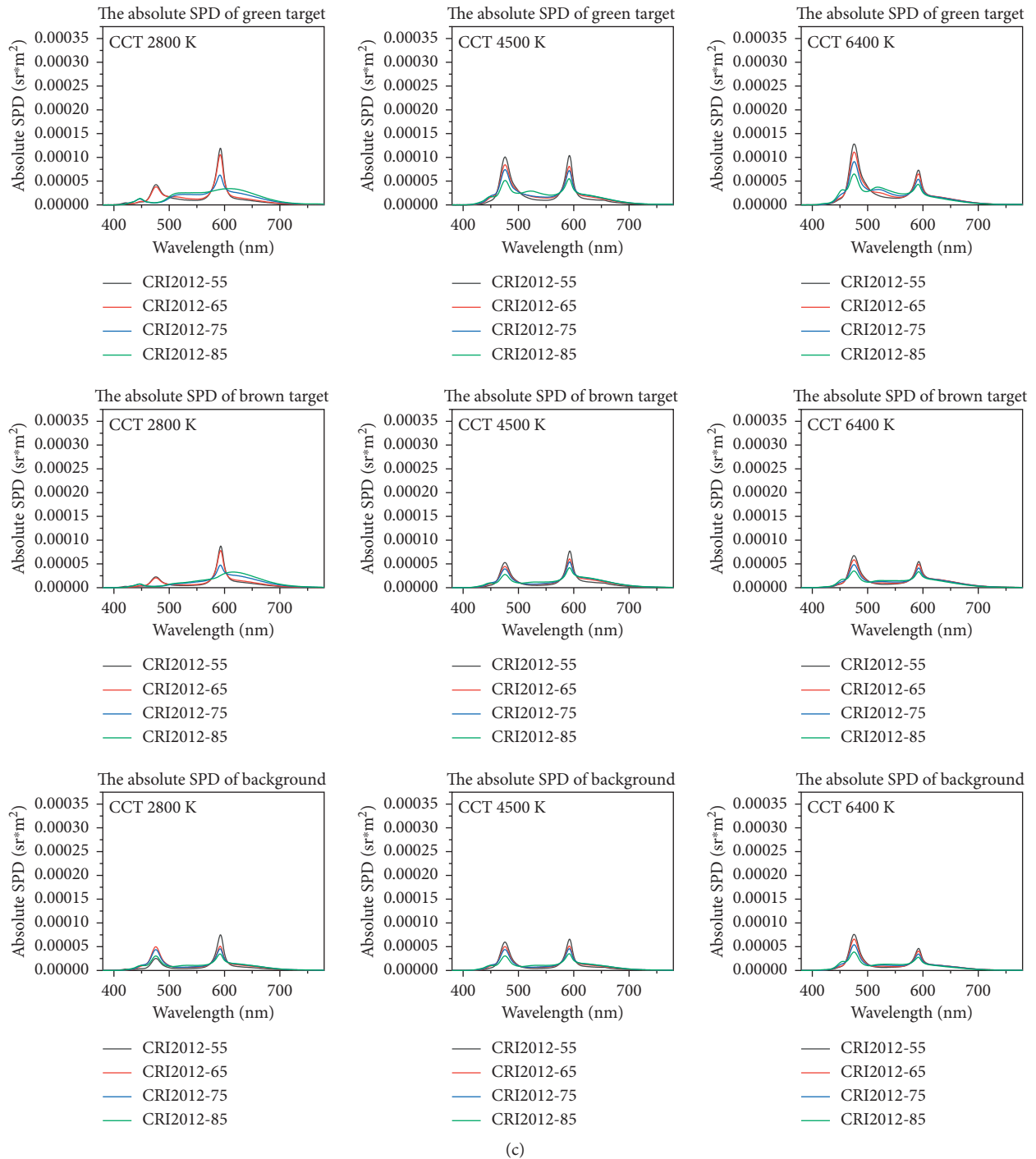


FIGURE 3: Absolute SPD of targets with different CRI2012s and CCT.

Thirdly, the experimenter changed the CCT and CRI2012 of LED cube, colour, position, and direction of the targets, and repeat the above steps again until each kind of light environment and colours have completed the experiment. Figure 9 shows the real perspective of the observers.

The colour of the indicator will carry useful information in the real tunnel, so it is fast and accurate to discriminate the colour is conducive to the driver to quickly understand

the road information. So, we designed a colour discrimination experiment based on the reaction time experiment. Considering majority of observers cannot accurately identify the colour when the CRI2012 of the LED is 55, so in the colour discrimination experiment, the CRI2012 of the LED is set to 3 CRI2012s (65, 75, and 85) and 3 CCTs (2800K, 4500K, and 6400K). The time required for the observer to discriminate colours under different CRI2012s and CCTs was measured.

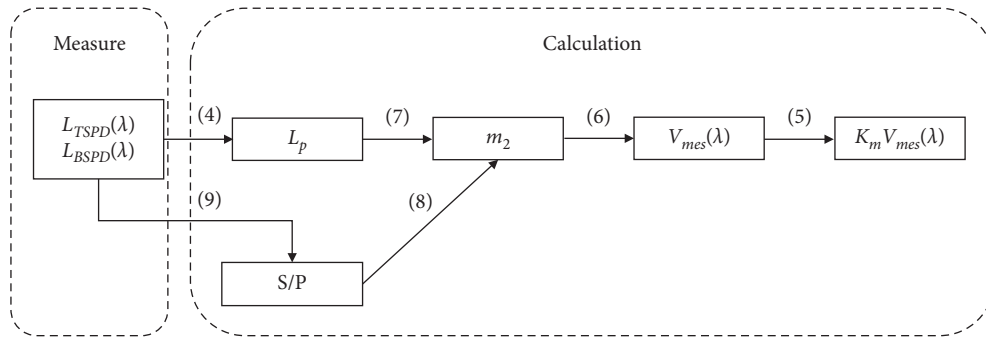


FIGURE 4: The calculation process of  $k_m V_{mes}(\lambda)$ .

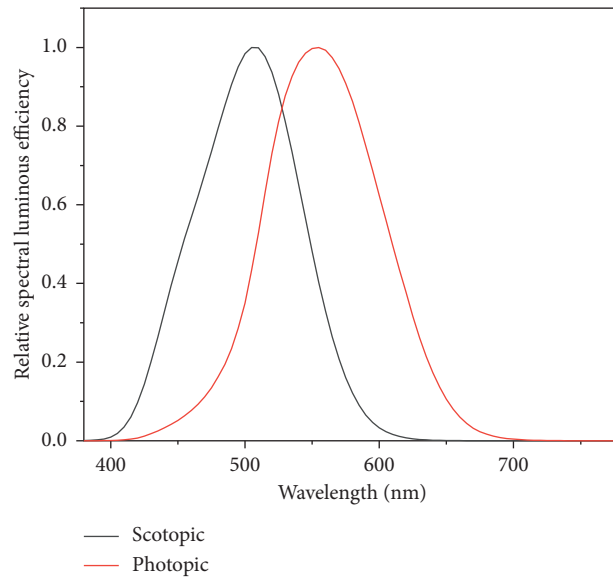


FIGURE 5: Relative spectral luminous efficiency curves of photopic and scotopic.

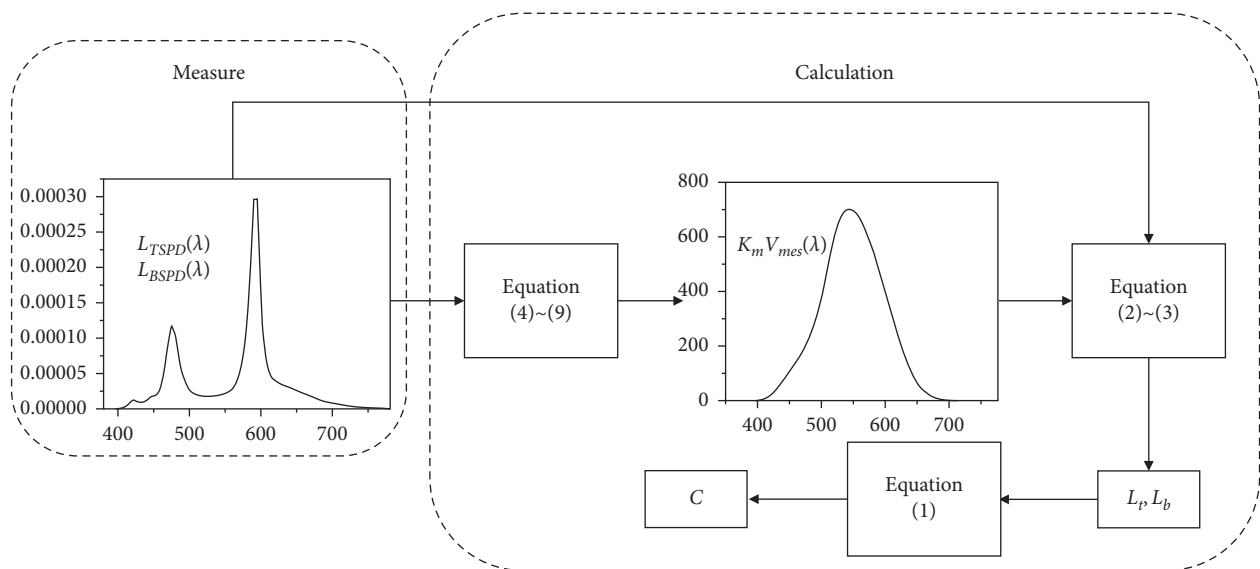


FIGURE 6: The calculation process of C.

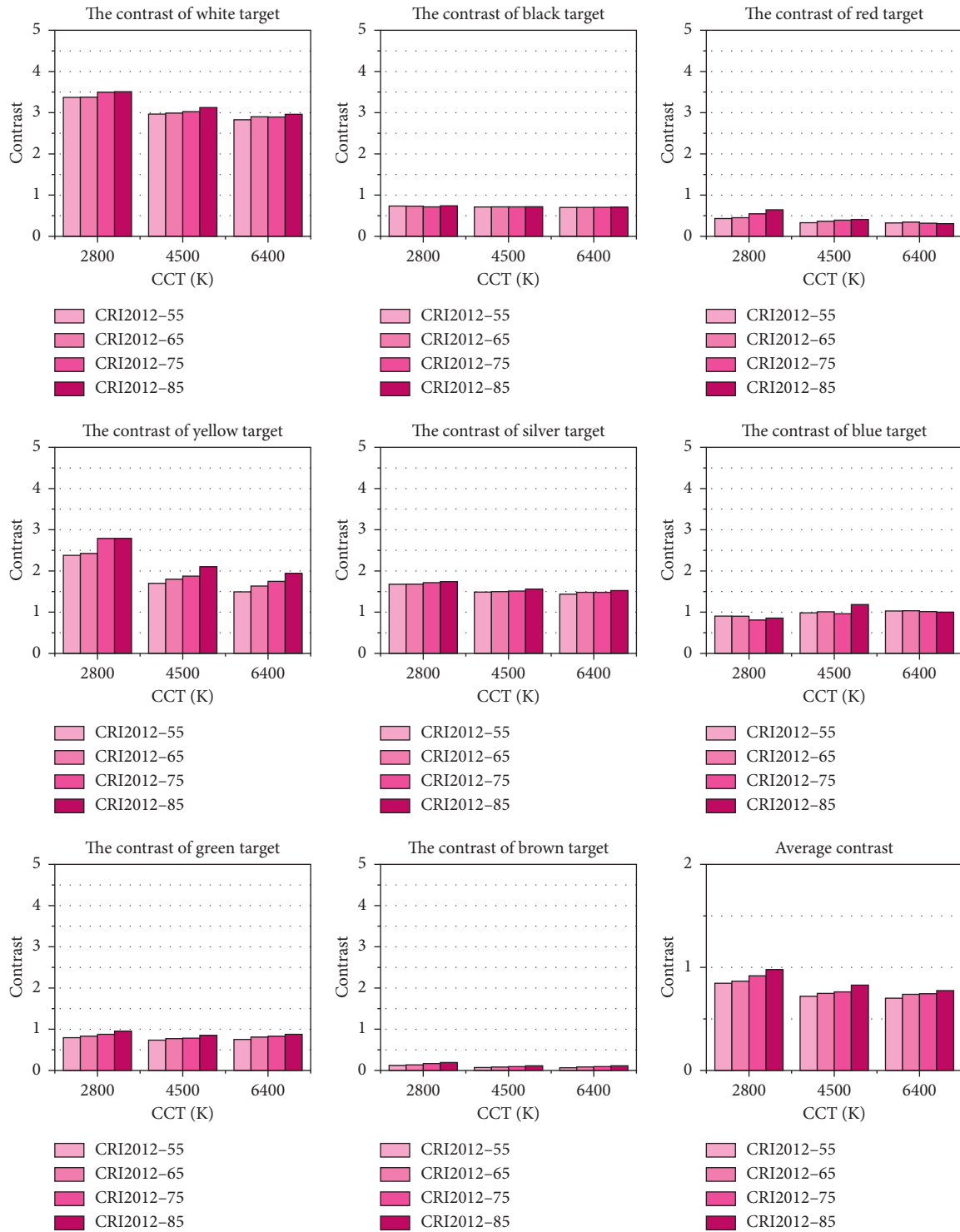


FIGURE 7: The calculation results of C.

In order to reduce the experimental error, the observers are required to perform the experiment three times to familiarize with the process, and recording of the results is not needed. After each experiment, the observer is required to rest for 3 minutes to prevent the interference of visual fatigue on the experimental results. And, the observers can also select and play music or radio during the experiment according to their usual driving habits.

4.5. *Experimental Feasibility Analysis.* Although there are some differences between the laboratory and the real tunnel environment, such as the luminance in the tunnel, the reflection spectrum of obstacles, and the distance of observing obstacles, however, this paper studies the law between CRI2012 and reaction time; the differences will not affect the intrinsic law between CRI2012 and reaction time, so the results in the laboratory will still contribute to the tunnel



FIGURE 8: Targets used in the experiment with different colours.

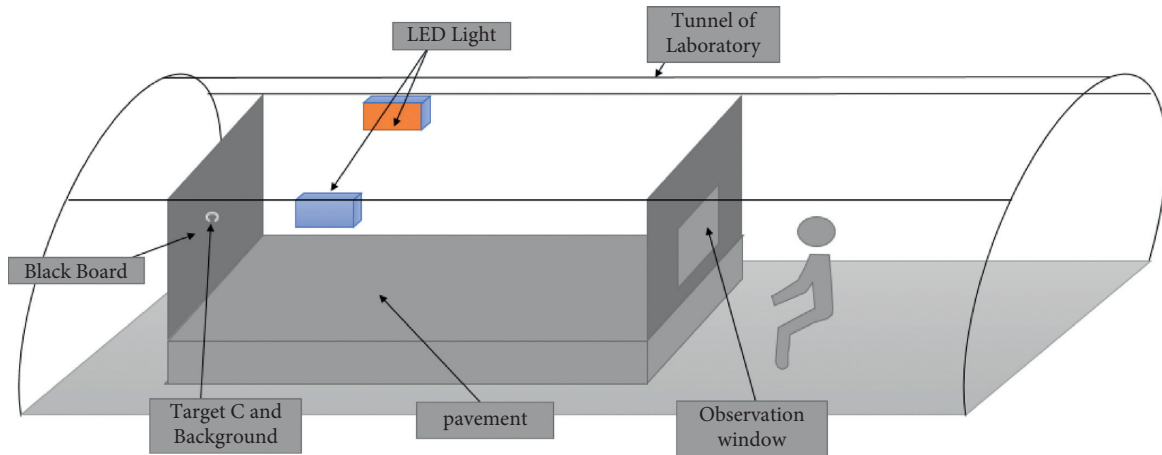


FIGURE 9: Real scene of the simulated tunnel in the laboratory.



FIGURE 10: Schematic diagram of the simulated tunnel.

lighting. In addition, changing the light conditions is easy in the laboratory, which helps to reduce the error. In a real highway tunnel, it is almost impossible to change the lighting conditions. Figure 11 shows the visual of the actual

tunnel interior zone and the visual of the observers in the experiment to illustrate the feasibility of the experiment. This method can accurately measure the reaction time of human eyes in the tunnel.

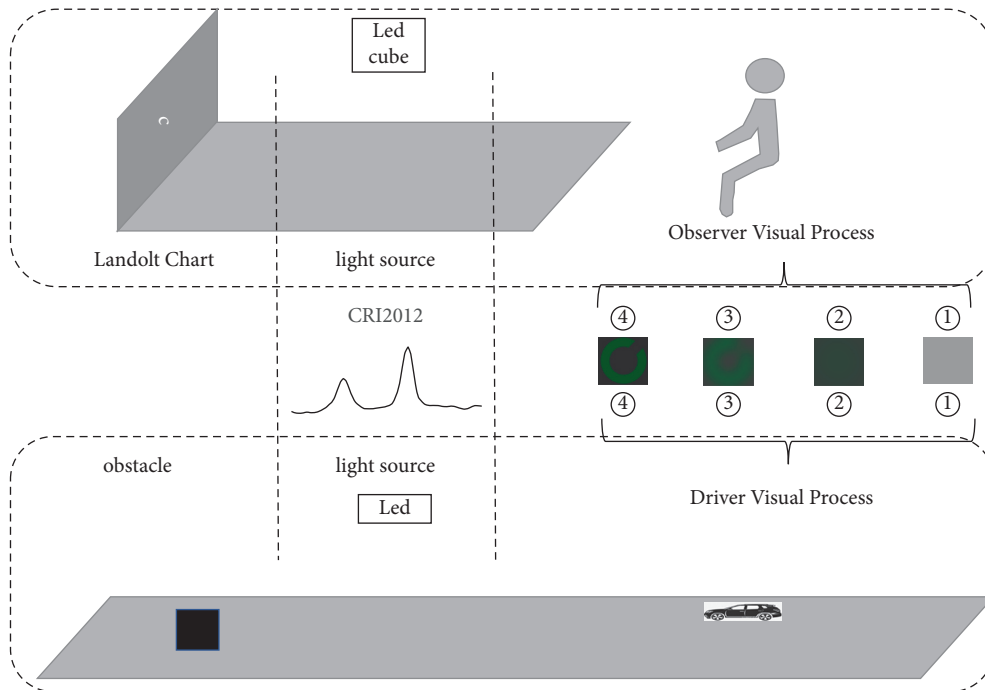


FIGURE 11: Comparison of the visual process in laboratory and visual process in real tunnels.

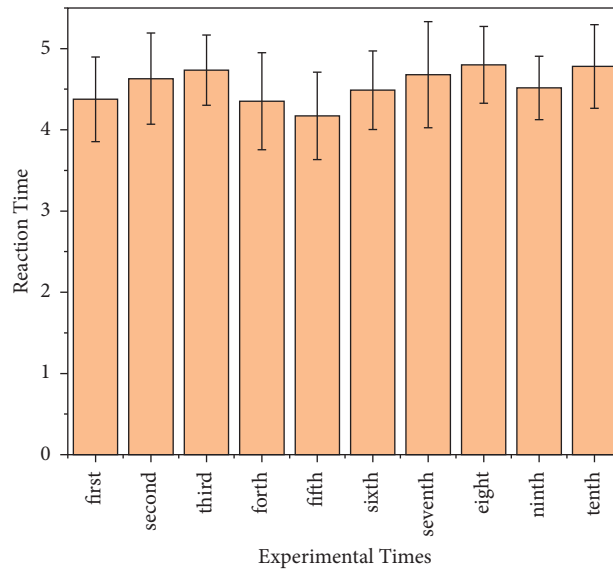


FIGURE 12: Ten repetitions' reaction time of ten observers.

### 5. Results and Discussion

To measure the error of the experiment, ten of thirty observers were asked to perform the preliminary experiment 10 times using the black target and LED cubes with CRI2012 of 75 and CCT of 4500K. The reaction time of the ten observers is shown in Figure 12. There was no correlation between the number of experiments and the reaction time.

Figures 13 and 14 show the average reaction time of all observers under different CRI2012s and CCTs. Figure 13

shows the average reaction time of observers to the eight colours of the target. The reaction time decreases with the increase of CRI2012, which agrees with the theoretical results in Section 3. In Figure 14, the experimental data of most colours showed that the reaction time decreased with the increase of CRI2012. The reaction time of yellow, white, and silver is too short due to the high contrast; therefore, the error is large. However, it is easy to see that high CRI2012 have a positive effect on shortening the reaction time.



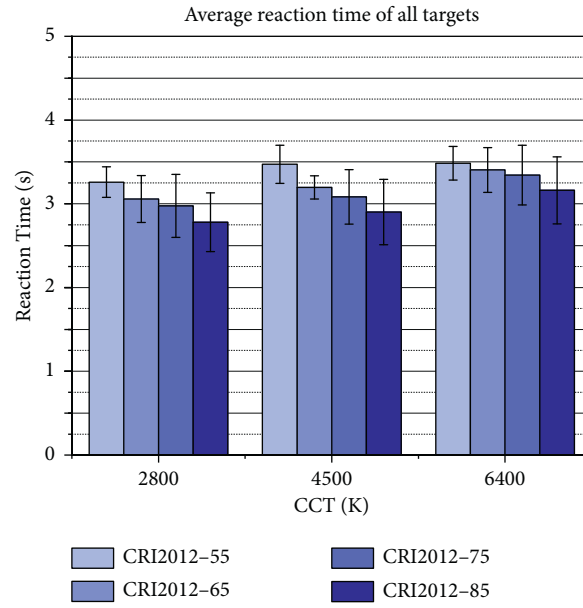


FIGURE 13: All colour's average reaction time under 12 lighting conditions.

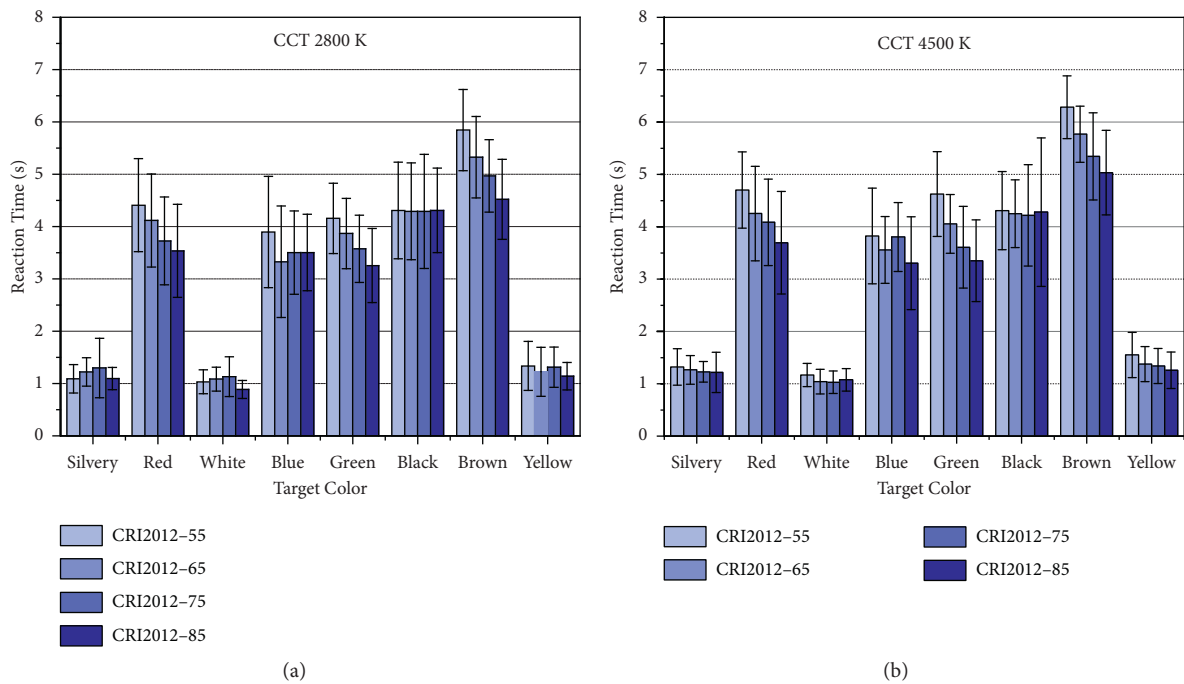


FIGURE 14: Continued.

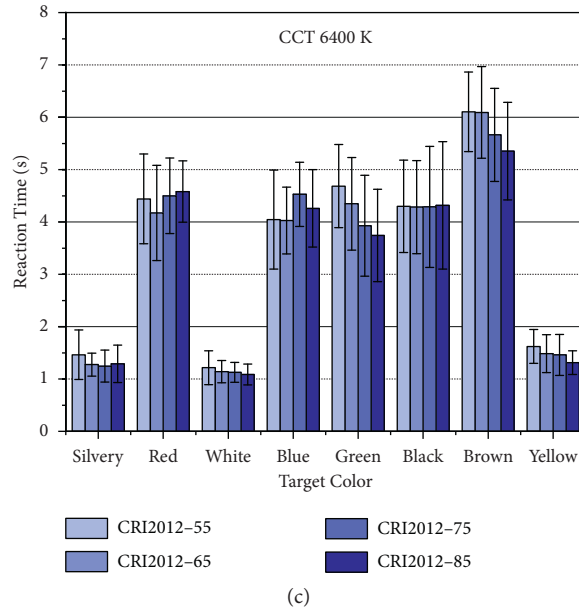


FIGURE 14: The reaction time of all observers under different CRI2012s and CCTs.

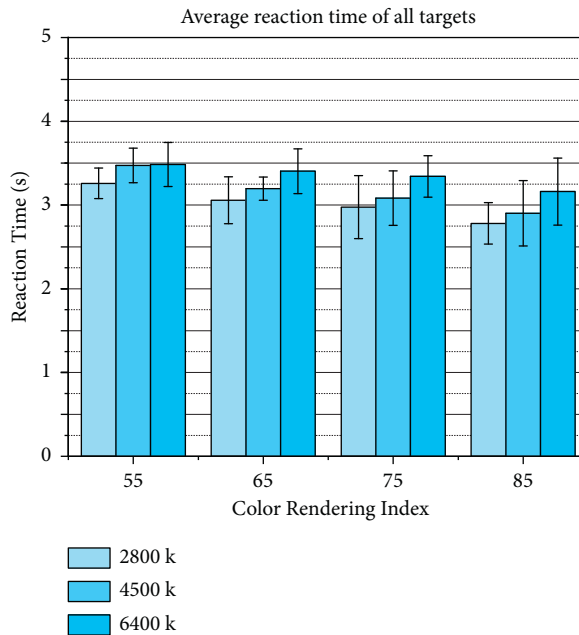


FIGURE 15: All colour’s average reaction time under 12 lighting conditions.

Although this paper mainly studies the impact of CRI2012 on reaction time, the influence of CCT on reaction time is also considered. Figures 15 and 16 show the impact of CCT on the reaction time. Figure 15 shows the average reaction time of observers to the eight colours of the target. From the calculation results of the average value shown in Figure 17, the reaction time increases with the increase of CCT. In Figure 16, the experimental data of most colours showed that the reaction time decreased with the decrease of CCT.

The diffuse reflectance will have a greater impact on the contrast resolution of the human eyes, thereby affecting the reaction speed. Figure 18 shows the SPDs of eight targets with different colours in sunlight, the SPD of the background in sunlight, and the SPD of the sunlight measured by a Konica-Minolta CS2000. The results of the experiment showed that the diffuse reflectance of white, yellow, and silver was relatively high, and the reaction time of human eyes to these three colours was the least. Although the diffuse reflectance of red is higher than that of blue and

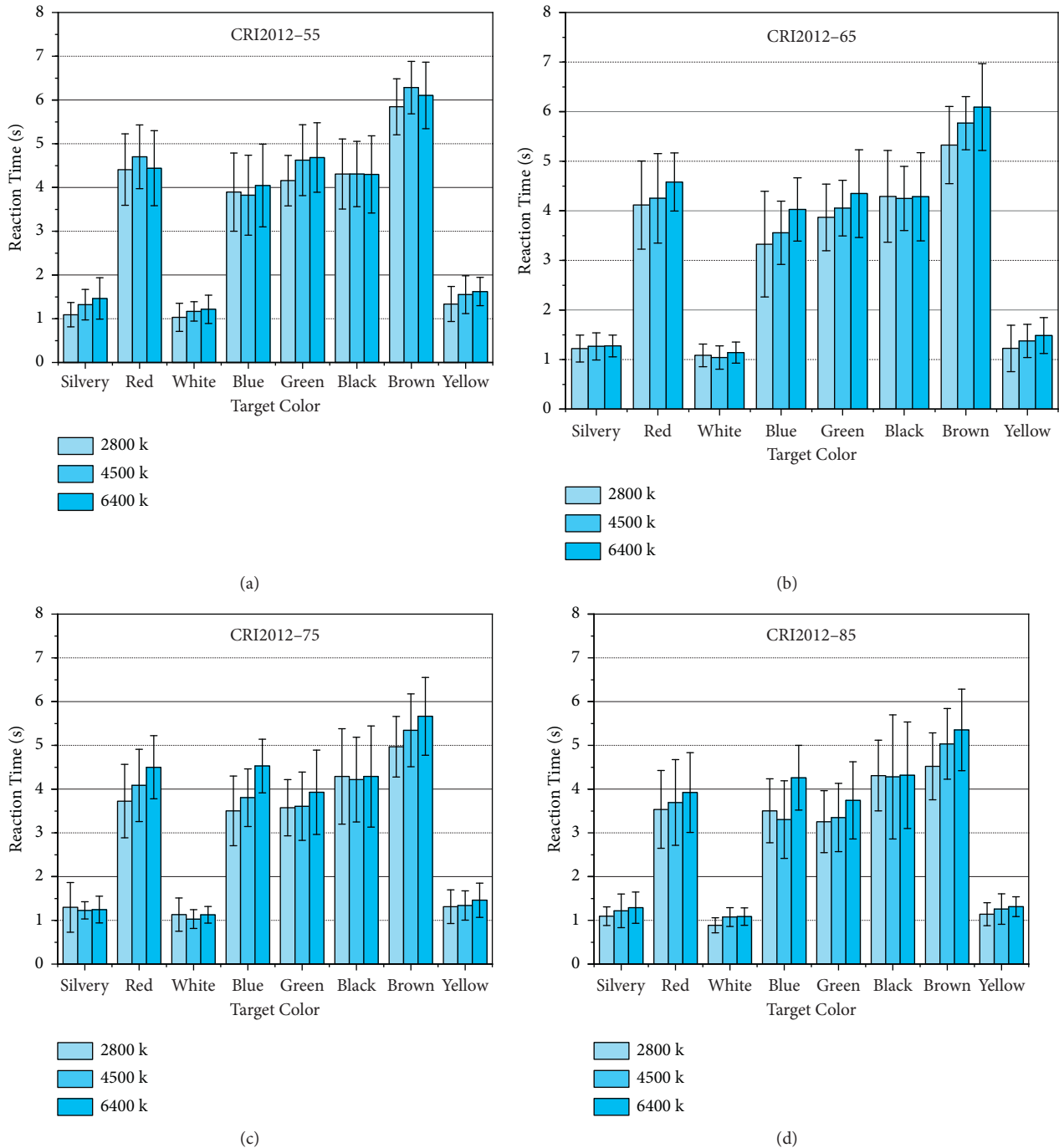


FIGURE 16: The reaction time of all observers under different CRI2012s and CCTs.

green and close to silver, it can be seen that the red target reflects red ray, and the silver reflects more evenly. The blue, green reflection spectrum components are mainly blue ray, while human eyes are more sensitive to blue light. Therefore, red, blue, and green had no difference in reaction time. Although the reflectance of black is lower than brown, it is far from the luminance of background, and the brown and background are too close, so it is difficult to be recognized.

Table 2 shows the significance analysis with reaction time as the dependent variable; the independent variable

is CRI2012, CCT, and colour of targets. When the significance  $p$  value of some independent variable and the dependent variable is less than 0.05, it indicates that there is a significant correlation between the two variables. The smaller the value of  $p$ , the stronger the correlation between the two variables.

In Table 2, the correlation between colour of targets and reaction time is the strongest, followed by CRI2012, and finally CCT. The  $p$  values of colour of targets, CCT, and CRI2012 were all less than 0.05, so the significant

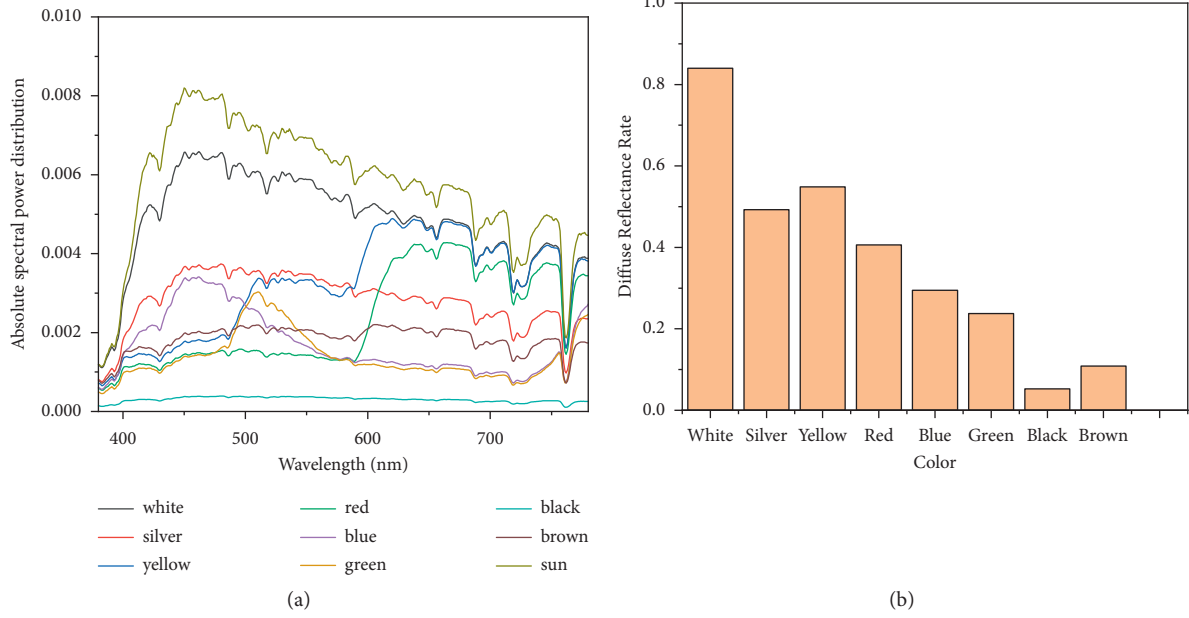


FIGURE 17: (a) The SPDs of eight targets with different colours of targets and backgrounds. (b) The diffuse reflectance of eight targets with different colours.

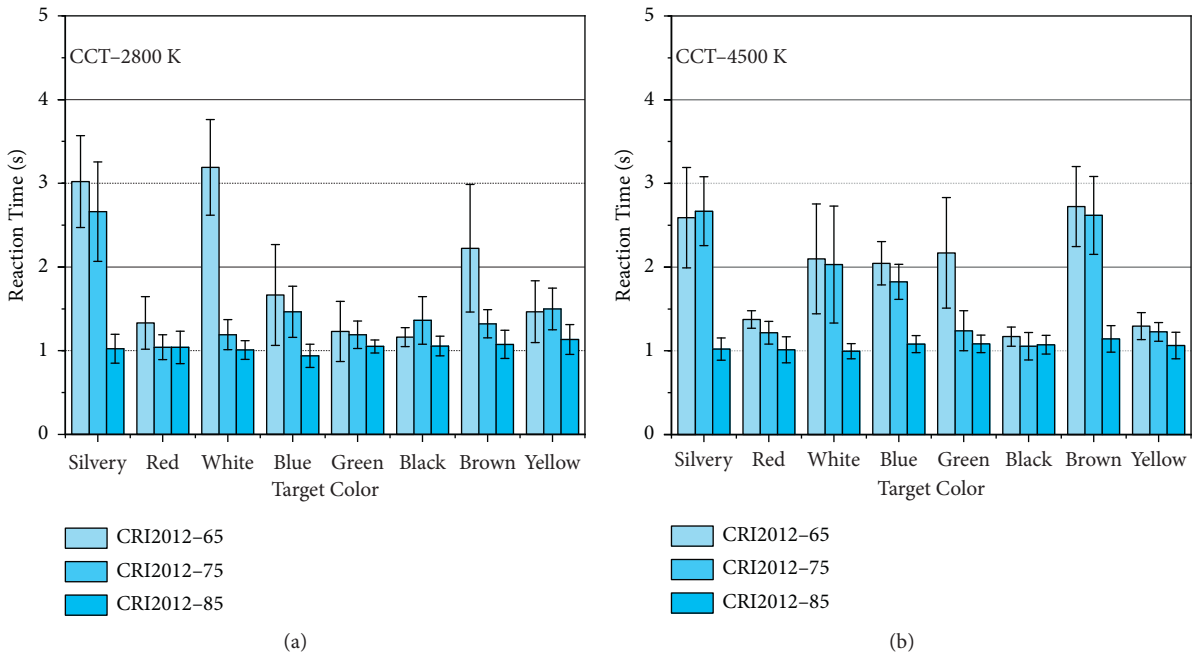
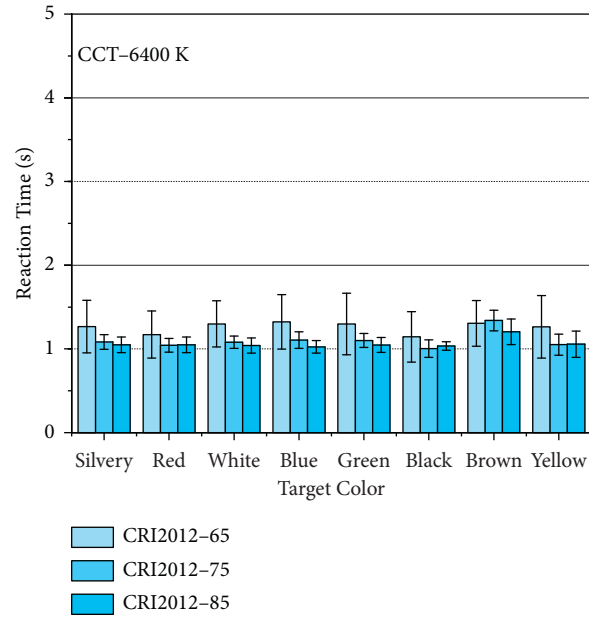


FIGURE 18: Continued.

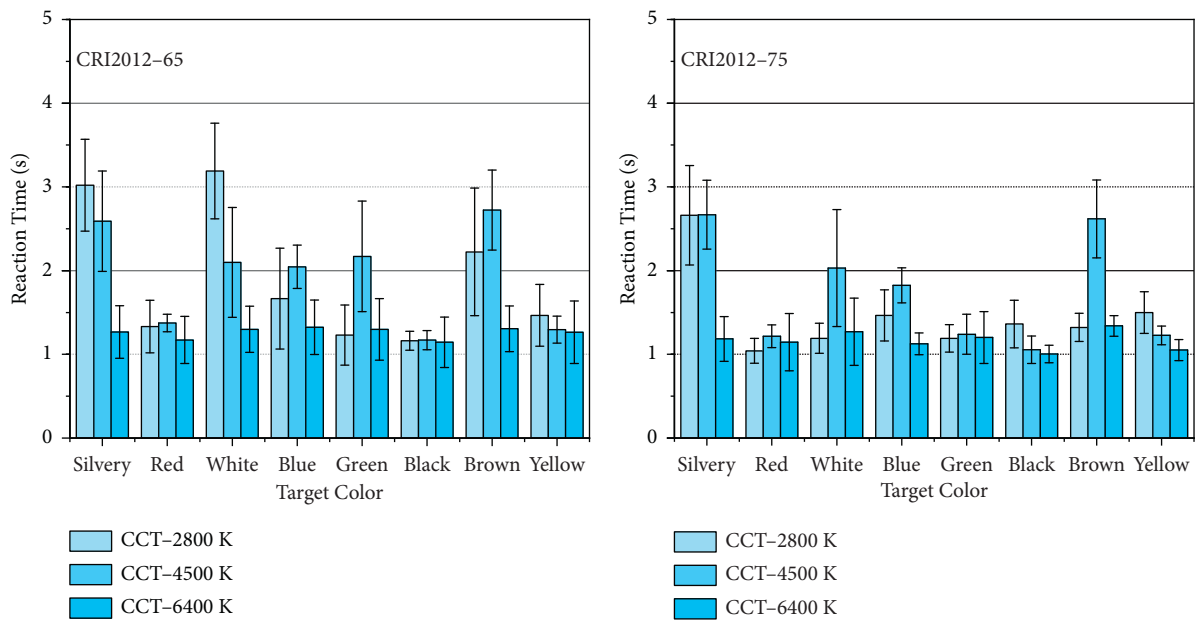


(c)

FIGURE 18: The reaction time of all observers under different CRI2012s and CCTs.

TABLE 2: Correlation analysis of all experimental data.

Significance ( $p$ )	Reaction time
CRI2012	$p = 0.005$
CCT	$p = 0.011$
Colour of target	$p < 0.001$



(a)

(b)

FIGURE 19: Continued.



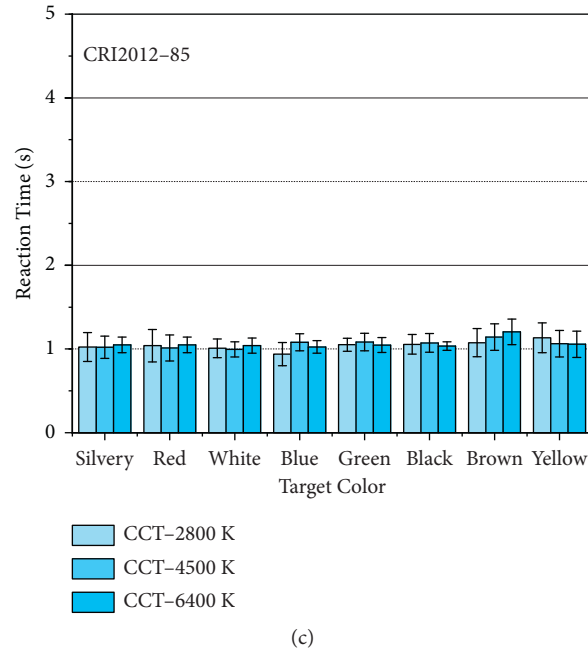


FIGURE 19: The reaction time of all observers under different CRI2012s and CCTs.

correlation between the reaction time and the three factors is strong. However, only considering the impact of LEDs on reaction time, the impact of CRI2012 is greater than that of CCT.

In Figure 17, the experimental data of most colours showed that the colour discrimination time decreased with the increase of CRI2012. Especially, CRI2012 on reducing colour discrimination time has a significant effect when CCT is 2800K and 4500k. In Figure 19, the experimental data of most colours showed that there are no rules with colour discrimination time and CCT. The colour discrimination time with different CCTs is almost the same when CRI 2012 is 85.

Table 3 shows the significance analysis with colour discrimination time as the dependent variable, and the independent variable is CRI2012, CCT, and colour of targets. From the table where the  $p$  values of colour of targets, CCT, and CRI2012 were all less than 0.05 and close to 0, the significant correlation between the reaction time and the three factors is strong.

Because changing both CRI2012s and CCTs will affect the reaction time, which means only consider the impact of CCT or CRI2012 is incomprehensive. The experimental results show that using LEDs of low CCT and high CRI2012 in the tunnel can help to reduce the reaction time of drivers. The results agree with the results in Section 3 too. The results of colour discrimination experiments show that high CRI2012 can improve the speed of colour recognition, which is very beneficial for drivers to observe the indicator and understand the road. Comprehensive experimental results show that the LED with CRI2012 and low CCT is conducive to the driver's rapid and accurate recognition of target and colour of targets. Yellow, white, and silver can be used on the walls, traffic signs, and working clothes of the staff in the tunnel, which are conducive to the driver to find target quickly and clearly.

TABLE 3: Correlation analysis of all experimental data.

Significance ( $p$ )	Colour discrimination time
CRI2012	$p < 0.001$
CCT	$p < 0.001$
Colour of targets	$p < 0.001$

## 6. Conclusions

In this paper, a theoretical analysis and experiment were carried out to investigate the impact of LED colour rendering on reaction time of human eyes in the tunnel interior zone. Firstly, the impact of accidents in the tunnel interior zone is expounded, the types and causes of accidents in the tunnel interior zone and the significance of shortening the reaction time of human eyes were analysed.

Next, several commonly used colour rendering evaluation indexes were also discussed, and CRI2012 was more suitable for evaluating the colour rendering of LEDs in the tunnel. The impact of CRI2012 on contrast is analysed based on the mesopic model MES-2. Low CCT and high CRI2012 can effectively improve the contrast of the target.

Next, a reaction time experiment and a colour discrimination time were designed; one investigates the relationship between CRI2012 and reaction time; another investigates the relationship between CRI2012 and colour discrimination time. Thirty observers attended the experiment.

Then, an experiment was used to measure the reaction time and colour discrimination time of the human eye under different lighting conditions. The results of comprehensive experiments show that the LEDs with low CCT and high CRI2012 have a positive effect on shortening the reaction

time and colour discrimination time of human eyes. This is conducive to reduce the probability of accidents at the tunnel. The experimental results agree with the results calculation in Section 3. High CRI2012 enables drivers to quickly and accurately identify colours. The experimental results also provide suggestions for the colour of warning signs or facilities at the tunnel.

## Data Availability

The data used to support the findings of the study are available from corresponding author upon request.

## Conflicts of Interest

The authors declare that they have no conflicts of interest.

## Acknowledgments

This paper was supported in part by the National Natural Science Foundation of China, under Grant 61701069. This paper was supported in part by the Fundamental Research Funds for the Central Universities of China, under Grants 3132019340 and 3132019200.

## References

- [1] S. Bassan, "Overview of traffic safety aspects and design in road tunnels," *IATSS Research*, vol. 40, no. 1, pp. 35–46, 2016.
- [2] B. Liang, S. He, L. Tähkämö et al., "Lighting for road tunnels: the influence of CCT of light sources on reaction time," *Displays*, vol. 61, Article ID 101931, 2020.
- [3] I. Benekos and D. Diamantidis, "On risk assessment and risk acceptance of dangerous goods transportation through road tunnels in Greece," *Safety Science*, vol. 91, pp. 1–10, 2017.
- [4] H. Wan, Z. Du, and Q. Yan, "The speed control effect of highway tunnel sidewall markings based on color and temporal frequency," *Journal of Advanced Transportation*, vol. 50, no. 7, pp. 1352–1365, 2016.
- [5] Y. Liu, J. Chen, Q. Zhang, and J. Weng, "Influence of light source color temperature on traffic safety at tunnel entrance based on reaction time," *Journal of Highway and Transportation Research and Development*, vol. 32, p. 114, 2015.
- [6] A. Shimojo, H. Takagi, and H. Onuma, "A simulation study of driving performance in long tunnel," in *Proceedings of Vehicle Navigation & Information Systems Conference*, Seattle, WA, USA, August 1995.
- [7] J. S. Yeung and Y. D. Wong, "The effect of road tunnel environment on car following behaviour," *Accident Analysis & Prevention*, vol. 70, pp. 100–109, 2014.
- [8] S. Bassan, "Research. Sight distance and horizontal curve aspects in the design of road tunnels vs. highways," *Tunnelling and Underground Space Technology*, vol. 45, pp. 214–226, 2015.
- [9] European Committee for Standardization, *Lighting Applications-Tunnel Lighting*, CEN CR 14380, Brussels, Belgium, 2003.
- [10] China Communications Press, *Guidelines for Design of Lighting of Highway Tunnels*, Ministry of Transport of People's Republic of China, Beijing, China, 2014.
- [11] J. H. Oh, Y. J. Eo, S. J. Yang, and Y. R. Do, "High-color-quality multipackage phosphor-converted LEDs for yellow photolithography room lamp," *IEEE Photonics Journal*, vol. 7, no. 2, pp. 1–8, 2015.
- [12] E. F. Schubert and J. K. Kim, "Solid-state light sources getting smart," *Science*, vol. 308, no. 5726, pp. 1274–1278, 2005.
- [13] H. Y. H. Yi, L. Z. L. Zheyang, W. A. W. Aiguo, L. C. L. Changbin, and F. S. F. Shouzhong, "Research on intelligent control of tunnel lighting system based on LED," in *Proceedings of the International Conference on Optoelectronics & Image Processing*, Washington, DC, USA, November 2010.
- [14] B. Mao, P. Niu, and C. Huang, "The design of the drive control chip for the solar LED lighting system," *Modern Applied Science*, vol. 2, p. 75, 2009.
- [15] P. Elejoste, I. Angulo, A. Perallos et al., "An easy to deploy street light control system based on wireless communication and LED technology," *Sensors*, vol. 13, no. 5, pp. 6492–6523, 2013.
- [16] F. Leccese, "Remote-control system of high efficiency and intelligent street lighting using a zigbee network of devices and sensors," *IEEE Transactions on Power Delivery*, vol. 28, pp. 21–28, 2012.
- [17] C.-S. Lee, J. Y. Shin, J. Nam, S. Park, S. Y. Chun, and J.-S. Jang, "P1-16: the effect of visual stimuli of LED lighting by color temperature and illuminance control on attention and meditation level of mind," *I-Perception*, vol. 3, no. 9, p. 630, 2012.
- [18] A. Zabiliūtė, R. Vaicekuskas, P. Vitta, and A. Žukauskas, "Phosphor-converted LEDs with low circadian action for outdoor lighting," *Optics Letters*, vol. 39, no. 3, pp. 563–566, 2014.
- [19] H. Jin, S. Jin, L. Chen, S. Cen, and K. Yuan, "Research on the lighting performance of LED street lights with different color temperatures," *IEEE Photonics Journal*, vol. 7, no. 6, pp. 1–9, 2015.
- [20] L. Dong, L. Qin, W. Xu, and L. Zhang, "The impact of LED correlated color temperature on visual performance under mesopic conditions," *IEEE Photonics Journal*, vol. 9, no. 6, pp. 1–16, 2017.
- [21] K. Yamamoto and T. Nagasawa, "Visibility and color-rendering properties of light sources in tunnel lighting," in *Proceedings of 26th Session of the CIE*, Beijing, China, July 2007.
- [22] M. Deng and Y. Dai, "The effect of tunnel light source and tunnel light color to drivers' visual performance," *Journal of Chongqing University. Natural Science Edition*, vol. 39, pp. 140–145, 2016.
- [23] X. Zhang, J. Hu, R. Wang, X. Gao, and L. He, "The comprehensive efficiency analysis of tunnel lighting based on visual performance," *Advances in Mechanical Engineering*, vol. 9, no. 4, Article ID 168781401769644, 2017.
- [24] A. M. Colaco, S. G. Colaco, C. P. Kurian, and S. G. Kini, "Color characterization of multicolor multichip LED luminaire for indoor," *Journal of Building Engineering*, vol. 18, pp. 19–32, 2018.
- [25] J. Laski, C. A. Brunault, R. Schmidt, and S. C. Ryu, "An exploratory study of retail lighting with continuous modulation of color rendering properties to influence shoppers' spatial range of browsing," *Journal of Business Research*, vol. 111, pp. 148–162, 2020.
- [26] F. Szabó, R. Kéri, J. Schanda, P. Csuti, and E. Mihálykó-Orbán, "A study of preferred colour rendering of light sources: home lighting," *Lighting Research and Technology*, vol. 48, no. 2, pp. 103–125, 2016.

- [27] M. Islam, R. Dangol, M. Hyvärinen, P. Bhusal, M. Puolakka, and L. Halonen, "User acceptance studies for LED office lighting: lamp spectrum, spatial brightness and illuminance," *Lighting Research and Technology*, vol. 47, no. 1, pp. 54–79, 2015.
- [28] S. Jost-Boissard, M. Fontoynt, and J. Blanc-Gonnet, "Perceived lighting quality of LED sources for the presentation of fruit and vegetables," *Journal of Modern Optics*, vol. 56, no. 13, pp. 1420–1432, 2009.
- [29] J. C. Shin, H. Yaguchi, and S. Shioiri, "Change of color appearance in photopic, mesopic and scotopic vision," *Optical Review*, vol. 11, no. 4, pp. 265–271, 2004.
- [30] Central Bureau of the CIE, *Method of Measuring and Specifying Colour Rendering Properties of Light Sources*, Central Bureau of the CIE, Vienna, Austria.
- [31] W. Davis, "Measuring color quality of light sources - art. no. 63370L," in *Proceedings of the Sixth International Conference on Solid State Lighting*, I. T. Ferguson, N. Narendran, T. Taguchi, and I. E. Ashdown, Eds., p. L3370, San Diego, CA, USA, September 2006.
- [32] K. Smet, J. Schanda, L. Whitehead, and R. Luo, "CRI2012: a proposal for updating the CIE colour rendering index," *Lighting Research and Technology*, vol. 45, no. 6, pp. 689–709, 2013.
- [33] N. Pousset, G. Obein, and A. Razet, "Visual experiment on LED lighting quality with color quality scale colored samples," in *Proceedings of the CIE 2010 Lighting Quality and Energy Efficiency*, Vienna, Austria, August 2010.
- [34] K. Lin, N. Liao, D. Zhao, S. Dong, and Y. Li, "Chromatic contrast dependence of reaction time to random-dot stereograms at isoluminance," *Color Research & Application*, vol. 41, no. 6, pp. 564–570, 2016.
- [35] X. Cai, J. Weng, Y. Hu, and F. J. S. Du, "Research on optimal values of contrast revealing coefficient in road tunnel lighting," *Sadhana*, vol. 45, 2020.
- [36] M. S. Mahadevan, H. E. Bedell, and S. B. Stevenson, "The influence of endogenous attention on contrast perception, contrast discrimination, and saccadic reaction time," *Vision Research*, vol. 143, pp. 89–102, 2018.
- [37] C. An-Seop, K. Intae, K. Hyunsun, and S. Arom, "Evaluation of the visibility of colored objects under LED lighting with various correlated color temperatures," *Color Research & Application*, vol. 42, 2017.
- [38] M. Rea, J. Bullough, J. Freyssinier-Nova, and A. Bierman, "Technology. A proposed unified system of photometry," *Lighting Research and Technology*, vol. 36, no. 2, pp. 85–109, 2004.
- [39] M. Eloholma and L. Halonen, "New model for mesopic photometry and its application to road lighting," *Leukos*, vol. 2, no. 4, pp. 263–293, 2006.
- [40] Y. He, M. Rea, A. Bierman, and J. Bullough, "Evaluating light source efficacy under mesopic conditions using reaction times," *Journal of the Illuminating Engineering Society*, vol. 26, no. 1, pp. 125–138, 1997.
- [41] D. A. Tipton and E. Medicine, "A review of vision physiology," *Aviation Space & Environmental Medicine*, vol. 55, pp. 145–9, 1984.
- [42] M. S. Rea and J. D. Bullough, "Making the move to a unified system of photometry," *Lighting Research and Technology*, vol. 39, no. 4, pp. 393–408, 2007.

## Research Article

# Optimization Model of Network-Level Pavement Maintenance Decision considering User Travel Time and Vehicle Fuel Consumption Costs

Leilei Chen <sup>1,2</sup>, Zepeng Fan <sup>3</sup>, Pengfei Liu <sup>3</sup>, and Zhendong Qian<sup>1</sup>

<sup>1</sup>Key Laboratory of Safety and Risk Management on Transport Infrastructures, Ministry of Transport, Southeast University, Nanjing, China

<sup>2</sup>Intelligent Transportation System Research Center, Southeast University, Nanjing, China

<sup>3</sup>Institute of Highway Engineering, RWTH Aachen University, Aachen, Germany

Correspondence should be addressed to Zepeng Fan; fan@isac.rwth-aachen.de

Received 10 April 2021; Revised 27 July 2021; Accepted 17 August 2021; Published 27 August 2021

Academic Editor: Adolfo Preciado

Copyright © 2021 Leilei Chen et al. This is an open access article distributed under the Creative Commons Attribution License, which permits unrestricted use, distribution, and reproduction in any medium, provided the original work is properly cited.

The maintenance management decisions of network-level asphalt pavements have long been a challenge to highway agencies, and a great amount of factors have been involved. In this study, a network-level optimization method was established by integrating the maintenance benefits into the zero-one programming optimization model. An optimized performance evaluation method of asphalt pavement was proposed which contains 11 different kinds of combinations. The benefit model quantifies the cost savings of user travel time and vehicle fuel consumption to the pavement condition index (PCI) and ride quality index (RQI), respectively. Based on the simplified evaluation method as well as the quantified maintenance benefit model, an optimization model was established by employing the zero-one programming. This optimization model aimed to maximize the improvements/price ratio of pavement maintenance for the whole pavement network. The calculation results present the optimal strategies of maintenance for every road section in the network. The applicability of the newly proposed model was validated by a case study. The methodology developed in this study helps to offer guidelines to highway agencies in managing and making decisions about network-level pavement maintenance.

## 1. Introduction

After decades of development, the scale of highway networks in many countries has gradually improved, and they have or are about to face a major shift from the stage of “pavement construction as the main” to “pavement maintenance first.” Therefore, pavement maintenance and management issues have attracted more and more attention. In this case, the pavement maintenance management system (PMMS), as a systematic and scientific management and decision support tool, can better optimize and improve the management and decision-making ability of the highway networks. The road in its entire life cycle will get better use performance and higher service levels [1].

The essence of performance evaluation on the pavement service is analysis of the extent to which the pavement

performance meets the specified requirements in terms of the investigated pavement condition data. Based on the obtained analysis and evaluation results, the pavement performance can be estimated and the detailed maintenance strategies for the pavement can be planned [2].

The pavement performance evaluation is usually carried out in two aspects, namely, pavement structural and functional evaluations [3, 4]. The surface distress condition belongs to the structural condition evaluation, which also consists of the structural bearing capacity [5]. The pavement functional evaluation includes driving quality, service level, and safety [6, 7]. The pavement performance can be evaluated with a single evaluation index or with a comprehensive evaluation index. Specifically, the single evaluation index is mainly for analysis and evaluation of one of the use performances, while multiple single evaluation indexes are



weighted and integrated as the comprehensive evaluation index for evaluation. In another word, the single evaluation index reflects the condition of a certain performance of the pavement and the comprehensive evaluation index denotes the comprehensive conditions of the pavement service performance [8]. In practice, various parameters are afflicted with large uncertainty. Ignoring the uncertainty may lead to a suboptimal plan adversely affecting the network conditions. Some optimization frameworks for network-level pavement maintenance and rehabilitation planning considering the uncertain nature of pavement deterioration have been developed [9].

The benefit of pavement maintenance is the sum of the direct and the indirect benefits, which arise from the improvement of road conditions by implementing the pavement maintenance on expressways. The benefit calculation of the pavement maintenance projects does not only directly reflect the assessment effectiveness of pavement maintenance but is also an important prerequisite for the proper selection of pavement maintenance methods in the next step. Maintenance managers must allocate their limited budgets among competing alternatives. The absence of simpler decision-making methods exacerbates this issue [10].

Different approaches and perspectives have been developed on the specific indicators and contents of pavement maintenance benefit calculation; for example, the World Bank defined the benefits of road projects into three aspects, namely, benefits arising from the saving in vehicle operating costs, saving in user time costs, and saving in traffic accident reduction. These aspects of benefits are taken account in the specific road project benefit evaluation in many countries, including the United States, United Kingdom, and Japan. Some researchers suggest that not only the short-term, direct, and quantitative economic benefits but also long-term, indirect, and qualitative economic benefits should be considered [11]. Moreover, the economic impact is suggested to be taken into account in the analysis of cost effectiveness [12]. Based on practical experience, the benefits calculation of pavement maintenance projects in China at present mainly considers the benefits of operating costs reduction, the benefits of user travel time saving, the benefits of traffic accidents reduction, and the improvement of the quality of transportation services [13].

Based on the proposed indicators, the problem of finding the best pavement maintenance method can be modeled as a combinatorial optimization problem [14]. Different algorithms have been developed to solve the optimization decision model that can be applied in highway asset management [15–19]. Recently, a binary cuckoo search (BCS) algorithm was implemented to a pavement maintenance management system to solve the optimization problem. The results of a comparison between genetic algorithms (GAs) and the BCS clearly justify the advantages of the search paths underlying the BCS in alleviating premature convergence [20]. Furthermore, several applications using different optimization decision models to improve the overall pavement maintenance solution at the network level can be found. For example, a multiobjective decision-aid tool (MODAT) was developed by testing with data from the

Estradas de Portugal's Pavement Management System. The MODAT uses a multiobjective deterministic section-linked optimization model with different possible goals [21].

However, due to the lack of maintenance experience, the large scale of maintenance requirements, and the shortage of maintenance funds resources, a comprehensive and scientific decision-making method has not yet been established so far. How to establish efficient and scientific pavement maintenance and management methods, improve operational efficiency, meet high-quality pavement maintenance needs, and meet various transportation needs has become important problems encountered in pavement management [22].

This study proposes a network-level pavement maintenance and rehabilitation optimization model considering the costs of user travel time and vehicle fuel consumption. Firstly, the evaluation indicators used in the model were listed. Afterwards, the optimization method of pavement maintenance used in China was briefly introduced. Next, the estimation method of road user costs which was integrated in the optimization method was presented. Based on the theoretical basis, a network-level optimization method considering road user costs was proposed and described in detail. Finally, a case study using the developed optimization method was shown.

## 2. Theoretical Basis

*2.1. Evaluation Indicators of Asphalt Pavement.* A globally popular pavement performance indicator is the Pavement Condition Index (PCI). It is a numeric index between 0 and 100, which was originally developed by the US Army and later standardized by the ASTM [23]. The PCI reflects the number of the distresses on the pavement and their extent. Therefore, a newly constructed road has a PCI of 100, and as it deteriorates over time and becomes impassable, its PCI approaches 0. Computing the PCI requires data about several types of distresses and their severity as follows: potholes, fatigue cracking, rutting, block cracking, edge cracking, longitudinal and transverse cracking, patching, shoving, bleeding, polished aggregate, and raveling [24]. The PCI can be determined by the following equation [25]:

$$PCI = 100 - \sum_{i=1}^n \sum_{j=1}^{m_i} DP_{ij} W_{ij}, \quad (1)$$

where  $i$  and  $j$  are counters for distress types and severity levels, respectively;  $n$  is the total number of observed distress types;  $m_i$  is the number of severity level for the distress type  $i$ ;  $DP_{ij}$  is the deduct value that varies with distress type  $i$  and severity  $j$ ; and  $W_{ij}$  is an adjustment weight when the pavement with distress type  $i$  reaches the severity level  $m$ .

Pavement roughness is an indispensable criterion in the evaluation of pavement performance, which plays an important role not only in the service life of the pavement but also in the economy of operation and the capacity of vehicles and traffic safety. The Ride Quality Index (RQI) can be used as a standard to evaluate the pavement roughness. The relationship between International Roughness Index (IRI) and

RQI, according to the Highway Performance Assessment Standards (JTG H20-2007) [25], can be expressed by following equation:

$$RQI = \frac{100}{1 + a_0 e^{(a_1 \cdot IRI)}}, \quad (2)$$

where  $a_0$  and  $a_1$  are the standard parameters with the values of 0.026 and 0.65, respectively [25].

Skid resistance (or friction) of road surfaces plays a significant role in road safety as the friction between tire, and pavement is a critical contributing factor in reducing potential crashes. This safety performance is also a major criterion for evaluating the service performance of pavements. The structural texture of a pavement greatly affects its skid resistance. The Skid Resistance Index (SRI) of pavement is used to evaluate its skid resistance performance. According to the Highway Performance Assessment Standards (JTG H20-2007) [25], the relationship between the directly measured Sideway Force Coefficient (SFC) and SRI can be described by the following equation:

$$SRI = \left( \frac{100 - SRI_{\min}}{1 + a_0 e^{(a_1 \cdot SFC)}} \right) + SRI_{\min}, \quad (3)$$

where  $SRI_{\min}$  is the skid resistance limit and  $a_0$  and  $a_1$  are the standard parameters with the values of 28.6 and  $-0.105$ , respectively.

Deflection is an effective index to reflect the pavement bearing capacity and structural strength. Measuring deflection has the advantages of being convenient, intuitive, economical, and efficient. According to Highway Performance Assessment Standards (JTG5210-2018) [26], Pavement Structural Strength Index (PSSI) is determined by the allowable pavement deflection, the actually measured pavement deflection, and the model parameters, among which the model parameters are fixed values. When the road structure's own characteristics are determined (such as highway grade and pavement structure type), the pavement's allowable deflection is also uniquely determined [27]. Therefore, the strength of the pavement structure is determined by the measured pavement deflection value as follows:

$$PSSI = \frac{100}{1 + 15.71 e^{-5.19SSI}}, \quad (4)$$

where SSI is the structure strength index and can be calculated with  $SSI = l_R/l_0$  and  $l_R$  and  $l_0$  are the allowed and measured deformations of the asphalt pavement, respectively.

The Pavement Quality Index (PQI) is the overall "score" given to a pavement section with a range from 0 to 100. The value of 100 represents a road in excellent condition (usually when it is initially constructed). PQI is an output metric that is a function of PCI, RQI, SRI, and PSSI according to [28] as follows:

$$PQI = \omega_{PCI}PCI + \omega_{RQI}RQI + \omega_{SRI}SRI + \omega_{PSSI}PSSI. \quad (5)$$

The weight  $\omega$  of each index is not fixed but fluctuates in a certain range, which depends on the actual road condition

and different maintenance strategies. This can be adjusted appropriately in the recommended range given in the technical specifications, but the values of 0.35, 0.35, 0.1, and 0.2 are generally recommended for the four parameters, respectively.

*2.2. Optimization of Pavement Performance Evaluation Method.* Pavement service performance evaluation includes several indicators such as PCI, RQI, SRI, and PSSI, which is a comprehensive evaluation system. Although PQI can reflect the comprehensive maintenance condition of the pavement, it is necessary to determine the maintenance strategy depending on the specific circumstance, i.e., only using the PQI to develop detailed maintenance strategies is not appropriate. In order to consider the pros and cons of each performance conditions, it requires combining the different pavement performance conditions with different grades for each evaluation indicator, which facilitates the optimization of maintenance decisions.

Current standards in China classify the four indicators (PCI, RQI, SRI, and PSSI) into five levels: excellent, good, fair, poor, and very poor. Therefore, there are in total 625 different combined states, and each state has different maintenance measures, making thousands of possible situations. As a result, the scale of optimization decision-making is too complex and is not conducive to solving. It is necessary to analyze and study the combined states of pavement performance to reduce unnecessary combined states and further reduce the scale of optimization decision-making. In this study, on basis of analyzing the specific state combinations according to the relevant technical specifications [28], a simplification was adopted by emerging the similar levels to reduce the condition combinations. In particular, the condition levels for the PCI and RQI indexes were adjusted by combining the excellent [90–100] and good [80–90] levels as good [80–100] and also combining fair [70–80] and poor [60–70] as fair [60–80]. For the SRI and PSSI indexes, only two condition levels were retained which are sufficient and insufficient. The details for the finalized combinations are shown in Table 1.

It is seen from Table 1 that a total of  $3 \times 3 \times 2 \times 2 = 36$  different condition combinations of asphalt pavement performances after simplification can be summarized. Through this simplification not only the demands of optimization decision-making are fulfilled but also its scale is greatly reduced, which is more beneficial to decisions and solutions. Moreover, it is worth noting that most of these conditions are still of no practical significance. For instance, if the PSSI index is evaluated to be insufficient, structural reinforcement must be conducted regardless of other three indexes. If the SRI index is evaluated to be insufficient but the PSSI index is in the sufficient condition, the anti-skidding layer must be paved to restore the skid resistance regardless of other three indexes. The special requirements on the SRI and PSSI indexes lead to a significant decrease in the effective combinations of pavement condition. In the actual decision-making process, only the combinations with actual significance are necessary for further analysis and the



TABLE 1: Simplified combinations of the pavement performance condition.

	Verbal rating (numerical rating)		
PCI	Good [80–100]	Fair [60–80]	Poor [0–60]
RQI	Good [80–100]	Fair [60–80]	Poor [0–60]
SRI	Sufficient [62–100]	Insufficient [0–62]	
PSSI	Sufficient [80–100]	Insufficient [0–80]	

corresponding appropriate maintenance strategies will be selected consequently. Table 2 shows the maintenance strategies for each combination of conditions.

As can be seen in Table 2, only 11 condition combinations are of practical significance for the pavement performance for the maintenance decision optimization problem. Moreover, two combinations (10 and 11) will be eliminated in the later decision optimization due to the demands of the mandatory maintenance strategies. Only the remaining 9 combinations require decision optimizations, and consequently, the scale of decision optimization is reduced.

**2.3. Estimation of User Costs.** The benefits of expressway pavement maintenance projects can be mainly represented in various related cost savings. The American Association of State Highway and Transportation (AASHTO) defines the benefits of pavement maintenance projects as the vehicle travel cost savings, the travel time savings, the traffic accident reduction, and the vehicle exhaust emission reduction. In this study, the user cost savings are defined including the costs of user travel time and the vehicle travel fuel consumption.

**2.3.1. Cost Savings in User Travel Time.** The user travel time cost is the value that arises due to the existence of an opportunity cost of the time consumed by the vehicle during the trip [29, 30]. The savings in user travel time cost after implementing pavement maintenance  $\Delta T$  can be expressed by the following equation [13]:

$$\Delta T = \theta \cdot Q \cdot (T_0 - T_1), \quad (6)$$

where  $\theta$  is the converting coefficient of the travel time value,  $Q$  is the traffic volume of the road section,  $T_0$  is the travel time of a single vehicle before maintenance, and  $T_1$  is the travel time of a single vehicle after maintenance. The converting coefficient  $\theta$  is calculated through  $\theta = \text{GDP}/(\text{population} \times \text{average working time})$ . Calculation of equation (6) requires a functional relationship between the user travel time of the road section and the pavement condition. PCI is then adopted as an indicator for the pavement condition. The functional relationship between  $T$  and the PCI can be obtained through tests on a large number of road sections, which is expressed as follows [13]:

$$T = \alpha \cdot l \cdot (\text{PCI} - \eta)^\beta + \frac{l}{v_0}, \quad (7)$$

where  $l$  is the section distance,  $v_0$  is the maximal design speed, and  $\alpha$ ,  $\beta$ , and  $\eta$  are the parameters to be determined.

TABLE 2: Condition combinations of the expressway asphalt pavement performance.

Combination	PCI	RQI	SRI	PSSI
1	Good	Good	Sufficient	Sufficient
2	Fair	Good	Sufficient	Sufficient
3	Poor	Good	Sufficient	Sufficient
4	Good	Fair	Sufficient	Sufficient
5	Fair	Fair	Sufficient	Sufficient
6	Poor	Fair	Sufficient	Sufficient
7	Good	Poor	Sufficient	Sufficient
8	Fair	Poor	Sufficient	Sufficient
9	Poor	Poor	Sufficient	Sufficient
10			Insufficient	Sufficient
11				Insufficient

Therefore, the savings in user travel time costs after the pavement maintenance can be represented as follows:

$$\Delta T = \theta \cdot Q \cdot \alpha \cdot l \cdot [(\text{PCI}_0 - \eta)^\beta - (\text{PCI}_1 - \eta)^\beta], \quad (8)$$

where  $\text{PCI}_0$  represents the PCI value of the road before maintenance and  $\text{PCI}_1$  represents the PCI value of the road after maintenance.

**2.3.2. Cost Savings in Vehicle Travel Fuel Consumption.** Fuel consumption cost refers to energy expenses consumed by the vehicle in the travel process [31–34]. According to [35], for a minivan, which is selected as the standard vehicle in this study, the relationship among the fuel consumption, the vehicle speed, and the IRI can be expressed by the following equation:

$$O = 0.0040141 \cdot V^2 - 0.56612 \cdot V + 25.29872 + 0.56222 \cdot \text{IRI}, \quad (9)$$

where  $O$  is the fuel consumption L/100 km and  $V$  is the vehicle speed. When assuming that the vehicle is traveling at speed of 80 km/h, the relationship between the fuel consumption and the IRI can be described by following equation:

$$O = 0.56222 \cdot \text{IRI} + 5.69936. \quad (10)$$

Based on equation (10), the cost savings in fuel consumption after pavement maintenance can be expressed as

$$\Delta O = 0.56222 \cdot g \cdot (\text{IRI}_0 - \text{IRI}_1) \cdot l \cdot Q, \quad (11)$$

where  $g$  is the fuel price,  $\text{IRI}_0$  represents the IRI value of the road before maintenance, and  $\text{IRI}_1$  represents the PCI value of the road after maintenance.

### 3. Development of the Optimization Model of Pavement Maintenance at Network Level

**3.1. Problem Statement and Basic Hypotheses.** In this study, the selected problem in the pavement maintenance is defined as a highway network consisting of  $N_1$  roads. According to Section 2.2, there are  $N_2 = 11$  combinations of pavement performance conditions. The performance conditions of different sections in the same road may be significantly different, and the proportion of the  $i$ -th road under the  $j$ -th combination at a given time is denoted as  $d_{i,j}$ . A total of  $N_3$  maintenance strategies are implemented for the highway. To ensure the basic traffic capacity, a minimum value  $N_{PQI}$  is generally required for the PQI of the road network after applying the maintenance strategies. Based on this restriction, the maintenance strategies for different roads and performance conditions of road sections are determined to ensure that the performance price ratio of the maintenance is maximized. This means the ratio of road user cost savings to the invested maintenance cost is maximized.

The following hypotheses are proposed in this study for developing the optimization model of pavement maintenance at network level:

- (1) In accordance with the requirements of sustainable development, the service level and pavement performance of the road throughout its life cycle do not seriously decline, which means during the planning of the maintenance optimization in the current year, the condition of the service level and pavement performance of the road in the previous year must be considered.
- (2) Among the 11 combinations of road performance conditions given in Section 2.2, the 10th and 11th conditions are excluded from the maintenance optimizations due to its regular maintenance strategies. Therefore, in the actual optimization model,  $N_2$  is reduced from 11 to 9.
- (3) For any road section, only one maintenance strategy is adopted in the current maintenance cycle.
- (4) The effects of the increase in traffic volume in the following year on the estimated user costs are neglected.
- (5) The implementation of the maintenance does not change the capacity of the road section.
- (6) The maintenance measures can reach the required standard values.

**3.2. Development of the Optimization Model.** According to the maintenance requirements mentioned in earlier section, this study adopts the zero-one integer programming method [36] to construct the maintenance optimization decision model for network-level roads, which are shown in following equations.

The objective function is as follows:

$$\max \frac{\sum_{i=1}^{N_1} \sum_{j=1}^{N_2} \sum_{k=1}^{N_3} (\Delta T_{i,j,k} + \Delta O_{i,j,k})}{\sum_{i=1}^{N_1} \sum_{j=1}^{N_2} \sum_{k=1}^{N_3} C_{i,j,k}} \quad (12)$$

The constrains are as follows:

$$\sum_{k=1}^{N_3} x_{i,j,k} = 1, \quad (i = 1, 2, \dots, N_1; j = 1, 2, \dots, N_2; k = 1, 2, \dots, N_3), \quad (13)$$

$$\frac{\sum_{i=1}^{N_1} \sum_{j=1}^{N_2} \sum_{k=1}^{N_3} x_{i,j,k} \cdot l_i \cdot d_{i,j} \cdot e_{j,k}}{\sum_{i=1}^{N_1} l_i} \geq N_{PQI}, \quad (14)$$

$$x_{i,j,k} = \{0, 1\}, \quad (15)$$

where  $\Delta T_{i,j,k}$  is the saved user travel time costs after applying the  $k$ -th maintenance strategy for the  $i$ -th road section under the  $j$ -th combination condition,  $\Delta O_{i,j,k}$  is the saved fuel consumption from vehicles after applying the  $k$ -th maintenance strategy for the  $i$ -th road section under the  $j$ -th combination condition,  $C_{i,j,k}$  is the maintenance cost for applying the  $k$ -th maintenance strategy for the  $i$ -th road section under the  $j$ -th combination condition,  $l_i$  is the total mileages of the  $i$ -th road,  $d_{i,j}$  is the proportion of the  $i$ -th road under the  $j$ -th combination condition, and  $e_{j,k}$  is the PQI value after applying the  $k$ -th maintenance strategy for the road section under the  $j$ -th combination condition. With equation (13), every road section is ensured a maintenance strategy, and according to the requirements in the actual maintenance of pavements, when a road section is not applied with a special maintenance strategy, the measures for routine road maintenance are still required as necessary. Equation (14) restricts the overall maintenance quality of the road network which guarantees that the average PQI of the road network after maintenance is above 90. Equation (15) defines the 0-1 dummy variable  $x_{i,j,k}$  for the zero-one integer programming method used in the current study. The variable  $x_{i,j,k}$  has a value of either 0 or 1. A value of 1 for  $x_{i,j,k}$  indicates that the  $k$ -th maintenance strategy is applied for the  $i$ -th road section under the  $j$ -th combination condition or 0 otherwise.

Referring to Section 2.3,  $\Delta T_{i,j,k}$ ,  $\Delta O_{i,j,k}$ , and  $C_{i,j,k}$  can be determined by following equations:

$$\Delta T_{i,j,k} = \theta \cdot Q_i \cdot \Delta t_{i,j,k}, \quad (16)$$

$$\Delta O_{i,j,k} = Q_i \cdot \Delta o_{i,j,k}, \quad (17)$$

$$\Delta C_{i,j,k} = x_{i,j,k} \cdot l_i \cdot d_{i,j} \cdot p_{i,k}, \quad (18)$$

where  $Q_i$  is the traffic volume of  $i$ -th road section,  $\Delta t_{i,j,k}$  is the saved user travel time from each vehicle after applying the  $k$ -th maintenance strategy for the  $i$ -th road section under the  $j$ -th combination condition,  $\Delta o_{i,j,k}$  is the saved fuel consumption from each vehicle after applying the  $k$ -th maintenance strategy for the  $i$ -th road section under the  $j$ -th combination condition, and  $p_{i,k}$  is the maintenance cost per

kilometer for the  $i$ -th road applying the  $k$ -th maintenance strategy.

$\Delta t_{i,j,k}$  and  $\Delta o_{i,j,k}$  can be obtained through

$$\begin{aligned}\Delta t_{i,j,k} &= l_i \cdot d_{i,j} \cdot t_{j,k}, \\ \Delta o_{i,j,k} &= l_i \cdot d_{i,j} \cdot g \cdot o_{j,k},\end{aligned}\quad (19)$$

where  $t_{j,k}$  and  $o_{j,k}$  are the saved user travel time and saved fuel consumption from each vehicle after applying the  $k$ -th maintenance strategy for the  $j$ -th combination condition in unit kilometer, respectively.

By adopting equations (8) and (11),  $t_{j,k}$  and  $o_{j,k}$  can be determined with following equations:

$$\begin{aligned}t_{j,k} &= \alpha \cdot \left[ (\text{PCI}_0 - \eta)^\beta - (\text{PCI}_1 - \eta)^\beta \right], \\ o_{j,k} &= 0.56222 \cdot (\text{IRI}_0 - \text{IRI}_1),\end{aligned}\quad (20)$$

where  $\text{PCI}_1$  denotes the pavement condition index of the road under the  $j$ -th combination condition after applying the  $k$ -th maintenance strategy,  $\text{PCI}_0$  represents the pavement condition index of the road under the  $j$ -th combination condition before applying the  $k$ -th maintenance strategy,  $\text{IRI}_1$  expresses the international roughness index of the road under the  $j$ -th combination condition after applying the  $k$ -th maintenance strategy, and  $\text{IRI}_0$  denotes the international roughness index of the road under the  $j$ -th combination condition before applying the  $k$ -th maintenance strategy.

### 3.3. Case Study

**3.3.1. Background and Input Parameters.** Based on operating road sections in Shaanxi, China, the model developed in this study was applied to optimize the maintenance plan decision. Ten expressways were investigated, and all of them are asphalt pavements [37]. The corresponding mileages and traffic volumes are shown in Table 3.

After testing the pavement, the distributions of different combinations of pavement conditions within this network in the current year are presented in Table 4.

By conducting field investigations in different road sections, the costs of five common maintenance strategies for different road sections in this network were determined, as listed in Table 5.

After a comprehensive survey of the current year regarding the gross domestic product (GDP), the population size, and the average working time in Shaanxi Province, the time value conversion coefficient  $\theta$  and the current local fuel price  $g$  were determined with values of 15.34 and 6.73 Yuan/L, respectively. The value of  $N_{\text{PQI}} = 90$  is adopted in this case which is suggested by the transport agency.

The determination of the three coefficient matrices  $e_{j,k}$ ,  $t_{j,k}$ , and  $o_{j,k}$  is required for the application of the model developed in this study. For  $e_{j,k}$ , PQI can be determined by equation (5), and the averaged values of the pavement performance indicators were adopted in the calculation. In this study, it was assumed that routine maintenance cannot improve the pavement performance evaluation index. The PCI indicator is increased by two levels, and RQI is increased by one level when paving an overlay [38]. For the skid resistance performance index SRI, the optimal level is restored when paving an anti-skid layer, conducting the pavement reconstruction or structural reinforcement. For the pavement structural strength index PSSI, the optimal level is restored by conducting a pavement reconstruction or structural reinforcement [38]. For instance, if road section is now in the condition of combination 5, the maintenance strategy of overlay paving is adopted. This means that the PCI and RQI indexes were increased from 70 to 70 to be 95 and 90, respectively. However, the other two indexes remain unchanged. Then, the PQI of this road after maintenance can be calculated through equation (5) as  $\text{PQI} = 0.35 \times 95 + 0.35 \times 90 + 0.1 \times 81 + 0.2 \times 90 = 90.85$ . Based on these assumptions, the PQI values after applying different maintenance strategies under different combinations are shown in Table 6.

The corresponding coefficient matrices of  $t_{j,k}$  and  $o_{j,k}$  are shown in Tables 7 and 8, respectively.

**3.3.2. Optimal Maintenance Decision Based on the Calculation Results.** Based on the determined coefficient matrices, the developed model was calculated using lingo software and the optimal maintenance methods were chosen based on the calculation results. The details are shown in Table 9.

It is found from Table 9 that the strategy of structural reinforcement is more preferable than the strategy of pavement rehabilitation for the road sections that are in poor performance. This is expected since the benefits of these two strategies are nearly the same, but the price of rehabilitation is obviously higher than that of structural reinforcement. The method of paving an anti-skid layer is not adopted by the pavements with sufficient skid resistance because this method fails to improve the PCI and RQI indicators. The maximum value of the objective function is 1.73, indicating that 1.73 Yuan of user cost can be saved per unit of pavement maintenance investment. It is worth noting that the total amount of maintenance cost was not limited in the current model. However, the proposed model can be readily modified to take into account the limit-maintenance-cost cases by introducing an additional constraint on the amount of maintenance cost.

TABLE 3: Information on mileage and traffic volume of expressway in the road network.

Road number	1	2	3	4	5	6	7	8	9	10
Mileage (km)	221	105	141	214	138	87	54	165	69	145
Daily traffic volume	15968	25634	17964	9654	14003	20658	10298	18635	22384	17520

TABLE 4: Distributions of different expressway pavement condition combinations in the road network.

Combination	Road number									
	1	2	3	4	5	6	7	8	9	10
1	0.85	0.62	1	1	0.92	0.82	0.86	0.78	0.9	0.85
2	0.05	0.06	0	0	0.08	0.11	0.06	0.09	0.1	0.1
3	0	0	0	0	0	0	0	0	0	0
4	0.1	0.11	0	0	0	0.07	0.08	0.11	0	0.05
5	0	0.06	0	0	0	0	0	0	0	0
6	0	0	0	0	0	0	0	0	0	0
7	0	0.05	0	0	0	0	0	0	0	0
8	0	0.06	0	0	0	0	0	0	0	0
9	0	0	0	0	0	0	0	0	0	0
10	0	0.04	0	0	0	0	0	0.02	0	0
11	0	0	0	0	0	0	0	0	0	0

TABLE 5: Cost of different road sections with different maintenance strategies (10000Yuan/m<sup>2</sup>).

	Road number									
	1	2	3	4	5	6	7	8	9	10
Routine maintenance	5	5	4.5	4.5	5	4	4.5	4	5	4
Paving of overlay	20	20	18	18	20	15	18	15	20	15
Paving of anti-skid layer	15	15	13	13	15	12	13	12	15	12
Pavement reconstruction	50	50	47	47	50	42	47	42	50	42
Structural reinforcement	40	40	36	36	40	32	36	32	40	32

TABLE 6: PQI values after applying different maintenance strategies under different combinations.

Combination	Routine maintenance	Paving of overlay	Paving of anti-skid layer	Pavement reconstruction	Structural reinforcement
1	89.1	92.6	90.5	95	95
2	82.1	92.6	83.5	95	95
3	68.1	90.85	69.5	95	95
4	82.1	90.85	83.5	95	95
5	75.1	90.85	76.5	95	95
6	61.1	89.1	62.5	95	95
7	68.1	83.85	69.5	95	95
8	61.1	83.85	62.5	95	95
9	47.1	82.1	48.5	95	95

TABLE 7: The  $t_{j,k}$  matrix used in the developed model.

Combination	Routine maintenance	Paving of overlay	Paving of anti-skid layer	Pavement reconstruction	Structural reinforcement
1	0	0.0000015	0	0.0000014530	0.0000014530
2	0	0.0000088	0	0.0000088458	0.0000088458
3	0	0.0001232	0	0.0001246440	0.0001246440
4	0	0.0000015	0	0.0000014530	0.0000014530
5	0	0.0000088	0	0.0000088458	0.0000088458
6	0	0.0001232	0	0.0001246440	0.0001246440
7	0	0.0000015	0	0.0000014530	0.0000014530
8	0	0.0000088	0	0.0000088458	0.0000088458
9	0	0.0001232	0	0.0001246440	0.0001246440

TABLE 8: The  $o_{j,k}$  matrix used in the developed model.

Combination	Routine maintenance	Paving of overlay	Paving of anti-skid layer	Pavement reconstruction	Structural reinforcement
1	0	0.6463060	0	0.6463059708	0.6463059708
2	0	0.6463060	0	0.6463059708	0.6463059708
3	0	0.6463060	0	0.6463059708	0.6463059708
4	0	1.1676243	0	1.8139302766	1.8139302766
5	0	1.1676243	0	1.8139302766	1.8139302766
6	0	1.1676243	0	1.8139302766	1.8139302766
7	0	1.4657549	0	3.2939468546	3.2939468546
8	0	1.4657549	0	3.2939468546	3.2939468546
9	0	1.4657549	0	3.2939468546	3.2939468546

TABLE 9: Optimal maintenance methods on the different road sections under different combinations.

Combination	Road number									
	1	2	3	4	5	6	7	8	9	10
1	I	II	II	I	I	II	I	II	II	II
2	I	II			I	II	I	II	II	II
3										
4	II	V				V	II	V		II
5		V								
6										
7		V								
8		V								
9										
10		III						III		
11										

I denotes the routine maintain, II represents paving of overlay, III indicates the paving of anti-skid layer, IV refers to the pavement rehabilitation, and V denotes the structural reinforcement.

#### 4. Conclusions and Outlook

This study presents the development and implementation of a network-level optimization method within a pavement management information system. The network-level optimization method integrates the estimation method of road user costs including the user travel time and vehicle fuel consumption, and it provides the highway agencies the ability to making better and more reasonable managing and making decisions about network-level pavement maintenance. The major conclusions of this study are as follows.

The performance evaluation method of asphalt pavement was optimized to include 11 different combinations. The benefit model of asphalt pavement maintenance was established by taking the user cost into account, which includes cost savings in both user travel time and vehicle fuel consumption. Based on the simplified evaluation method of pavement performance as well as the quantified estimation method of user cost, an optimization model was established. The new model is capable of (1) maximizing the improvements/price ratio of pavement maintenance for the given road network and (2) determining the corresponding strategy of maintenance for any road section in the road network. The optimization model developed in the current study paves the path for the integrating of user travel time and vehicle fuel consumption costs into the application network-level road maintenance decision. It is worth noting

that the model established here can be readily extended for the investigation of more complicated road networks or consideration of other impact factors.

For future research, more components of user cost (e.g., vehicle tire wearing cost and vehicle safety cost) as well as the environment costs including exhaust emission pollution cost and traffic noise pollution cost should be incorporated into the optimization model. The effects of the increase in traffic volume in the following year on the estimation of user costs should be considered.

#### Data Availability

The data used to support the findings of this study are included within the article.

#### Conflicts of Interest

The authors declare that they have no conflicts of interest.

#### Acknowledgments

The financial support from the Fundamental Research Funds for the Central Universities (Grant Project No. 2242021k30034) is gratefully acknowledged.

#### References

- [1] G. Loprencipe, A. Pantuso, and P. Di Mascio, "Sustainable pavement management system in urban areas considering the vehicle operating costs," *Sustainability*, vol. 9, no. 3, p. 453, 2017.
- [2] P. Liu, F. Otto, D. Wang, M. Oeser, and H. Balck, "Measurement and evaluation on deterioration of asphalt pavements by geophones," *Measurement*, vol. 109, pp. 223–232, 2017.
- [3] O. Elbagalati, M. Elseifi, K. Gaspard, and Z. Zhang, "Development of the pavement structural health index based on falling weight deflectometer testing," *International Journal of Pavement Engineering*, vol. 19, no. 1, pp. 1–8, 2018.
- [4] X. Cai, D. Wang, and J. Yu, "Evaluation of the functional performance of paving materials based on the driving wheel pavement analyzer," *Applied Sciences*, vol. 10, no. 7, p. 2410, 2020.
- [5] P. Liu, D. Wang, F. Otto, J. Hu, and M. Oeser, "Application of semi-analytical finite element method to evaluate asphalt pavement bearing capacity," *International Journal of Pavement Engineering*, vol. 19, no. 6, pp. 479–488, 2018.



- [6] J. Zhang, M. Wang, D. Wang, X. Li, B. Song, and P. Liu, "Feasibility study on measurement of a physiological index value with an electrocardiogram tester to evaluate the pavement evenness and driving comfort," *Measurement*, vol. 117, pp. 1–7, 2018.
- [7] P. Liu, V. Ravee, D. Wang, and M. Oeser, "Study of the influence of pavement unevenness on the mechanical response of asphalt pavement by means of the finite element method," *Journal of Traffic and Transportation Engineering*, vol. 5, no. 3, pp. 169–180, 2018.
- [8] K. Kalita and P. Rajbongshi, "Variability characterisation of input parameters in pavement performance evaluation," *Road Materials and Pavement Design*, vol. 16, no. 1, pp. 172–185, 2015.
- [9] A. Fani, A. Golroo, S. Ali Mirhassani, and A. H. Gandomi, "Pavement maintenance and rehabilitation planning optimisation under budget and pavement deterioration uncertainty," *International Journal of Pavement Engineering*, pp. 1–11, 2020.
- [10] M. Jesus, S. Akyildiz, D. R. Bish, and D. A. Krueger, "Network-level optimization of pavement maintenance renewal strategies," *Advanced Engineering Informatics*, vol. 25, no. 4, pp. 699–712, 2011.
- [11] Z. Li, *Multicriteria Highway Programming Incorporating Risk and Uncertainty: A Methodology for Highway Asset Management System*, Purdue University, West Lafayette, IN, USA, 2004.
- [12] Y. Pan, *Mechanism of Pavement Management System*, China Communications Press, Beijing, China, 1998.
- [13] X. Mao, *Research on improvement of expressway pavement maintenance decision*, ph.D. Thesis, Chang'an University, Xi'an, China, 2015.
- [14] J. Santos, A. Ferreira, and G. Flintsch, "An adaptive hybrid genetic algorithm for pavement management," *International Journal of Pavement Engineering*, vol. 20, no. 3, pp. 266–286, 2019.
- [15] C. Blum and A. Roli, "Metaheuristics in combinatorial optimization," *ACM Computing Surveys*, vol. 35, no. 3, pp. 268–308, 2003.
- [16] N. R. Tayebi, F. M. Nejad, and M. Mola, "Comparison between GA and PSO in analyzing pavement management activities," *Journal of Transportation Engineering*, vol. 140, no. 1, pp. 99–104, 2014.
- [17] V. Yepes, C. Torres-Machi, A. Chamorro, and E. Pellicer, "Optimal pavement maintenance programs based on a hybrid greedy randomized adaptive search procedure algorithm," *Journal of Civil Engineering and Management*, vol. 22, no. 4, pp. 540–550, 2016.
- [18] Z. Li and K. C. Sinha, "Methodology for multicriteria decision making in highway asset management," *Transportation Research Record: Journal of the Transportation Research Board*, vol. 1885, no. 1, pp. 79–87, 2004.
- [19] J. C. Chu and K.-H. Huang, "Mathematical programming framework for modeling and comparing network-level pavement maintenance strategies," *Transportation Research Part B: Methodological*, vol. 109, pp. 1–25, 2018.
- [20] F. Xiao, S. Yang, J. Cheng, M. Hou, and C. Wang, "A binary cuckoo search for combinatorial optimization in multiyear pavement maintenance programs," *Advances in Civil Engineering*, vol. 2020, Article ID 8851325, 12 pages, 2020.
- [21] S. Meneses and A. Ferreira, "Pavement maintenance programming considering two objectives: maintenance costs and user costs," *International Journal of Pavement Engineering*, vol. 14, no. 2, pp. 206–221, 2013.
- [22] S. A. Hosseini and O. Smadi, "How prediction accuracy can affect the decision-making process in pavement management system," *Infrastructure*, vol. 6, no. 2, p. 28, 2021.
- [23] D. Astm, *Standard Practice for Roads and Parking Lots Pavement Condition Index Surveys*, Standard Publication, London, UK, 2009.
- [24] S. M. Piryonesi and T. E. El-Diraby, "Examining the relationship between two road performance indicators: pavement condition index and international roughness index," *Transportation Geotechnics*, vol. 26, Article ID 100441, 2021.
- [25] M. China, *Highway Performance Assessment Standards: JTG H20-2007*, Standard Press of China, Beijing, China, 2007.
- [26] M. China, *Highway Performance Assessment Standards: JTG 5210-2018*, Standard Press of China, Beijing, China, 2018.
- [27] Q. Yang and S. Zhou, "Theoretical analysis of pavement deflection response sensitivity under steady-state excitation," *International Journal of Transportation Science and Technology*, 2020.
- [28] M. China, *Technical Specifications for Maintenance of Highway Asphalt Pavement: JTJ 073*, Standard Press of China, Beijing, China, 2001.
- [29] G. S. Becker, "A theory of the allocation of time," *Economic Journal*, vol. 75, pp. 93–517, 1965.
- [30] W. Mark, "A review of British evidence on time and service quality valuations," *Transportation Research Part E*, vol. 37, pp. 107–128, 2001.
- [31] G. Scora and M. Barth, *Comprehensive Modal Emissions Model (CMEM), Version 3.01. User Guide*, Centre for environmental research and technology. University of California, Riverside, CA, USA, 2006.
- [32] K. T. Chau, Y. S. Wong, and C. C. Chan, "Evsim - a PC-based simulation tool for an electric vehicle technology course," *International Journal of Electrical Engineering Education*, vol. 37, no. 2, pp. 167–179, 2000.
- [33] H. C. Frey, N. M. Roupail, H. Zhai, T. L. Farias, and G. A. Gonçalves, "Comparing real-world fuel consumption for diesel- and hydrogen-fueled transit buses and implication for emissions," *Transportation Research Part D: Transport and Environment*, vol. 12, no. 4, pp. 281–291, 2007.
- [34] C. M. Silva, T. L. Farias, H. C. Frey, and N. M. Roupail, "Evaluation of numerical models for simulation of real-world hot-stabilized fuel consumption and emissions of gasoline light-duty vehicles," *Transportation Research Part D: Transport and Environment*, vol. 11, no. 5, pp. 377–385, 2006.
- [35] Y. Zhou and H. R. Zhang, "Research on relation between of surface characteristics and fuel consumption," *Highways*, vol. 1, no. 1, pp. 30–36, 2005.
- [36] M. Wang, Y. Wang, X. Gao, and C. Sweetapple, "Combination and placement of sustainable drainage system devices based on zero-one integer programming and schemes sampling," *Journal of Environmental Management*, vol. 238, pp. 59–63, 2019.
- [37] S. Cao, *Research on Network Maintenance Decision of Expressway Asphalt Pavement Based on Matter Element Analysis*, Master Thesis, Chang'an University, Xi'an, China, 2018.
- [38] Y. Pan, P. Zheng, A. Zheng, S. Bao, and Z. Wu, "Analysis model of investment for major and intermediate maintenance of asphalt pavement," *China Journal of Highway and Transport*, vol. 5, no. 3, pp. 14–21, 1992.



## Research Article

# Mixing Ratios and Cementing Mechanism of Similar Silty Mudstone Materials for Model Tests

Hong-Yuan Fu,<sup>1</sup> Shuang-Xing Qi ,<sup>2</sup> Zhen-Ning Shi ,<sup>3</sup> and Ling Zeng <sup>2</sup>

<sup>1</sup>School of Civil Engineering, National Engineering Laboratory of Highway Maintenance Technology, Changsha University of Science & Technology, Changsha 410114, China

<sup>2</sup>School of Civil Engineering, Changsha University of Science & Technology, Changsha 410114, China

<sup>3</sup>School of Traffic & Transportation Engineering, National Engineering Laboratory of Highway Maintenance Technology, Changsha University of Science & Technology, Changsha 410114, China

Correspondence should be addressed to Ling Zeng; [zl001@csust.edu.cn](mailto:zl001@csust.edu.cn)

Received 8 April 2021; Accepted 31 July 2021; Published 18 August 2021

Academic Editor: Guoyang Lu

Copyright © 2021 Hong-Yuan Fu et al. This is an open access article distributed under the Creative Commons Attribution License, which permits unrestricted use, distribution, and reproduction in any medium, provided the original work is properly cited.

The similarity model test is one of the important means to study the engineering properties of soft rock. This study aims to develop similar materials for silty mudstone, which has characteristics of low strength and water expansion, based on traditional materials including gypsum, barite powder, clay minerals, and distilled water. The orthogonal design method was used to determine the mixing ratios of the similar materials. The density, uniaxial compressive strength, tensile strength, elastic modulus, and Poisson's ratio were selected as control indicators of the similar materials. The results show that the water content is the dominant factor for the density, tensile strength, elastic modulus, and Poisson's ratio of the similar materials of silty mudstone, while the gypsum content is the dominant factor for the uniaxial compressive strength. The physical and mechanical properties of the similar material samples with water content of 19%, barite powder ratio of 32%, and gypsum mass of 250 g show good similarity to those of the raw silty mudstone. The water absorption and expansibility of similar materials with clay mineral ratio of 12% are consistent with those of the raw silty mudstone. The scanning electron microscopy (SEM) observation indicates that the similar material with optimal mixing ratios exhibits a similar microstructure to that of silty mudstone.

## 1. Introduction

Silty mudstone shows obvious characteristics of water absorption and expansion, so its mechanical properties deteriorate easily under a long-term influence of rainfall. As a result, instability often takes place in silty mudstone slopes, which is a major geological problem encountered in the engineering construction in southern China [1–3]. In geotechnical tests, intact samples are often required in order to better consider the influences of single factor or multiple factors. However, natural silty mudstone usually contains numerous joints and fissures due to weathering. Thus, it is difficult to extract completely intact samples without initial random damage. Moreover, the preparation of undisturbed raw samples is quite expensive because of the need for high-precision equipment. If the physical and mechanical

properties are measured from raw rock samples with unknown initial damages, they are not suitable to be used in numerical simulations and guiding practical engineering. Also, because of complicated practical conditions, there are few applicable and cheap field testing approaches for the determination of physical and mechanical properties of silty mudstone.

By contrast, the use of similar materials enables not only eliminating the influence of initial damage but also pre-fabricating fractures. In this way, the influence of different fracture morphology on the strength of rock mass can be analyzed [4–6]. Since similar materials have many advantages, they are widely employed to study the influence of single factor and multiple factors on many scientific problems [7]. For instance, similar materials were employed to prepare specimens for laboratory tests to determine the

physical and mechanical properties of rocks, which are important input parameters for numerical simulations [8, 9]. Similar materials can also be adopted to prepare physical models for similarity model tests, so the connection between models and prototypes can be identified [10, 11]. Finally, the engineering performance of the prototype can be predicted according to the similarity criterion [12, 13].

In recent years, the research results of similar materials of different types of rocks show that the key to improve the similarity between similar materials and raw rocks is to choose the right raw materials and adopt reasonable proportions [14–16]. For example, Yang et al. [17], Chen and Fen [18], Wang et al. [19], Liu and Liu [20], and He et al. [21] among others studied the mixing ratios of similar materials for different types of soft rocks, such as red-bed soft rock, carbonaceous phyllite rock, and coal rock. The above scholars first selected appropriate raw materials and used orthogonal tables to design the mixing ratios of similar materials. Secondly, uniaxial compression tests, splitting tests, and triaxial compression tests were conducted to measure the physical and mechanical properties of similar materials. Then, compared with different types of target rocks, similar rock-like materials suitable for various types of target rocks were determined. Finally, the optimal mixing ratio that satisfies the similarity was obtained [22, 23]. In addition, Wang et al. [24] carried out creep tests on the similar developed materials of a soft rock. The authors stated that the creep parameters of similar materials basically met the similarity with the raw rock by parameter inversion, laying a foundation for similar materials to simulate the creep characteristics of the soft rock. Chu et al. [25] developed a similar material that conforms to the rheology of soft rock, which can be used to simulate the rheological characteristics of soft sandy mudstone. Although the scholars mentioned above have studied the similar materials of soft rocks and their related characteristics, the research on the characteristics of water absorption and expansion of similar materials for soft rocks is rarely involved.

In the process of designing similar materials, the cementation is an important means to make similar material samples reach the strength of the raw rock. Gypsum, as a common cementing material, is widely used in the development of similar materials of soft rocks. Existing studies have shown that the strength of similar materials formed by gypsum cementation can simulate the diagenetic strength of various raw rocks under geological actions [26, 27]. In addition, some scholars have carried out many investigations of the cementation of clay minerals. For instance, Xie et al. [28] analyzed the microstructure of attapulgite by scanning electron microscopy (SEM); they concluded that the cementation performance of clay minerals was inseparable from the microstructure. Yang et al. [29] analyzed the microstructure of cementing products by means of SEM. Therefore, the similar materials formed by cementation can meet the requirements of simulating the strength of raw soft rocks, and the cementation mechanism can be revealed via SEM.

This paper presents an experimental work to develop similar materials of silty mudstone for physical model tests. Gypsum and barite powder are selected as the cementing

material and aggregate, respectively, and clay minerals (i.e., illite, montmorillonite, and chlorite) are used as swelling additives. Firstly, a series of mixing ratios are designed according to an orthogonal table. Secondly, the physical and mechanical properties of similar materials of various mixing ratios are studied by laboratory tests; the influences of different factors on the properties are examined by sensitive analysis. Afterward, the water absorption and expansibility of similar materials are measured. Therefore, the mixing ratios that can satisfy the mechanical properties and the water-expansion characteristic of silty mudstone are obtained. Finally, the cementing mechanism of similar materials of silty mudstone is revealed by SEM. The similar developed material can well simulate the engineering behavior of silty mudstone, which lays a foundation for the similarity model tests of engineering cases involved in silty mudstone.

## 2. Design of Similar Materials

**2.1. Similarity Ratio.** The dimensional analysis method was used to determine the similarity ratios of properties of the similar material to those of the raw rock. Based on the three basic dimensions, that is, length (L), time (T), and mass (M), the dimensions of other important physical and mechanical properties were deduced. In this study, the similarity ratios in terms of length (L), time (T), and mass (M) are considered to be 1, which means the length, time, and mass involving similar materials are exactly the same as those of the raw rock. Then, the similarity ratios of other properties can be obtained, as shown in Table 1. Therefore, the target properties of similar materials are derived from the properties of the raw rock based on the similarity ratios [13, 14].

**2.2. Material Selection.** The strongly weathered silty mudstone collected from the Yuelu Mountain (Changsha, China) was selected as the prototype. X-ray diffraction analysis showed that silty mudstone is mainly composed of quartz, illite, montmorillonite, chlorite, and feldspar, as shown in Figure 1 and Table 2. According to Editorial Board of Engineering Geology Handbook [30], the density, uniaxial compressive strength, tensile strength, elastic modulus, and Poisson's ratio are the most important properties of silty mudstone. Thus, these physical and mechanical properties were used as the controlling indicators to design similar materials (see Table 3).

Previous studies showed the possibility to produce similar materials of rocks with gypsum, barite powder, and clay [26, 27, 31]. Therefore, barite powder, gypsum, and clay minerals were selected to develop similar materials of silty mudstone. Among the above materials, barite powder works as aggregate, gypsum serves as the cementing agent, and clay minerals (montmorillonite : illite : chlorite = 1 : 0.14 : 0.23, which is consistent with proportions of the raw rock) are used as swelling additives to control the water-absorption and water-expansion characteristics of similar materials. Deionized water was also adopted to form similar materials. The grain size distributions of the above raw materials are shown in Figure 2.

TABLE 1: Dimensional analysis.

Property	Dimension	Similar relationship	Similarity ratio
Length	(L)	$C_L$	1
Time	(T)	$C_T$	1
Mass	(M)	$C_M$	1
Density	$(M)(L)^{-3}$	$C_\rho$	1
Tensile strength	$(M)(L)^{-1}(T)^{-2}$	$C_M C_T^{-1} C_L^{-2}$	1
Uniaxial compressive strength	$(M)(L)^{-1}(T)^{-2}$	$C_M C_T^{-1} C_L^{-2}$	1
Modulus of elasticity	$(M)(L)^{-1}(T)^{-2}$	$C_M C_T^{-1} C_L^{-2}$	1
Poisson's ratio	(1)	1	1

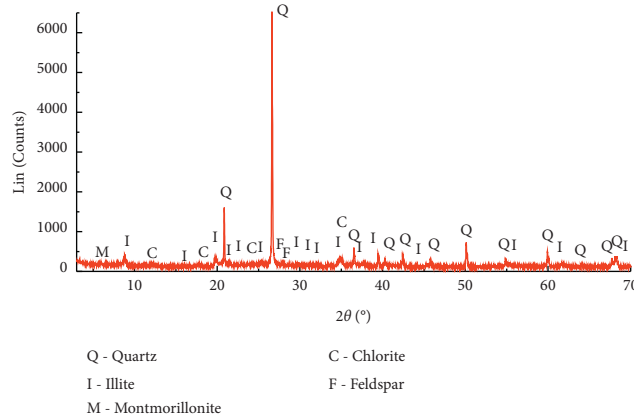


FIGURE 1: X-ray diffraction pattern of silty mudstone.

TABLE 2: Mineral compositions of silty mudstone.

Quartz (%)	Illite (%)	Montmorillonite (%)	Chlorite (%)	Feldspar (%)	Other (%)
49.3	27.1	3.7	6.3	4.1	<1

TABLE 3: Main physical and mechanical properties of silty mudstone.

Density $\rho$ (g/cm <sup>3</sup> )	Uniaxial compressive strength $\sigma_c$ (MPa)	Tensile strength $\sigma_t$ (MPa)	Modulus of elasticity $E$ (GPa)	Poisson's ratio $\nu$
2.01	13.95	1.24	1.38	0.22

**2.3. Orthogonal Design Scheme.** The orthogonal design was employed to study the mixing ratios in order to improve the efficiency of developing similar materials. The evaluated properties included the density, uniaxial compressive strength, tensile strength, elastic modulus, and Poisson's ratio. The orthogonal test design is an efficient, fast, and economic method for experimental design with the consideration of multiple factors and levels [32]. With this method, one can obtain the best combination of levels for different factors with a small number of samples based on an orthogonal array.

Because the content of every component has a dominant influence on the physical and mechanic properties of similar materials [13], the water content, barite powder ratio, gypsum mass, and clay mineral ratio were chosen as factors in the orthogonal test design. The barite powder ratio is the ratio of the mass of barite powder to the total mass of gypsum and barite powder, and the clay mineral ratio is the mass ratio of clay minerals to all solid components. After a large number of trial tests, the suitable levels of the four factors that could make similar materials have close physical

and mechanical properties as the raw rock are as follows: water content (factor A) = 23%–17%, barite powder ratio (factor B) = 44%–26%, gypsum mass (factor C) = 225 g–300 g, and clay mineral ratio (factor D) = 0%–18%.

The specific experimental schemes are shown in Table 4. During the experiment, each test scheme was repeated four times, and the average value was taken for analysis. Since the materials were reconstituted artificial rocks that had quite homogeneous structures, four parallel tests were basically enough to characterize their main properties [19, 33].

**2.4. Secondary Refinement Test Scheme.** Silty mudstone has obvious water-absorption and water-expansion characteristics. Some scholars pointed out that the disintegration of mudstone is caused by water expansion of rock, dissolution of cementing substance, and wetting-heating cycles [34].

It was reported that clay minerals have a great influence on water absorption and expansion of soils [35]. Thus, secondary refinement test schemes were considered in order

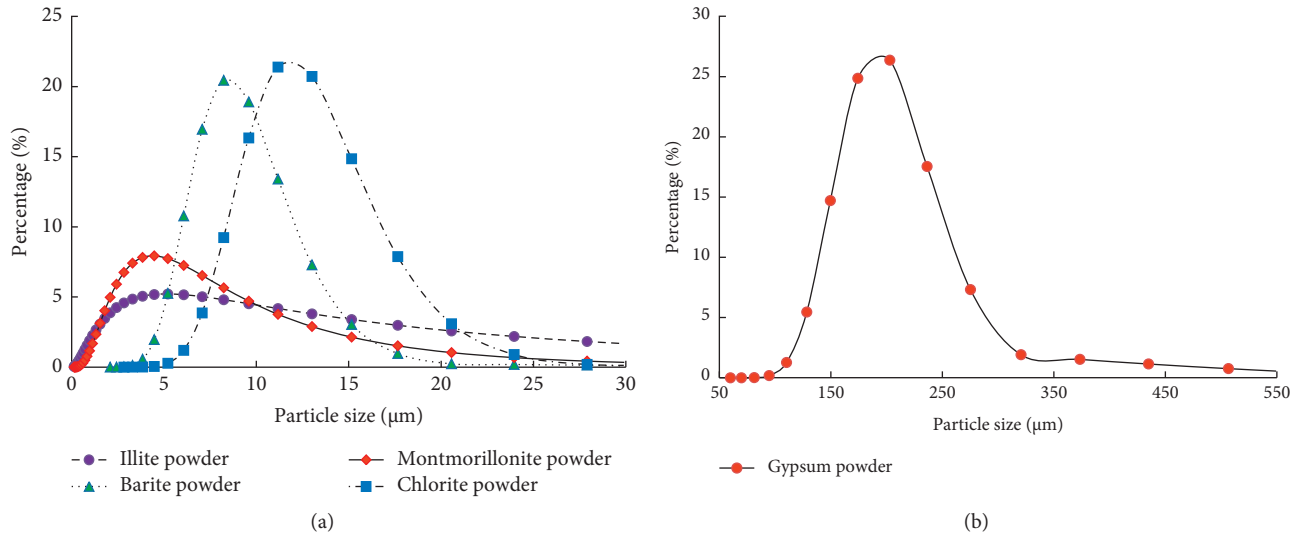


FIGURE 2: Particle size distributions of different raw materials: (a) clay minerals and barite powder; (b) gypsum powder.

TABLE 4: Experimental scheme.

Scheme	Factor			
	A (water content, %)	B (barite powder ratio, %)	C (gypsum mass, g)	D (clay mineral ratio, %)
1	23 (level 1)	44 (level 1)	225 (level 1)	0 (level 1)
2	23	38 (level 2)	250 (level 2)	6 (level 2)
3	23	32 (level 3)	275 (level 3)	12 (level 3)
4	23	26 (level 4)	300 (level 4)	18 (level 4)
5	21 (level 2)	44	250	12
6	21	38	225	18
7	21	32	300	0
8	21	26	275	6
9	19 (level 3)	44	275	18
10	19	38	300	12
11	19	32	225	6
12	19	26	250	0
13	17 (level 4)	44	300	6
14	17	38	275	0
15	17	32	250	18
16	17	26	225	12

to examine the water-absorption and water-expansion characteristics of similar materials at varying factor D (clay mineral ratio) (Table 5). If the relationship between the water-absorption and water-expansion characteristics and clay mineral ratios is determined, the design of a similar material that has the same water-absorption and water-expansion characteristics as the raw rock can be realized by simply adjusting the clay mineral ratio. Water-absorption tests and expansibility tests were carried out to measure the water-absorption and water-expansion characteristics.

### 3. Experimental Details

**3.1. Sample Preparation.** A standardized method was designed to reduce the interference of human factors in the process of sample preparation. According to the IRSM [36], cylindrical samples for uniaxial compression tests had

diameters of 50 mm and heights of 50 mm, and those for splitting tests had diameters of 50 mm and heights of 100 mm.

The standardized procedure for sample preparation is illustrated in Figure 3. To prepare the sample, solid materials (see Table 3) were added to the stirring tank and mixed at a constant speed for 5 min and then deionized water was added to the solid materials and they were mixed again for 5 min. Afterward, the formed mixture was filled into a mold in three layers, and each layer was statically compacted for 2 min using the YAW-300 press machine produced by Jinan Zhongluchang Testing Machine Manufacturing Company (Figure 4(a)). Subsequently, the sample together with the mold was placed into a curing box at a temperature of  $20 \pm 3^\circ\text{C}$  and a humidity of 95% for 24 h. After demolding, the sample was continuously cured for 28 d. Finally, the samples with smooth surfaces and without obvious defects were selected.

TABLE 5: Secondary refinement test scheme of similar materials.

Scheme	Factor			
	A (water content %)	B (barite powder ratio %)	C (gypsum mass g)	D (clay mineral ratio %)
S1	19	32	250	0
S2	19	32	250	6
S3	19	32	250	12
S4	19	32	250	18

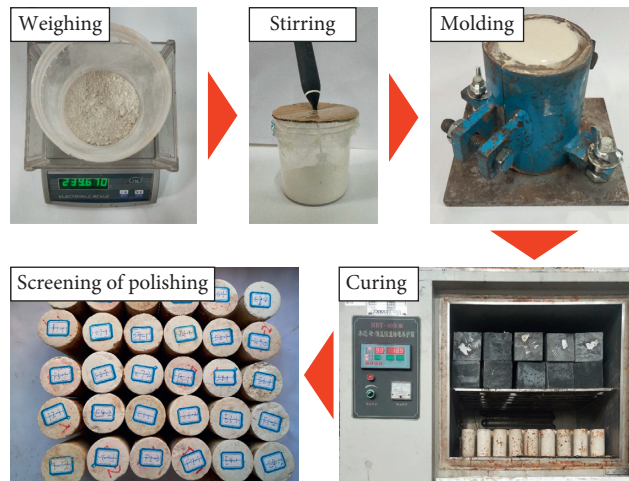


FIGURE 3: Sample preparation process.

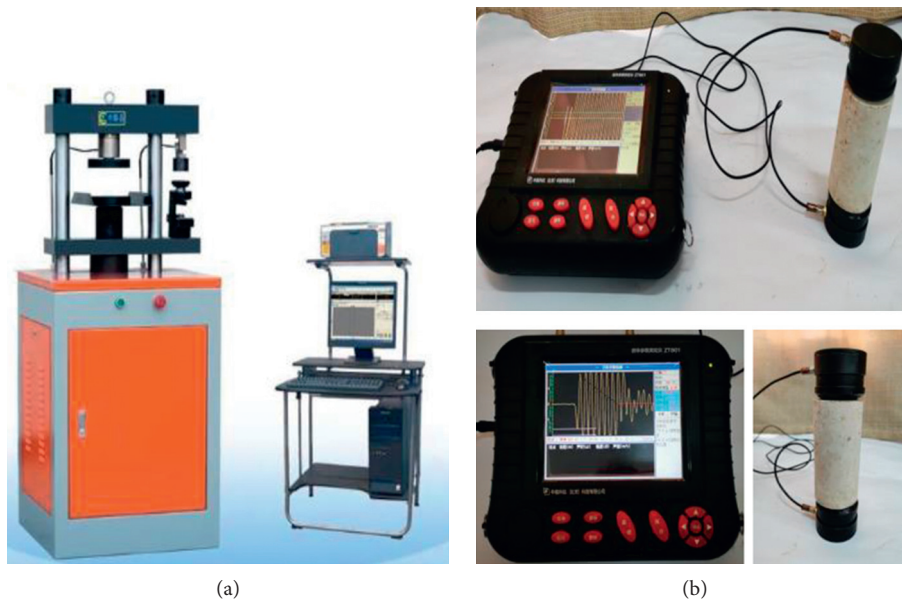


FIGURE 4: Continued.



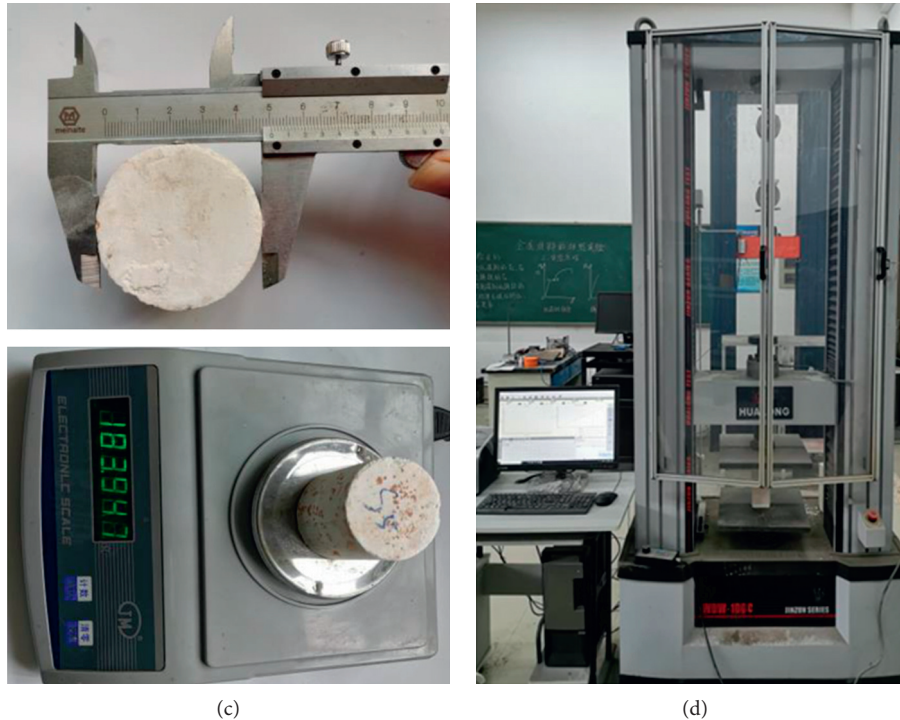


FIGURE 4: Testing equipment: (a) YAW-300 press machine; (b) ZT801 ultrasonic wave velocity tester; (c) vernier caliper and electronic balance; (d) universal pressure testing machine.

**3.2. Sample Screening.** In the process of making similar materials, some defects may exist in the samples because of nonuniform stirring, big air bubbles, and other uncontrollable factors. In particular, internal defects cannot be discerned by the naked eye. The existence of defects that vary from sample to sample will definitely bring about errors to the experimental results. According to the existing research, the physical properties of the rock itself can affect the propagation speed of ultrasonic waves in rocks [3, 37]. Therefore, the physical and mechanical properties of rock can be inferred indirectly by measuring the velocity of ultrasonic wave in rock mass [38–40].

In the current study, the velocities of ultrasonic waves in all similar material samples were detected by the rock mass parameter tester ZT801 (Figure 4(b)). The specific test results are presented in Table 6. It shows that the ultrasonic wave velocities of the similar materials fall between 2.84 km/s and 3.25 km/s. The samples in each scheme have very close ultrasonic wave velocities, which ensure that these samples have similar initial conditions.

### 3.3. Experimental Methods

**3.3.1. Physical and Mechanical Tests.** The density, uniaxial compressive strength, tensile strength, elastic modulus, and Poisson's ratio of the samples were measured using the samples prepared according to the orthogonal design table (Table 4).

The density of each sample was measured before mechanical tests. As shown in Figure 4(c), the volume of each

sample was determined by a vernier caliper with precision of 0.02 mm, while the mass was weighed using an electronic balance with precision of 0.01 g.

Uniaxial compression tests and splitting tests were conducted via a universal pressure testing machine (see Figure 4(d)). Cylindrical samples for uniaxial compression tests had diameters of 50 mm and heights of 50 mm [36, 41]. The maximum load and the accuracy of the testing machine are 100 kN and 0.001 N, respectively. The whole test process is in accordance with the Chinese specification (GB/T 50266-2013). The loading rates were 0.8 MPa/s and 0.4 MPa/s for uniaxial compression tests and splitting tests, respectively.

According to the method recommended by GB/T 50266-2013 [42], the elastic modulus can be estimated based on the slope of the stress-strain curve obtained by uniaxial compression tests. Poisson's ratio was measured via the resistance strain gauge method [43, 44]. In this method, the ratio of transverse strain increment to longitudinal strain increment was measured, and thus Poisson's ratio of each sample could be calculated.

#### 3.3.2. Water-Absorption Tests and Expansibility Tests.

The water absorption and saturated water absorption of the rock and similar materials were measured by free water-absorption tests [42, 45]. Five raw rock samples or similar material samples were used for each test scheme. The main testing procedures were as follows:

- (1) The sample was put in the oven at a temperature of 105°C–110°C. After drying for 12–24 h, the sample

TABLE 6: Ultrasonic wave velocities of similar material samples.

Scheme	Sample 1 (km/s)	Sample 2 (km/s)	Sample 3 (km/s)	Sample 4 (km/s)	Sample 5 (km/s)	Difference (km/s)
1	2.98	2.99	3.00	2.99	2.99	0.01
2	2.91	2.90	2.98	3.06	3.01	0.16
3	2.96	2.94	3.02	3.05	3.10	0.16
4	2.94	2.95	2.97	2.96	2.96	0.03
5	2.92	2.95	3.01	3.05	3.02	0.12
6	3.15	3.14	3.25	3.18	3.21	0.12
7	2.99	2.97	3.01	3.01	3.04	0.07
8	2.86	2.84	2.90	2.96	2.90	0.12
9	3.10	3.12	3.08	3.00	3.13	0.13
10	2.97	2.94	2.91	2.91	2.90	0.06
11	3.05	3.07	2.99	2.99	3.01	0.08
12	3.08	3.09	3.03	3.05	3.00	0.10
13	3.00	2.99	2.97	3.00	2.99	0.03
14	2.97	2.99	2.98	2.99	2.99	0.02
15	3.00	3.01	3.06	3.09	3.01	0.09
16	2.97	2.98	2.98	2.98	2.95	0.04

was taken out and cooled down to the room temperature ( $20^{\circ}\text{C} \pm 2^{\circ}\text{C}$ ). The mass ( $m_d$ ) of the sample is then recorded (accuracy: 0.01 g).

- (2) Determination of the natural water absorption: first, the dried sample was placed in a water container. Then, water was filled to 1/4 of the height of the sample. Two hours later, water was filled into the container to reach a level between 1/2 and 3/4 of the height of the sample. After 6 h, water was continuously added to a height of 20 mm above the top surface of the sample. In this way, the air in the sample could escape easily. After 48 h immersion in water, the sample was taken out, and the surface water was wiped off with a piece of wet gauze. The sample mass ( $m_1$ ) was measured again. Thus, the water absorption can be calculated by

$$w_a = \frac{m_1 - m_d}{m_d} \times 100, \quad (1)$$

where  $w_a$  is the water absorption of the sample.

- (3) Determination of the saturated water absorption: the dried sample was placed in a vacuum container, and the water level inside the container was 20 mm higher than the top surface of the sample. Then, a vacuum pump was started to evacuate the container. The vacuum pressure should reach and remain at 100 kPa for not less than 4 h. Afterward, the specimen was remained in the container for 4 h at the atmosphere pressure. Then the specimen was taken out and dried with a piece of wet gauze. Finally, the mass ( $m_2$ ) of the sample was measured. The water absorption can be calculated by the following expression:

$$w_{\text{sat}} = \frac{m_2 - m_d}{m_d} \times 100, \quad (2)$$

where  $w_{\text{sat}}$  is the saturated water absorption of the sample.

Free water-expansion tests were also conducted in order to evaluate the water-expansion characteristic of similar materials and the raw rock (JTG E41-2005). Five samples were used for each test scheme in Table 5. The free expansion rate of the material was defined as

$$P_H = \frac{\Delta H}{H} \times 100, \quad (3)$$

where  $P_H$  is the axial free expansion rate;  $\Delta H$  is the axial deformation of the sample;  $H$  is the initial axial height of the sample.

**3.3.3. SEM Observations.** Scanning electron microscopy (SEM) observations were performed to examine the microstructure of similar materials and further confirm the similarity in water-absorption and water-expansion properties, since they are highly dependent on pore structures. SEM observations were conducted on the horizontal and vertical planes on the small specimens extracted from the cylindrical samples for secondary refinement tests (Table 5). Two cuboids with dimensions of 20 mm  $\times$  10 mm  $\times$  10 mm were extracted from the core of each sample [37, 46]. The longitudinal directions of the cuboids were parallel or perpendicular to the axial direction of the cylindrical sample. This method for small-sample extractions is similar to that presented in the work of Gao et al. [46, 47]. Before SEM observations, the observation planes of the sample were coated with thin layers of gold under vacuum. The purpose was to make the plane electrically conductive in order to prevent any charge build-up on the sample. Thereafter, the sample was placed in the chamber of a scanning electron microscope (ZEISS EVO MA10) for observation. A series of SEM images with different magnifications were saved from typical areas in the observation plane of each sample. Finally, the surface morphology (e.g., pore sizes and porosity) of the sample was analyzed following the method described in the work of Gao et al. [48].

## 4. Results and Discussion

**4.1. Mixing Ratios for Similarity in Physical and Mechanical Properties.** In this section, the influences of various factors (i.e., A, water content; B, barite powder ratio; C, gypsum mass; and D, clay mineral ratio) on the physical and mechanical properties (i.e., the density, uniaxial compressive strength, tensile strength, elastic modulus, and Poisson's ratio) of similar materials are examined. Then, the optimal mixing ratios for similar materials to have similar physical and mechanical behaviors to those of the raw silty mudstone are determined. In addition, typical stress-strain curves and failure modes of similar materials and the raw rock after uniaxial compression tests are compared and discussed.

**4.1.1. Results of Physical and Mechanical Tests.** Table 7 summarizes the mean results of parallel samples in each test scheme arranged according to the orthogonal design. It shows that the density of the prepared similar materials varies from 1.82 to 2.08 g/cm<sup>3</sup>, the range of uniaxial compressive strength is between 8.28 and 18.19 MPa, and the tensile strength falls between 1.01 and 4.00 MPa. It is also observed that the elastic modulus changes from 1.01 to 2.38 GPa, and Poisson's ratio ranges from 0.20 to 0.40. Comparing the results in Table 7 with those in Table 3, one can note that the properties (target values) of silty mudstone are covered by the data of similar materials. This confirms that the physical and mechanical behaviors of silty mudstone can be simulated with similar materials.

**4.1.2. Sensitivity Analysis.** Range analysis and variance analysis are conducted to investigate the sensitivity of physical and mechanical properties to various factors.

(1) Sensitivity analysis of factors affecting rock density: As can be seen from Table 8 and Figure 5, factor A (water content) and factor C (gypsum mass) have the greatest influence on the density of similar materials. According to the rank, the influence degree of each factor on the density of similar materials is  $A \approx C > B \approx D$ . Thus, the main controlling factors that influence the density of similar materials are factor A (water content) and factor C (gypsum mass).

The results of variance analysis of the density are shown in Table 8. Under the condition of a confidence level of 0.1, the critical value of significance is 5.390. It is observed that factors A (water content) and C (gypsum mass) had significant influences on the density of similar materials, while factors B (barite powder ratio) and D (clay mineral ratio) showed fewer influences. This is consistent with the result of range analysis (Table 9).

As shown in Table 3, the average density of the raw rock is 2.01 g/cm<sup>3</sup>. This target value is between the results of similar materials when the evaluation index is  $K_2$  and  $K_3$  regarding factor A, and it equals the result when the evaluation index is  $K_2$  regarding factor C (Table 8). Thus, the suitable factor A (water content) is 19% (level 2) and 21%

(level 3), and the optimal factor C (gypsum mass) is 250 g (level 2) in order to bring such a target physical property to similar materials.

(2) Sensitivity analysis of factors affecting uniaxial compressive strength: Table 10 and Figure 6 show that factor C (gypsum mass) has the highest influence and factor D (clay mineral ratio) has the second highest influence on the uniaxial compressive strength of similar materials. According to the rank, the influence degree of each factor on the uniaxial compressive strength of similar materials is  $C \approx D > A \approx B$ . The analysis indicates that factors C (gypsum mass) and D (clay mineral ratio) play a leading role in controlling the uniaxial compressive strength of similar material samples.

Table 11 shows the results of variance analysis of the uniaxial compressive strength of similar materials. One can note that, as far as uniaxial compressive strength is concerned, the influences of those examined factors on uniaxial compressive strength are all not so significant.

(3) Sensitivity analysis of factors affecting tensile strength: Table 12 and Figure 7 present the results of range analysis of the tensile strength of similar materials. It is noted that factor A (water content) has the greatest influence on the tensile strength of similar materials. According to the influence degree of each factor on the tensile strength, the factors are ranked as  $A > B > D > C$ . The analysis shows that factor A (water content) and factor B (barite powder ratio) play a dominant role in controlling the tensile strength of similar material samples.

Table 13 lists the results of variance analysis of the tensile strength of similar materials. One can note that factor A (water content) and factor B (barite powder ratio) have significant influence on the tensile strength, while the other factors show limited influences. This is also in agreement with the result of range analysis (Table 12).

(4) Sensitivity analysis of factors affecting elastic modulus. It is observed from Table 14 and Figure 8 that factor A (water content) has the most significant influence on the elastic modulus of similar materials. According to the rank, the influence degree of each factor on the elastic modulus of similar material samples is  $A > D \approx B > C$ . The analysis shows that factor A (water content) plays a dominant role in controlling the elastic modulus of similar material samples. The relationship between other factors and the elastic modulus of the sample is not very obvious.

Furthermore, according to the results of variance analysis (Table 15), it is noted that factor A (water content) has a significant influence on the tensile strength, while other factors do not show significant influences, which confirms the results of range analysis.

As shown in Table 3, the average elastic modulus of the raw rock is 1.38 GPa. Combined with Table 15 and Table 4, one can conclude that the optimal water content is 19% in order to prepare a similar material that has similar elastic modulus as the raw silty mudstone.

(5) Sensitivity analysis of factors affecting Poisson's ratio: Based on the results shown in Table 16 and Figure 9, one can rank the examined factors as  $A \approx D \approx B \approx C$  according to the degree of their influences on Poisson's ratio of similar

TABLE 7: Physical and mechanical properties of similar materials.

Scheme	Density $\rho(\text{g/cm}^3)$	Uniaxial compressive strength $\sigma_c$ (MPa)	Tensile strength $\sigma_t$ (MPa)	Elastic modulus $E$ (GPa)	Poisson's ratio $\nu$
1	1.95	13.54	2.94	1.74	0.28
2	1.91	11.91	3.33	1.61	0.23
3	1.84	10.74	2.72	1.40	0.27
4	1.82	11.65	4.00	1.35	0.25
5	2.05	10.22	1.99	1.64	0.40
6	2.08	18.19	2.08	2.38	0.20
7	1.97	9.01	1.47	1.60	0.27
8	1.89	12.74	2.89	1.81	0.38
9	2.08	8.28	1.01	1.07	0.21
10	1.92	9.24	1.70	1.38	0.22
11	2.05	14.18	1.61	1.33	0.23
12	2.05	12.24	2.84	1.29	0.21
13	2.01	13.69	3.73	1.96	0.38
14	1.99	13.09	3.92	1.34	0.31
15	2.02	13.58	3.05	1.33	0.22
16	2.08	10.47	3.81	1.01	0.21

TABLE 8: Range analysis of rock density.

Evaluation indexes	Density ( $\text{g/cm}^3$ )			
	Factor A (water content)	Factor B (barite powder ratio)	Factor C (gypsum mass)	Factor D (clay mineral ratio)
$K_1$	1.88	2.02	2.04	1.99
$K_2$	2.00	1.98	2.01	1.97
$K_3$	2.03	1.97	1.95	1.97
$K_4$	2.03	1.96	1.93	2.00
Range value $R$	0.15	0.06	0.11	0.04
Rank	1	3	2	4

Note.  $K_i$  ( $i = 1, 2, 3, 4$ ) represents the mean of the density values corresponding to level  $i$  of a factor;  $R = \max(K_i) - \min(K_i)$  ( $i = 1, 2, 3, \text{ and } 4$ ).

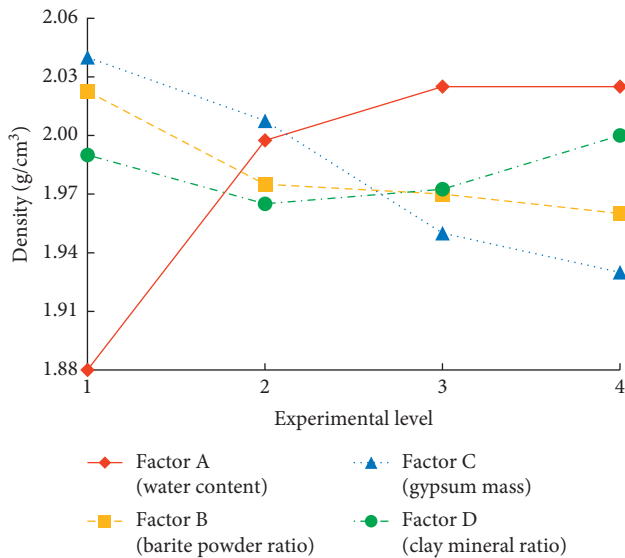


FIGURE 5: Range analysis of the factors affecting density.

material samples. Therefore, Poisson's ratio is hard to judge by factors A–D.

The results of variance analysis shown in Table 17 indicate that, regarding Poisson's ratio, the influences of all factors are not significant. This is consistent with the results of range analysis.

Based on the above sensitivity analyses, the optimal mixing ratios of similar materials that show good similarity to those of the raw silty mudstone in terms of the physical and mechanical properties are determined. The optimal water content is 19%, the optimal barite powder ratio is 32%, and the optimal gypsum mass is 250 g. However, factor D (clay mineral ratio) is still not determined because it has no clear contribution to the above physical and mechanical properties of similar materials.

4.1.3. *Typical Stress-Strain Curves and Failure Characteristics.* Figure 10(a) presents typical stress-strain curves of similar materials and silty mudstone obtained from uniaxial compression tests. Figure 10(b) illustrates the corresponding failure modes of the samples.

A comparative analysis of the failure modes of similar material samples and the raw rock is conducted. The silty mudstone sample shows an obvious shear failure after uniaxial compression tests, which is in line with the results reported [49]. It is also noted that the shear failure modes of similar material samples are quite similar to those of the raw rock under uniaxial compression tests (Figure 10).

4.2. *Mixing Ratios for Similarity in Water Absorption and Expansion.* In this section, the influence of factor D (clay mineral ratio) on the water-absorption and water-expansion

TABLE 9: Variance analysis of density.

Factor	A (water content)	B (barite powder ratio)	C (gypsum mass)	D (clay mineral ratio)	Error
Variance value $S^2$	0.057	0.009	0.031	0.003	0
Degrees of freedom $F$	3	3	3	3	3
Univariate significance	19.000 Significant	3.000 Insignificant	10.333 Significant	1.000 Insignificant	

Note.  $S^2$  represents the mean of the density variance value corresponding to level  $i$  of a factor;  $S^2 = \sum_{i=1}^4 (K_i - (1/4) \sum_{i=1}^4 K_i)^2/5$ .

TABLE 10: Range analysis of uniaxial compressive strength.

Evaluation indexes	Uniaxial compressive strength (MPa)			
	Factor A (water content)	Factor B (barite powder ratio)	Factor C (gypsum mass)	Factor D (clay mineral ratio)
$K_1$	11.96	11.43	14.10	11.97
$K_2$	12.54	13.11	11.99	13.13
$K_3$	10.99	11.88	11.21	10.17
$K_4$	14.71	11.78	10.90	13.13
Range value $R$	1.72	1.68	3.20	2.96
Rank	3	4	1	2

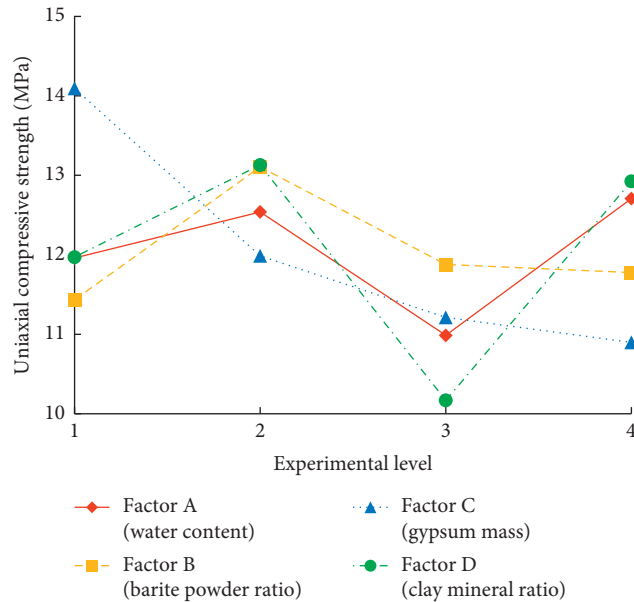


FIGURE 6: Range analysis of the factors affecting uniaxial compressive strength.

TABLE 11: Variance analysis of uniaxial compressive strength.

Factor	A (water content)	B (barite powder ratio)	C (gypsum mass)	D (clay mineral ratio)	Error
Variance value $S^2$	7.259	6.420	24.862	21.929	222.47
Degrees of freedom $F$	3	3	3	3	3
Univariate significance	0.033 Insignificant	0.029 Insignificant	0.112 Insignificant	0.099 Insignificant	

characteristics of similar materials is analyzed. Most importantly, the optimal level of factor D (clay mineral ratio) is determined.

As shown in Figure 11, the average natural water absorption of the raw silty mudstone is 10.85%, and the average saturated water absorption is 11.83%. According to the secondary refinement test scheme, the average natural

water absorption rates of similar material samples in schemes S1–S4 with different clay mineral ratios are 8.41%, 9.82%, 10.86%, and 11.52%, respectively. The average saturated water absorption is 9.89%, 10.85%, 11.84%, and 12.33%, respectively. Moreover, the average natural water absorption and saturated water absorption of similar material samples increase with the increase of clay mineral



TABLE 12: Range analysis of tensile strength.

Evaluation indexes	Tensile strength (MPa)			
	Factor A (water content)	Factor B (barite powder ratio)	Factor C (gypsum mass)	Factor D (clay mineral ratio)
$K_1$	3.25	2.42	2.61	2.79
$K_2$	2.11	2.76	2.81	2.89
$K_3$	1.79	2.21	2.64	2.56
$K_4$	3.63	3.39	2.73	2.54
Range value $R$	1.84	1.17	0.19	0.36
Rank	1	2	4	3

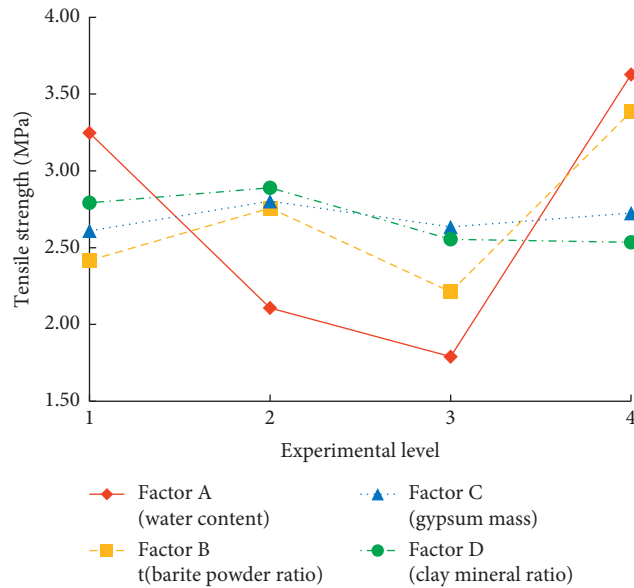


FIGURE 7: Range analysis of the factors affecting tensile strength.

TABLE 13: Variance analysis of tensile strength.

Factor	A (water content)	B (barite powder ratio)	C (gypsum mass)	D (clay mineral ratio)	Error
Variance value $S^2$	9.356	3.159	0.093	0.371	0.090
Degrees of freedom $F$	3	3	3	3	3
Univariate significance	Significant	Significant	Insignificant	Insignificant	

TABLE 14: Range analysis of elastic modulus.

Evaluation indexes	Elastic modulus (GPa)			
	Factor A (water content)	Factor B (barite powder ratio)	Factor C (gypsum mass)	Factor D (clay mineral ratio)
$K_1$	1.53	1.60	1.62	1.49
$K_2$	1.86	1.68	1.48	1.68
$K_3$	1.27	1.42	1.41	1.36
$K_4$	1.41	1.37	1.57	1.53
Range value $R$	0.59	0.31	0.21	0.32
Rank	1	3	4	2

ratio. Therefore, the change of clay mineral ratio enables controlling the water absorption of similar materials. Based on the test data, one can note that the average water absorption of the similar material samples in the third test scheme S3 is the closest to the average value of the raw rock (the error is less than 1%).

Figure 12 shows that the variation curve of free expansion rates of similar material samples and silty mudstone can be divided into three stages. The first is the rapid expansion stage ( $t < 2$  h), during which the average axial expansion rates of similar material samples with different clay mineral ratios and raw rocks increase rapidly to the final

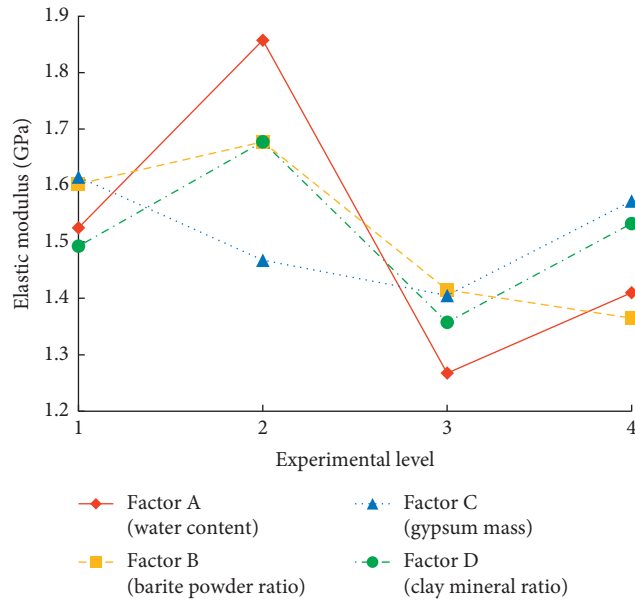


FIGURE 8: Range analysis of the factors affecting elastic modulus.

TABLE 15: Variance analysis of elastic modulus.

Factor	A (water content)	B (barite powder ratio)	C (gypsum mass)	D (clay mineral ratio)	Error
$S^2$	0.759	0.266	0.111	0.208	0.110
Degrees of freedom $F$	3	3	3	3	3
Univariate significance	6.838	2.396	1.000	1.874	
	Significant	Insignificant	Insignificant	Insignificant	

TABLE 16: Range analysis of Poisson's ratio.

Evaluation indexes	Poisson's ratio			
	Factor A (water content)	Factor B (barite powder ratio)	Factor C (gypsum mass)	Factor D (clay mineral ratio)
$K_1$	0.26	0.32	0.23	0.27
$K_2$	0.31	0.24	0.27	0.31
$K_3$	0.22	0.25	0.29	0.28
$K_4$	0.28	0.26	0.28	0.22
Range value $R$	0.10	0.08	0.06	0.09
Rank	1	3	4	2

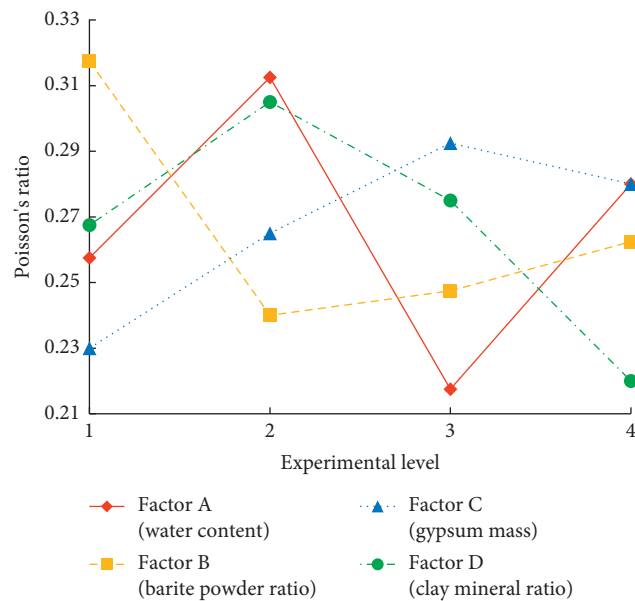
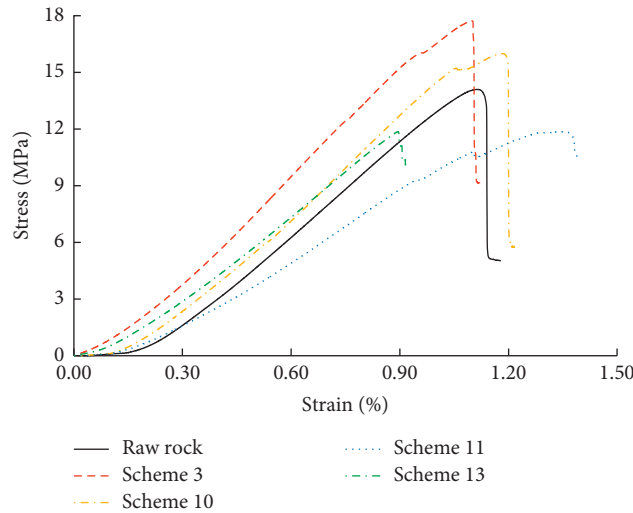


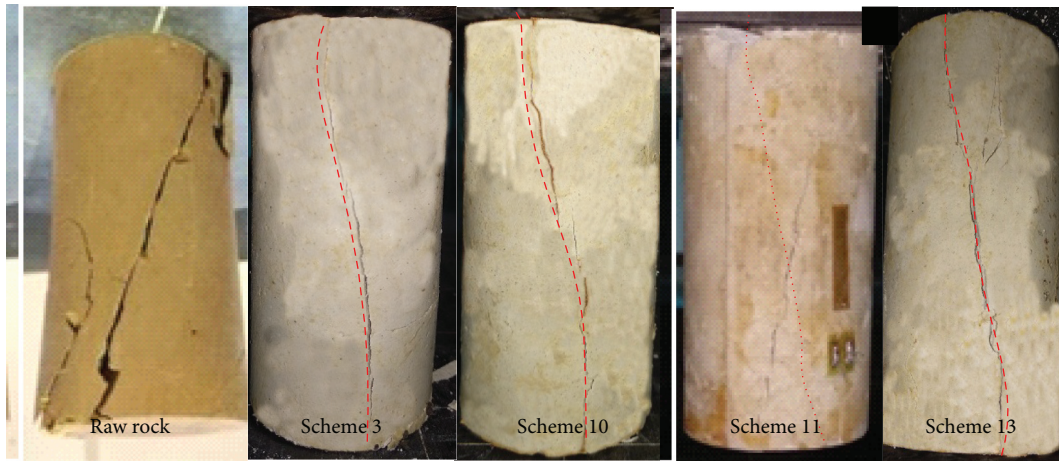
FIGURE 9: Range analysis of the factors affecting Poisson's ratio.

TABLE 17: Variance analysis of Poisson’s ratio.

Factor	A (water content)	B (barite powder ratio)	C (gypsum mass)	D (clay mineral ratio)	Error
Variance value $S^2$	0.019	0.015	0.009	0.015	0.010
Degrees of freedom $F$	3	3	3	3	3
Univariate significance	2.111	1.667	1.000	1.667	
	Insignificant	Insignificant	Insignificant	Insignificant	



(a)



(b)

FIGURE 10: Typical stress-strain curve and failure modes diagram: (a) stress-strain curves; (b) failure modes.

average axial expansion rates of 0.1154%, 0.1238%, 0.1342%, 0.1966%, and 0.1369%, respectively. Later, the expansion rates of all samples enter the constant expansion stage ( $t = 2-15$  h). In this stage, the similar material samples S1~S4 and the raw rock show a constant linear growth rate of  $11.54 \times 10^{-5}/\text{min}$ ,  $12.38 \times 10^{-5}/\text{min}$ ,  $13.42 \times 10^{-5}/\text{min}$ ,  $19.66 \times 10^{-5}/\text{min}$ , and  $13.86 \times 10^{-5}/\text{min}$ , respectively. Afterward, the expansion rate of all samples enters the deceleration stage ( $t = 15-120$  h), and the expansion rate is gradually stabilized. This period takes a long time, accounting for 87.5% of the total expansion stage. It can be seen that similar materials have similar water absorption and

expansibility with the raw rock. The expansion rates of samples S1~S4 are all within the range of the raw rock, and the expansion rates gradually increase with the increase of clay mineral ratio. Among them, the curves of the axial expansion rates of sample S3 (whose clay mineral ratio is 12%) are the closest to the average value of the raw rock.

Table 18 summarizes the mean physical parameters of the similar material samples prepared at optimal water content (19%), barite powder ratio (32%), and gypsum mass (250 g) but different clay mineral ratios (0–18%). The data of raw rock samples are also included for comparison purposes. One can note that the similar material samples in test

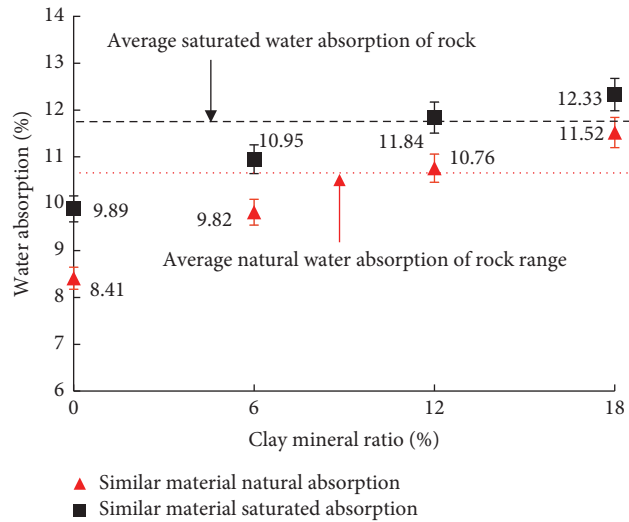


FIGURE 11: Water absorption and saturated water absorption.

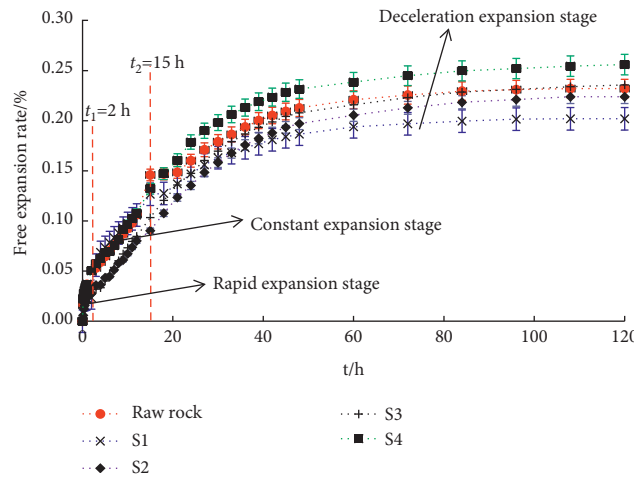


FIGURE 12: Axial expansion rate curve of silty mudstone and similar materials.

TABLE 18: Basic physical parameters of similar material samples and raw rock samples.

Scheme	Mass (g)	Diameter (cm)	Hight (cm)	Volume (cm <sup>3</sup> )	Dry density (g/cm <sup>3</sup> )	Porosity (%)
S1	198.28	5.002	5.012	98.44	1.68	43.26
S2	198.32	4.998	5.002	98.48	1.69	40.38
S3	198.48	5.006	5.008	98.52	1.74	38.54
S4	199.02	5.004	5.026	98.79	1.80	36.80
Raw rock	198.72	5.002	5.028	98.75	1.73	38.71

scheme S3 show the most similar density and porosity as the raw rock samples. This result further confirms the optimal values of water content, barite powder ratio, gypsum mass, and clay mineral ratio.

Based on the above analysis, the optimal ratios of similar materials are determined, which allows producing a similar material that has similar physical and mechanical properties as well as water-absorption and water-expansion characteristics to the mean properties of silty mudstone in the Yuelu Mountain (Changsha, China). These optimal ratios

can provide referencing guidance for the design of similar materials for silty mudstone in other regions.

**4.3. Microstructure of Similar Materials.** SEM observations were performed on small specimens extracted from cylindrical similar material samples and raw rock samples. Figure 13 shows the SEM images of horizontal and vertical planes of similar material specimens (S1–S4) and a raw rock specimen. In SEM images, the white arrow represents barite



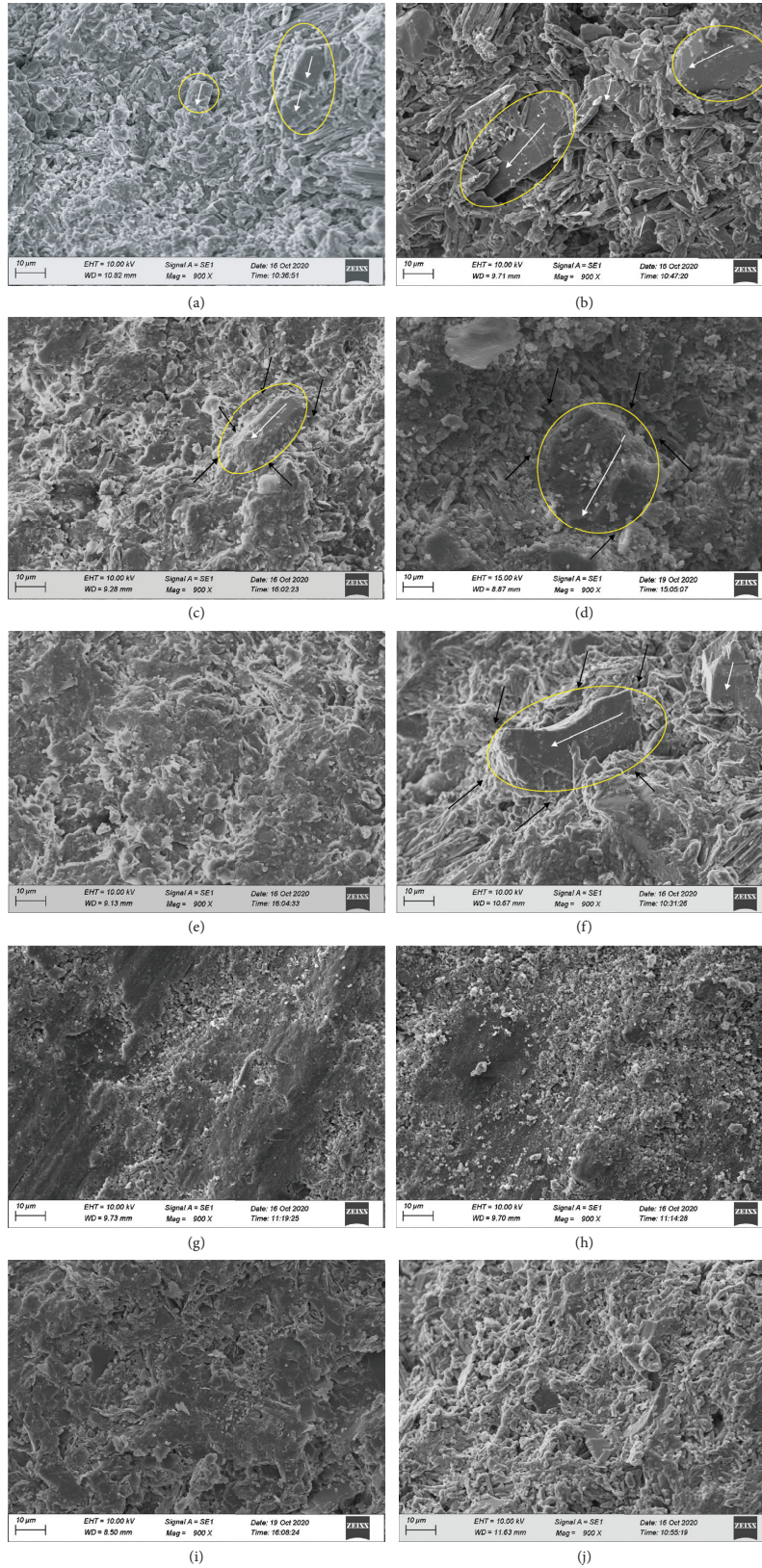


FIGURE 13: SEM images of raw rock and similar material specimens: (a,b) S1 specimen (0%); (c, d) S2 specimen (6%); (e, f) S3 specimen (12%); (g, h) S4 specimen (18%); (i, j) raw rock specimen.



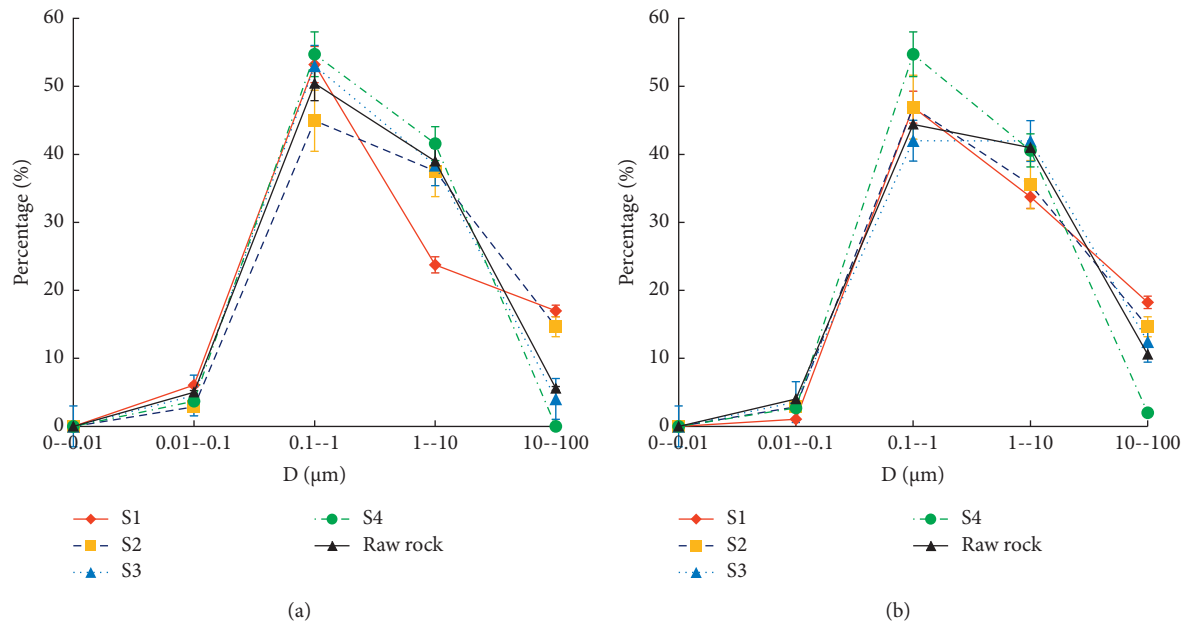


FIGURE 14: Relationship between pore area ratio and pore diameter: (a) in the horizontal plane and (b) in the vertical plane.

particles, and the black arrow represents clay mineral particles. It can be observed that when the clay mineral ratio is 0% (Figures 13(a) and 13(b)), the surface of barite particles is not fully wrapped by gypsum, and there are a lot of pores around. Due to compaction, barite particles and gypsum particles are mainly arranged face to face in the horizontal plane. Barite particles and gypsum particles mainly appear in the form of particle edge in the vertical plane, forming a large number of pores. With the increase of the clay mineral ratio, the SEM images are shown in Figures 13(c)–13(f). The pores between gypsum and barite particles are continuously filled with clay mineral particles, and the pores are fully filled in the horizontal plane; in particular, when the clay mineral ratio is 18% (Figures 13(g) and 13(h)), there are almost no large pores in the horizontal plane and vertical plane. From the SEM image taken from the horizontal plane of the raw rock in Figure 13(i), it can be observed that the surface of the rock particles is flat and smooth due to sedimentation, but it still contains small primary pores. From the SEM image of the vertical plane of the raw rock sample (Figure 13(j)), it can be observed that the raw rock is formed by cementation of the raw rock particles, resulting in large pores around the particles.

It is noted that, for similar material specimens with different clay mineral ratios, the horizontal plane is very dense compared to the vertical plane, but the horizontal plane has many small primary pores in the vertical plane. This is mainly due to the pressure on the horizontal plane in the process of protolith diagenesis and sample making of similar materials, resulting in the face-to-face arrangement of particles. In the similar material specimens, with the increase of clay mineral ratio, the angular barite particles are gradually wrapped by gypsum, clay minerals, and hydration products, and the structure becomes more and more

compact, and the pores decrease gradually. Finally, a dense structure without obvious pores is formed. The specific changes have been marked with ellipse in the figure. The main reasons for the above phenomena are the following: Gypsum and clay minerals gradually react with water, needle-like and rod-shaped gypsum crystals gradually disappear in the process of hydration reaction, the pores between particles are constantly filled, and the barite particles that do not participate in the hydration reaction are constantly wrapped; finally, with the hydration reaction, most of the gypsum is hydration products. The gel package has no edges and corners, forming a dense whole and a certain degree of strength. At the same time, hydration products are cemented and filled with intergranular voids, and pores are constantly reduced, forming a denser structure that plays a strong supporting role. In a word, with the increase of clay mineral ratio, the pores in the horizontal and vertical planes of similar material specimens are less and less, and the structure is more compact. When the clay mineral ratio is 12% (scheme S3), the dense structure is generated because of the hydration of gypsum and the filling of clay minerals; meanwhile, there are some pores on this basis, similar to pore morphology of the raw rock. When the clay mineral ratio is 18% (scheme S4), there are almost no pores and the structural morphology is very close in the horizontal plane and vertical plane of the similar material specimen. A quantitative analysis of the pore structures of all specimens is made based on the image processing method described in [47]; and the results are presented in Figure 14. It can be seen that most of pores in both the horizontal and vertical planes of all specimens have diameters between 0.01 and 100  $\mu\text{m}$ . When the clay mineral ratio is 12%, the pore size distribution of the similar material specimen in scheme S3 is very close to that of the raw rock specimen.

## 5. Conclusion

Based on the physical and mechanical properties of silty mudstone, the similar materials of silty mudstone with water absorption and expansibility were developed based on traditional materials including gypsum, barite powder, clay minerals (i.e., montmorillonite, illite, and chlorite), and distilled water. Specific conclusions are as follows:

- (1) The water content plays an important role in controlling the density, tensile strength, and elastic modulus of the similar material samples. The effect of barite powder ratio on the uniaxial compressive strength was significant. Gypsum mass also has a significant effect on the density of similar materials.
- (2) For similar materials with the proposed mixing ratios, the density is 1.82–2.08 g/cm<sup>3</sup>, the uniaxial compressive strength is 8.28–18.19 MPa, the tensile strength is 1.01–4.00 MPa, the elastic modulus is 1.01–2.38 GPa, and Poisson's ratio is 0.20–0.40. Similar materials produced at a water content of 19%, a barite powder ratio of 32%, and a gypsum mass of 250 g show the best similarity to the raw rock in terms of physical and mechanical properties.
- (3) The optimal mixing ratios were finally identified based on the results of the secondary refinement tests. Except for the optimal water content of 19%, optimal barite powder ratio of 32%, and optimal gypsum mass of 250 g, the optimal clay mineral ratio is 12%. These optimal ratios can provide referencing guidance for the design of similar materials for silty mudstone in other regions.
- (4) The raw rock surface is very dense, but there are many small primary pores. With the increase of clay mineral ratio, the absorption of similar materials increases continuously. The pores in similar material samples with a clay mineral ratio of 12% are filled by gypsum hydration products and clay minerals; thus, these similar material samples have similar water absorption and water expansion to those of the raw rock.

## Data Availability

Some or all data, models, or codes that support the findings of this study are available from the corresponding author upon reasonable request.

## Conflicts of Interest

The authors declare that they have no conflicts of interest.

## Acknowledgments

The authors acknowledge the financial supports received from the National Natural Science Foundation of China (nos. 51838001, 51878070, 51908069, and 51908073), the Key Research and Development Program of Hunan Province (no. 2019SK2171), the Open Fund of National Engineering

Laboratory of Highway Maintenance Technology, Changsha University of Science and Technology (no. kfj170103), and the Research and Innovative Program for Graduates of Hunan Province (no. CX20190654).

## References

- [1] T. Hamza and T. K. Raghuvanshi, "GIS based landslide hazard evaluation and zonation—a case from Jeldu district, central Ethiopia," *Journal of King Saud University Science*, vol. 29, no. 2, pp. 151–165, 2017.
- [2] T. K. Raghuvanshi, "Plane failure in rock slopes—a review on stability analysis techniques," *Journal of King Saud University Science*, vol. 31, no. 1, pp. 101–109, 2019.
- [3] L. Zeng, F. Li, Q.-F. Gao, X. Yao, and G. Wang, "Insight into the fracturing of silty mudstone in cyclic hydrothermal environments based on computed tomography," *Transportation Geotechnics*, vol. 26, Article ID 100432, 2021.
- [4] C. Y. Jia, H. L. Wang, X. Z. Sun et al., "Similar material simulation test of overlying strata characteristics of isolated working face mining with thick-hard strata," *Geotechnical & Geological Engineering*, vol. 38, no. 2, pp. 1121–1132, 2019.
- [5] Z.-H. Li, Q. Lou, E.-Y. Wang, S.-J. Liu, and Y. Niu, "Study on acoustic-electric-heat effect of coal and rock failure processes under uniaxial compression," *Journal of Geophysics and Engineering*, vol. 15, no. 1, pp. 71–80, 2018.
- [6] B. Zhang, H. Wang, L. Yuan, S. Li, and Z. Liu, "Ultra-low permeability rock-analogue material for gas-solid coupling model tests," *International Journal of Physical Modelling in Geotechnics*, vol. 21, no. 2, pp. 85–97, 2021.
- [7] R. Phillips and K. Chi, "Modelling ice rubble-rock berm interaction," *International Journal of Physical Modelling in Geotechnics*, vol. 15, no. 1, pp. 35–43, 2015.
- [8] J. Zhang, J. Peng, L. Zeng, J. Li, and F. Li, "Rapid estimation of resilient modulus of subgrade soils using performance-related soil properties," *International Journal of Pavement Engineering*, vol. 22, no. 6, pp. 732–739, 2019.
- [9] P. Zhao, R. Zhuo, S. Li, and H. Lin, "Experimental research on the properties of "solid-gas" coupling physical simulation similar materials and testing by computer of gas in coal rock," *Wireless Personal Communications*, vol. 102, no. 2, pp. 1539–1556, 2018.
- [10] Q. Liu, S. Chen, S. Wang, J. Chai, and D. Zhang, "Experimental development process of a new cement and gypsum-cemented similar material considering the effect of moisture," *Geofluids*, vol. 2020, Article ID 8831801, 14 pages, 2020.
- [11] J. Zhang, Z. Wang, and Z. Song, "Numerical study on movement of dynamic strata in combined open-pit and underground mining based on similar material simulation experiment," *Arabian Journal of Geosciences*, vol. 13, no. 16, pp. 1–15, 2020.
- [12] G. Lu, H. Wang, Y. Zhang et al., "The hydro-mechanical interaction in novel polyurethane-bound pervious pavement by considering the saturation states in unbound granular base course," *International Journal of Pavement Engineering*, vol. 2021, Article ID 1915490, 2021.
- [13] J.-j. Wang, Z.-n. Shi, L. Zeng, and S.-x. Qi, "The effects of different nanoadditives on the physical and mechanical properties of similar silty mudstone materials," *Advances in Civil Engineering*, vol. 2020, Article ID 8850436, 11 pages, 2020.
- [14] Z.-W. Deng, Q.-F. Gao, H. Dong, and L.-X. Li, "Dynamic responses of the shallow foundation of an onshore wind

- turbine,” *International Journal of Physical Modelling in Geotechnics*, vol. 19, no. 5, pp. 247–260, 2019.
- [15] C.-I. Dong, G. Zhao, X. Lu, X. Meng, Y. Li, and X. Cheng, “Similar simulation device for unloading effect of deep roadway excavation and its application,” *Journal of Mountain Science*, vol. 15, no. 5, pp. 1115–1128, 2018.
- [16] X. M. Shi, B. G. Liu, Y. Y. Xiang, and Y. Qi, “A Method for selecting similar materials for rocks in scaled physical modeling tests,” *Journal of Mining Science*, vol. 54, no. 6, pp. 938–948, 2018.
- [17] X. Yang, C. Y. Zhou, Z. Liu et al., “Experimental study on mix proportion of similar materials for weathered mudstone,” *Chinese Journal of Rock Mechanics and Engineering*, vol. 35, no. 3, pp. 549–557, 2016.
- [18] Z. M. Chen and Y. S. Fen, “Study on similar materials of carbonaceous phyllite,” *Bulletin of the Chinese Ceramic Society*, vol. 36, no. 12, pp. 4234–4241, 2017.
- [19] X. Wang, X. Liu, E. Wang et al., “Experimental research of the AE responses and fracture evolution characteristics for sand-paraffin similar material,” *Construction and Building Materials*, vol. 132, pp. 446–456, 2017.
- [20] S. Liu and W. Liu, “Experimental development process of a new fluid-solid coupling similar-material based on the orthogonal test,” *Processes*, vol. 6, no. 11, p. 211, 2018.
- [21] S. Q. He, L. Z. Jin, S. N. Ou, and X. H. Ming, “Soft coal solid-gas coupling similar material for coal and gas outburst simulation tests,” *Journal of Geophysics and Engineering*, vol. 15, no. 5, pp. 2033–2046, 2018.
- [22] B. Haimson and J. Ovacich, “Borehole instability in high-porosity Berea sandstone and factors affecting dimensions and shape of fracture-like breakouts,” *Engineering Geology*, vol. 69, no. 3, pp. 219–231, 2003.
- [23] W.-b. Sun, F. Zhou, J.-l. Shao, H.-q. Du, and Y.-c. Xue, “Development status and prospects of mine physical similar material simulation experiments,” *Geotechnical & Geological Engineering*, vol. 37, no. 4, pp. 3025–3036, 2019.
- [24] J. G. Wang, W. F. Liu, B. Liang et al., “On the similar material for creep characteristic study of weak and broken oil shale,” *Journal of Experimental Mechanics*, vol. 31, no. 2, pp. 263–268, 2016.
- [25] Z. F. Chu, B. G. Liu, D. R. Ren et al., “Development of rheology similar material of soft rock and its application in mode,” *Rock and Soil Mechanics*, vol. 40, no. 6, pp. 2172–2182, 2019.
- [26] X. H. Diao, K. Wang, and P. Y. Fu, “Study on proportioning of similar material to swelling rock,” *Applied Mechanics and Materials*, vol. 501–504, pp. 439–443, 2014.
- [27] Y. B. Ning, H. M. Tang, B. C. Zhang et al., “Research on rock similar material proportioning test based on orthogonal design and its application in base friction physical model test,” *Rock and Soil Mechanics*, vol. 41, no. 6, pp. 1–11, 2019.
- [28] J. J. Xie, T. H. Chen, H. B. Liu, and Q. Xie, “Development and application of palygorskite clays from Jiangsu and Anhui provinces,” *Bulletin of the Chinese Ceramic Society*, vol. 46, no. 5, pp. 746–754, 2018.
- [29] W. Yang, R. P. Chen, and X. Chen, “Application of molecular dynamics simulation method in micro-properties of clay minerals,” *Chinese Journal of Geotechnical Engineering*, vol. 41, no. 1, pp. 181–184, 2019.
- [30] Editorial Board of Engineering Geology Handbook, *Engineering Geology Handbook*, China Building Industry Press, Beijing, China, 5th edition, 1992.
- [31] H. Zhou, J. Chen, C. Q. Zhang, Y. Zhu, J. Lu, and Y. Jiang, “Experimental study of the rockburst model material with low-strength and high-brittleness,” *Rock and Soil Mechanics*, vol. 40, no. 6, pp. 2039–2049, 2019.
- [32] Z. Li, Z. Li, T. T. Nguyen, and S. Chen, “Orthogonal chemical reaction optimization algorithm for global numerical optimization problems,” *Expert Systems with Applications*, vol. 42, no. 6, pp. 3242–3252, 2015.
- [33] S. Zhang, G. Fan, D. Zhang, M. Chen, and C. Zhang, “Study on material properties and similar material proportion of weakly cemented water-resisting strata,” *Arabian Journal of Geosciences*, vol. 12, no. 11, p. 340, 2019.
- [34] L. Zeng, H.-C. Yu, J. Liu, Q.-F. Gao, and H.-B. Bian, “Mechanical behaviour of disintegrated carbonaceous mudstone under stress and cyclic drying/wetting,” *Construction and Building Materials*, vol. 282, p. 122656, 2021.
- [35] L. Zeng, J.-T. Luo, J. Liu, Q.-F. Gao, and H.-B. Bian, “Disintegration characteristics and mechanisms of carbonaceous mudstone subjected to load and cyclic drying–wetting,” *Journal of Materials in Civil Engineering*, vol. 33, no. 8, Article ID 04021195, 2021.
- [36] E. Hoek, D. Wood, and S. A. Shah, “A modified Hoek-Brown failure criterion for jointed rock masses,” in *Proceedings of the Rock Characterization Symposium of ISRM*, Thomas Telford Publishing, London, UK, September 1992.
- [37] L. Zeng, L. Xiao, J. Zhang, and H. Fu, “The role of nanotechnology in subgrade and pavement engineering: a review,” *Journal of Nanoscience and Nanotechnology*, vol. 20, no. 8, pp. 4607–4618, 2020.
- [38] P. Mielke, K. Bär, and I. Sass, “Determining the relationship of thermal conductivity and compressional wave velocity of common rock types as a basis for reservoir characterization,” *Journal of Applied Geophysics*, vol. 140, pp. 135–144, 2017.
- [39] P. Yan, C. Zhang, Q. Gao, and W. Lu, “Acoustic wave test on mechanical properties variation of rocks under different damage degrees,” *Rock and Soil Mechanics*, vol. 36, no. 12, pp. 3425–3432, 2015.
- [40] L. Zeng, X. Yao, J. Zhang, Q.-F. Gao, J. Chen, and Y. Gui, “Ponded infiltration and spatial-temporal prediction of the water content of silty mudstone,” *Bulletin of Engineering Geology and the Environment*, vol. 79, no. 10, pp. 5371–5383, 2020.
- [41] Z. Song, Y. Cheng, X. Tian, J. Wang, and T. Yang, “Mechanical properties of limestone from Maixi tunnel under hydro-mechanical coupling,” *Arabian Journal of Geosciences*, vol. 13, no. 11, pp. 1–13, 2020.
- [42] GB/T 2013, *Standard for Test Methods of Engineering Rock Mass GB/T 50266-2013*, China Planning Press, Beijing, China, 2013.
- [43] M. C. Acar, Z. Gündüz, and H. B. Kara, “Modulus of elasticity determination of rocks using compressometer, strain gauge and LVDT,” in *Proceedings of ACE 2014 11th International Congress on Advances in Civil Engineering*, vol. 11, pp. 1–6, Istanbul, Turkey, October 2014.
- [44] E. Komurlu, F. Cihangir, A. Kesimal, and S. Demir, “Effect of adhesive type on the measurement of modulus of elasticity using electrical resistance strain gauges,” *Arabian Journal for Science and Engineering*, vol. 41, no. 2, pp. 433–441, 2016.
- [45] JTG 2005, *Test Methods of Rock for Highway Engineering JTG E41-2005*, Ministry of Transport of the People’s Republic of China, Beijing, China, 2005.
- [46] Q.-F. Gao, F. Zeng, Z.-N. Shi, and R. Zhang, “Evolution of unsaturated shear strength and microstructure of a compacted silty clay on wetting paths,” *International Journal of Geomechanics*, 2021.

- [47] Q. Gao, Z. Shi, J. Luo, and J. Liu, "Microstructural insight into permeability and water retention property of compacted binary silty clay," *Journal of Central South University*, vol. 27, no. 7, pp. 2068–2081, 2020.
- [48] Q. F. Gao, M. Jrad, M. Hattab, F. Jean-Marie, and A. Lamine Ighil, "Pore morphology, porosity, and pore size distribution in kaolinitic remolded clays under triaxial loading," *International Journal of Geomechanics*, vol. 20, no. 6, Article ID 04020057, 2020.
- [49] H. Y. Fu, J. C. Chen, L. Zeng, and X. Qiu, "Experiment on the effects of temperature and humidity on uniaxial mechanical properties of silty mudstone," *China Civil Engineering Journal*, vol. 52, no. 1, pp. 89–98, 2019.

## Research Article

# Prediction-Based Maintenance of Existing Bridges Using Neural Network and Sensitivity Analysis

Pengyong Miao 

Graduate School of Engineering, Hokkaido University, Sapporo, Japan

Correspondence should be addressed to Pengyong Miao; miaopengyong@eis.hokudai.ac.jp

Received 9 June 2021; Accepted 15 July 2021; Published 28 July 2021

Academic Editor: Pengfei Liu

Copyright © 2021 Pengyong Miao. This is an open access article distributed under the Creative Commons Attribution License, which permits unrestricted use, distribution, and reproduction in any medium, provided the original work is properly cited.

Bridge deterioration is affected by various factors. However, neither the relationships between these factors and deterioration are explicitly determined, nor the relative effect of each factor on deterioration is well understood. This study proposed a methodology to resolve these issues by integrating an artificial neural network (ANN) and sensitivity analysis method. The ANN was used to predict deterioration, and the sensitivity analysis method was applied to evaluate the influence of each factor on deterioration. Testing the methodology with 3,368 bridge inspection data pieces indicates that (1) the developed ANN obtained an accuracy of about 65%; and (2) seven factors were identified affecting deterioration. The established ANN model has equivalent performance for three deterioration grades and four types of bridges. Two sensitivity analysis (the Shapley value and the Sobol indices) methods were compared, and they identified the same five most important factors. Consequently, the methodology can effectively avoid the uncertainty of factors on deterioration by providing a relative importance list of factors. The methodology's predictive ability and factor importance identification ability make it suitable for decision-makers to understand the deterioration situations and to schedule a further inspection and corresponding maintenance strategies.

## 1. Introduction

Bridges that are in use for many years suffer various degrees of deterioration. Many studies have been conducted to evaluate the impacts of individual factors on deterioration [1]. However, the practical bridge is a complicated system project, the relationships between deterioration-related factors and deterioration are not explicitly determined, neither is the relative impact of each factor on deterioration. Maintenance engineers inspect and evaluate the conditions of bridges and record these results at regular intervals. Over time, databases with large numbers of maintenance items are obtained, which provides a possibility to establish the relationships between factors and deterioration and to assess the impact of each factor. In addition, proper prediction-based maintenance strategies are more economical to keep the soundness of bridges than corrective maintenance, because the corrective maintenance focuses on postfailure repair and is usually insufficient to ensure structural safety [2]. Furthermore, the inspection is labor-intensive and time-

consuming. Therefore, there are untapped potentials and needs to utilize maintenance databases for predicting deterioration to determine seriously deteriorated bridge for implementing further inspection and making maintenance strategies. To fulfill these needs, an inspection database is brought into new data processing methods (including neural network and sensitivity analysis) to predict deterioration in grade and to determine the factors affecting deterioration. The potentially influencing factors include bridge design and construction quality, bridge geometry, materials, repairs, traffic volume, and surrounding environments.

Appropriate artificial neural network (ANN) architectures can be trained on the maintenance databases to predict the future deterioration situations [3]. The noteworthy characteristic of an ANN is its learning ability. In the process of establishing an ANN model, the network processes the inputs and obtains an output, compares the output with the ideal response, and calculates the errors. Then the parameters of connections ( $W_1$  and  $W_2$  in Figure 1) are updated according to the errors. If the network paradigm and



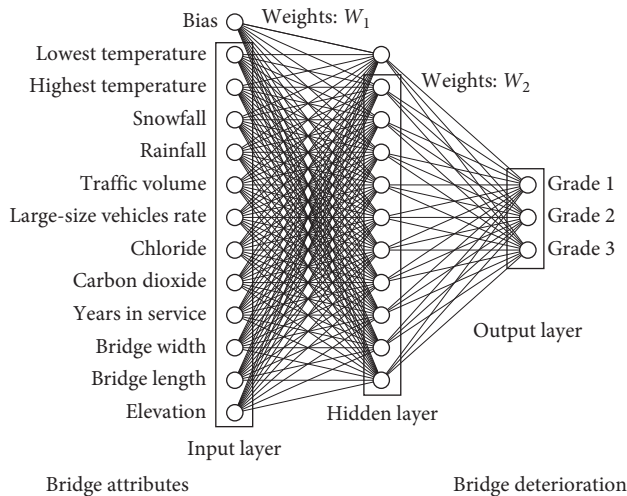


FIGURE 1: Configuration of a neural network used for prediction.

parameters are appropriately designed, these can result in satisfactory forecasting performance. In the maintenance of existing bridges, an ANN can assist maintenance work in establishing the relationships between the potential factors and the deterioration grades of bridges to predict the deterioration.

Since an ANN is usually trained by using a set of data from a database, the results only explain the relationships between all inputs (factors) and output (prediction). Through the relationships, it is difficult to understand the contribution of each factor on a specific prediction. Therefore, the relationship established by an ANN becomes a “black box” [4]. Although an ANN model can provide prediction and show better performance, its application in the practical maintenance of bridges is limited owing to the ignorance of the influence of each factor on the prediction.

In summary, not only should the prediction model using an ANN be established to determine the deterioration situations but also each factor’s importance should be calculated to understand the reasons for deterioration. In addition, the applied database must contain high-quality data for formulating a deterioration prediction model with optimal performance and making convincing explanations for factors affecting deterioration. Therefore, the data quality of the applied inspection database must be checked carefully before it is conducted in analysis.

This study introduced the development and verification of a proposed methodology that can be used to predict bridge deterioration and to determine the reasons for deterioration. Specifically, an ANN was applied to analyze an inspection database for establishing a prediction model, whereby the deterioration grades can be predicted to determine the seriously deteriorated bridge. The performance of the established ANN model was evaluated for different deterioration grades and different types of bridges. In addition, the Shapley value method [5, 6] and the Sobol indices [6, 7] were used to calculate the importance of all factors. Furthermore, the Shapley value method were applied to the prediction model for further analyzing the estimated

importance, broken down by factors, deterioration grades, bridge types, and environments. Finally, two bridges were taken as examples to illustrate the practical application of the proposed method.

## 2. Background

Maintenance is essential to keep structures sound, serviceable, and safe. In many countries, condition assessment of existing bridges is carried out mainly through periodic inspections [8–10]. Based on the assessment results, necessary interventions or further inspections are scheduled. Since prediction-based maintenance can prevent further deterioration and keep bridges in sound conditions with lower costs compared with corrective maintenance, prediction-based maintenance is widely used [2]. Prediction-based maintenance depends heavily on the accurate prediction of deterioration. Potential approaches are described below.

The approaches commonly used in predicting deterioration include two categories: the deterministic model and the probabilistic model [11]. The deterministic model deals with certain and known variables. Hyman et al. [12] pointed out that deterioration is related to the age of bridge through a piecewise linear regression model. Busa et al. [13] used linear regression to model bridge deterioration and concluded that age and daily traffic are two important factors. Abu-Tair [14] discussed the application of the factor method in predicting deterioration and noted that this method is highly subjective. Pan et al. [15] presented a matrix-driven fuzzy linear regression model to predict bridge conditions. Similarly, Kim et al. [16] applied a sigmoid function and nondestructive evaluation data to evaluate the deterioration of a bridge deck. Jeong et al. [17] developed a nonlinear regression model for determining the expected service life of a bridge. Although the performance of bridges in their service life can be described by the formulas of deterministic models, these models ignored the uncertainty of deterioration [18].

In addition, some researchers have focused on probabilistic models, in which the mostly used deterioration model is the Markov chain. Li et al. [19] and Wellalage et al. [20] used the Markov chain-based deterioration model to predict bridge conditions. However, an optimal transition probability matrix is difficult to obtain. Agrawal et al. [18] compared the Markov chain with the Weibull distribution and concluded the later method would be better. Time-based models present the time distribution of the duration taken by bridges to change their condition from one to another. A set of variables (factors) are used for this process such as environmental exposure, design attributes, and maintenance schedule. These types of models were used in the studies done by Mauch and Madanat [21] and Lee et al. [22]. In their approaches, a series of random variables (factors) with different distributions determined the performance of bridges.

Except for the deterministic and probabilistic models, the ANN has been applied to practical maintenance engineering [23–25], as it can solve multivariate problems. In the application of the ANN to maintenance, Sobanjo [26] used

the inspection records for 50 bridge superstructures to predict bridge deterioration that inputs only the age of bridge and outputs the deterioration condition of bridge superstructure. Huang [27] identified eleven significant factors and developed an ANN model with these factors to predict deterioration of bridge decks. Using the same operation, Al-Hussein [11] designed an ANN to estimate the deterioration by considering the structure types, component types, exposure environments, and defects. Lim and Chi [28] considered the factors of identification, structure, inspection, and environment, and developed an ANN to predict the number of damage occurrences on bridge decks and their severity with the accuracy of about 95%. None of these researchers discussed, however, the specific influences of factors on bridge deterioration.

Inspired by these studies, we applied the ANN to analyze an inspection database towards predicting deterioration of existing bridges to optimize further inspection and formulate maintenance strategies. However, Zhang et al. [4] and Caruana et al. [29] noted that the ANN can give rise to a black box problem. Although the ANN model can predict deterioration given influencing factors, the prediction model provides only one predicted value without knowing the reasons for deterioration. This makes it difficult for engineers to trust the prediction, to understand what factors affect the prediction, and to determine targeted intervention. To solve these difficulties, the proposed methodology integrates an ANN and the sensitivity analysis method. An ANN predicts the deterioration in grades, and the sensitivity analysis method calculates the relative importance of factors on deterioration.

### 3. Proposed Methodology

The methodology consists of the following two parts: a prediction model and sensitivity analysis approaches, as shown in Figure 2.

**3.1. Prediction Part.** Accurate prediction of bridge deterioration is essential for the planning of further inspection, maintenance, and repair at lower cost. To predict deterioration, the ANN is applied to analyze an inspection database for establishing a prediction model. Maintenance data with high quality should be extracted and classified into the following two categories: potential factors affecting deterioration and the deterioration grades. Since many factors will affect the deterioration, all potential external and internal factors likely to influence the bridges should be highlighted [30]. The influential factors for consideration include those of bridge design and geometries, applied materials, environment, loading, and others, which will be elaborated in Section 4.1.1. However, this does not mean that each factor has the same impact on the bridge deterioration. Therefore, it is necessary for the proposed methodology to identify the significant factors from the many insignificant factors [31].

Given the characteristics of the ANN, the prediction part can be applied to establish the optimal relationships between the potential factors and the deterioration grades, as

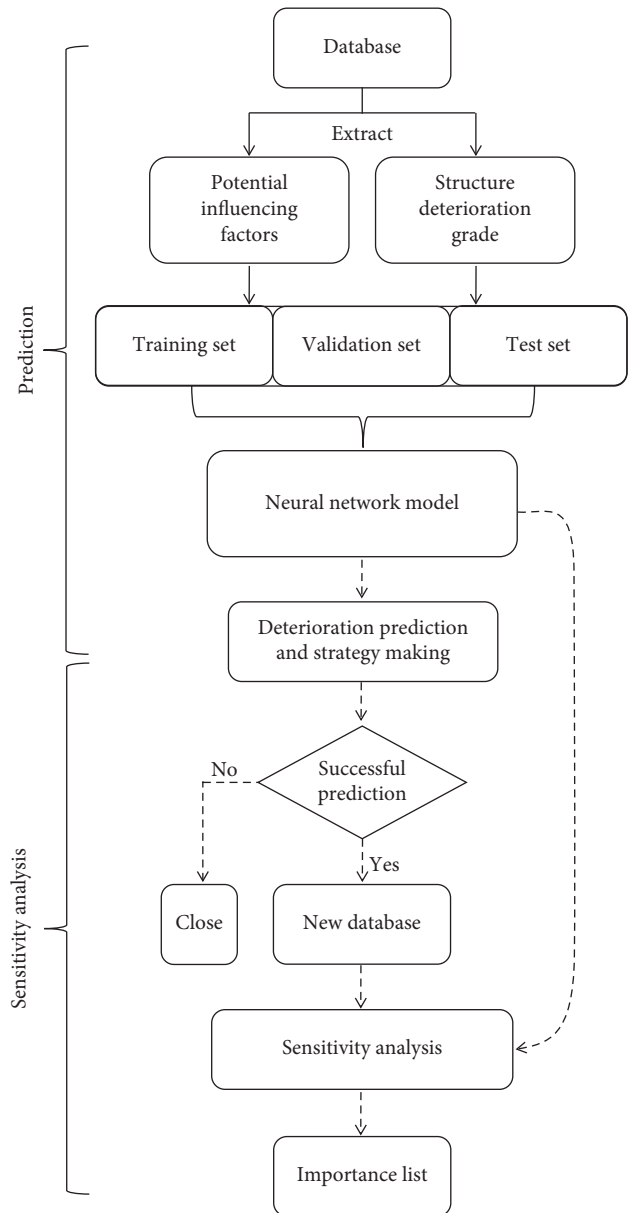


FIGURE 2: Proposed methodology.

illustrated in Figure 1. Details of ANN refer to Goodfellow et al. [32] and Guliyev [33]. The performance of the prediction model can be improved by continuously integrating new inspection data to update the model. Accordingly, two parameter matrices of  $W_1$  and  $W_2$  in Figure 1 can be obtained, which represent the whole relationships between the inputs and the outputs. However, those two parameter matrices make the relationships hard to be understood because they indicate the complicated nonlinear computation. In other words, the contribution of each factor on deterioration is difficult to determine directly from the prediction model.

**3.2. Sensitivity Analysis.** Sensitivity analysis can be applied to overcome the uncertainty of factors on deterioration,

because sensitivity analysis can tell engineers what factors affect the deterioration and their relative importance. This study applied two sensitivity analysis methods: Shapley value and Sobol indices, as described below. A prediction can be explained by assuming that each factor of the instance is a “player” in a game and the prediction is the payout. Shapley values show how to fairly distribute the “payout” among the factors [34]. Next, the Shapley value method is briefly introduced. The set of  $m$  potentially influencing factors is represented by  $N = \{x_1, x_2, \dots, x_m\}$ , and any permutation  $S$  of  $N$  is a coalition. The characteristic function  $v$  maps all coalitions to “payout,” which in our case is the deterioration grade. The function  $v$  has the following definitions: if  $S$  is a permutation (coalition) of all factors; then  $v(S)$  describes the total impact of all factors in coalition  $S$  [35]. The value of  $v(S)$  is determined by inputting  $S$  in the prediction model.

The importance  $\varphi_i(v)$  of factor  $x_i$  is determined as follows:

$$\varphi_i(v) = \frac{\sum_{S \subseteq N} (((m - |S| - 1)!|S|!)/m!) (v(S \cup \{x_i\}) - v(S))}{\{i\}}, \quad (1)$$

where  $m$  is the number of factors. The sum extends over all subsets  $S$  of  $N$  excluding factor  $x_i$ . The formula can be interpreted as follows: the contribution of factor  $x_i$  in  $S$  is  $v(S \cup \{x_i\}) - v(S)$ ; the average of this contribution over the possible coalitions is the final contribution of this factor. In our case,  $\varphi(v)$  refers to the deterioration grade and is defined as

$$\varphi(v) = \sum_i \varphi_i(v). \quad (2)$$

The Shapley value method can calculate the relative importance of each factor, regardless of the complexity of the prediction model. Therefore, it can explain any prediction model [35]. The calculated importance is related to the magnitude of difference in the prediction values when a factor is considered (such as bridge width) versus when it is not considered (such as when bridge width is unknown) [5]. In summary, the Shapley value method identifies all factors and evaluates their relative importance, enabling an engineer to figure out factors that significantly influence the deterioration and formulate a corresponding intervention strategy.

Except for the Shapley value method, Sobol indices [6, 7] is another useful method to detect the sensitivity of predictions to inputs. In this study, these two methods will be compared using an actual case in Section 4.3. Conforming to the descriptions of these two methods, we present the specific steps to achieve the sensitivity analysis of the predictions, as shown in Figure 2. Given values of factors, the deterioration grades can be predicted (Section 3.1), with some predictions being successful and the rest being unsuccessful. All successfully predicted bridges are extracted to form a new database. Since unsuccessful predictions may lead to incorrect importance estimates, the Shapley value and Sobol indices methods are applied to the new database to detect the sensitivity of the prediction model to each factor.

## 4. Case Study

An inspection database of 3,386 bridges in Hokkaido in Japan was employed to verify the effectiveness of the methodology. These bridges are inspected every five years [8] and their locations are shown in Figure 3. The entire verification process will be described from data preparation, establishment of prediction model, and estimation of factor importance.

**4.1. Data Preparation.** We eliminated incomplete and unreasonable data from the original database and selected 3,368 out of 3,386 bridges. Specifically, the bridges with unknown ages were discarded. In conjunction with the age constrain, the constraint of nondecreasing deterioration grade was introduced. For example, a bridge is assessed grade 2 in an inspection and assessed grade 1 in the next inspection; this kind of bridge was not considered. Then, the data for the selected bridges were divided into potentially influencing factors and the deterioration grades.

**4.1.1. Potentially Influencing Factors.** Factors that have the potential to affect deterioration were regarded as “inputs” in the prediction model. The bridge features, such as bridge length, bridge width, elevation, and years in service, were extracted from the inspection database. Temperature and carbon dioxide concentration were obtained from Japan Meteorological Agency [36]. Traffic volume was obtained from the traffic survey [37, 38]. Airborne salt was calculated according to previous studies [39, 40]. In summary, the potentially influencing factors include bridge geometry, environment, loading conditions, and others, as listed in Table 1. There are many other factors that would affect the deterioration but are not considered, such as fatigue crack, design, and construction quality. The main reason is the inability to collect relevant data. However, this deficiency will force us to collect more data to improve our future work and encourage modifying the data capturing method in the future inspection. More details are described below for the factors of traffic volume and airborne salt. This study considered four types of bridges, including PC, RC, PC and RC hybrid, and steel bridges.

### (1) Rate of the large-size vehicles

According to the survey of daily traffic volume [37, 38], the proportion of large-size vehicles (including bus, lorry, construction heavy equipment, and other special equipment)  $R_v$  can be calculated by

$$R_v = \frac{\text{number of large size vehicles daily}}{\text{daily traffic volume}} \times 100\%. \quad (3)$$

### (2) Airborne salt

The bridges within 1 km of the coastline are considered influenced by the airborne salt. The airborne salt concentration can be calculated by the following equation [39]:

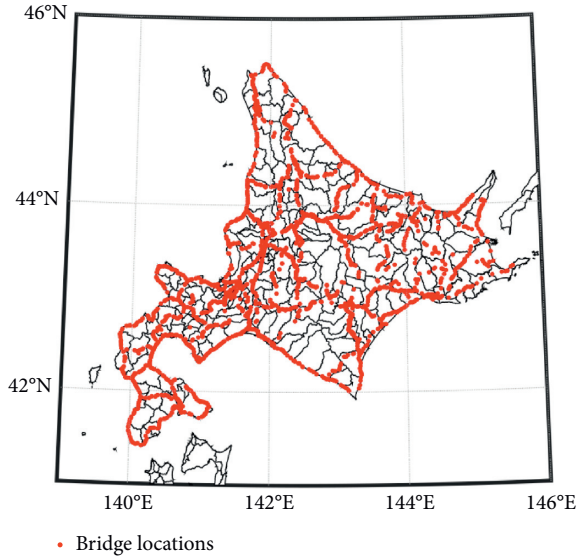


FIGURE 3: Locations of the bridges.

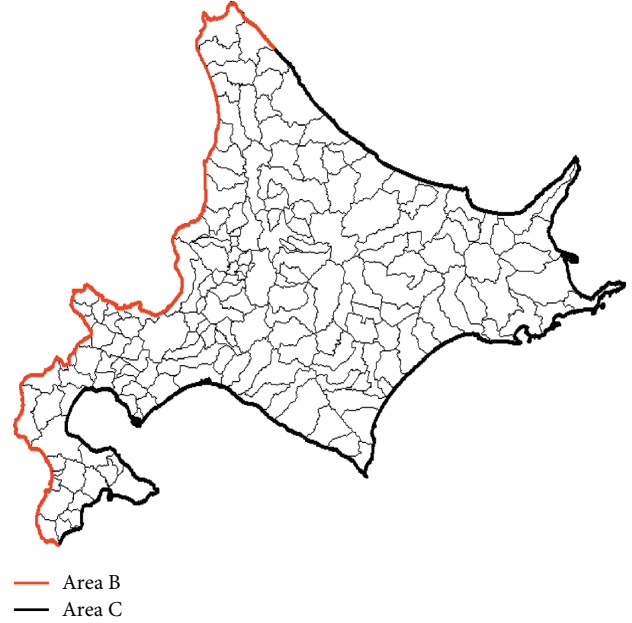


FIGURE 4: Salt damage area classification in Hokkaido.

TABLE 1: Potentially influencing factors.

Attributes (unit)	
Bridge geometry factors	Length (m)
	Width (m)
Environmental factors	Elevation (m)
	Yearly highest and lowest temperatures (°C)
	Carbon dioxide concentration (ppm)
	Airborne salt concentration (mdd·NaCl)
	Yearly average snowfall (cm)
Loading condition	Yearly average rainfall (cm)
	Daily traffic volume (vehicles/day) <sup>a</sup>
Other	Rate of the large-size vehicles (%/day)
	Years in service (years)
	Bridge type

<sup>a</sup>Statistics on traffic volume include large and small vehicles [37].

$$C_{ab} = C_1 \cdot x^{-b}, \quad (4)$$

where  $C_{ab}$  is airborne salt concentration (mdd · NaCl);  $C_1$  is 1 km equivalent airborne salt concentration (mdd·NaCl);  $x$  is the distance from coastline (km); and  $b$  is the degree of distance attenuation ( $b = 0.6$ ).

$C_1$  for areas B and C shown in Figure 4 is 1.174 and 0.072, respectively [39]. Afterwards, empirical equation (5) [40] can be used to compute the chloride ion concentration that adheres to the surface of the concrete.

$$C_0 = -0.016 \times C_{ab}^2 + C_{ab} + 1.7 (C_{ab} \leq 30), \quad (5)$$

where  $C_0$  is chloride ion concentration of concrete surface ( $\text{kg}/\text{m}^3$ ); and  $C_{ab}$  is airborne salt concentration at the bridge location (mdd · NaCl).

**4.1.2. Deterioration Grades.** The deterioration grades are used to understand the conditions of the bridges. According to the inspection guidelines [8], the deterioration situations of bridges are categorized as follows: grade 1: healthy; grade 2: preventive maintenance required; grade 3: early action required; and grade 4: emergency action required. The grades and corresponding descriptions are given in Table 2. Since grade 4 is considered a critical condition, meaning that these bridges have to be subjected to a repair timely, this philosophy results in the infrequent occurrence of grade 4. Therefore, grade 3 is considered to be the upper threshold, because grade 3 indicates the necessity of early actions. This consideration prompted us to build a prediction model to predict the situation before an emergency occurs. The prediction model can be taken as a tool to distinguish seriously and nonseriously deteriorated bridge. Then, the seriously deteriorated bridge can be introduced to the detailed inspection and maintenance.

**4.1.3. Data Characteristics Analysis.** Twelve factors listed in Table 1 are investigated. Since different factors are measured on different ranges, values of these factors are necessary to be adjusted to a common scale to improve the efficiency of the training process. As listed in Table 3, all the factors were scaled within 0-1. Years in service indicate the bridge age after it was built. Carbon dioxide refers to the concentration near the ground at the bridge location. Large-size car vehicles rate is calculated by equation (3). The type of bridge was excluded when establishing the ANN model, as it is irrational to represent different bridge types with a number. Although it is possible to build models for different types of bridges, the lack of sufficient data on each type of bridge limits this attempt. Discussions regarding the performance of the ANN model on different types of bridges are described in Section 4.2.2.

TABLE 2: Inspection grades and corresponding conditions of bridges.

Grade	Conditions	Descriptions
1	Healthy	A state that the function of the structure is not disturbed.
2	Preventive action required	Although the function of the structure is not hindered, it is desirable to take measures from the viewpoint of preventive maintenance.
3	Early action required	The function of the structure has interfered and measures should be taken as soon as possible.
4	Emergency action required	A condition in which the function of the structure has been or is likely to be impaired, and measures should be taken urgently.

TABLE 3: Scaled values of each influencing factor.

Factor	Original data range	After scaled	
		Mean	Standard deviation
Elevation (m)	-0.3~1,106	0.0909	0.1347
Bridge length (m)	2~1,433	0.0444	0.0844
Bridge width (m)	0.7~50	0.2129	0.1124
Years in service (years)	1~84	0.3833	0.2008
Carbon dioxide (ppm)	348.86~409.87	0.3933	0.2413
Chloride (kg/m <sup>3</sup> )	0~17.3	0.057	0.1376
Large-size vehicles rate (%)	0~62.6	0.3076	0.1786
Traffic volume (daily)	0~56,874	0.0946	0.1143
Rainfall (cm)	776~1,491	0.3617	0.2268
Snowfall (cm)	12.0~1,263.8	0.4493	0.2166
Highest temperature (°C)	16~26	0.7025	0.1737
Lowest temperature (°C)	-11~-3	0.5851	0.2361

## 4.2. Prediction Model

**4.2.1. Model Establishment.** The twelve factors in Table 3 and three deterioration grades were used to construct an ANN model. The optimal configuration for the ANN model was determined by trial and error. A higher accuracy was considered better performance of a prediction model. In the trial and error, various values were tested for each parameter [32], as listed in Table 4. Figure 5 depicts the nonlinear activation functions used in the trial and error. The softmax was applied between the hidden layer and the output layer. Relu and tanh were applied between the input and hidden layers.

Considering all combinations of the five parameters, 112 cases were tested. In each trial, stratified sampling was used to randomly divide the dataset into the training, testing, and validation subsets, which accounted for 70%, 15%, and 15% of the maintenance database, respectively. Then each case was tested three times to obtain an average value to eliminate the variance. Afterwards, analysis of variance (ANOVA) analysis was applied to the testing results to examine the significance of each parameter on training/validation accuracy. A  $p$  value of 0.05 or less is considered to have a significant influence on deterioration. The  $p$  value summarized in Table 4 indicates that the learning rate and learning algorithm influence training/validation accuracy significantly. Looking through the testing results, the ANN produces higher accuracy when it has one hidden layer of ten neurons, has the activation function of Relu, and is trained with the adaptive moment estimation (Adam) algorithm with the learning rate of 0.01.

The expected ANN consisted of a  $3,368 \times 13$  matrix as the inputs (including the bias) and a  $3,368 \times 1$  matrix as the output. As the initial values of  $W_1$  and  $W_2$  (Figure 1) are randomly assigned during training, the predicted grades are usually inconsistent with the actual grades. The cross-entropy value expressed in equation (6) was used to calculate the error between the actual and the predicted grades.  $M$  is the number of samples,  $C$  is the number of classes,  $\eta_j$  denotes the weight for class  $j$  to deal with sample imbalance, and  $p_j$  represents the probability that a sample belongs to class  $j$ . If a sample belongs to class  $j$ ,  $y_j = 1$ ; otherwise  $y_j = 0$ .

$$\text{Cross entropy} = - \sum_{i=1}^M \sum_{j=1}^C \eta_j y_j \log(p_j). \quad (6)$$

The training and validation iterated 2000 times, and the error between the predicted value and the ground truth was evaluated by using the cross-entropy. As shown in Figure 6, the accuracy converges to approximately 65%, and the error converges to approximately 0.2. The accuracy and the error show that the established model is some distance from perfection. Future endeavors are necessary to improve the established model by actions described in Section 5.2.

**4.2.2. Evaluation of the Prediction Model.** The performance of the prediction model was evaluated using five metrics. The definitions in terms of these metrics were introduced in Figure 7 taking grade 1 as an example. TP, TN, FP, and FN refer to true positives, true negatives, false positives, and false negatives, respectively. Recall or true positive rate (TPR) is



TABLE 4: Configuration test results.

Parameters	Parameters	$p$ value	
		Training	Validation
Number of hidden layers	1, 2	0.5489	0.1154
Number of hidden neurons	5, 10	0.4236	0.8454
Learning rate	0.01, 0.001	0.0003 <sup>a</sup>	0.0038 <sup>a</sup>
Learning algorithm	SGD, RMSProp, Adagrad, Adadelta, Adam, AdaMax, Nadam	$5.513 \times 10^{-14a}$	$8.490 \times 10^{-15a}$
Hidden activation function	ReLu, tanh	0.4904	0.7622

<sup>a</sup>Significant at 95% level of confidence.

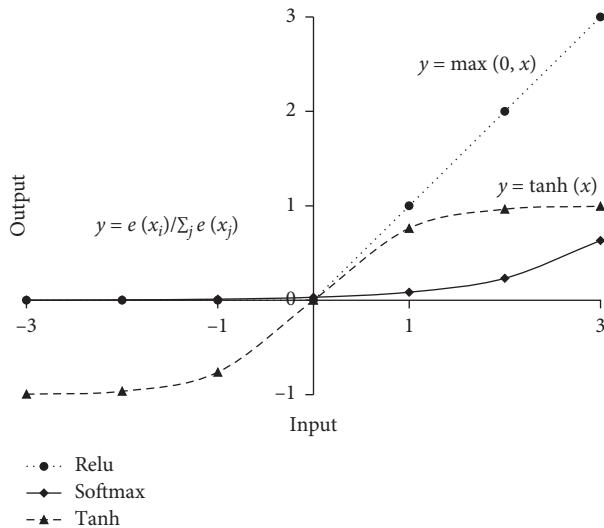


FIGURE 5: Nonlinear activation functions.

the ratio of correct predictions to all grade 1 bridges. Precision is the ratio of correct predictions to all predictions of grade 1. The  $F1$  score is the harmonic mean of the recall and precision. The true negative rate (TNR) indicates the ratio of correct predictions on other grade bridges to the total number of other grade bridges. A model is considered better performance with higher values of these metrics. For details about these metrics, refer to Goodfellow et al. [32].

Figure 8 shows these metrics' values of the ANN model for the three deterioration grades. The results indicate that the established model has equivalent performance for the three deterioration grades. In addition, the model is applied to PC, RC, mixed, and steel bridges to evaluate the model's performance for corresponding type of bridge. Figure 9 shows that the model has equivalent performance regardless of the types of bridges. Although the established model is not yet perfect, the established model is unbiased for the different deterioration grades and different types of bridges.

**4.3. Estimation of Factor Importance.** Using the prediction model, successful predictions were made for 2,161 out of the 3,368 bridges. Therefore, a new database of 2,161 bridges was set up. The Shapley value and Sobol indices methods were then applied to perform the sensitivity analysis of each factor from the new database. The calculated sensitivities were normalized to show their relative importance, as indicated in

Figure 10. The five most important factors determined by the Sobol indices and Shapley value method are the same, although their values are different. Bridge length and years in service were determined to be the most important factors affecting the deterioration. In addition, traffic volume, lowest temperature, and chloride ions are the three external factors that influence deterioration, which is consistent with known findings. Therefore, the Shapley value method was considered a suitable solution to determine the contribution of factors on deterioration. Furthermore, the Shapley value method was applied to analyze the new database from other aspects.

**4.3.1. Distribution of Each Potentially Influencing Factor.** According to the Shapley value method, the estimated importance of all factors was calculated for each bridge. The estimated importance of all bridges separated by each factor is shown in Figure 11. The estimated importance indicates the relative importance of each factor for a bridge. A positive value represents that the factor will accelerate the deterioration, and negative value means that the factor will slow down the deterioration. Therefore, six factors (such as years in service, carbon dioxide concentration, and the chloride ion concentration) showed accelerated effects on deterioration. Other factors (such as elevation, bridge length, and bridge width, rate of the large-size vehicles, rainfall, and highest temperature) did not show consistent effects. Only the six factors with acceleration were discussed hereafter. In addition, Figure 11 revealed that the estimated importance of lowest temperature was negatively related to the measured value. The estimated importance of other five accelerated factors, such as years in service and traffic volume, showed positive correlations with the measured values.

**4.3.2. Estimated Importance of Each Grade.** To compare the estimated importance between different grades, the average importance of the six factors for its respective grade was computed, as shown in Figure 12. Of all the factors, years in service and traffic volume are the two most significant factors for all grades. Other factors have relatively fewer impacts. Since the service time of grade 1 bridges is generally short, environmental factors such as lowest temperature and chloride ions have not had a significant impact. Therefore, the traffic volume is the most significant factor. As time goes by, the importance gap between the years in service and the traffic volume traffic has narrowed, as shown in grade 2. The results indicate that the relative importance of the years in

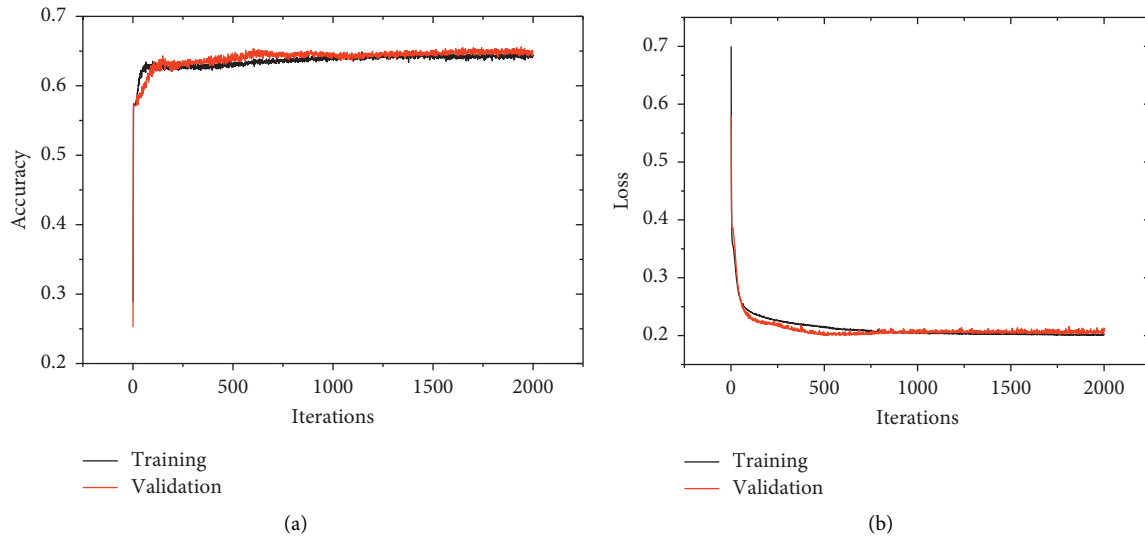


FIGURE 6: Loss and accuracy.

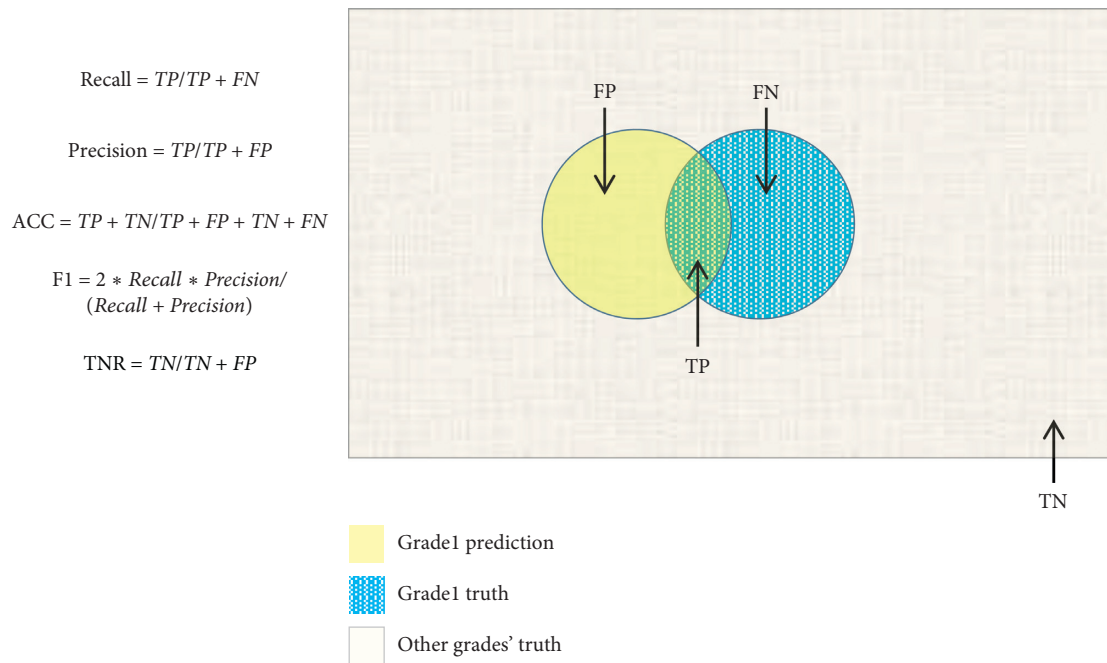


FIGURE 7: Performance evaluation metrics used in this study (taking grade 1 for example).

service has increased, and its impact on deterioration has also increased. Further, the importance of the years in service and the traffic volume is almost the same in grade 3. In addition, the influences of the lowest temperature and the chloride are increased. Because the bridges in grade 3 have been in service for an average of more than 46 years, a relatively smaller importance of a factor does not mean the factor is unimportant, because the cumulative effects of these factors are not considered. Therefore, various factors should be comprehensively considered to provide recommendations for future maintenance. In addition, intervention is performed for some bridges, which is difficult to be considered in our methodology.

**4.3.3. Estimated Importance of Different Structure Type.** The deterioration differs for different types of bridges. To observe whether the estimated importance can reflect the differences caused by different types of bridges, the average estimated importance of all factors, broken down by structure types, is shown in Figure 13.

Similar to the findings in previous sections, the years in service and the traffic volume are the two most significant factors for all the bridge types. The distribution of these factors differs in different bridge types. For the PC bridges, other factors are less important relative to the years in service, as PC bridges are generally able to withstand harsher conditions and have better durability. Compared with the PC bridge, the importance

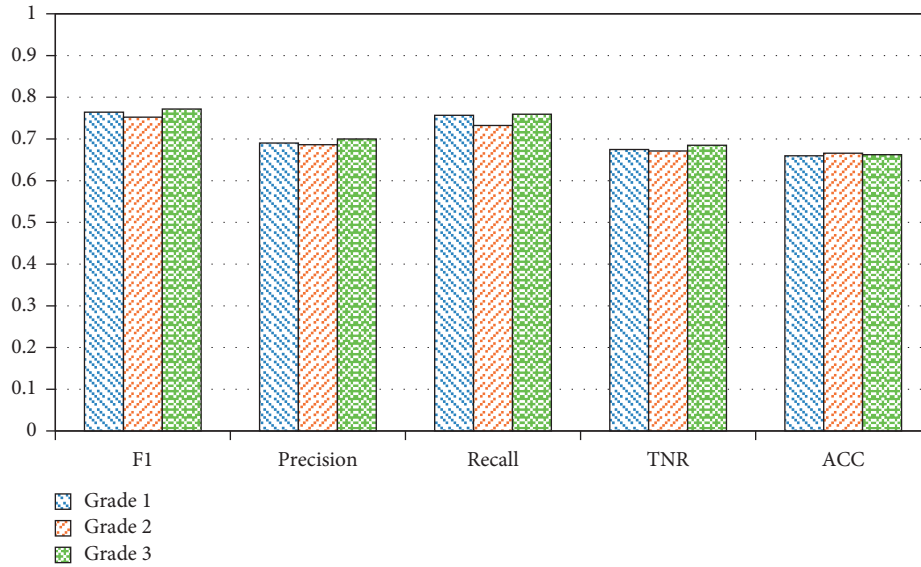


FIGURE 8: Performances of the established neural network for different grades.

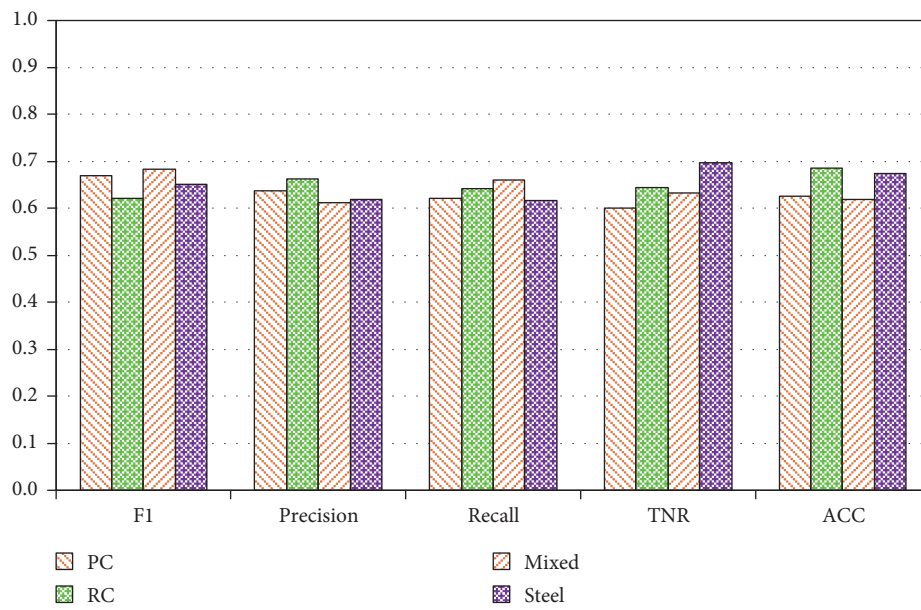


FIGURE 9: Performances of the established neural network for different types of bridges.

of the RC bridge is more uniformly distributed, because RC bridges are more susceptible to loads (traffic volume) and environmental factors (lowest temperature and chloride ion). The mixed bridge is almost in the middle of the PC bridge and RC bridge. For steel bridges, the importance of traffic volume is increased because the average daily traffic volume of this type of bridge in the applied database is usually more than 10,000 and usually accommodates many large vehicles (3337 vehicles/day).

As a result, the bridge type is determined to be another reason to lead to differences in deterioration. As for other researcher’s findings [27], materials and surrounding environments should be the most significant factors. Since the database regarding the bridge materials is unavailable, this study did not consider the differences induced by the

materials. In terms of the environment, bridges will be divided into two groups depending on the bridge is located in coastal or noncoastal regions, which will be discussed later.

4.3.4. Estimated Importance of Different Environments.

Since bridges in coastal areas are exposed to extremely severe environments for materials [41], the environments of bridges were divided into coastal and noncoastal regions according to bridge locations, and the average importance for these two environments was calculated, as shown in Figure 14. For bridges in noncoastal areas, the distribution of these factors is the same as in the previous sections, except that the estimation for chloride ion is zero because deicing

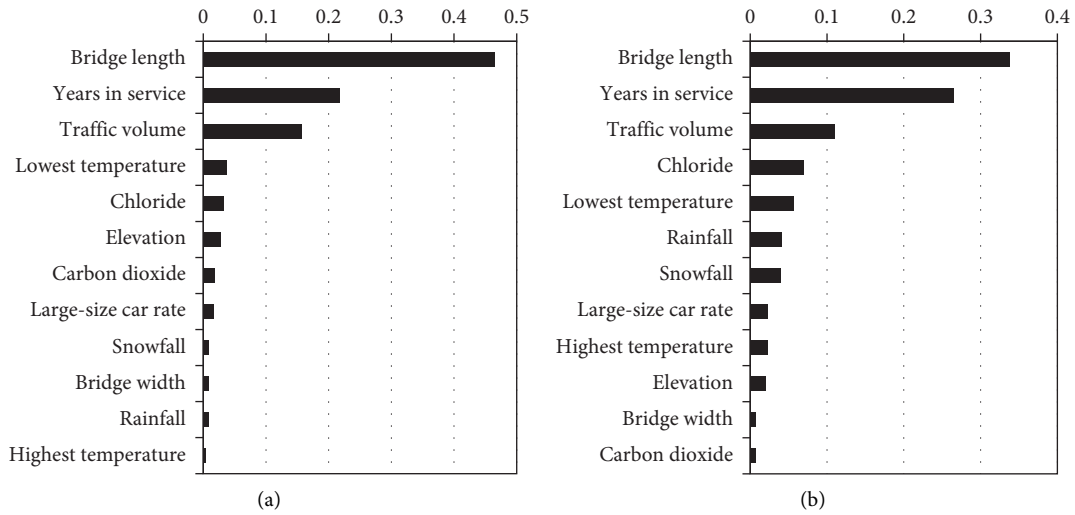


FIGURE 10: Sensitivity analysis by (a) Shapley indices and (b) Sobol value methods.

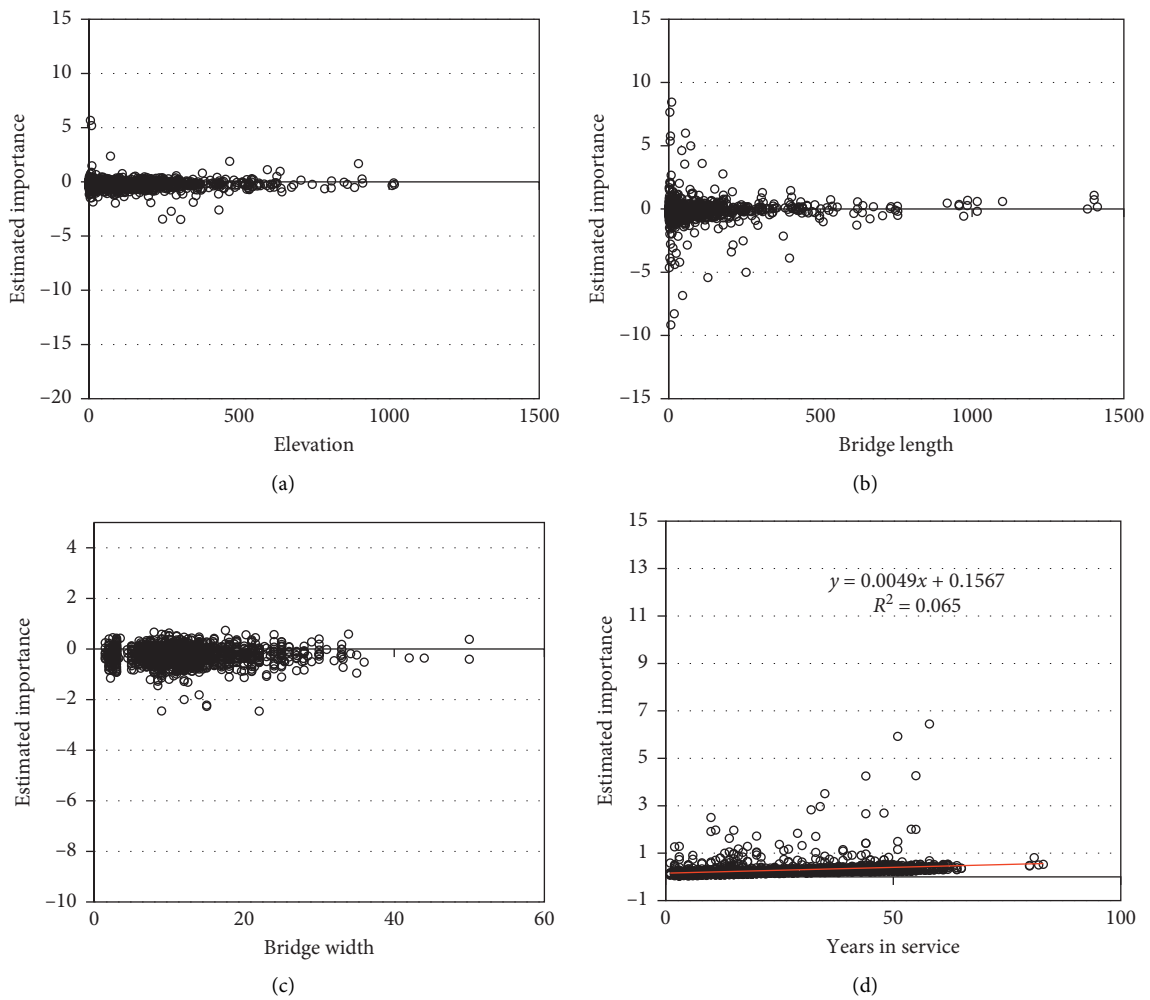
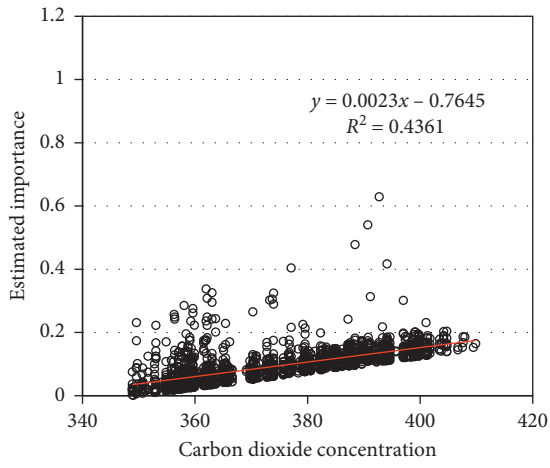
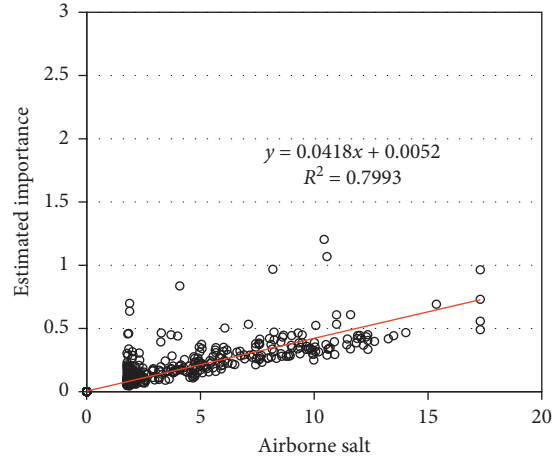


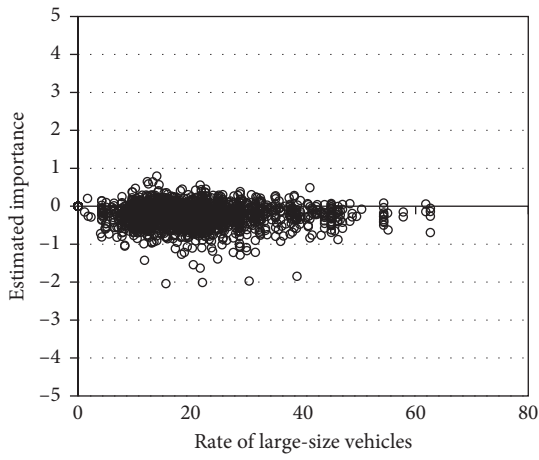
FIGURE 11: Continued.



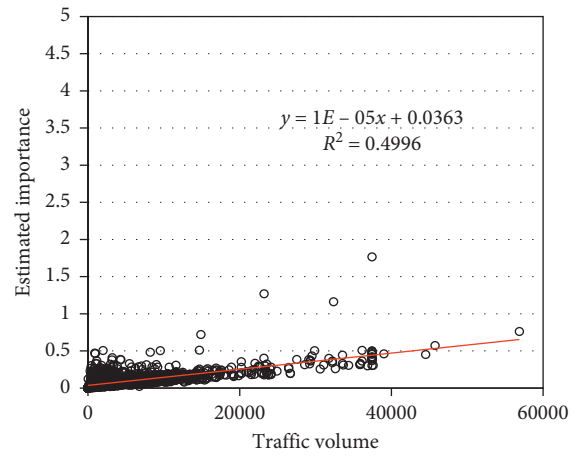
(e)



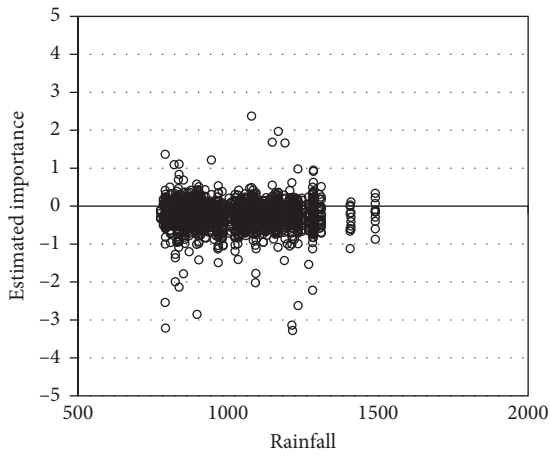
(f)



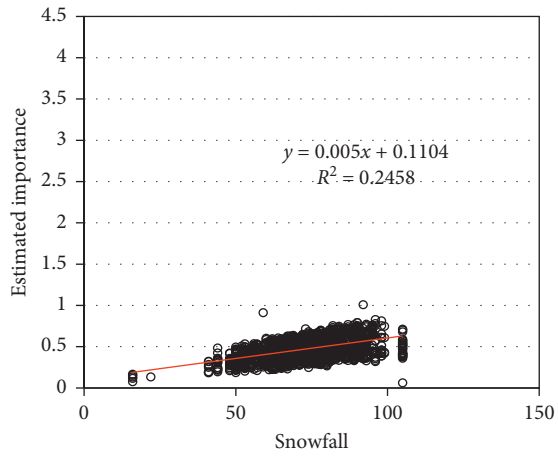
(g)



(h)



(i)



(j)

FIGURE 11: Continued.



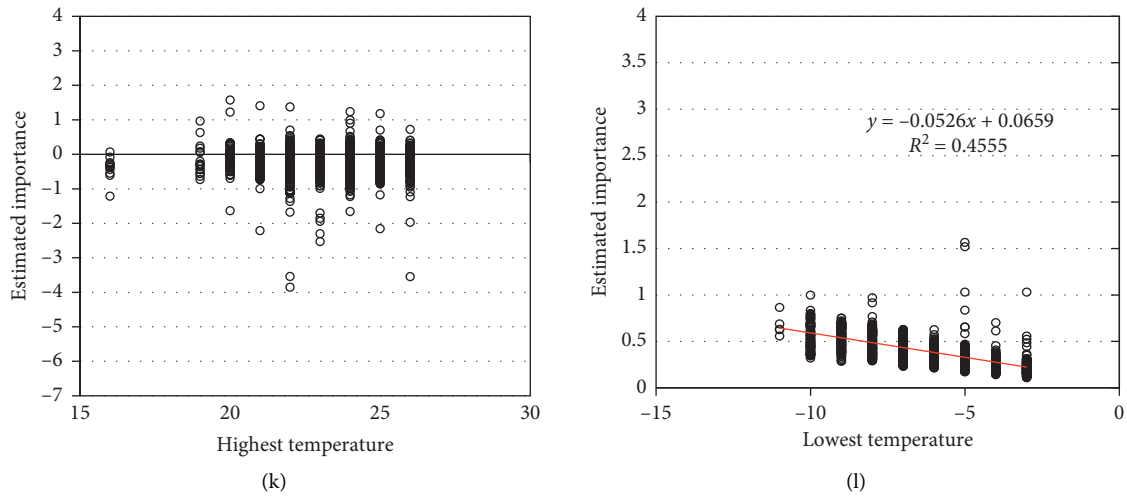


FIGURE 11: Estimated importance of each factor for all bridges.

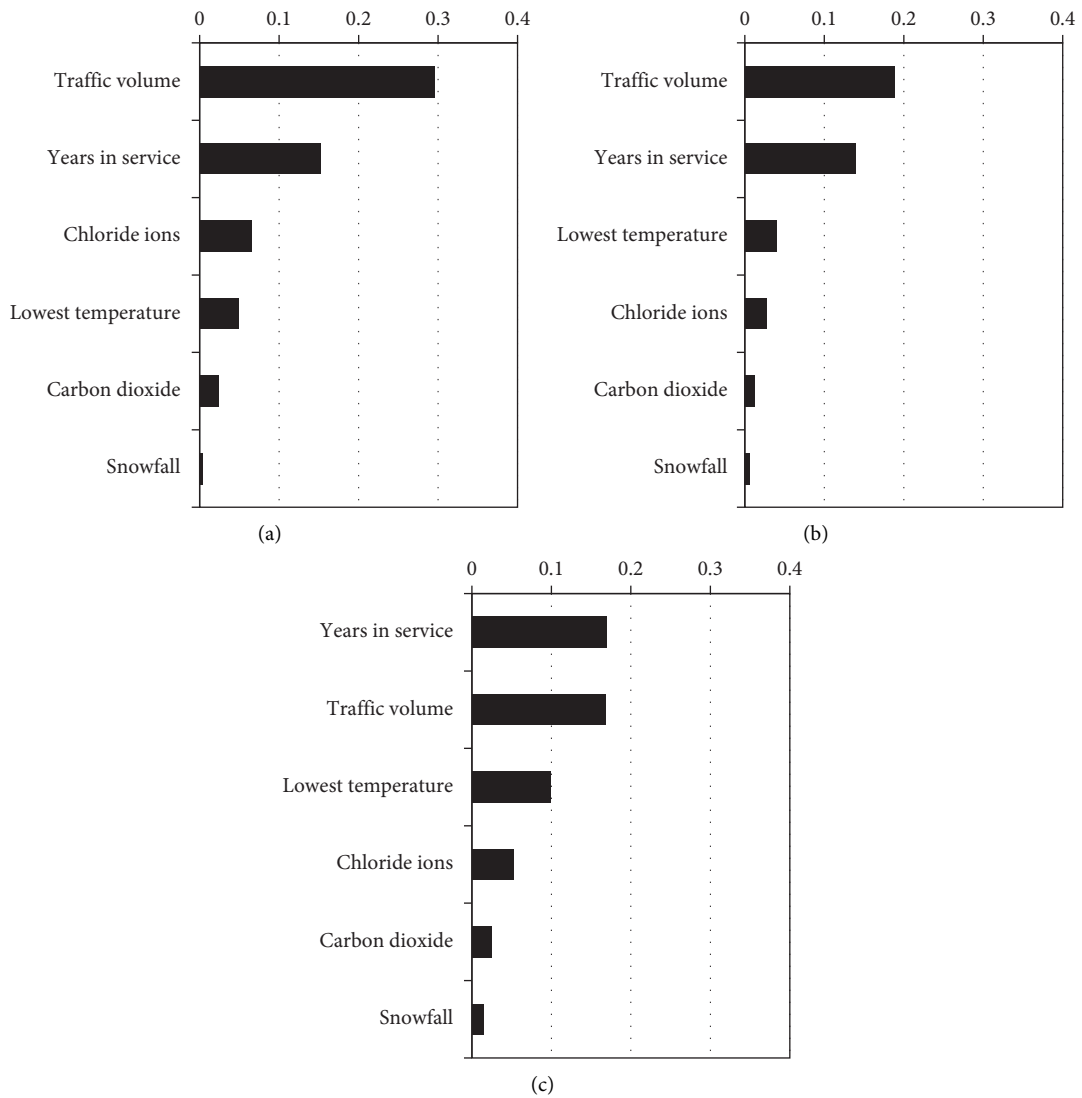


FIGURE 12: Average importance of each factor, broken down by grade. (a) Grade 1, (b) grade 2, (c) grade 3.

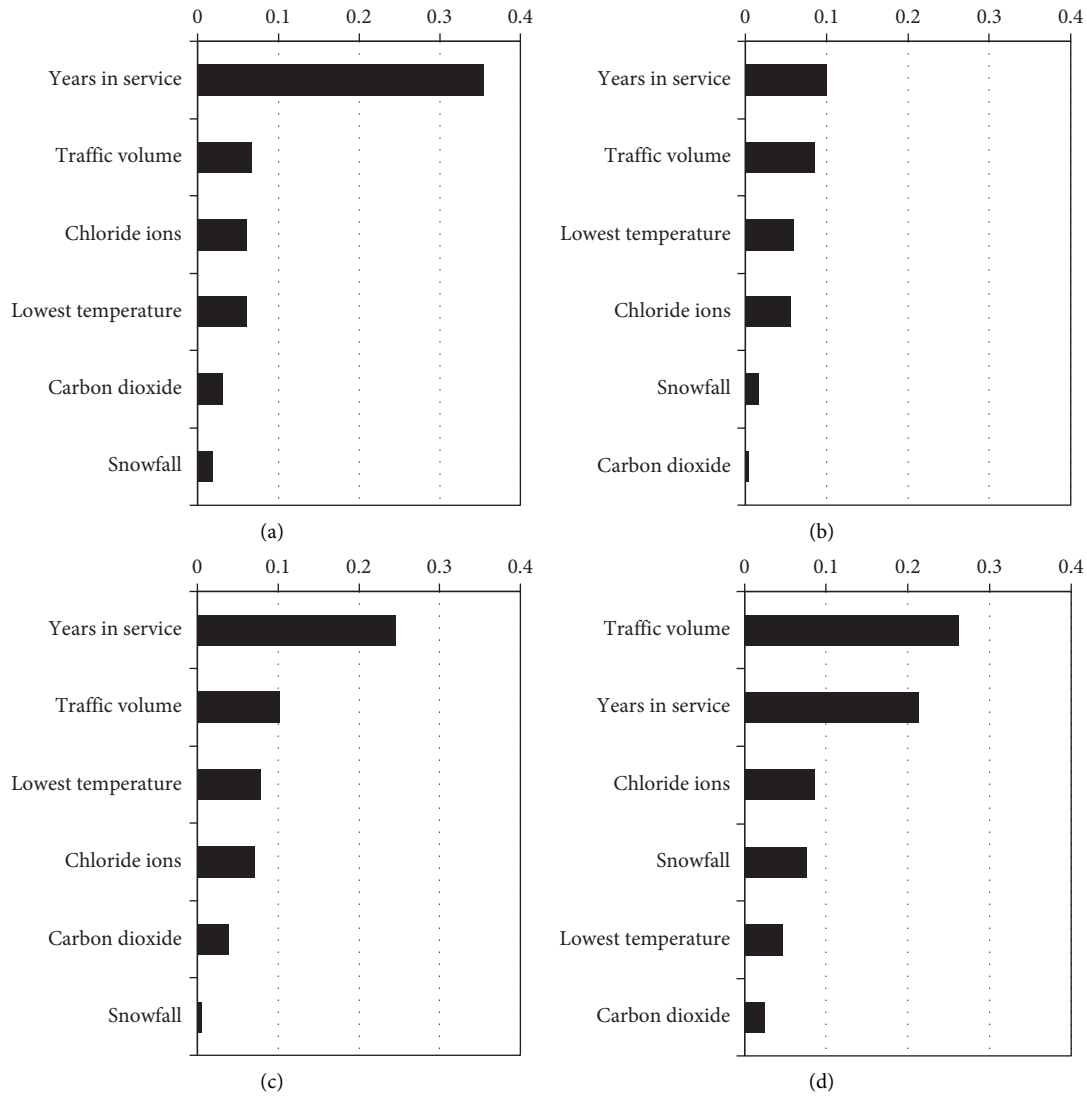


FIGURE 13: Average importance of each factor, broken down by the bridge type. (a) PC, (b) RC, (c) mixed, and (d) steel.

salt was not considered. Compared with noncoastal conditions, the impact of chloride ions in coastal region is greatly increased. In addition, the traffic volume and lowest temperature were identified two crucial factors regardless of the coastal region or noncoastal region.

The results indicated that the bridges in coastal areas are more strongly affected by airborne salt, and the estimated importance of the sensitivity analysis meets reality. In summary, there is a reasonable agreement between the estimated factors with accelerated effects and factors already known to affect the deterioration. Therefore, the sensitivity analysis can identify factors influencing deterioration and can calculate their relative importance.

### 5. Discussions

The practical usage of the proposed methodology was described using two bridges as examples. In addition, the limitations of this study were discussed.

**5.1. Formulation of Maintenance Strategy.** In practical, the established ANN can be applied to obtain the degradation progress of the targeted bridges to support the detailed inspection and maintenance, as described by taking bridges A and B as examples (Table 5). Bridges A and B were inspected in 2016 and 2015, respectively, and both of them were assessed to be grade 1. Bridges A and B have been in service for twelve years and fifty years, respectively. By updating the values of the factors listed in Table 5, the deterioration situation of the bridge can be predicted through the prediction model. As a result, the deterioration progresses of bridges A and B over time are shown in Figure 15. The results reveal that bridge A will stay at grade 1 for a long time, while bridge B will degrade to grade 3 soon.

Figure 16 shows the estimated importance of each factor for bridges A and B. The results show that the years in service, chloride ions, and traffic volume are the three most significant factors for these bridges. The other three factors have relatively fewer influences.

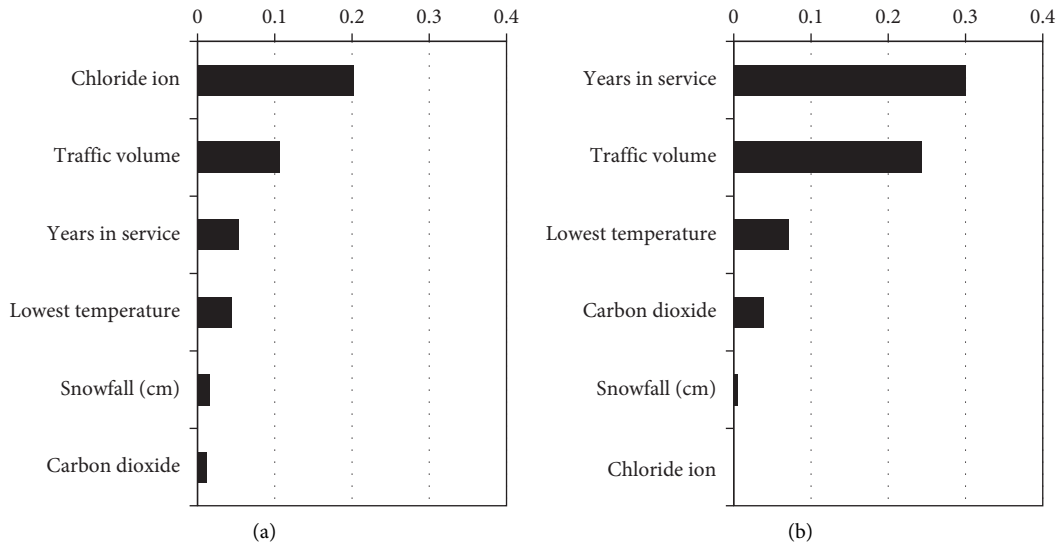


FIGURE 14: Average importance of each factor, broken down by (a) coastal region and (b) noncoastal region.

TABLE 5: Information of bridges A and B.

	Bridge A	Bridge B
Elevation (m)	3	2.9
Bridge length (m)	35	12.54
Bridge width (m)	9.5	11
Years in service (years)	12	50
Carbon dioxide (ppm)	393.32	356.38
Chloride (kg/m <sup>3</sup> )	2.2	2
Large-size vehicles rate (%/day)	15.3	20.3
Traffic volume (vehicles/day)	1057	13233
Rainfall (cm)	954	1060
Snowfall (cm)	345.77	635.60
Highest temperature (°C)	19	24
Lowest temperature (°C)	-3	-3

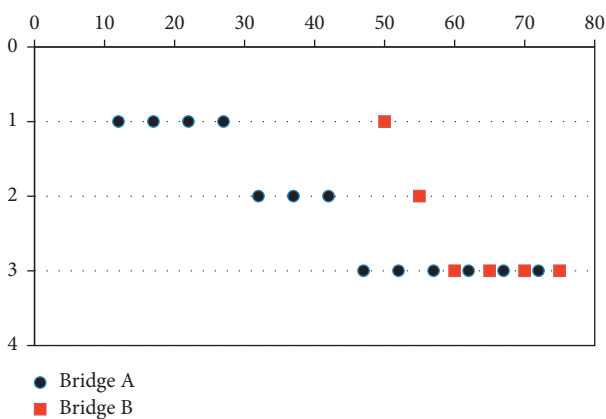


FIGURE 15: Prediction of the deterioration grades for bridges A and B.

However, the estimated importance for the two bridges shows significant differences. For bridge A, the most significant factor is the traffic volume; the other factors are relatively lower. Because bridge A has been in service for only 12 years, the natural degradation of the materials is not obvious, and

the impact of carbonation and chloride ion is still tiny. Considering bridge A will remain in grade 1 for the next 20 years, no special maintenance is necessary for bridge A in ten years. As bridge B has been in service for 50 years and has recently accommodated many large-size vehicles, the lowest temperature, traffic volume, and chloride ion have all had essential impacts except for years in service. In addition, the deterioration of bridge B will worsen from grade 1 to 3 soon, according to the deterioration curve in Figure 15. Therefore, bridge B should be introduced to the detailed inspection and fully maintained in five years. The results indicate that even though the deterioration of bridge A and bridge B are both being grade 1, the calculated relative importance of all factors is different. Obviously, the estimated relative importance can reflect the bridge’s properties and the reasons for deterioration. Additionally, further inspection and corresponding maintenance strategies can be set up.

5.2. Limitations. In this study, a methodology was proposed to predict deterioration and analyze the reasons for deterioration. The prediction model does not provide quantitative results for the deterioration situation of the bridge, but

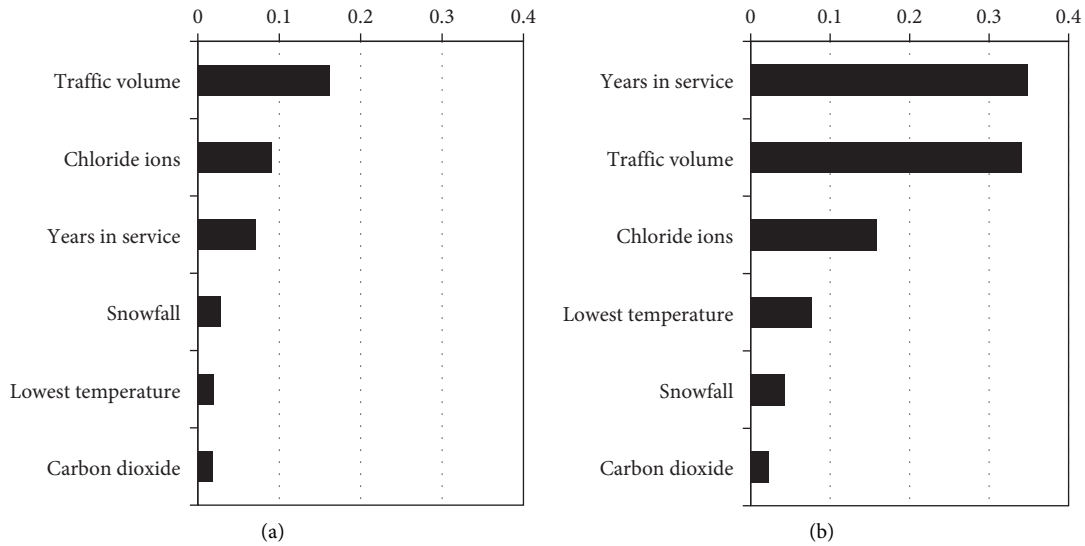


FIGURE 16: Estimated importance value for (a) bridge A and (b) bridge B.

it can be used as a supplementary tool in the preliminary inspection stage to distinguish seriously and nonseriously deteriorated bridges. Then, the seriously deteriorated bridge can be introduced to the detailed inspection and post-maintenance. Although the methodology is verified by a practical database, this study should still be regarded as an initial and ideal attempt. In this attempt, the bridge's specific materials was not considered in the deterioration predictions. For this reason, the analyzed results deviate from the practical situation to some extent. In addition, several other factors are associated with deterioration but are not considered, such as the application of deicing salt, design strength, and intervention histories. Furthermore, the deterioration differences in various components of the same bridge were not taken into account.

Because the applied database excludes bridges in grade 4, the established model can only predict the deterioration situation of grade 3 and before. These deficiencies will encourage us to collect more data for improving future work. In assessing a factor's importance, the Shapley value method considers all possible influencing factors. But sometimes, the calculated importance is unreasonable because Shapley value method does not satisfy rational constraints. Since the deterioration grade is evaluated subjectively, the grades are not quantitatively relating to the deterioration situation. This leads to a bias in the calculated importance.

Future attempts could focus on collecting more relevant factors for improved interpretations of factors that contribute to deterioration. Another future improvement will be to modify the prediction and sensitivity analysis model, the integration of more high-quality data, and the quantitation of the deterioration grades.

## 6. Conclusions

This study proposed a methodology to integrate an artificial neural network (ANN) with sensitivity analysis method. The

ANN was performed to predict deterioration to determine further inspection and maintenance timing. The sensitivity analysis method offered insights into the prediction model to understand the reasons for deterioration. From the verification results using an inspection database, the following conclusions can be drawn:

- (1) The combination of an ANN and sensitivity analysis method can effectively avoid the uncertainty of factors on deterioration to some extent. Therefore, the methodology can make predictions and understand factors affecting the predictions with the importance list of all influencing factors.
- (2) An ANN was established considering twelve influencing factors as inputs and three deterioration grades as outputs. The established ANN obtained an accuracy of about 65%. Although the model's performance is not yet perfect, the predictability is still acceptable considering the complexity of the existing bridges. In addition, the model has equivalent performance for three deterioration grades and four types of bridges. Practically, the deterioration progress of a bridge can be formulated to determine the detailed inspection and maintenance timing.
- (3) The Sobol indices and Shapley value methods can identify the reasons for deterioration by performing the sensitivity analysis, and they show consistency for the five most important factors. This is an important step towards applying the neural network to practical maintenance because the sensitivity analysis converts abstract and inexplicable predictions into the relative importance of factors that are easy for engineers to understand and act on.
- (4) From the estimated importance of factors, six factors were identified that would accelerate deterioration. They are years in service, carbon dioxide concentration, chloride ion concentration, traffic volume,

snowfall, and lowest temperature. In addition, the analysis revealed that the bridge type is another significant reason to induce deterioration differences. The truth that the significant differences for bridges between coastal and noncoastal areas are the airborne salt was also revealed in the sensitivity analysis. The relative importance list of factors offers engineers the possibility of figuring out factors that significantly affect deterioration and formulating interventions accordingly for a specific bridge.

In the future, endeavors will be enforced to solve the limitations described in Section 5.2 to improve the performance of the proposed methodology.

### Data Availability

The data used in the present study can be made available upon request from the authors.

### Conflicts of Interest

The authors declare that they have no conflicts of interest.

### References

- [1] C. Andrade, "Propagation of reinforcement corrosion: principles, testing and modelling," *Materials and Structures*, vol. 52, no. 1, p. 2, 2019.
- [2] C. Stenström, P. Norrbin, A. Parida, and U. Kumar, "Preventive and corrective maintenance - cost comparison and cost-benefit analysis," *Structure and Infrastructure Engineering*, vol. 12, no. 5, pp. 603–617, 2016.
- [3] D. E. Rumelhart, G. E. Hinton, and R. J. Williams, "Learning representations by back-propagating errors," *Nature*, vol. 323, no. 6088, pp. 533–536, 1986.
- [4] Z. Zhang, M. W. Beck, and M. W. Beck, "Opening the black box of neural networks: methods for interpreting neural network models in clinical applications," *Annals of Translational Medicine*, vol. 6, no. 11, p. 216, 2018.
- [5] S. M. Lundberg, B. Nair, and M. S. Vavilala, "Explainable machine-learning predictions for the prevention of hypoxaemia during surgery," *Nature Biomedical Engineering*, vol. 2, no. 10, pp. 749–760, 2018.
- [6] A. B. Owen, "Sobol' indices and Shapley value," *SIAM/ASA Journal on Uncertainty Quantification*, vol. 2, no. 1, pp. 245–251, 2014.
- [7] I. M. Sobol, "Global sensitivity indices for nonlinear mathematical models and their Monte Carlo estimates," *Mathematics and Computers in Simulation*, vol. 55, no. 1–3, pp. 271–280, 2001.
- [8] MLIT, "Guidelines for regular inspection of road bridges, MLIT," 2018, [https://www.mlit.go.jp/road/sisaku/yobohozen/tenken/yobo4\\_1.pdf](https://www.mlit.go.jp/road/sisaku/yobohozen/tenken/yobo4_1.pdf).
- [9] S. Lee and N. Kalos, "Non-destructive testing methods in the U.S. for bridge inspection and maintenance," *KSCSE Journal of Civil Engineering*, vol. 18, no. 5, pp. 1322–1331, 2014.
- [10] Y. Jeong, W. Kim, I. Lee, and J. Lee, "Bridge inspection practices and bridge management programs in China, Japan, Korea, and U.S.," *Journal of Structural Integrity and Maintenance*, vol. 3, no. 2, pp. 126–135, 2018.
- [11] A. Al-Hussein, "Estimating bridge deterioration age using artificial neural networks," <https://bpace.buid.ac.ae/handle/1234/1128> Doctoral dissertation, The British University in Dubai, 2017.
- [12] W. Hyman, D. Hughes, and T. Dobson, "The least cost mix of bridge replacement and repair work on wisconsin's state highways over time—a computer simulation," Technical Rep., WisDOT, Madison, WI, USA, 1983.
- [13] G. Busa, M. Ben-Akiva, and O. Buyukozturk, *Modeling Concrete Deck Deterioration*, Department of Civil Engineering, Massachusetts Institute of Technology, Cambridge, MA, USA, 1985.
- [14] A. Abu-Tair, C. McParland, J. Lyness, and A. Nadjai, "Predictive models of deterioration rates of bridges using the factor method based on historic inspection data," in *Proceedings of the 9th International Conference on Durability of Building Materials and Components (DBMC)*, Brisbane, Australia, March 2002.
- [15] N.-F. Pan, T.-C. Lin, and N.-H. Pan, "Estimating bridge performance based on a matrix-driven fuzzy linear regression model," *Automation in Construction*, vol. 18, no. 5, pp. 578–586, 2009.
- [16] J. Kim, N. Gucunski, and K. Dinh, "Deterioration and predictive condition modeling of concrete bridge decks based on data from periodic NDE surveys," *Journal of Infrastructure Methodologies*, vol. 25, no. 2, Article ID 04019010, 2019.
- [17] Y. Jeong, W. Kim, I. Lee, and J. Lee, "Bridge service life estimation considering inspection reliability," *KSCSE Journal of Civil Engineering*, vol. 21, no. 5, pp. 1882–1893, 2017.
- [18] A. K. Agrawal, A. Kawaguchi, and Z. Chen, "Deterioration rates of typical bridge elements in New York," *Journal of Bridge Engineering*, vol. 15, no. 4, pp. 419–429, 2010.
- [19] L. Li, L. Sun, and G. Ning, "Deterioration prediction of urban bridges on network level using Markov-chain model," *Mathematical Problems in Engineering*, vol. 2014, Article ID 728107, 10 pages, 2014.
- [20] N. K. W. Wellalage, T. Zhang, and R. Dwight, "Calibrating Markov chain-based deterioration models for predicting future conditions of railway bridge elements," *Journal of Bridge Engineering*, vol. 20, no. 2, Article ID 04014060, 2015.
- [21] M. Mauch and S. Madanat, "Semiparametric hazard rate models of reinforced concrete bridge deck deterioration," *Journal of Infrastructure Systems*, vol. 7, no. 2, pp. 49–57, 2001.
- [22] L. S. Lee, "Rehabilitation and service life estimation of bridge superstructures," in *Service Life Estimation and Extension of Civil Engineering Structures* Woodhead Publishing, Cambridge, England, 2011.
- [23] R. S. Adhikari, O. Moselhi, and A. Bagchi, "Image-based retrieval of concrete crack properties for bridge inspection," *Automation in Construction*, vol. 39, pp. 180–194, 2014.
- [24] O. A. Hodhod and H. I. Ahmed, "Developing an artificial neural network model to evaluate chloride diffusivity in high performance concrete," *HBRC Journal*, vol. 9, no. 1, pp. 15–21, 2013.
- [25] I. Mikami, S. Tanaka, and A. Kurachi, "Expert system with learning ability for retrofitting steel bridges," *Journal of Computing in Civil Engineering*, vol. 8, no. 1, pp. 88–102, 1994.
- [26] J. O. Sobanjo, "A neural network approach to modeling bridge deterioration," in *Computing in Civil Engineering*, pp. 623–626, ASCE, Reston, VA, USA, 1997.
- [27] Y.-H. Huang, "Artificial neural network model of bridge deterioration," *Journal of Performance of Constructed Facilities*, vol. 24, no. 6, pp. 597–602, 2010.
- [28] S. Lim and S. Chi, "Bridge damage prediction using deep neural network," *Computing in Civil Engineering 2019, Smart*



- Cities, Sustainability, and Resilience*, American Society of Civil Engineers, Reston, VA, USA, pp. 219–225, 2019.
- [29] R. Caruana, Y. Lou, J. Gehrke, P. Koch, M. Sturm, and N. Elhadad, “Intelligible models for HealthCare,” in *Proceedings of the 21st ACM SIGKDD International Conference on Knowledge Discovery and Data Mining*, pp. 1721–1730, ACM, Sydney, Australia, August 2015.
- [30] F. Ming, C. Du, Y. Liu, X. Shi, and D. Li, “Concrete durability under different circumstances based on multi-factor effects,” *Sciences in Cold and Arid Regions*, vol. 9, no. 4, pp. 384–391, 2018.
- [31] ISO 15686-1, *Buildings and Construction Assets–Service Life Planning–Part 1: General Principles and Framework*, ISO, Geneva, Switzerland, 2011.
- [32] I. Goodfellow, Y. Bengio, and A. Courville, *Deep Learning*, MIT Press, Cambridge, MA, USA, 2016.
- [33] N. J. Guliyev and V. E. Ismailov, “A single hidden layer feedforward network with only one neuron in the hidden layer can approximate any univariate function,” *Neural Computation*, vol. 28, no. 7, pp. 1289–1304, 2016.
- [34] A. B. Owen and C. Prieur, “On Shapley value for measuring importance of dependent inputs,” *SIAM/ASA Journal on Uncertainty Quantification*, vol. 5, no. 1, pp. 986–1002, 2017.
- [35] I. E. Kumar, S. Venkatasubramanian, C. Scheidegger, and S. Friedler, “Problems with Shapley-value-based explanations as feature importance measures,” 2020, <https://arxiv.org/abs/2002.11097>.
- [36] JMA, “Annual changes of carbon dioxide concentration by locations,” Japan Meteorological Agency, 2019, <https://ds.data.jma.go.jp/ghg/kanshi/co2timeser/co2timeser.html>.
- [37] MLIT, “Guidelines for general traffic survey,” MLIT, 2010, <http://www.mlit.go.jp/road/census/h22-1/data/kasyorep.pdf>.
- [38] MLIT, “National road and street traffic situation survey (general traffic volume survey),” 2015, <http://www.mlit.go.jp/road/census/h27/index.html>.
- [39] R. Kobayashi, “Survey on salinity penetration of existing bridges along the coast of oshima peninsula, Hokkaido, special report on survey report at 2009 diagnosis workshop,” *Concrete Diagnosis Page*, vol. 48, no. 7, pp. 52–55, 2010.
- [40] JSCE, *Standard Specifications for Concrete Structures (Design)*, Japan Society of Civil Engineers, JSCE Guidelines for Concrete, Tokyo, Japan, 2012.
- [41] H. Yokota, “Practical application of life-cycle management system for shore protection facilities,” *Structure and Infrastructure Engineering*, vol. 13, no. 1, pp. 34–43, 2017.

## Research Article

# The Undrained Characteristics of Tengger Desert Sand from True Triaxial Testing

Xuefeng Li <sup>1,2</sup>, Weinan Lu <sup>1</sup>, Zhigang Ma <sup>1</sup> and Ni Tuo <sup>1</sup>

<sup>1</sup>School of Physics and Electronic-Electronic Engineering, Ningxia University, Yinchuan 750021, China

<sup>2</sup>Solid Mechanics Institute, Ningxia University, Yinchuan 750021, China

Correspondence should be addressed to Xuefeng Li; [lixuefeng1928@163.com](mailto:lixuefeng1928@163.com)

Received 26 April 2021; Revised 8 June 2021; Accepted 26 June 2021; Published 7 July 2021

Academic Editor: Pengfei Liu

Copyright © 2021 Xuefeng Li et al. This is an open access article distributed under the Creative Commons Attribution License, which permits unrestricted use, distribution, and reproduction in any medium, provided the original work is properly cited.

Aimed at the characteristics of aeolian sand under rapid construction conditions in desert geotechnical engineering, a series of the true triaxial undrained test were carried out on the GDS apparatus. The 3D deformation, failure, and other characteristics of the dense sand are obtained. Under the condition of same  $p_c$ , the state transition point where the void water pressure changes from increasing to decreasing appears earlier and leads to enhanced dilatancy with the increase of  $b$ , which means the enhanced dilatancy of dense sand caused the increase in strength. The results of the same  $b$  shows that the void water pressure generally indicates a decrease at low confining pressure and an increase at high confining pressure, indicating that the aeolian sand shows dilatancy at low confining pressure and contraction at high confining pressure. The state transition point increases with the increase of  $p_c$ , but all points tend to the same critical state line and state transition line. When  $b = 0$ , the critical state line is  $q = 1.57 p'$ , and the state transition line is  $q = 1.23 p'$ . When  $b = 1$ , the critical state line is  $q = 1.24 p'$ , and the state transition line is  $q = 1.04 p'$ . The results at same  $b$  obtained the unified critical state line and the state transition line. Therefore, the true triaxial test can obtain the unified relationship of void ratio,  $p_c$  and  $b$ , which overcomes the fact that the existing test cannot consider the influence of  $b$ . The test results provide a basis data for the design, construction, and maintenance of geotechnical engineering in Tengger Desert.

## 1. Introduction

The policy of Western development in China has greatly promoted the infrastructure construction in desert areas, and a large number of desert geotechnical engineering will be built [1]; however, the experimental research on aeolian sand is lagging behind. Tengger Desert is the fourth largest desert in China, covering an area of 42,700 square kilometers. Due to its arid nature environment and aeolian characteristics, aeolian sand is characterized by fine particles, irregular morphology, poor surface activity, low water content, and high permeability. Restricted by arid natural environment and underdeveloped social conditions in the west of China, the test results of aeolian sand are scarce, and only a few test results serve the engineering construction, such as the construction of roads [2], railways [3, 4], and

power transmission lines [5, 6] crossing the desert, and its eco-environmental construction. A targeted research has been done on accidents such as quicksand, collapse, and excessive settlement of the superstructure during construction [7]. The research on the compaction characteristics of subgrade [8–10] shows that the aeolian sand has a high degree of compaction under dry conditions and saturated conditions, so it has the unique characteristics of compaction “bimodal,” which provides a dry compaction technology of subgrade construction in the desert area. Aeolian sand is also collapsible, which is attributed to the high content of fine sand and low dry density [11, 12]. Wang et al. [13] found that the sand collapsibility is indirectly verified by the additional settlement of the sand after wetting. The bimodal characteristics and the collapsibility are two unique properties of aeolian sand obtained from the tests at present.

However, many other properties of aeolian sand in 3D space, such as the strength, the stress-strain relationship, the dilatancy, and the critical state, have rarely been studied.

In practical engineering, the characteristics of sand are meaningful in 3D stress state [14, 15]. However, there are relatively few results from triaxial tests of aeolian sand in China. For the true triaxial test of aeolian sand, only Li et al. [16] carried out the drainage test of Tengger Desert sand. For the conventional triaxial test, Deng [17] and Song [18] had carried out static-dynamic tests. Zhang et al. [19], Zhang et al. [20], and Li et al. [21] studied on the freeze-thaw cycle properties. Li and Zhang [22] carried out undrained tests for the Mu Us Desert sand with different confining pressure. Hao et al. [23] studied the structural strength index of unsaturated sand. The study of Badanagki's [24] undrained test for the Sahara sand states that the shear strength decreases with the increase of relative compaction.

At present, only the true triaxial tests of other types of sand are studied, but the results are relatively few. Choi et al. [25] carried out true triaxial tests for drained and undrained with different stress path. Suits et al. [26] studied the influence of intermediate principal stress on the stress-strain relationships and found that the obvious anisotropy was shown in the sand. Lade and Wang [27] studied the deformation and failure characteristics of sand with the different densities and found that the peak failure of sand was mainly caused by shear bands. For Toyoura sand, Yamada and Ishihara [28] and Yoshimine et al. [29] found that the larger  $b$  is, the greater the void water pressure is, which has a greater impact on the deformation. Pan et al. [30] found that triaxial compression and triaxial extension tests show significantly different characteristics and triaxial compression is characterized by shear dilatation but the extension test is dominated by strain softening. For the Fujian standard sand, Xu et al. [31] found that the  $b$ -value has little effect on stress ratio, and Li and Yang [32] found that the confining pressure has little effect on the strength of the specimen. For the Ottawa sand, Murthy et al. [33] found that the critical state of the drainage test is the same as the undrained test, and the undrained shear strength increases with the increase of specimen density. For Shanghai sily sand, Hu et al. [34] found that the peak stress is raised with the increase of the confining pressure at failure, but the relationships between shear stress and the  $b$ -value are complicated. Liang and Ping [35] found that the peak shear stress increases with the increase of  $b$  and the void water pressure first increases and then decreases. Therefore, in geotechnical engineering [36] the sand foundation will lose its bearing capacity due to the increase of void water pressure under the condition of instantaneous strong load or cyclic load. So it is necessary to carry out the undrained test.

The research on the strength of subgrade has accumulated some experience, which mainly focuses on highway design, construction technology, and meteorological and hydrological detection in the Tengger Desert area. However, the results of triaxial tests on aeolian sand are seriously lacking, which affect the understanding of its engineering characteristics. Especially because the critical state line of sand is not unique, it is mainly affected by the stress path and

anisotropy [37, 39]. The true triaxial test can be used to study various complex stress paths and the critical state of soil in true 3D space. In this paper, the true triaxial undrained test of aeolian sand in Tengger Desert is carried out by the British GDS true triaxial apparatus. The deformation, failure, dilatancy, and critical state characteristics of sand are studied with different  $b$ -values and  $p_c$ . Through the analysis of void water pressure, generalized shear stress, stress ratio, and other mechanical characteristics, the undrained strength of Tengger Desert sand will be explored.

## 2. The True Triaxial Equipment

The British GDS true triaxial apparatus is used (Figure 1) in this paper, which can carry out the static and dynamic quick loading test. As shown in Figures 1 and 2, the specimen is placed in the pressure chamber, and the pressure is applied by the rigid loading plates and flexible loading systems. Rigid loading is controlled by a servo motor and flexible loading is applied by water. The flexible load is controlled by the pneumatic controller. The air pressure controller is connected to the air collector and air pump, indicated by the green line in Figure 1. For more detailed introduction of the loading method, see reference [16].

## 3. Test Processes and Schemes

*3.1. Introduction to the Test.* The sand is collected from Tengger Desert in the Shapotou area, Zhongwei City, Ningxia Hui Autonomous Region, where is the distribution area of typical aeolian sand. The sand particle size of 0.075~0.5 mm accounts for more than 90%. The size gradation and some physical properties of aeolian sand are shown in Table 1. According to the Unified Soil Classification System, Tengger Desert sand is fine sand [40]. The size of the specimen is 75 × 75 × 150 mm. According to the method of layering compaction, the cuboid specimen is divided into 10 layers. The relative compaction of the specimen is controlled at 0.7. The weight of the specimen is 1291 g. A dry deposition method is used for the preparation specimen.

The specimen is saturated by two steps: one is head saturation, and another is backpressure saturation. After the backpressure saturation, the void water pressure coefficient ( $B$ ) is computed. If  $B$  reaches more than 95%, the specimen can be considered to be saturated fully.  $B$  represents the saturation degree of the specimen, when  $B = 0$ , the specimen is completely dried, and when  $B = 1$ , the specimen is saturated 100%. The consolidation adopts an isotropic method of rigid and flexible combination. The criterion for the end of consolidation is that the change of water volume in the backpressure controller does not exceed 1% of the total amount within a certain time (30 min).

In the shearing process, the strain control loading can be adopted to ensure constant  $b$ -value, and the strain control can also better control the collision of rigid loading. According to the definition of  $b$ -value, the expression equation (1) of the intermediate principal strain coefficient

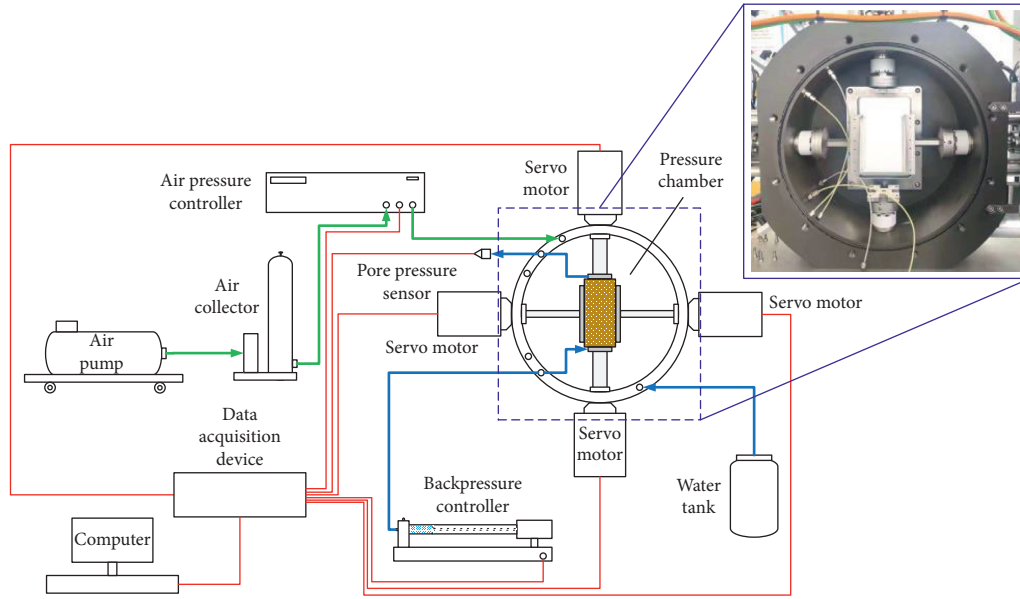


FIGURE 1: The true triaxial test system.

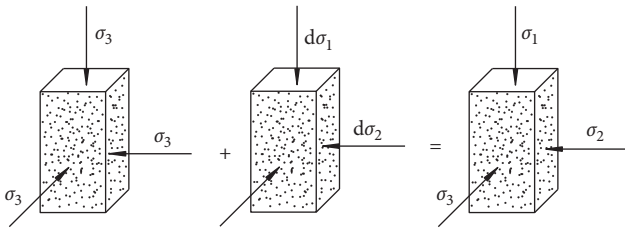


FIGURE 2: Loading diagram.

( $b_\epsilon$ ) is given. The strain control loading under the condition of constant  $b$  can be realized through equations (1) and (2):

$$b_\epsilon = \frac{\epsilon_2 - \epsilon_3}{\epsilon_1 - \epsilon_3} \quad (0 \leq b_\epsilon \leq 1), \quad (1)$$

where  $\epsilon_1, \epsilon_2$ , and  $\epsilon_3$  are the maximum principal strain, the intermediate principal strain, and the minimum principal strain, respectively.

Under the undrained condition, the volume of the soil sample remains unchanged, and the strain satisfies

$$\epsilon_v = \epsilon_1 + \epsilon_2 + \epsilon_3, \quad (2)$$

where  $\epsilon_v$  is the volume strain.

According to equations (1) and (2), the incremental relation is

$$\begin{cases} d\epsilon_1 = d\epsilon_1, \\ d\epsilon_2 = b_\epsilon d\epsilon_1, \\ d\epsilon_3 = 0, \end{cases} \quad (3)$$

where  $d\epsilon_1, d\epsilon_2$ , and  $d\epsilon_3$  are the increment of maximum principal strain, intermediate principal strain, and minimum principal strain, respectively. From equation (3), the loading method of constant  $b$ -value is performed. The loading in the

direction of  $\epsilon_1$  and  $\epsilon_2$  is rigid, and the loading in the direction of  $\epsilon_3$  is flexible (Figure 2). The pressure on the flexible surface is a constant, and two rigid plates in equation (3) can be used to control the intermediate principal stress coefficient.

**3.2. Test Schemes.** Three group schemes are designed in this experiment. The first is to adopt the  $b$ -values of 0, 0.25, 0.5, and 1, respectively, under the condition of keeping  $p_c$  equal to 100 kPa. In the shearing progress,  $b$ -value and  $p_c$  are constant. The stress paths are shown in Figure 3(a).

The second is to adopt  $p_c$  of 50 kPa, 100 kPa, 200 kPa, 400 kPa, and 800 kPa, respectively, with  $b = 0$ . The purpose is to obtain the critical state line, state transition line, and the stress-strain relationship of dense aeolian sand under the undrained condition with  $b = 0$ . The stress paths are shown in Figure 3(b).

The third is to adopt  $p_c$  of 50 kPa, 100 kPa, and 200 kPa, respectively, with  $b = 1$ . The purpose is to obtain the critical state line and state transition line of the aeolian sand under the undrained condition with  $b = 1$ . The stress path is shown in Figure 3(c).

In the direction of  $\sigma_1$ , the speed of strain loading is 0.315 mm/min, 0.315 mm equivalent to 0.21% of the height of specimen. The maximum vertical displacement is 37.5 mm, 37.5 mm equivalent to a maximum  $\epsilon_1$  of 25%. In Figure 3, the horizontal axis and vertical axis are the mean principal stress  $p$  and generalized shear stress  $q$ , which are  $p = ((\sigma_1 + \sigma_2 + \sigma_3)/3)$  and  $q = \sqrt{((\sigma_1 - \sigma_2)^2 + (\sigma_2 - \sigma_3)^2 + (\sigma_3 - \sigma_1)^2)/2}$ .

## 4. Test Results and Analysis

**4.1. The Stress Path of the Test.** The purpose of the tests is to study the strength and the stress-strain relationship of dense sand in the different stress paths space. As designed in the schemes, it is to study the deformation and strength of sand with the same  $p_c$  and different  $b$ -values, as well as the stress-

TABLE 1: The main physical properties of aeolian sand.

Maximum dry density	Minimum dry density	Moisture content (%)	Grain composition				
			>0.75 mm (%)	0.75~0.5 mm (%)	0.5~0.25 mm (%)	0.25~0.1 mm (%)	<0.1 mm
1.62 g/cm <sup>3</sup>	1.36 g/cm <sup>3</sup>	0.14	0.07	3.83	94.41	1.69	0

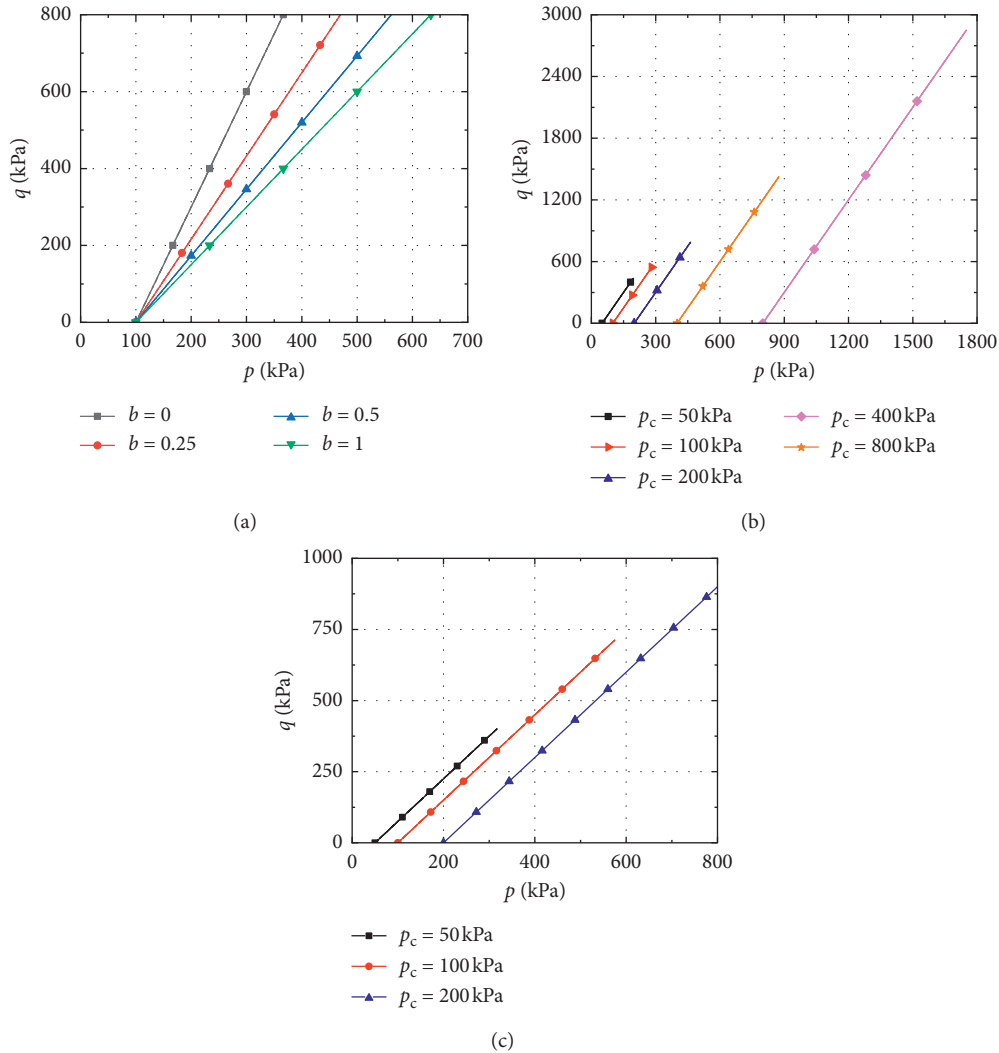


FIGURE 3: The designed stress path of the test. (a) The first group. (b) The second group. (c) The third group.

strain relationship under the same  $b$  and different  $p_c$  conditions, especially to focus on the variety of  $u$ ,  $p'$ ,  $q$ , and  $\eta$  to obtain the 3D deformation strength relationship, critical state line, and phase transition line of aeolian sand in Tengger Desert.

Figure 4 shows that the evolutions of the  $b$ -value in real time during the shearing process for all schemes. The data show that strain control loading can realize that the value of  $b$  remains constant during the loading process.

**4.2. The Strength and Deformation of Different  $b$  at the Same Confining Pressure.** Figure 5 shows that the  $u - \varepsilon_1$  curves of the four  $b$ -values can be divided into two stages: the increasing and decreasing stages of  $u$ . The increasing of  $u$  indicated that the specimen is compressed at the initial shearing stage and the void water volume inside the specimen is compressed. In the decreasing stages, the aeolian sand is excessively dilated from contraction to dilatation, and the void ratio of sand is increased, which lead to a drop



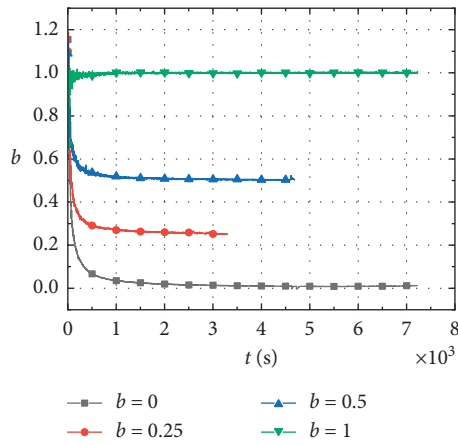


FIGURE 4: The measured value of stress path.

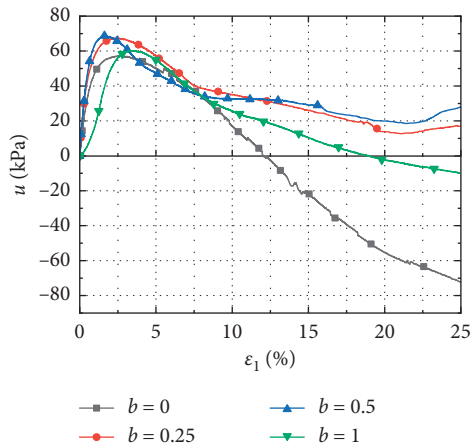


FIGURE 5: Change of void water pressure with different  $b$ -values at  $p_c = 100$  kPa.

in void water pressure. The transition point from contraction to dilatation is focused around  $\varepsilon_1 = 2.5\%$ . Except for  $b = 1$ , the degree of dilatation after the state transition point showed a decreasing trend with the increase of  $b$ -value. The possible reason is that when  $b = 1$ , the direction of  $\sigma_1$  is in the horizontal direction of the specimen, and the anisotropy of the sand in these direction affects its dilatancy.

Figure 6(a) shows that all the stress-strain curves of different  $b$ -values show the shear hardening at  $p_c = 100$  kPa and  $q$  gradually increases with the increase of  $\varepsilon_1$ . When  $\varepsilon_1 < 10\%$ , all curves have the similar trend. But when  $\varepsilon_1 \geq 10\%$ , the curves affected by void water pressure and dilatancy are quite different. Figure 6(b) the relationships between  $p'$  and  $q$  shows that the contraction decreases with the increase of  $b$ -value before the state transition point and then the curves tend to be straight after the point and the slope of the straight line increases. When  $b = 1$ , the difference of the curves is related to the direction change of  $\sigma_1$ .

Figure 6(c) shows the same pattern for the stress ratio. With the increase of  $\varepsilon_1$ ,  $\eta$  increased rapidly before reaching a critical state and then  $\eta$  reached stability. When  $\varepsilon_1 < 5\%$ , the  $b$ -value has a greater effect on curves and the slope increases with the  $b$ -value increases.

### 4.3. The Characteristics of the Critical State

4.3.1. *The Critical State Line and the State Transition Line of  $b = 0$ .* Figure 7 shows the changes of void water pressure under the conditions of different  $p_c$  at  $b = 0$ . On the whole, the trends of the void water pressure are increasing first and then decreasing; it means that the dense aeolian sand shows the pattern of first contraction and then dilatancy. Before the state transition point, the rate of void water pressure increases with the increase of  $p_c$ , and the contraction become more obvious. After the state transition point, the void water pressure decreases with the increase of  $p_c$ . When  $p_c$  reaches 800 kPa, the decreasing trends of void water pressure are weakened. The positive value of void water pressure indicates that the dilatancy become more and more obvious.

Figure 8(a) shows the stress-strain relationship of dense aeolian sand under the conditions of different  $p_c$  at  $b = 0$ . The curves are all hardened, and  $q$  increased with the increase of  $p_c$ . The results in Figure 8(b) show that the curves of all different  $p_c$  and the same  $b$  tend to the same critical state,  $q = 1.57p'$ . The state transition line from shear contraction to dilatancy under the undrained can be obtained as  $q = 1.23p'$ . In Figure 8(c), the relationships of  $\eta - \varepsilon_1$  can obtain the same  $\eta$  of 1.57, which is the same as the critical state line.

4.3.2. *The Critical State Line and the State Transition Line of  $b = 1$ .* Figure 9 shows the changes of void water pressure of dense aeolian sand under conditions of different  $p_c$  when  $b = 1$ . The void water pressure is shown a trend of increasing first and then decreasing. However, the increase is greater than that in Figure 7, which indicates that the contraction of  $b = 0$  is stronger than that of  $b = 1$  at the same  $p_c$ . When  $p_c$  reaches 200 kPa, void water pressure is a positive value. Dense aeolian sand shows a shear contraction characteristic.

Figure 10(a) shows the stress-strain relationship of dense aeolian sand under the conditions of different  $p_c$  at  $b = 1$ . The curves are still hardened, and the generalized shear stress increases with the increase of  $p_c$ , but the hardened trend is weaker than that in Figure 8(a) at the same  $p_c$  and  $b = 0$ . The results in Figure 10(b) show that all curves tend to the same critical state line and the same state transition line, and they are  $q = 1.24p'$  and  $q = 1.04p'$ . Compared with Figure 8(b), the critical state line and the state transition line are significantly smaller than those at  $b = 1$ . In Figure 10(c), the curves between the stress ratio and the large principal strain can obtain the same stress ratio of 1.24, which is the same critical state line.

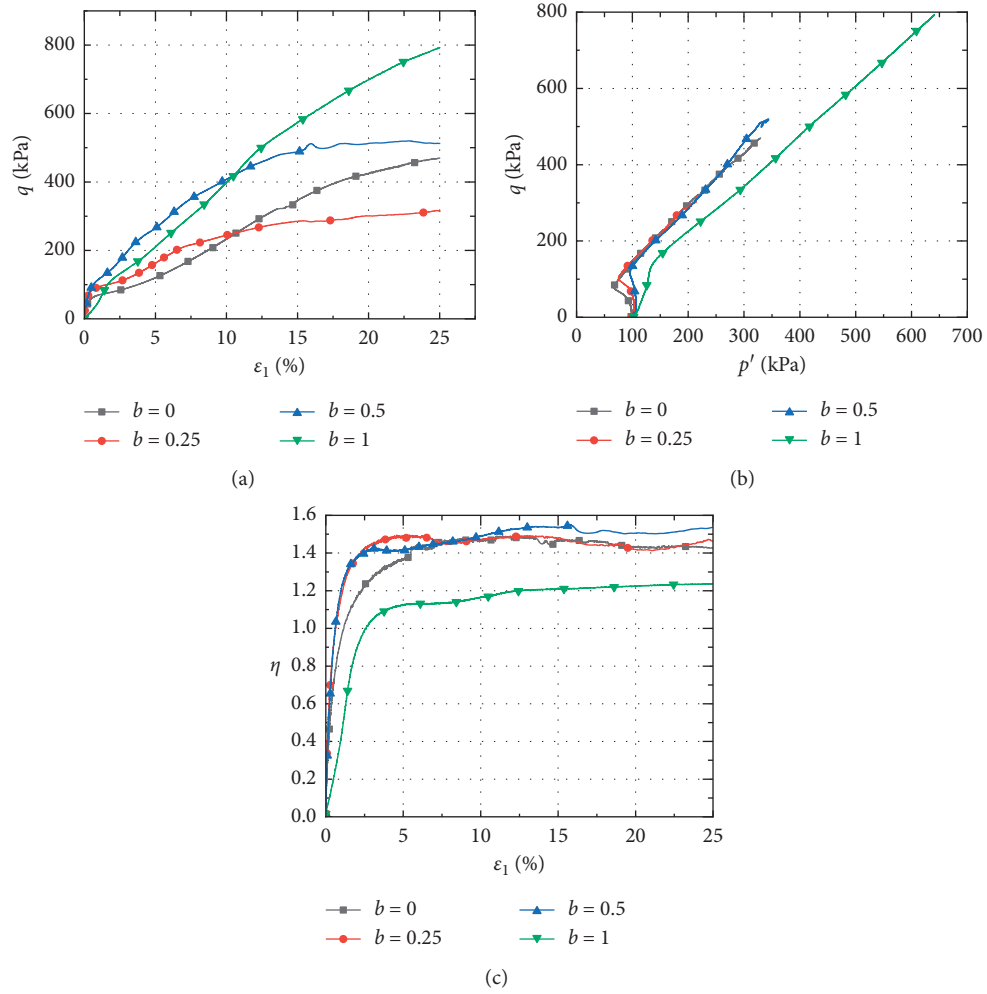


FIGURE 6: Stress-strain relationships of different  $b$ -values at  $p_c = 100$  kPa. (a) Relationships of  $q - \epsilon_1$ . (b) Relationships of  $p' - q$ . (c) Relationships of  $\eta - \epsilon_1$ .

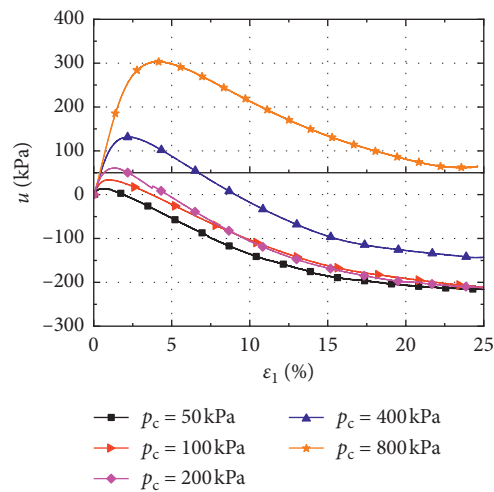


FIGURE 7: The variation of void water pressure at  $b = 0$ .

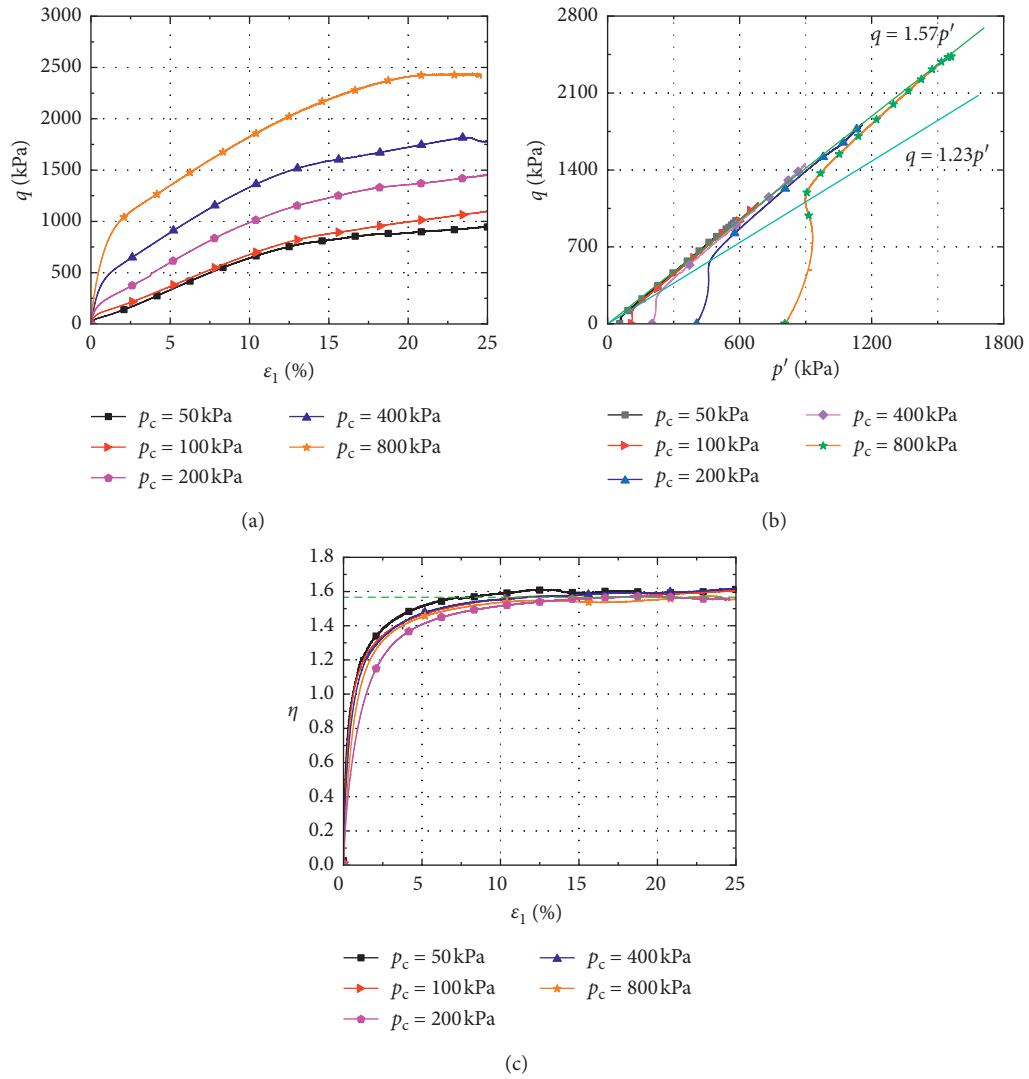


FIGURE 8: Stress-strain relationship and critical state line at  $b=0$ . (a) The stress-strain relationships. (b) The critical state line and the state transition line in  $p' - q$  space. (c) The critical state line of stress ratio and strain space.

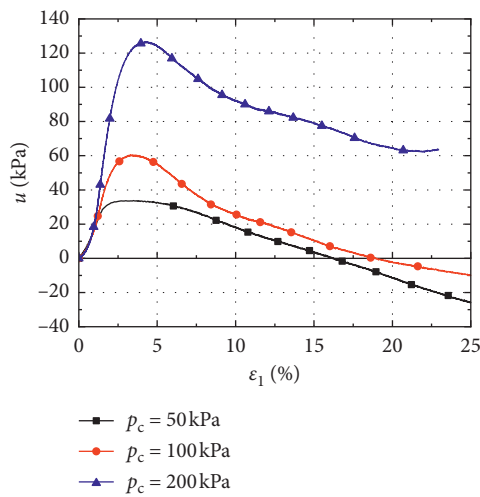


FIGURE 9: The variation of void water pressure at  $b=1$ .

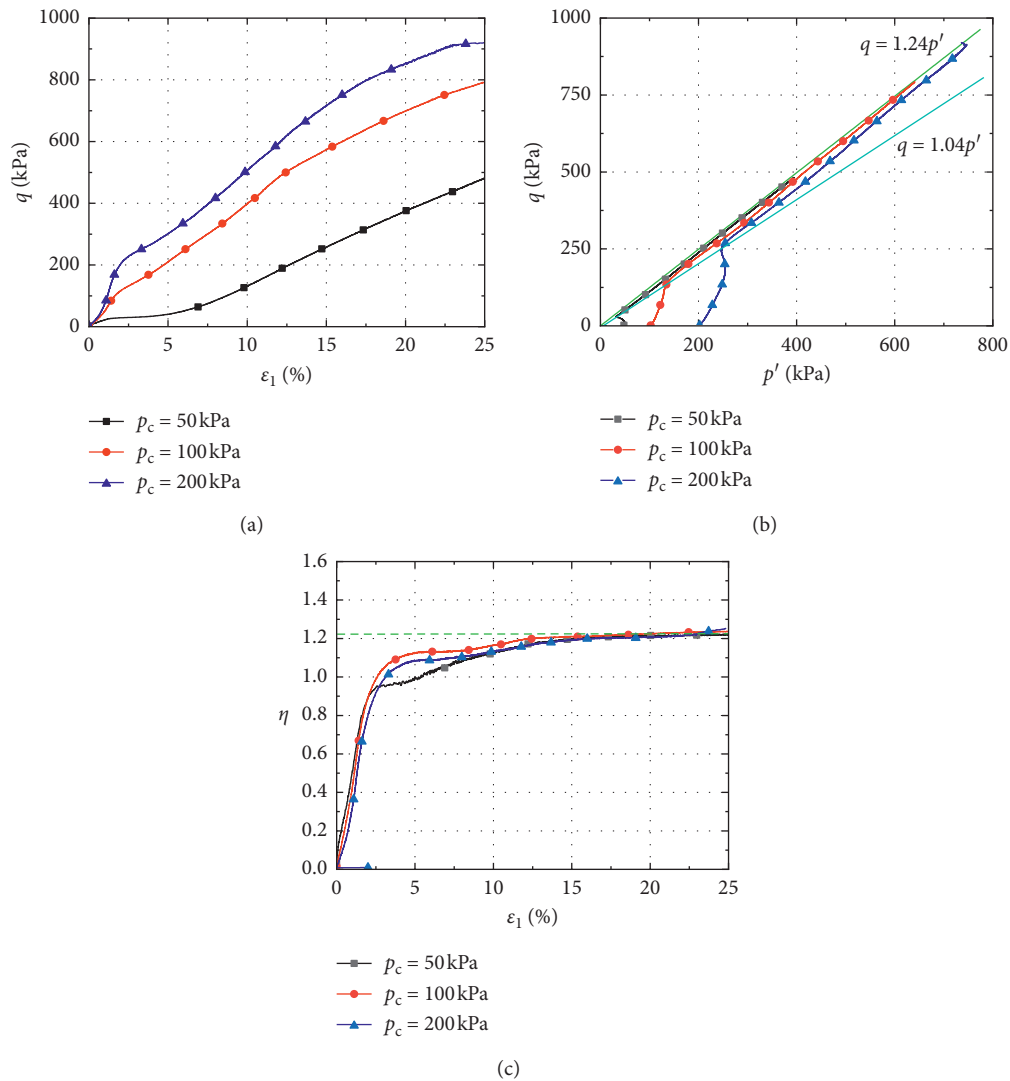


FIGURE 10: The stress-strain relationships and the critical state line at  $b = 1$ . (a) The stress-strain relationships. (b) The critical state line and the state transition line in  $p' - q$  space. (c) The critical state line of stress ratio.

## 5. Conclusions

In order to make up the shortage of experimental data for aeolian sand in Tengger Desert, this paper obtains the critical state line and state transition line of aeolian sand under different 3D stress path conditions, as well as different  $b$ -values at the same  $p_c$ . To grasp the true 3D mechanical properties of dense aeolian sand, a series of undrained tests were carried out using the British GDS true triaxial test system. The main conclusions are as follows:

- (1) The test adopts the strain control method, which realizes the constant  $b$ -value of proportional stress loading by controlling the middle principal strain coefficient and verifies the accuracy of the strain control by real-time monitoring of the  $b$ -value.
- (2) The results of different  $b$ -values at the same  $p_c$  show that the dilatancy of dense aeolian sand increased with the  $b$ -value according to the change of void water pressure. In  $p' - q$  space and  $\eta - \varepsilon_1$  space, the strength of aeolian sand increases with the  $b$ -value, which is consistent with the test design. When  $b = 1$ , the direction of the maximum principal stress is changed to the horizontal direction, and the stress-strain relationships are consistent with the design, which indicates that it is greatly influenced by anisotropy.
- (3) Two commonly used limit state lines in geotechnical engineering are obtained from the test. The critical state line and phase transition line are obtained with the same  $b$ -value and different  $p_c$ . When  $b = 0$ , the

critical state line and phase transition line are greater than  $b = 1$ , and the rules of dilatancy are relatively stable. The results fully confirm the purpose of the test design and provide the data for geotechnical engineering design, construction, and maintenance in the Tengger Desert area.

## Abbreviations

$b$ or $b$ -value:	Intermediate principal stress coefficients
$q$ :	Generalized shear stress (kPa)
$P$ :	Mean principal stress (kPa)
$p_c$ :	Effective confining pressure during consolidation (kPa)
$p'$ :	Effective mean principal stress (kPa)
$B$ :	Void water pressure coefficient
$\sigma_1$ :	Maximum principal stress (kPa)
$\sigma_2$ :	Intermediate principal stress (kPa)
$\sigma_3$ :	Minimum principal stress (kPa)
$b_\varepsilon$ :	Intermediate principal strain coefficient
$\varepsilon_1$ :	Maximum principal strain
$\varepsilon_2$ :	Intermediate principal strain
$\varepsilon_3$ :	Minimum principal strain
$\varepsilon_v$ :	Volume strain
$d\varepsilon_1$ :	The increment of maximum principal strain
$d\varepsilon_2$ :	The increment of intermediate principal strain
$d\varepsilon_3$ :	The increment of minimum principal strain
$\eta$ :	Stress ratio
$u$ :	Void water pressure (kPa)
$t$ :	Time (s).

## Data Availability

The data used to support the findings of this study are available from the corresponding author upon request.

## Conflicts of Interest

The authors declare that there are no conflicts of interest regarding the publication of this paper.

## Acknowledgments

This work was financially supported by the Key R&D Program of Ningxia Hui Autonomous Region Projects of International Cooperation and Exchanges (No. 2018DWHZ0084), the National Key R&D Program of China (No. 2017YFC0504404), and the Projects for Leading Talents of Science and Technology Innovation of Ningxia (No. KJT2019001), and these supports are gratefully acknowledged.

## References

- [1] H. Xie, F. Ma, and S. Wu, "Numerical simulation of sand transport around the highway in sandy desert area," *Journal of Desert Research*, vol. 39, no. 2, pp. 151–157, 2019.
- [2] Y. Feng, *Compaction Technology Study of Tengger Desert Aeolian Sand Subgrade*, Chang'an University, Xi'an, China, 2017.
- [3] M. Li, L. Chen, and W. Chen, "The moisture problem of sand-fixing afforestation in Zhongwei section along Bao Lan railway in Tengger Desert," *Chinese Science Bulletin*, vol. 8, pp. 249–251, 1958.
- [4] C. Liu, G. Wu, Y. Zhang, and Y. Yang, "Research on features and compaction coefficient of subgrade aeolian sand filling for heavy haul railway in Mu Us Desert," *Subgrade Engineering*, vol. 6, pp. 138–142, 2016.
- [5] W. Ma, "The engineering characteristics of silt-sand foundation in Tengeli Desert Zone," *China Rural Water and Hydropower*, vol. 11, pp. 74–77, 2004.
- [6] Z. Zeng, M. Zhang, Z. Liang, and F. Shan, "Engineering geological features of eolian deposit sandy soil ground at southern edge of the Tenggelii Desert," *Northwest Water Power*, vol. 3, pp. 18–20, 2001.
- [7] H. Che and Y. Zhu, "Experimental study of strengthening technology for a tunnel constructed in Aeolian sand stratum," *Chinese Journal of Rock Mechanics and Engineering*, vol. 3, pp. 206–213, 1993.
- [8] Y. Yuan and X. Wang, "Experimental research on compaction characteristics of Aeolian sand," *Chinese Journal of Geotechnical Engineering*, vol. 29, no. 3, pp. 360–365, 2007.
- [9] Z. Li, Y. Cao, N. Liang, and Y. Mei, "Compaction mechanism of aeolian sand," *China Journal of Highway and Transport*, vol. 19, no. 5, pp. 6–11, 2006.
- [10] C. Xue, H. Li, and B. Hu, "Mechanical analysis on the new type of semi-rigid asphalt pavement structure based on dynamic parameters," *Highways*, vol. 6, pp. 20–24, 2013.
- [11] Z. Zeng, M. Zhang, and M. Huang, "A study on the collapsibility of aeolian sand in the southern margin of Tengger Deserts," *Journal of Gansu Sciences*, vol. 2, pp. 63–68, 2000.
- [12] J. Su, "Study on collapsibility of sandy soil for desert sand," *Geotechnical Engineering World*, vol. 4, no. 8, pp. 27–29, 2001.
- [13] Q. Wang, Y. Liu, X. Fu, and W. Ren, "Reliability analysis for wetting deformation and stability of sand soil roadbed," *China Journal of Highway and Transport*, vol. 20, no. 6, pp. 7–12, 2007.
- [14] X. Lü, M. Huang, and J. Qian, "The onset of strain localization in cross-anisotropic soils under true triaxial condition," *Soils and Foundations*, vol. 51, no. 4, pp. 693–700, 2011.
- [15] X. Lü, M. Huang, and J. Qian, "Influences of loading direction and intermediate principal stress ratio on the initiation of strain localization in cross-anisotropic sand," *Acta Geotechnica*, vol. 13, no. 3, pp. 619–633, 2017.
- [16] X. Li, Z. Ma, W. Lu, and Y. Wang, "True-triaxial drained test of Tengger Desert sand," *Advances in Civil Engineering*, vol. 2020, Article ID 8851165, 11 pages, 2020.
- [17] Y. Deng, X. Li, Wang, Y. Song, and J. Peng, "Study on dynamic strength of the Aeolian sand in Maowusu Desert area," *Engineering Mechanics*, vol. 29, no. 12, pp. 281–286, 2012.
- [18] Y. Song, *Test Study on the Mechanical Property of the Aeolian Sand and the Bearing Capacity of the Aeolian Sand Ground of Mu Us Desert*, Chang'an University, Xi'an, China, 2011.
- [19] X. Zhang, J. Li, F. Yi, Q. Sun, Z. Qu, and Y. Hu, "Dynamic tests and damage mechanism of frozen aeolian soil in western Liaoning area of China," *Chinese Journal of Geotechnical Engineering*, vol. 40, no. 2, pp. 370–377, 2018.
- [20] S. Zhang, C.-A. Tang, X.-D. Zhang, Z.-C. Zhang, and J.-X. Jin, "Cumulative plastic strain of frozen aeolian soil under highway dynamic loading," *Cold Regions Science and Technology*, vol. 120, pp. 89–95, 2015.



- [21] J. Li, F. Wang, F. Yi, F. Wu, J. Liu, and Z. Lin, "Effect of freeze-thaw cycles on triaxial strength property damage to cement improved aeolian sand (CIAS)," *Materials*, vol. 12, no. 17, 2019.
- [22] J. Li and Y. Zhang, "Undrained monotonic and dynamic triaxial properties of the aeolian sand," *Earth and Environmental Science*, vol. 242, no. 6, 2019.
- [23] H. Yong, W. Li, and Q. Yu, "A test study on the impact of dry density and water content on the structural strength index of intact unsaturated aeolian soil," *Electronic Journal of Geotechnical Engineering*, vol. 20, pp. 1933–1945, 2015.
- [24] M. Badanagki, *Shear Strength and Stiffness of a Sahara Sand from Libya*, Colorado State University, Fort Collins, CO, USA, 2011.
- [25] C. Choi, A. Pedro, and D. Michael, "Development of a true triaxial apparatus for sands and gravels," *Geotechnical Testing Journal*, vol. 31, no. 1, pp. 32–44, 2008.
- [26] L. Suits, T. Sheahan, L. Ibsen, and U. Prasstrup, "The Danish rigid boundary true triaxial apparatus for soil testing," *Geotechnical Testing Journal*, vol. 25, no. 3, pp. 254–265, 2002.
- [27] P. Lade and Q. Wang, "Analysis of shear banding in true triaxial tests on sand," *Journal of Engineering Mechanics-ASCE*, vol. 127, no. 8, 2001.
- [28] Y. Yamada and K. Ishihara, "Undrained deformation characteristics of loose sand under three-dimensional stress conditions," *Soils and Foundations*, vol. 21, no. 1, pp. 97–107, 1981.
- [29] M. Yoshimine, K. Ishihara, and W. Vargas, "Effects of principal stress direction and intermediate principal stress on undrained shear behavior of sand," *Soils and Foundations*, vol. 38, no. 3, pp. 179–188, 1998.
- [30] K. Pan, Z. Yang, and T. Xu, "Impact of static preshearing on undrained anisotropy and shear characteristics of sand," *International Journal of Geomechanics*, vol. 18, no. 12, pp. 1–12, 2018.
- [31] C. Xu, M. Luan, Y. He, Y. Guo, and M. Li, "Effect of intermediate principal stress on undrained behavior of saturated loose sands under monotonic shearing," *Rock and Soil Mechanics*, vol. 5, pp. 689–693, 2006.
- [32] J. Li and X. Yang, "The strength properties of the coarse sand with various fine sand contents," *Soil Eng. and Foundation*, vol. 30, no. 6, pp. 721–725, 2016.
- [33] T. G. Murthy, D. Loukidis, J. A. H. Carraro, M. Prezzi, and R. Salgado, "Undrained monotonic response of clean and silty sands," *Géotechnique*, vol. 57, no. 3, pp. 273–288, 2007.
- [34] P. Hu, M. Huang, S. Ma, and X. Lü, "True triaxial tests and strength characteristics of silty sand," *Rock and Soil Mechanics*, vol. 322, pp. 465–470, 2011.
- [35] M. Liang and H. Ping, "True triaxial tests and strength characteristics study on silty sand," in *Proceedings of the 2017 2nd International Conference on Test, Measurement and Computational Method*, TCMCM, Beijing, China, May 2017.
- [36] Y. Wu, J. Cui, J. Huang, W. Zhang, N. Yoshimoto, and L. Wen, "Correlation of critical state strength properties with particle shape and surface fractal dimension of clinker ash," *International Journal of Geomechanics*, vol. 21, 2021.
- [37] X. Li and Y. F. Dafalias, "Anisotropic critical state theory: role of fabric," *Journal of Engineering Mechanics*, vol. 138, no. 3, pp. 263–275, 2011.
- [38] A. Sadrekarimi and S. M. Olson, "Residual state of sands," *Journal of Geotechnical and Geoenvironmental Engineering*, vol. 140, no. 4, 2013.
- [39] Y. Wu, N. Li, and X. Wang, "Experimental investigation on mechanical behavior and particle crushing of calcareous sand retrieved from South China Sea," *Engineering Geology*, vol. 280, 2021.
- [40] ASTM2487, *Standard Practice for Classification of Soils for Engineering Purpose (Unified Soil Classification System)*, ASTM, West Conshohocken, PA, USA, 2017.

## Research Article

# Mechanical and Mesoscale Analyses of Cement Stabilized Macadam Prepared by Vibratory and Nonvibratory Mixing Techniques

Jijing Wang <sup>1</sup> and Zhihua Tan <sup>2</sup>

<sup>1</sup>School of Traffic & Transportation Engineering, Changsha University of Science & Technology, Changsha 410004, China

<sup>2</sup>Changsha University of Science & Technology, Changsha 410004, China

Correspondence should be addressed to Zhihua Tan; luck@csust.edu.cn

Received 16 December 2020; Revised 18 January 2021; Accepted 1 February 2021; Published 10 February 2021

Academic Editor: Pengfei Liu

Copyright © 2021 Jijing Wang and Zhihua Tan. This is an open access article distributed under the Creative Commons Attribution License, which permits unrestricted use, distribution, and reproduction in any medium, provided the original work is properly cited.

The objective of this study is to analyze the effects of mixing techniques on the mechanical behavior and meso-structure of cement-treated aggregate. Different specimens were prepared by vibratory and nonvibratory mixing techniques. X-ray CT scans were performed to illustrate the distribution of cement mortar on aggregate. The strength, modulus, and fatigue tests under different stress states were tested to reveal the impacts of mixing techniques. Then, the relationships between strengths and loading rates and that between moduli and stress levels were established. Hereafter, the S-N fatigue equation that modified with stress ratio related to loading rates was used to describe the fatigue performance. The results indicate that the cement mortar of specimens prepared by vibratory mixing was well-distributed on aggregates. The strength, modulus, and fatigue life of the specimens prepared by vibratory mixing were higher under the test condition threshold. Moreover, the growth rate of strength and modulus with loading for specimens prepared by vibratory mixing was slightly larger than that for specimens prepared by nonvibratory mixing. Compared with the cement-treated aggregates specimens prepared by nonvibratory mixing, the fatigue life of cement-treated aggregates specimens prepared by vibratory mixing had more stable stress sensitivity.

## 1. Introduction

The semirigid asphalt pavement is one of the leading asphalt pavement types in China, taking advantage of strong bearing capacity, high integrity, and satisfactory capacity to distribute upper loads [1, 2]. More than 90% of the bases of semirigid asphalt pavements in China use cement-treated aggregates [3, 4]. Cement-treated aggregates are generally preferred materials for the semirigid base due to its high overall strength, high stiffness, good moisture susceptibility, desirable fatigue resistance performances, and readily available raw materials [5, 6]. Cement-treated aggregates are usually prepared with aggregates of a suitable gradation and 3%–8% cement at the optimum water to cement ratio. The development of the strength of cement-treated aggregates is affected by

the properties of constituent materials as well as the mixing technique [7–9].

The reflection cracks are the primary distress of semirigid base asphalt pavement [10, 11]. In the literature, numerous studies were conducted to improve the pavement performance of cement-treated aggregates [12–14]. The influence of raw materials, cement content, and additives on the road performance of cement-treated aggregates was investigated. Microscopic analyses were also performed to optimize materials and design [15, 16]. Ngoc Kien Bui et al. [17] proposed a new method that replaces natural aggregate (NA) with different percentages of recycled aggregate (RA). It was found that the combination of RA and NA could significantly improve the mechanical properties of recycled aggregate concrete (RAC) compared with the traditional method. Federico Autelitano et al. [18] replaced part of the

aggregates in cement-treated aggregates with the electric arc furnace (EAF) slag. The authors stated that the compacted effect, durability, and mechanical properties of the modified mixture were significantly improved. Eziefula et al. [19] developed a new green concrete, i.e., shell aggregate concrete, which could be used as nonstructural and low-strength ordinary concrete. All results of the above studies showed that the mechanical properties of cement-treated aggregates are closely related to the aggregate properties. William Fedrigo et al. [20] used indirect tensile tests, triaxial tests, and bending tests to evaluate the effects of cement content, curing time, and compressive strength on the strength and stiffness of cement-treated aggregates. The results showed that the cement content had the most significant influence on the strength and stiffness of cement-treated aggregates among the above factors. Xuan et al. [21] established a parameter prediction model to characterize the mechanical properties of cement-treated aggregates. The authors reported that the unconfined compressive strength parameters could reflect the change of the mechanical properties of cement-treated aggregates. And, the unconfined compressive strength was mainly affected by the cement content, curing time, and degree of compaction. Therefore, the mechanical properties of cement-treated aggregates are closely related to cement content, and the impacts of cement content, curing time, and compaction could not be ignored.

Besides, many scholars have shown that the type, structure, and parameters of mixers significantly affect the mixing uniformity, mixing efficiency, and hardening behavior of mixtures [22–24]. Vibratory mixing has become a popular technique for stirring concrete. Shen et al. [25] introduced different types of vibratory mixing techniques and gave the comparison among those mixing methods. Zhao et al. [26] used the vibratory mixing technique to form cement-treated aggregates specimens based on orthogonal test designs. It was found that the mixing time had the most noteworthy influence on the compressive strength of cement-treated aggregates, the vibration frequency and mixing speed was second, and the wet mixing time had the least impact [27]. Jiang et al. [28] compared the road performance of cement-treated aggregates prepared by the vibratory method and static method and showed that the vibratory method-prepared specimens were closer to engineering practice. Zhang et al. [29–31] conducted long-term experimental research on the vibratory mixing of cement-treated aggregates. They stated that the vibratory mixing technique had a good wrapping effect on the coarse aggregate over traditional mixing technique so that cement-treated aggregates were more evenly mixed. And, they also found that the vibratory mixing technique could effectively improve the microscopic uniformity of cement-treated aggregates materials. Thus, this technique can promote a variety of dynamic effects of cement-treated aggregates materials, improve the structure formation process of concrete, and significantly improve the quality and efficiency of mixing. In the process of vibratory mixing, the mixing behavior realizes the macroscopic cyclic movement of the mixture, the purpose of which is to combine the materials; the vibratory behavior is used to accelerate the diffusion movement, the

intention of which is to mix the materials evenly [25, 32]. However, only a few researchers have revealed the influence mechanism of the mixing process on the road performance of cement-treated aggregates, and the research related to the influence of the mixing process on the mechanical properties of cement-treated aggregates materials is even insufficient.

Therefore, in this paper, the research has been conducted to verify the improving effects of vibratory mixing techniques from the perspective of mechanics and mesoscale structures. The influence of mixing techniques on the pavement performance of materials was demonstrated. X-ray CT scans were carried to analyze the meso-structure of two different types of cement-treated aggregate specimens. The cement mortar and its wrapping effect under different mixing processes were also compared. Then, the strength, modulus, and fatigue test of two different types of cement-treated aggregate specimens under different stress states were conducted under different loading rates. At the same time, the relationships between strength, modulus, and loading rates were established. The S-N fatigue equation associated with the loading rate was applied to characterize the fatigue properties of cement-treated aggregates.

## 2. Materials and Test Methods

### 2.1. Materials and Mixture Design

**2.1.1. Cement.** The PSB32.5R cement was used in this paper, and its properties are tested and shown in Table 1. It can be seen from the test results that the properties of the cement satisfied the requirements of the *Technical Guidelines for Construction of Highway Road bases (JTJ/T F20-2015)* (2015).

**2.1.2. Aggregate.** According to the source of local mineral materials, limestone was selected as the raw material for cement-treated aggregates. The properties of limestone aggregates were tested according to the *Chinese Test Methods of Aggregate for Highway Engineering (JTJ E42-2005)* (2005); the test results are listed in Table 2.

The gradation of aggregates is a crucial factor determining the mechanical properties of cement-treated aggregate. According to the Chinese Technical Guidelines for Construction of Highway Road bases (JTJ/T F20-2015) (2015), the gradation was selected based on the optimum service performance of the cement-treated aggregates; the gradation curve of limestone aggregates is shown in Figure 1.

**2.1.3. Mixture Proportion Design.** The PSB32.5R cement with different contents (i.e., 3%, 3.5%, 4%, 4.5%, and 5%) and limestone aggregates with the target gradation (Figure 1) was used to prepare cement-treated aggregates. Based on the requirements of Chinese Test Methods of Materials Stabilized with Inorganic Binders for Highway Engineering (JTJ E51-2009) (2009), the vibration compaction test was applied to determine the maximum dry density and optimum moisture content of the mixture. The test results are presented in Table 3; the maximum dry density of cement-

TABLE 1: Properties of PSB32.5R cement.

Property		Value	Technical requirement
Fineness		2.1	≤10
Stability (mm)		3	≤5
MgO content (%)		2.9	≤5
SO <sub>3</sub> content (%)		1.2	≤3.5%
Compressive strength of cement mortar (MPa)	3 days	24.9	≥10
	28 days	≥32.5	—
Setting time (min)	Initial setting	285	≥180
	Final setting	410	≥360

TABLE 2: Properties of limestone aggregate.

Property	Technical requirement	Test result of coarse aggregate			
		19~31.5 mm	9.5~19.5 mm	4.75~9.5 mm	0~4.75 mm
Content of flat and elongated particles (%)	≤20%	11.7	15.8	—	—
Crushing value (%)	≤26%	21.3	18.9	—	—
Bulk volume relative density (g/cm <sup>3</sup> )	—	2.230	2.730	2.607	2.589
Apparent density (g/cm <sup>3</sup> )	—	2.821	2.763	2.731	2.692
Water absorption (%)	—	0.4	0.6	1.3	—
Liquid limit of particles smaller than 0.6 mm	≤28%			23%	
Plastic index of particles smaller than 0.6 mm	≤9			3.2	

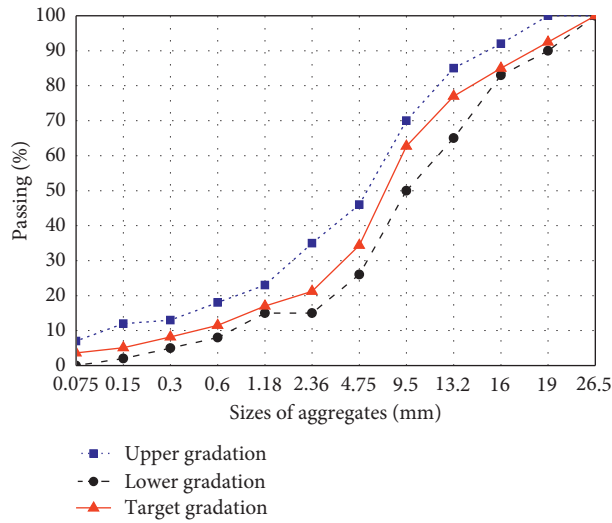


FIGURE 1: Gradation curve of limestone aggregates.

TABLE 3: Vibration compaction test results of cement-treated aggregates.

Cement content (%)	Maximum dry density (g/cm <sup>3</sup> )	Optimum moisture content (%)
3.0	2.380	4.9
3.5	2.398	4.8
4.0	2.413	4.8
4.5	2.429	4.8
5.0	2.431	4.9

treated aggregates increased with the cement content, but when the cement content exceeded 4.5%, the increasing amplitude decreased obviously. Thus, the optimum cement content of 4.5% was calculated, and the corresponding optimum moisture content and maximum dry density were 4.8% and 2.429 g/cm<sup>3</sup>, respectively.

2.2. *Specimen Preparation.* In order to analyze the influence of mixing techniques on the mechanical properties of cement-treated aggregates, the raw materials were mixed by the DETONG mixing equipment, which contained both vibratory and nonvibratory modes. And, the specimens were prepared using vibration compaction equipment.

Aggregates were sieved and then dried in an oven. After that, certain amounts of water, cement, and aggregate were mixed using the DETONG mixing equipment in the vibratory or nonvibratory mode for 40s. The vibratory frequency is determined based on the natural frequency of cement-treated aggregate for the purpose of resonance, and the amplitude is 0.5~2 mm. And then, cement-treated aggregate specimens with two different mixing techniques were prepared in the mold under vibratory compaction.

According to the requirements of Chinese Test Methods of Materials Stabilized with Inorganic Binders for Highway Engineering (JTG E51-2009) (2009), beam specimens with sizes of 150 mm × 150 mm × 550 mm and cylindrical specimens with height of 150 mm and diameter of 150 mm were prepared. Among them, the beam specimens were prepared for four-point bending tests, and cylindrical specimens were prepared for unconfined compression tests and indirect tensile tests. After demolding, the specimens that met the requirements were stored in a standard curing room (the relative humidity of not less than 95% and the temperature of  $20 \pm 2^\circ\text{C}$ ) for 90 days, as shown in Figure 2.

**2.3. Test Design.** In this study, X-ray CT was chosen to investigate the meso-structure of cement-treated aggregates prepared with different mixing techniques. The specimens were scanned with spacing of 0.9 mm at the voltage of 220 kV and the electric current of 10–40 mA.

The strength, modulus, and fatigue tests were performed to examine the effect of mixing techniques on the mechanical performances of cement-treated aggregates. Indirect tensile tests were carried out using the Material Test System (MTS) equipment. Loading rates of 5 MPa/s, 10 MPa/s, 20 MPa/s, 30 MPa/s, 40 MPa/s, and 50 MPa/s were considered in the strength tests. Modulus tests were conducted using a staged loading method, and the stress levels were 0.25 MPa, 0.5 MPa, 1 MPa, and 1.5 MPa. The indirect tensile fatigue tests under stress-control mode and the half-sine load with a frequency of 10 Hz and the stress levels were 0.25 MPa, 0.5 MPa, 1 MPa, and 1.5 MPa. Unconfined compression tests and four-point bending tests were also carried out using the MTS equipment, and the test method was similar to that for the indirect tensile test. The loading rates of 5 MPa/s, 10 MPa/s, 20 MPa/s, 30 MPa/s, 40 MPa/s, and 50 MPa/s were also considered in unconfined compression tests and four-point bending tests. The stress levels used in four-point bending tests were consistent with those in indirect tensile tests. Since the loading rate for unconfined compression tests was too large, the stress levels were set at 3.5 MPa, 6 MPa, 8 MPa, and 10 MPa to ensure the safety and operability of the test. Five replicate samples were used for each test.

### 3. Results and Analyses

**3.1. Effects of Mixing Techniques on the Strength.** Cement-treated aggregates specimens were prepared by vibratory and nonvibratory techniques. Then, the specimens were tested by MTS under three different stress states to

determine the strength. In this paper, the indirect tensile, unconfined compression tests, and four-point bending tests were chosen for the strength test.

In indirect tensile tests and unconfined compression tests, the loading rate was 1 mm/min. While the loading rate was 50 mm/min in four-point bending tests. The above choices were based on the Test Methods of Materials Stabilized with Inorganic Binders for Highway Engineering (JTG E51-2009) (2009).

The test results are shown in Figure 3.

It is noted from Figure 3 that the standard strength of the specimens prepared by vibratory mixing was higher than that of the specimens prepared by nonvibratory mixing. Under the standard test condition, the unconfined compressive strength (11.76 MPa) of the vibratory mixed specimen was about 18% larger than that (9.98 MPa) of nonvibratory mixed specimen; the indirect tensile strength (1.30 MPa) of the vibratory mixed specimen was about 15% higher than that (1.13 MPa) of nonvibratory mixed specimen; the bending tensile strength (1.31 MPa) of the vibratory mixed specimen was about 12% higher than that (1.17 MPa) of nonvibratory mixed specimen. This indicates that the vibratory mixing has a more significant effect on the increase of unconfined compressive strengths of cement-treated aggregates.

In order to investigate the relationship between the strength and loading rate of specimens prepared by vibratory and nonvibratory mixing under three different stress states, different loading rates were applied in the tests. Three sets of parallel tests were carried out at the same loading rate, and the relationship curves between strength and loading rate of three different stress states are presented in Figures 4–6.

Figures 4–6 show that the vibratory mixing had a more significant influence on the bending strength with the increased loading rate. As the loading rate continued to grow, both the unconfined compressive strength and the indirect tensile strength increase tended to be gentle.

Meanwhile, by comparing the parallel test strength results of the specimens prepared by vibratory and nonvibratory mixing, the coefficient of variation  $C_v$  is shown in Table 4. It can be found that vibratory mixing can significantly reduce the coefficient of variation, which indicates that the cement-treated aggregates prepared by vibratory mixing had higher strength stability than the cement-treated aggregates prepared by nonvibratory mixing.

**3.2. Effects of Mixing Techniques on the Modulus.** The specimens were prepared by vibratory and nonvibratory techniques. Then, the specimens were applied to determine the modulus of cement-treated aggregates by MTS under three different stress states. In this paper, the indirect tensile tests, unconfined compression tests, and four-point bending tests were chosen for the modulus test.

According to the Test Methods of Materials Stabilized with Inorganic Binders for Highway Engineering (JTG E51-2009) (2009), the loading rate for standard modulus tests was 1 mm/min in indirect tensile tests, unconfined compression tests, and four-point bending tests. The MTS obtained the





FIGURE 2: Preparation of cement-treated aggregate specimens.

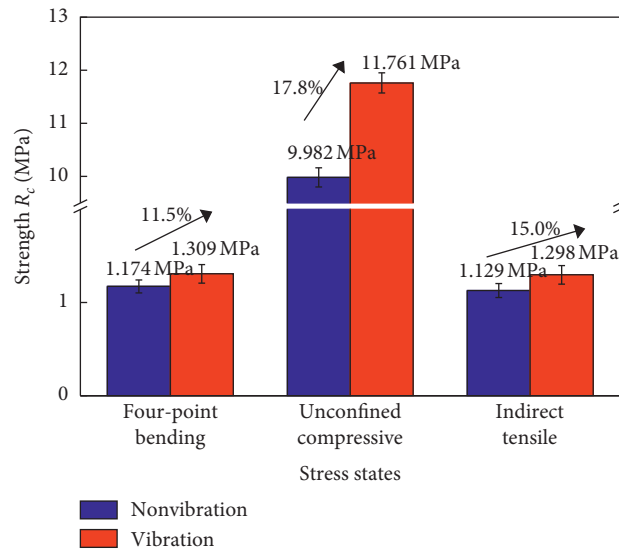


FIGURE 3: Standard strength of vibratory and nonvibratory mixed specimens under different stress states.

calculation data of cement-treated aggregate material modulus under three different stress states. The unconfined compressive modulus, the indirect tensile modulus, and the four-point bending modulus of specimens were calculated by using equations (1)–(3), respectively:

$$E_c = \frac{ph}{l}, \quad (1)$$

where  $E_c$  is the unconfined compressive modulus of the specimen (MPa);  $p$  is the unit pressure (MPa);  $h$  is the height of the specimen (mm);  $l$  is the rebound deformation of the specimen (mm):

$$E_i = \frac{P - P_0}{dl_x} (0.27 - 1.0 \mu), \quad (2)$$

where  $E_i$  is the indirect tensile modulus of the specimen (MPa);  $p$  is the load level (N);  $p_0$  is the initial load (N);  $d$  is the diameter of the specimen (mm); and  $l_x$  is the horizontal rebound deformation of the specimen (mm);  $\mu$  is Poisson ratio:

$$E_s = \frac{23L(p - p_0)^3}{108 \times b \times h^3 \times l}, \quad (3)$$

where  $E_s$  is the four-point bending modulus of the specimen (MPa);  $p$  is the load level (N);  $p_0$  is the minimum load (N);  $L$  is the span of the specimen (mm);  $l$  is the midspan rebound deformation (mm);  $b$  is the width of the midspan (mm); and  $h$  is the height of the midspan (mm).

Figure 7 presents the standard modulus of vibratory and non-vibratory specimens under different stress states. It is noted that the standard modulus of the specimens prepared by vibratory mixing was higher than that of the specimens prepared by nonvibratory mixing. Under the standard test condition, the unconfined compressive modulus (16996 MPa) of the vibratory mixed specimen was about 22% larger than that (13913 MPa) of nonvibratory mixed specimen; the indirect tensile modulus (11507 MPa) of the vibratory mixed specimens was about 20% larger than that (9608 MPa) of nonvibratory mixed specimen; the bending tensile modulus (1976 MPa) of the vibratory mixed specimen was about 13% larger than that (1754 MPa) of nonvibratory mixed specimen. It was found that the vibratory mixing has a

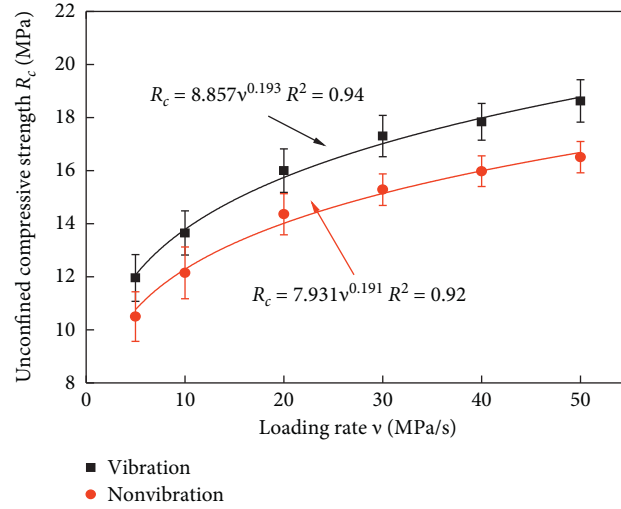


FIGURE 4: Unconfined compressive strength of cement-treated aggregates affected by loading rates.

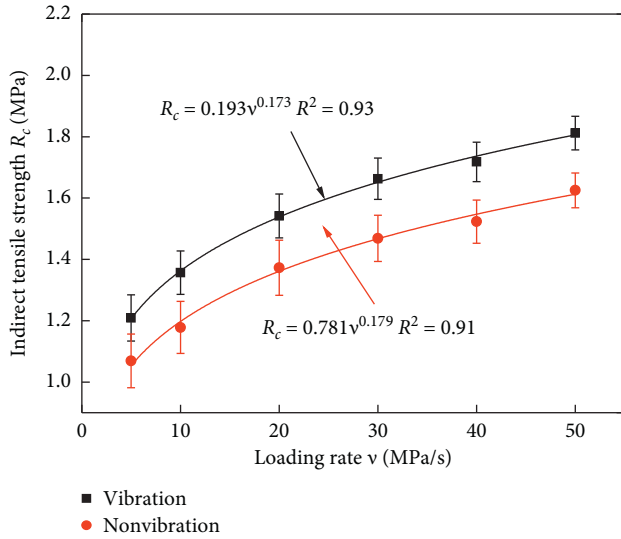


FIGURE 5: Indirect tensile strength of cement-treated aggregates affected by loading rates.

more significant influence on the increase of the standard modulus of cement-treated aggregates.

In order to explore the relationship between the modulus and stress level of cement-treated aggregates specimens prepared by vibratory and nonvibratory mixing under three different stress states, different stress levels were applied in each stress state. And, the modulus tests were performed using a staged loading mode. Four sets of parallel specimens were tested at the same stress level. The relationships between the modulus and the stress level under three different stress states are illustrated in Figures 8–10. It can be noted that as the stress level increased under each stress state, the modulus decreased with a linear function. The linear function equation was as follows:

$$E = k\sigma + m, \quad (4)$$

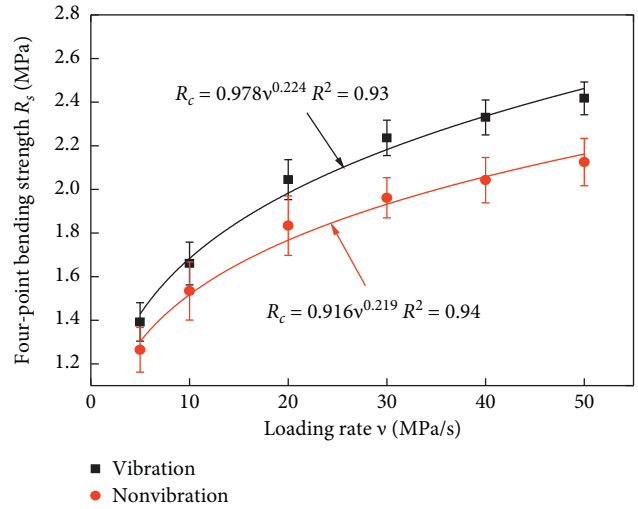


FIGURE 6: Bending tensile strength of cement-treated aggregates affected by loading rates.

where  $E$  is the modulus of the specimen (MPa);  $\sigma$  is the stress level (MPa); and  $k$  and  $m$  are the fitting parameters (see Table 5).

Figures 8–10 show that, with the increase in stress level, the vibratory mixing had a more positive influence on the attenuation of the unconfined compressive modulus. As the stress level continued to grow, the mitigation of indirect tensile modulus and bending tensile modulus under vibratory conditions was also gradually accelerated, which was slightly better than the attenuation of the tensile modulus under nonvibratory conditions.

The coefficient of variation  $C_v$  of modulus results of specimens prepared by vibratory and nonvibratory mixing is shown in Table 6. It is noted that the coefficient of variation of the modulus of the specimen prepared by vibratory mixing was lower than that of the specimen prepared by nonvibratory mixing. In other words, the vibratory mixing

TABLE 4: Coefficient of variation of strengths of specimens prepared by vibratory and nonvibratory mixing under different stress states.

Loading rate (MPa/s)	Mixing method	Coefficient of variation $C_v$ (%)		
		Unconfined compression	Indirect tensile	Bending tensile
5	Vibration	7.36	6.18	6.32
	Nonvibration	8.91	8.22	8.04
10	Vibration	5.04	5.15	5.82
	Nonvibration	8.02	7.24	8.71
20	Vibration	4.17	4.62	3.94
	Nonvibration	5.42	6.58	7.47
30	Vibration	3.53	4.02	3.14
	Nonvibration	3.92	5.15	4.69
40	Vibration	2.65	3.76	3.41
	Nonvibration	3.65	4.65	5.09
50	Vibration	3.41	3.02	2.91
	Nonvibration	3.58	3.54	5.12

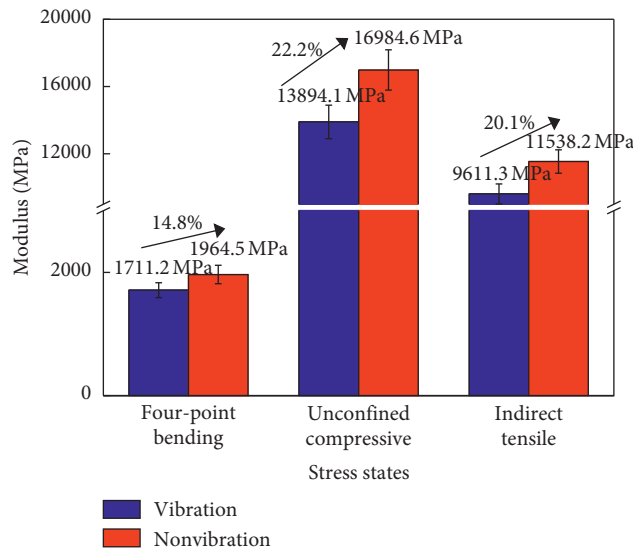


FIGURE 7: Standard modulus of vibratory and nonvibratory mixed specimens under different stress states.

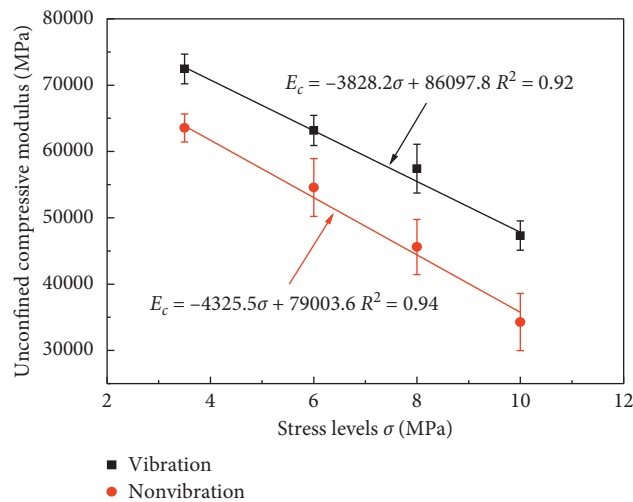


FIGURE 8: Unconfined compressive modulus of cement-treated aggregates affected by stress levels.

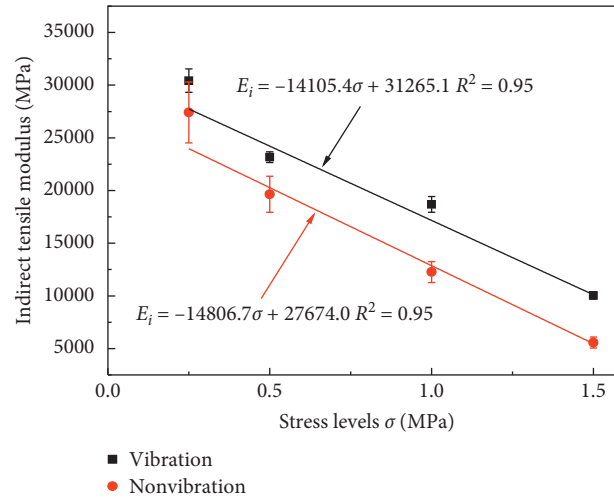


FIGURE 9: Indirect tensile modulus of cement-treated aggregates affected by stress levels.

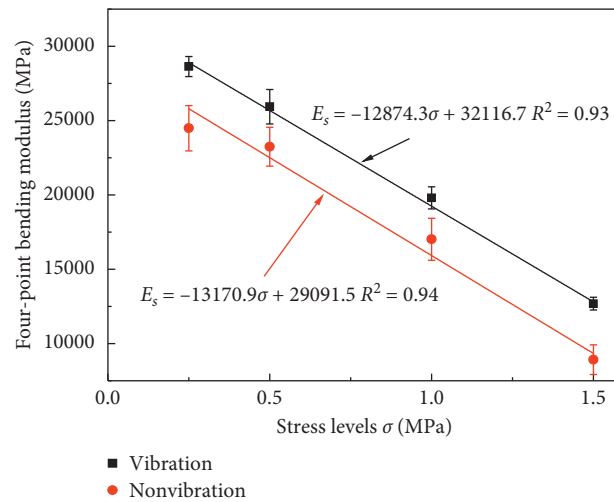


FIGURE 10: Four-point bending modulus of cement-treated aggregates affected by stress levels.

TABLE 5: Coefficients of variation of fatigue lives under different stress states.

Stress level (MPa)	Mixing method	Coefficient of variation $C_v$ (%)		
		Indirect tensile	Four-point bending	Unconfined compression
0.25	Vibration	8.88	6.73	—
	Nonvibration	9.62	10.56	—
0.5	Vibration	6.84	9.29	—
	Nonvibration	8.18	10.36	—
1.0	Vibration	5.61	6.09	—
	Nonvibration	7.72	7.70	—
1.5	Vibration	4.31	3.44	—
	Nonvibration	5.06	4.72	—
3.5	Vibration	—	—	9.65
	Nonvibration	—	—	11.97
6	Vibration	—	—	8.0
	Nonvibration	—	—	7.85
8	Vibration	—	—	4.28
	Nonvibration	—	—	8.36
10	Vibration	—	—	4.83
	Nonvibration	—	—	7.37

TABLE 6: Coefficient of variation of the modulus test results of specimens prepared by vibratory and nonvibratory mixing.

Stress level (MPa)	Mixing method	Coefficient of variation $C_v$ (%)		
		Indirect tensile	Four-point bending	Unconfined compression
0.25	Vibration	3.32	2.36	—
	Nonvibration	9.83	6.21	—
0.5	Vibration	2.01	4.46	—
	Nonvibration	7.57	5.64	—
1.0	Vibration	4.75	3.75	—
	Nonvibration	7.47	8.29	—
1.5	Vibration	4.00	3.35	—
	Nonvibration	7.85	8.38	—
3.5	Vibration	—	—	3.10
	Nonvibration	—	—	3.33
6	Vibration	—	—	3.66
	Nonvibration	—	—	7.58
8	Vibration	—	—	6.62
	Nonvibration	—	—	8.04
10	Vibration	—	—	5.22
	Nonvibration	—	—	11.89

had better adaptability and stability than the nonvibratory mixing.

**3.3. Fatigue Test Results and Analysis.** According to the Test Methods of Materials Stabilized with Inorganic Binders for Highway Engineering (JTG E51-2009) (2009), the stress-control mode and the continuous half-sine load with frequency of 10 Hz were used for the standard fatigue tests. And then, unconfined compression tests, indirect tensile tests, and four-point bending tests were carried out on the specimens with different mixing techniques. The unconfined compressive strength of the vibratory mixed specimen was 11.76 MPa, and the corresponding maximum load was 207.82 kN. By contrast, the unconfined compressive strength of the nonvibratory mixed specimen was 9.98 MPa, and the corresponding maximum load was 176.36 kN. Similarly, the indirect tensile strength of the vibratory mixed specimen was 1.298 MPa, and the corresponding maximum load was 46.60 kN. The indirect tensile strength of the nonvibratory specimen was 1.129 MPa, and the corresponding maximum load was 40.53 kN. The four-point bending strength of the vibratory specimen was 1.309 MPa, and the corresponding maximum load was 9.820 kN. The four-point bending strength of the nonvibratory specimen was 1.174 MPa, and the corresponding maximum load was 8.805 kN. And then, the standard strength test results under three different stress states were used as the standard fatigue test parameters, respectively. The selected stress ratio was 0.6 according to the specification (2009), and the fatigue test results are shown in Figure 11.

It is observed that under standard conditions the fatigue life of the specimens prepared by vibratory mixing was higher than that of the specimens prepared by nonvibratory mixing (Figures 11). Under the standard test condition (from 1060966 times to 1296586 times), the unconfined compressive fatigue life of the vibrating specimens was increased by about 22%. Under the standard

test condition (from 177355 times to 205411 times), the indirect tensile fatigue life of the vibrating specimens was increased by about 16%. Under the standard test condition (from 195864 times to 230538 times), the bending tensile fatigue life of the vibrating specimens was increased by about 18%. It is found that the vibratory mixing was more significant for the fatigue life under standard conditions increase of unconfined compressive fatigue test results.

In order to investigate the variation of fatigue life of specimens at different stress levels, the unconfined compression tests, indirect tensile tests, and four-point bending fatigue tests were carried out regarding standard fatigue test procedures. The real stress ratio was obtained by the following equation:

$$t_s = \frac{\sigma}{R_c}, \quad (5)$$

where  $t_s$  is the stress ratio related to loading rates;  $\sigma$  is the stress level (MPa); and  $R_c$  is the strength corresponding to the stress level (MPa).

The fatigue life results and the real stress ratio were fitted by equation (6) in double logarithmic coordinates, as shown in Figures 12–14:

$$\lg N_f = a - kt_s, \quad (6)$$

where  $N_f$  is the fatigue life of the specimen;  $t_s$  is the real ratio; and  $a, k$  are the fitting parameters.

Figures 12–14 show that the unconfined compressive, indirect tensile, and four-point bending fatigue life of the cement-treated aggregate varied significantly with the real stress ratio.

It is noted that the  $k$  value of the vibratory mixed specimen was significantly smaller than that of the nonvibratory mixed specimen. This indicates that vibratory mixing was able to alleviate the fatigue failure of the cement-treated aggregates under any stress state.



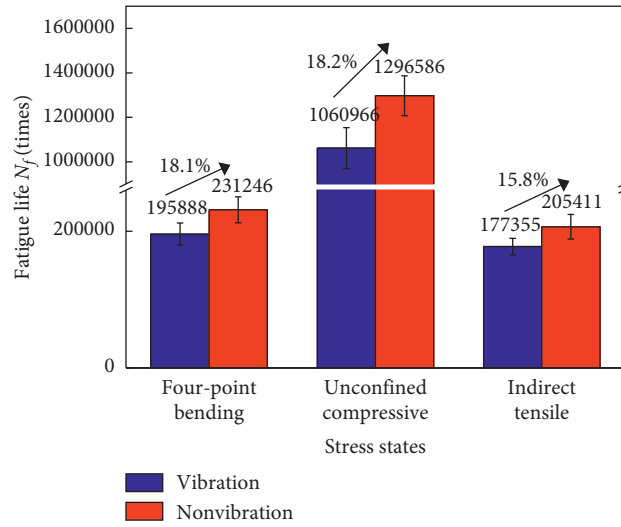


FIGURE 11: Standard fatigue life of vibratory and nonvibratory mixed specimens under different stress states.

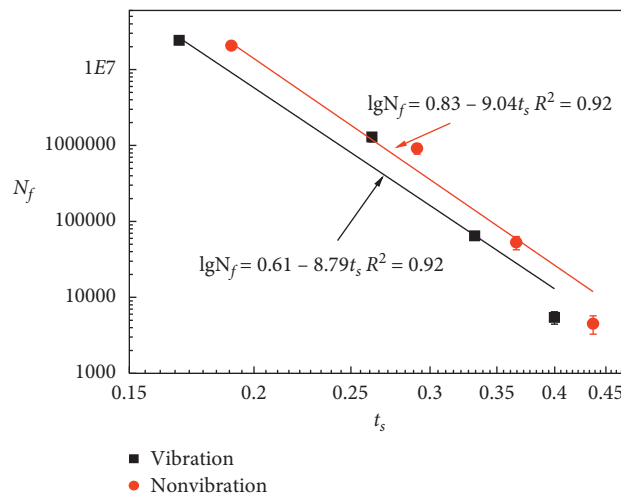


FIGURE 12: Unconfined compressive fatigue curve based on real stress ratio of specimens prepared with different mixing techniques.

The coefficients of variation  $C_v$  of fatigue life results are shown in Table 6. It is found that vibratory mixing can significantly reduce the coefficient of variation, which indicates that the cement-treated aggregates of the vibratory mixed specimen had better stress sensitivity in terms of fatigue performance than that of the nonvibratory mixed specimen.

**3.4. X-Ray CT Test Results and Analysis.** The cement-treated aggregate is a loose multiphase composite material, which has obvious nonuniform characteristics. Generally, it is easy to produce weak surfaces in the interior due to the uneven distribution of cementitious material and aggregate.

In order to study the dispersion of internal materials of cement-treated aggregates prepared by different mixing techniques, X-ray CT tests were carried out on the cylindrical specimens cured for 90 days. The X-ray CT test results of the circular cross section are shown in Figure 15.

It is observed that the specimens prepared by nonvibratory mixing had many voids between coarse aggregates. In other words, the voids were not filled by fine aggregates. By contrast, the specimens prepared by vibratory mixing had fewer voids and higher compactness. Fine aggregates in nonvibratory mixed specimens exhibited serious agglomeration. Because of the agglomeration of fine aggregates around coarse aggregates, coarse aggregates could be better wrapped. Since the emergence of the phenomenon of agglomeration, the coarse aggregates cannot be fully wrapped.

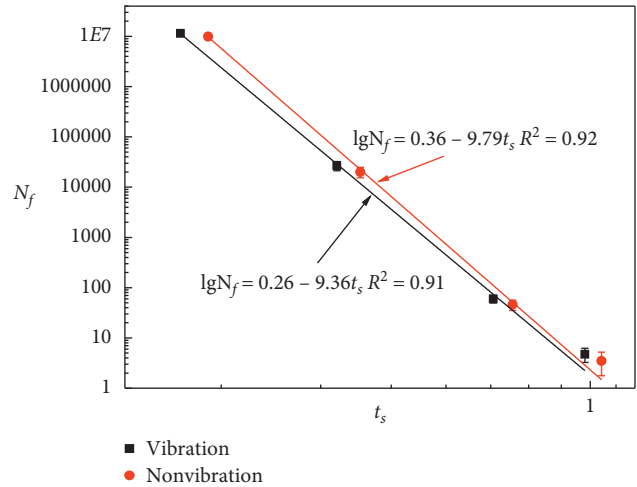


FIGURE 13: Indirect tensile fatigue curve based on real stress ratio of specimens prepared by different mixing techniques.

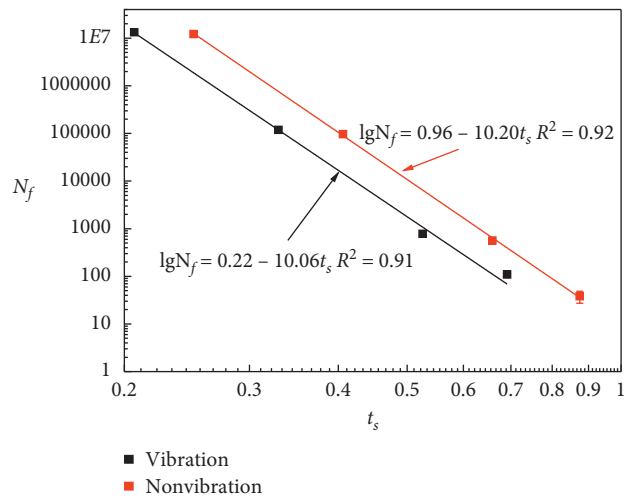


FIGURE 14: Four-point bending fatigue curve based on real stress ratio of specimens prepared by different mixing techniques.

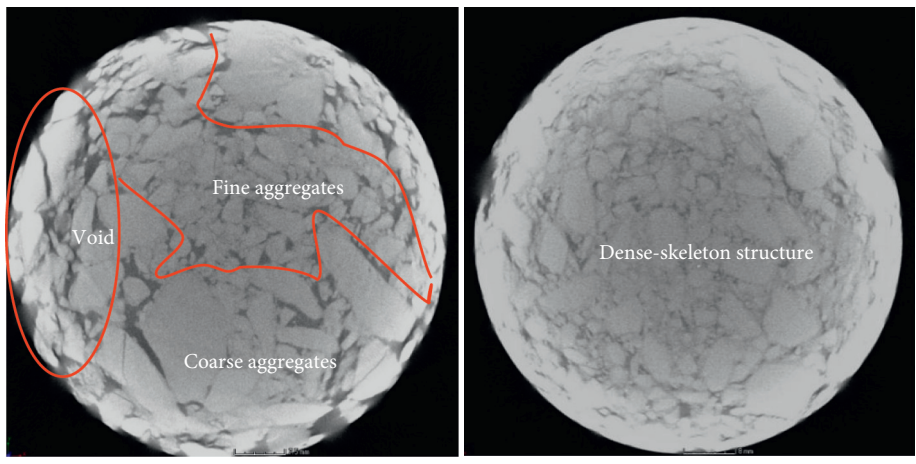


FIGURE 15: The X-ray CT test results of the circular cross section of cement-treated aggregates prepared by different mixing techniques.

## 4. Conclusions

In this study, the strength, modulus, and fatigue life of cement-treated aggregates specimens prepared by different mixing techniques were tested. Meanwhile, the meso-structure of cement-treated aggregates was analyzed by X-ray CT. The following conclusions can be drawn from this study:

- (1) Compared with the nonvibratory mixing technique, the vibratory mixing technique enables cement-treated aggregates to have higher strength, modulus, and fatigue life. Moreover, the vibratory mixing techniques for improving unconfined compressive strength, modulus, and fatigue life were significantly higher than the other two stress state, which will facilitate its promotion and application.
- (2) Vibratory mixing technique significantly weakened the agglomeration of fine aggregates, so coarse aggregates could be sufficiently wrapped by fine aggregates. Thereby the overall compactness of cement-treated aggregates was much improved by vibratory mixing.
- (3) Further work could be focused on establishing the relationship between the microscopic characteristics and the mechanical properties of cement-treated aggregates.

## Data Availability

The data used to support the findings of this study are available from the corresponding author upon request.

## Conflicts of Interest

The authors declare that they have no conflicts of interest.

## Acknowledgments

This work was supported by the National Natural Science Foundation of China (Grant nos. 51838001 and 51908069).

## References

- [1] Y. Zheng, P. Zhang, Y. Cai, Z. Jin, and E. Moshtagh, "Cracking resistance and mechanical properties of basalt fibers reinforced cement-stabilized macadam," *Composites Part B: Engineering*, vol. 165, pp. 312–334, 2019.
- [2] Q. Li, Z. Wang, Y. Li, and J. Shang, "Cold recycling of lime-fly ash stabilized macadam mixtures as pavement bases and subbases," *Construction and Building Materials*, vol. 169, pp. 306–314, 2018.
- [3] Y. Sun and L. Li, "Strength assessment and mechanism analysis of cement stabilized reclaimed lime-fly ash macadam," *Construction and Building Materials*, vol. 166, pp. 118–129, 2018.
- [4] T. Huang, S. Qi, H. Liu, H. Yu, and S. Li, "Shear properties of asphalt mixtures under triaxial compression," *Applied Sciences*, vol. 9, no. 7, p. 1489, 2019.
- [5] L. Song, Z. Song, C. Wang, X. Wang, and G. Yu, "Arch expansion characteristics of highway cement-stabilized macadam base in Xinjiang, China," *Construction and Building Materials*, vol. 215, pp. 264–274, 2019.
- [6] A.-M. Sha, "Material characteristics of semi-rigid base," *China Journal of Highway and Transport*, vol. 97, no. 1, pp. 1–5, 2008.
- [7] C. Deng, Y. Jiang, H. Lin, and X. Ji, "Mechanical-strength-growth law and predictive model for cement-stabilized macadam," *Construction and Building Materials*, vol. 215, pp. 582–594, 2019.
- [8] S. H. Chu, "Effect of paste volume on fresh and hardened properties of concrete," *Construction and Building Materials*, vol. 218, pp. 284–294, 2019.
- [9] T. Hemalatha, K. R. Ram Sundar, A. R. Murthy, and N. R. Iyer, "Influence of mixing protocol on fresh and hardened properties of self-compacting concrete," *Construction and Building Materials*, vol. 98, pp. 119–127, 2015.
- [10] C. Liu and S. Lv, "Analysis and comparison of different impacts of aging and loading frequency on fatigue characterization of asphalt concrete," *Journal of Materials in Civil Engineering*, vol. 32, no. 9, Article ID 04020240, 2020.
- [11] C. Liu and S. Lv, "Normalized characterization method for fatigue behavior of cement treated aggregates based on the yield criterion," *Construction and Building Materials*, vol. 228, pp. 1–9, 2019.
- [12] S. Du, "Influence of chemical additives on mixing procedures and performance properties of asphalt emulsion recycled mixture with reclaimed cement-stabilized macadam," *Construction and Building Materials*, vol. 118, pp. 146–154, 2016.
- [13] W. Li, L. Lang, Z. Lin, Z. Wang, and F. Zhang, "Characteristics of dry shrinkage and temperature shrinkage of cement-stabilized steel slag," *Construction and Building Materials*, vol. 134, pp. 540–548, 2017.
- [14] S. Lv, C. Liu, J. Lan, H. Zhang, J. Zheng, and Z. You, "Fatigue equation of cement-treated aggregate base materials under a true stress ratio," *Applied Sciences*, vol. 8, no. 5, p. 691, 2018.
- [15] C. Liu, S. Lv, D. Jin, and F. Qu, "Laboratory investigation for the road performance of asphalt mixtures modified by rock asphalt/styrene butadiene rubber," *Journal of Materials in Civil Engineering*, vol. 33, no. 3, p. 04020504, 2021.
- [16] J. Marchand, "The microstructures of dry concrete products," *Cement and Concrete Research*, vol. 26, no. 3, 1996.
- [17] S. Lv, Y. Jiang, and X. Peng, "Standardization to evaluate the lasting capacity of rubberized asphalt mixtures with different testing approaches," *Construction and Building Materials*, vol. 32, Article ID 121341, 2020.
- [18] F. Autelitano and F. Giuliani, "Electric arc furnace slags in cement-treated materials for road construction: mechanical and durability properties," *Construction and Building Materials*, vol. 113, pp. 280–289, 2016.
- [19] U. G. Eziefula, J. C. Ezeh, and B. I. Eziefula, "Properties of seashell aggregate concrete: a review," *Construction and Building Materials*, vol. 192, pp. 287–300, 2018.
- [20] W. Fedrigo, W. P. Núñez, M. A. Castañeda López, T. R. Kleinert, and J. A. P. Ceratti, "A study on the resilient modulus of cement-treated mixtures of RAP and aggregates using indirect tensile, triaxial and flexural tests," *Construction and Building Materials*, vol. 171, pp. 161–169, 2018.
- [21] C. Xia, "Unified characterizing fatigue performance of rubberized asphalt mixtures subjected to different loading modes," *Journal of Cleaner Production*, vol. 23, 2021.
- [22] J. Dils, G. De Schutter, and V. Boel, "Influence of mixing procedure and mixer type on fresh and hardened properties of concrete: a review," *Materials and Structures*, vol. 45, no. 11, pp. 1673–1683, 2012.

- [23] C. F. Ferraris, "Concrete mixing methods and concrete mixers: state of the art," *Journal of Research of the National Institute of Standards and Technology*, vol. 106, no. 2, pp. 391–399, 2001.
- [24] P.-K. Chang and Y.-N. Peng, "Influence of mixing techniques on properties of high performance concrete," *Cement and Concrete Research*, vol. 31, no. 1, pp. 87–95, 2001.
- [25] H. Shen, Z. S. Duan, and F. Li, "The evaluation about vibratory mixing methods," *Applied Mechanics and Materials*, vol. 219, pp. 2678–2682, 2012.
- [26] L. Zhao, "Influence of mixing methods on performance of compressive strength for cement stabilized macadam mixture," *China Journal of Highway and Transport*, vol. 31, no. 1, pp. 151–158, 2018.
- [27] J. Xue and Y. Jiang, "Analysis on the fatigue properties of vertical vibration compacted lime-fly ash-stabilized macadam," *Construction and Building Materials*, vol. 155, pp. 531–541, 2017.
- [28] Y.-J. Jiang, "Road performance and composition design of cement-ash stabilized aggregate of dense framework structure," *Journal of Chang'an University (Natural Science Edition)*, vol. 5, pp. 1–4, 2008.
- [29] L. Zhang and Z. Feng, "Process of concrete mixing and its evaluation," *Journal of Chang'an University (Natural Science Edition)*, vol. 31, no. 2, pp. 101–105, 2011.
- [30] L. Zhang, Z. Feng, and L. Zhao, "Test study of 1 m<sup>3</sup> vibratory concrete mixer with double-horizontal shafts," *Journal of Guangxi University (Natural Science Edition)*, vol. 38, no. 2, pp. 250–255, 2013.
- [31] Y. Yao, J. Ni, and J. Li, "Stress-dependent water retention of granite residual soil and its implications for ground settlement," *Computers and Geotechnics*, vol. 129, Article ID 103835, 2021.
- [32] H. Beitzel, Y. Charonnat, and M. Beitzel, "Assessment and classification of performance mixers," *Materials and Structures*, vol. 36, no. 4, pp. 250–264, 2003.